Quantification of Rock Damage from Small Explosions and Its Effect on Shear-Wave Generation

Mark Leidig
Jessie Bonner
Randolph J. Martin
Peter Boyd
Jim Lewkowicz

Weston Geophysical Corporation
181 Bedford St., Suite 1
Lexington, MA, 02420

Final Report

15 June 2009
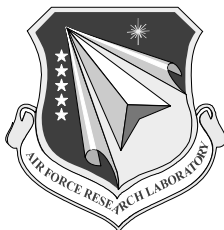
AIR FORCE RESEARCH LABORATOR
Space Vehicles Directorate
29 Randolph Rd.
AIR FORCE MATERIEL COMMAND
**HANSCOM AFB, MA 01731-3010**

NOTICES

Using Government drawings, specifications, or other data included in this document for any purpose other than Government procurement does not in any way obligate the U.S. Government. The fact that the Government formulated or supplied the drawings, specifications, or other data does not license the holder or any other person or corporation; or convey any rights or permission to manufacture, use, or sell any patented invention that may relate to them.

This report was cleared for public release and is available to the general public, including foreign nationals. Qualified requestors may obtain copies of this report from the Defense Technical Information Center (DTIC) (http://www.dtic.mil). All others should apply to the National Technical Information Service.

AFRL-RV-HA-TR-2009-1056 HAS BEEN REVIEWED AND IS APPROVED FOR PUBLICATION IN ACCORDANCE WITH ASSIGNED DISTRIBUTION STATEMENT.

ROBERT J. RAISTRICK
Contract Manager
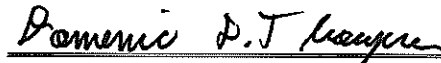
Domenic Thompson, Maj, USAF, Chief
Battlespace Surveillance Innovation Center

This report is published in the interest of scientific and technical information exchange, and its publication does not constitute the Government's approval or disapproval of its ideas or findings.

REPORT DOCUMENTATION PAGE

Form Approved
OMB No. 0704-0188

1. REPORT DATE *(DD-MM-YYYY)* 15-Jun-2009	2. REPORT TYPE Final Report	3. DATES COVERED *(From - To)* 15 May 2008-15 June 2009

4. TITLE AND SUBTITLE

Quantification of Rock Damage from Small Explosions and Its

Effect on Shear-Wave Generation

5a. CONTRACT NUMBER
FA8718-08-C-0044

5b. GRANT NUMBER
N/A

5c. PROGRAM ELEMENT NUMBER
62601F

6. AUTHOR(S)

Mark Leidig, Jessie Bonner, Randolph J. Martin, Peter Boyd,

and Jim Lewkowicz

5d. PROJECT NUMBER
1010

5e. TASK NUMBER
SM

5f. WORK UNIT NUMBER
A1

7. PERFORMING ORGANIZATION NAME(S) AND ADDRESS(ES)

Weston Geophysical Corporation
181 Bedford St., Suite 1
Lexington, MA 02420

8. PERFORMING ORGANIZATION REPORT NUMBER

9. SPONSORING / MONITORING AGENCY NAME(S) AND ADDRESS(ES)

Air Force Research Laboratory
29 Randolph Rd.
Hanscom AFB, MA 01731-3010

10. SPONSOR/MONITOR'S ACRONYM(S)

AFRL/RVBYE

11. SPONSOR/MONITOR'S REPORT NUMBER(S)
AFRL-RV-HA-TR-2009-1056

12. DISTRIBUTION / AVAILABILITY STATEMENT

Approved for Public Release; Distribution Unlimited.

13. SUPPLEMENTARY NOTES

14. ABSTRACT

Weston Geophysical Corp., New England Research, Inc., and several geotechnical consultants conducted the Vermont/New England Damage Experiment in central Vermont during July 2008. A series of five explosions using charges with yields of 135 and 270 lbs and three types of explosives were detonated in homogeneous, low fracture density granite. The goal of the experiment was to generate different amounts of rock damage around the source by using explosives with dramatically different velocities of detonation (VOD), and then relate the shear wave generation to the amount of damage. We used pre- and post-shot core analysis to quantify significant differences in the damage induced by the explosions. Velocities are slower, permeabilities are higher, resistivities are lower, and porosities are higher in the damaged intervals. These results are consistent with a microcrack scale fracture population that is enhanced by the blasts. Over 140 seismic sensors were installed to record the blasts. Peak particle velocity (PPV) studies found that the fastest VOD explosive, Composition B, expended much of its energy at the source pulverizing the surrounding rock, while the middle VOD explosive, heavy ANFO, produced the largest PPV. Source scaling studies found the black powder shot produced seismic amplitudes up to an order of magnitude less than the ANFO and COMP B amplitudes above 5 Hz, but created Rayleigh waves similar in amplitude to those from the ANFO shot. The black powder shot produced larger Rayleigh and Love waves than the COMP B shot. The ANFO and COMP B shots generated similar amplitudes above 8 Hz, but the ANFO source Rayleigh waves were up to twice as large and the Love waves were up to three times as large as those from the COMP B shot. These results indicate that rock damage may be responsible for some of the differences in surface and shear wave generation.

15. SUBJECT TERMS

Explosions, Seismic source mechanics, Rock damage, Shear-wave generation, Nuclear monitoring, Seismology

16. SECURITY CLASSIFICATION OF:

a. REPORT UNC	b. ABSTRACT UNC	c. THIS PAGE UNC

17. LIMITATION OF ABSTRACT
SAR

18. NUMBER OF PAGES
168

19a. NAME OF RESPONSIBLE PERSON
Robert Raistrick

19b. TELEPHONE NUMBER *(include area code)*
781-377-3726

Standard Form 298 (Rev. 8-98)
Prescribed by ANSI Std. Z39.18

Table of Contents

List of Figures

List of Tables

1. SUMMARY

Explosions generate *S* waves (*Lg*) that can be used as stable estimators of yield for nuclear explosion test sites in different emplacement media and under variable confinement conditions and tectonic stresses. Yet, the Nuclear Explosion Monitoring (NEM) research community has no unifying model for *S*-wave generation from explosions. Instead, there are only theories on the mechanisms for *S*-wave generation from explosions. Proposed explanations for the *Lg* phase include *pS* conversions at the free surface (Xie and Lay, 1994) and *Rg* generated by a compensated linear-vector dipole source (CLVD; Gupta *et al*., 1997; Patton and Taylor, 1995; Stevens *et al*., 2003a; Patton *et al*., 2005) that is scattered (Myers *et al*., 1999) into *S* and/or *Lg* along the propagation path due to topography (Myers, 2007) and/or geology heterogeneity (Lay and Xie, 2007). Modeling by Sammis (2003) has shown that crack nucleation and growth can generate significant *S* waves in the far-field. To date, it has been difficult to separate each mechanism in the available NEM datasets in order to quantify their relative effects on *S*-wave generation.

Two of the proposed mechanisms for *S*-wave generation involve secondary processes related to the damage and deformations caused by the explosions. First, outside the cavity radius, there is a "shell" of fragmented rock. Sammis (2002) theoretically showed that the integrated effect of the nucleation and growth of the fractures in this shell can generate secondary seismic waves as large as the *P* waves from the explosion itself.

The second proposed method is a Compensated Linear Vector Dipole (CLVD) source, which is an elastodynamic equivalent of a conical source. In this case, it is an inverted cone with apex at the detonation point (Patton *et al*., 2005). Media within the cone deforms and fails as a result of tensile stresses caused by the downgoing shock wave reflected off the free surface. Spallation is an obvious example of such failure. Driven block motions at depth, as envisioned by Masse (1981), is another example, which may have greater significance for seismic wave generation.

Weston Geophysical Corp., New England Research, Inc., and several geotechnical consultants conducted the Vermont Damage Experiment in central Vermont during July 2008. A series of five explosions using charges having yields of 135 and 270 lbs and three types of explosives were detonated in homogeneous low fracture density granite. The goal of the experiment was to generate different amounts of rock damage around the source by using explosives with dramatically different velocities of detonation (VOD), ranging from 0.5 to 8.1 km/sec, and then relate the shear wave generation to the amount of damage. Increased VOD causes increased borehole pressures, which exceed the rock's compressive breaking strength, and results in more extensive fracturing of the source rock. This zone of highly fractured rock prevents the explosive gases from being able to drive long fractures. In contrast, slower VOD explosives generate fewer fractures around the borehole, but the explosive gases are able to enter the cracks and drive long fractures. Surface observation of the test site confirmed this as few radial fractures were found for the fast VOD explosive, multiple small cracks were seen for the middle VOD explosive, and large fractures with surface displacement were found for the slowest VOD explosive.

We used pre- and post-shot core analysis to quantify significant differences in the damage induced by the explosions. The extent of damage can be characterized by determining rock properties. Laboratory measurements of ultrasonic velocities, permeability, resistivity and porosity are sensitive to the microcrack density in the granite. Velocities are slower, permeabilities are higher, resistivities are lower, and porosities are higher in the damaged intervals. These results are consistent with a microcrack scale fracture population that is enhanced by the blasts. This damage has been determined to extend vertically to as much as 6-7 meters from the explosive charge emplacement. Larger scale fractures are not apparent below the blasts, but are developed above the blast interval and they extend beyond the interval identified by the laboratory measurements.

Over 140 seismic sensors were installed to record the blast, ranging in distance from 5 m to 30 km. Peak particle velocity (PPV) studies found that the fastest VOD explosive, Composition B, expended much of its energy at the source pulverizing the surrounding rock. The middle VOD explosive, heavy ANFO, produced the largest PPV, while the slowest VOD explosive, black powder, produced PPV one-third the size of the ANFO PPV.

Source scaling studies found the black powder shot produced seismic amplitudes up to an order of magnitude less than the ANFO and COMP B amplitudes above 5 Hz, but created Rayleigh waves similar in amplitude to those from the ANFO shot. The black powder shot produced larger Rayleigh and Love waves than the COMP B shot. The ANFO and COMP B shots generated similar amplitudes above 8 Hz, but the ANFO source Rayleigh waves were up to twice as large and the Love waves were up to three times as large as those from the COMP B shot. The seismic waves followed an almost identical travel path indicating that differences in the source region (e.g., possibly damage) are responsible for the variations in surface and shear wave energy.

2. EXPERIMENT QUICKLOOK

INTRODUCTION

Weston Geophysical Corp., New England Research, Inc., and a variety of blasting and geotechnical consultants conducted the experimental field phase of the New England Damage Experiment (NEDE) in a granite quarry near Barre, VT, during the first three weeks of July 2008. The goal of this experiment was to characterize the damage around an explosion and to identify possible source(s) of shear wave generation. The velocity of explosive detonation (VOD) and resulting borehole pressures have been shown to influence the amount of damage from an explosion (http://www.johnex.com.au/index.php?section=105 (last accessed in June 2009)). A faster VOD generates higher pressures that crush the rock into a powder, which inhibits the explosive gasses during the crack forming processes. We detonated various types of explosives with significantly different VOD so we could examine the quantity of damage from each source. Seismic sensors were installed specifically to record this experiment. Pre-blast studies of the source rock properties were conducted and were compared to post-blast studies so that the damage generated by the explosions could be quantified. We have conducted initial analyses of the data to quantify the shear wave generation. The goal of this chapter of the report is to document the field project and the data collected.

Objective
Recent advances in explosion source theory indicate that the damage that occurs near an explosion is a prominent source of *S*-wave energy. The Ashby and Sammis (1990) model for crack nucleation and growth predicts *S*-wave generation in the far field (Figure 1; Sammis, 2002). Modeling by Patton *et al.* (2005) and Stevens *et al.* (2003a) have shown the importance of the cone of damage above a source, modeled by a compensated linear vector dipole (CLVD), in generating *Rg* in the near field and *S (Lg)* in the far field, respectively. The phenomenology in the CLVD regime includes block motions, crack damage, and spallation. The NEDE was conducted to test these theories and provide empirical data to aid in answering questions regarding shear wave generation mechanism(s).

Location
The NEDE was conducted in the Barre granite, a homogenous hard rock with low fracture density (Figure), to allow study of the damage zones and fractures created by a fully confined and contained explosion. Figure shows a general geologic map of Vermont with a black box showing the location of the Barre granite. The geology of Vermont is an extension of the Appalachian Mountains with structural trends that generally run in a north to northeast orientation. The Barre granite is a felsic intrusion into Silurian to Devonian age rocks of the Connecticut Valley-Gaspe Basin caused by melting due to closing of a basin and collision of continental landmasses (Doolan, 1996). Significant reshaping of the land occurred under thick ice sheets.
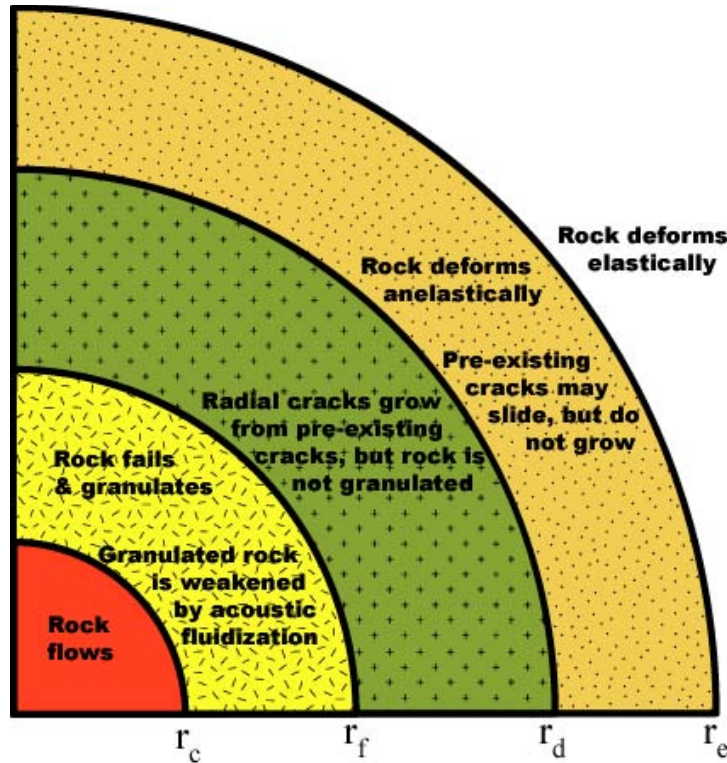
Figure 1. Rheology surrounding an underground explosion (after Rodean (1971) and modified by Sammis for acoustic fluidization from Melosh, 1979).

The fine-grained Barre grey granite has been quarried for over 100 years as a monument stone due its low fracture density and homogeneous composition. While coring the granite for our test applications, the driller often had to snap the core from the bottom of the hole due to a lack of naturally occurring fractures. A site near the active quarry pit was originally chosen for the blasts (Figure). The upper 50 feet of fractured and weathered granite had been stripped off at this site, which allowed us to be closer in depth to the relatively-unfractured, monument-quality Barre granite. Unfortunately, this site was too close to a nearby cell/radio tower and the active quarry wall to detonate our planned 400 lb explosions.

Core drilling at an alternative test site (Figure) was conducted further away from the active quarry wall and a nearby cell/radio tower. The alternative site would be far enough away from the sensitive structures so that the planned 400 lb blasts could be safely detonated. Unfortunately, the granite had a much higher fracture density (it was quarried for aggregate stone) and drilling encountered large schistosic xenoliths (Figure). This site was abandoned and the experiment was returned into the original location (Figure). In order to reduce the projected ground vibrations at the cell/radio tower and high wall of the active quarry to safe limits, we scaled the planned explosions down to ~200 lbs.

Figure 2. Photograph of 3-5 m thick relatively-unfractured sections of Barre granite. The test site was located behind this granite ledge.
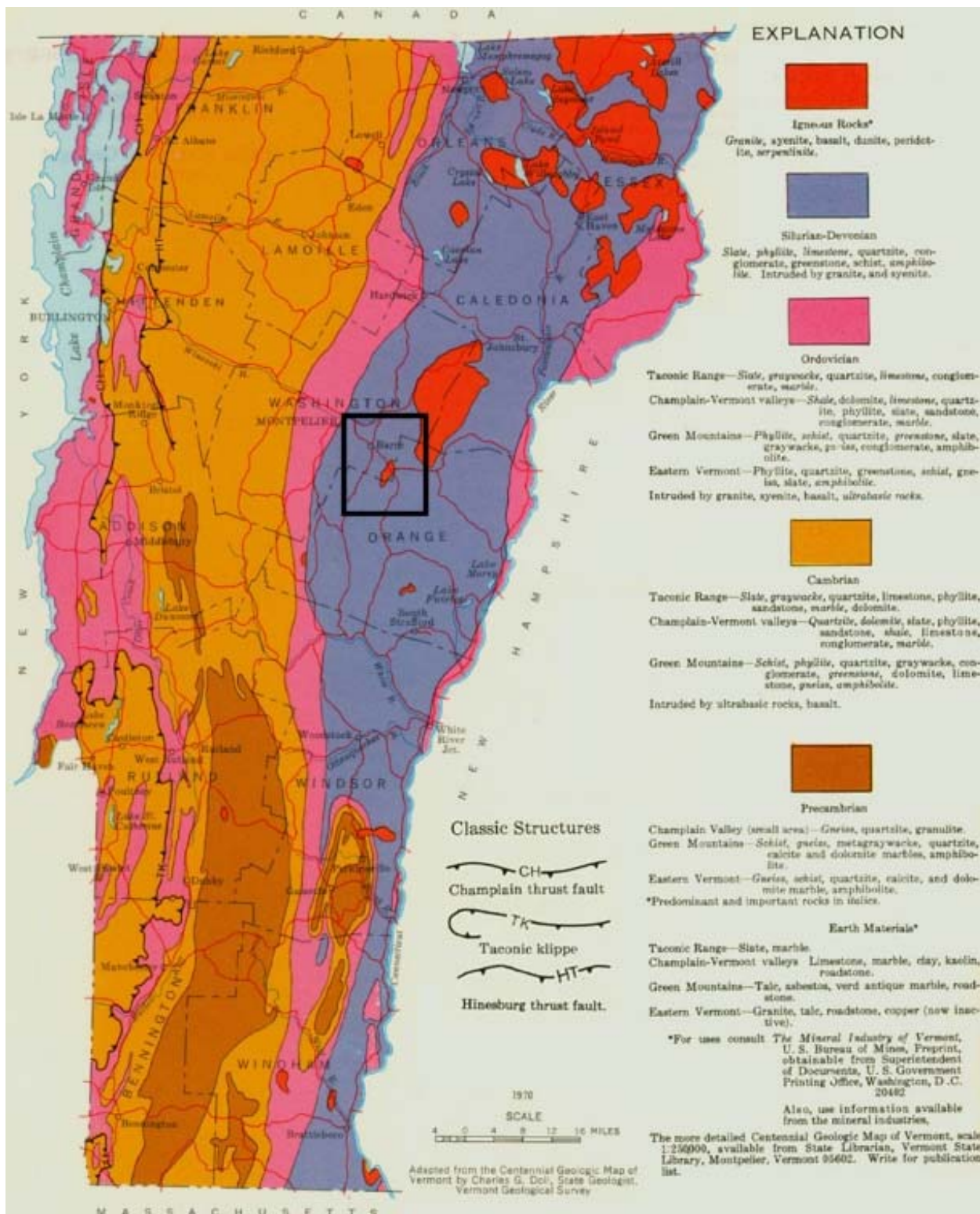
Figure 3. Geologic map (modified) from the Vermont Geological Survey. The black box highlights Barre, VT and the Barre granite igneous intrusion to the southeast. Source: http://www.anr.state.vt.us/DEC/GEO/images/geo5.JPG (last accessed June 2009)
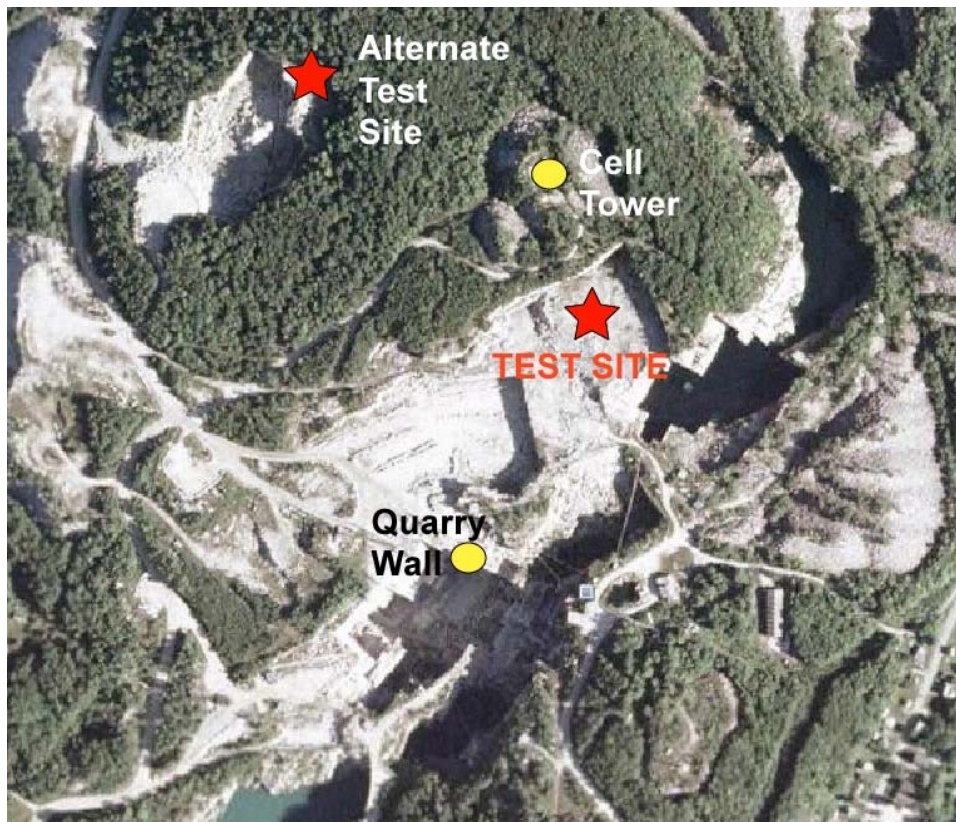
Figure 4. Location of the test site and alternative test site in relation to nearby structures.

Figure 5. Photo of the highly-fractured nature of the granite at the alternative test site (see Figure 4) and a contact with large xenoliths at the abandoned test site.

SEISMIC DEPLOYMENTS

The NEDE explosions were recorded on over 140 seismic instruments, including short-period seismometers, high-g accelerometers, and a high-resolution video camera, deployed at distances of less than 5 m to 30 km from the explosions. We recovered 99.7% of the data.

Near-Source Array

Jessie Bonner, James Britton, Katherine Murphy, Sam Huffstetler, Delaine Reiter, and Mark Leidig (Weston) deployed 6 short period Mark Product L4-3D seismometers, 2 Endevco 100 g accelerometers, and 5 TerraTek 40 g accelerometers in close proximity to the explosions to record the source phenomenology. All of these instruments recorded three components (3C) of motion. One of the accelerometers (N1B) was moved before each shot to be less than 5 m from the borehole to record shot time. In addition to acquiring shot time, these near-source data will be used in moment tensor inversions. Table 1 lists the locations and instrumentation deployed for the three-component near-source array. Figure shows the locations of the very close-in sensors and the shot locations. The remainder of the near-source stations, at distances of less than 1 km, can be seen in Figure 7.

Station N5 was across an 80 m deep quarry pit (Don Murray, pers. comm.), now filled with water. This pit may have an effect on the data at station N5 and the data for some shots at station N4. Station N2 was deployed above the test site on the edge of a high wall.

Table 1. Near-source 3C Sensors.

Station	Latitude	Longitude	Elev (m)	Channels 1-3	S/N	Channels 4-6	S/N	DAS	DISK	GPS
N1A	44.15785	-72.47808	503	Endevco	6			734	5715	663
N1B Shot 1	44.15782	-72.47852	501			Endevco	2	734	5715	663
N1B Shot 2	44.15803	-72.47814	508			Endevco	2	734	5715	663
N1B Shot 3	44.15783	-72.47773	507			Endevco	2	734	5715	663
N1B Shot 4	44.15749	-72.47793	506			Endevco	2	734	5715	663
N1B Shot 5	44.15752	-72.47753	503			Endevco	2	734	5715	663
N2	44.15826	-72.47862	533	L4-3D	189	TerraTek	7	738	87	664
N3	44.15724	-72.47930	492	L4-3D	257	TerraTek	9	716	5106	248
N4	44.15642	-72.47736	500	L4-3D	619	TerraTek	8	733	5959	669
N5	44.15687	-72.47575	506	L4-3D	37	TerraTek	6	739	5247	674
N6	44.15967	-72.48204	489	L4-3D	L41168			940F		4196
N7	44.15637	-72.47913	502	L4-3D	628	TerraTek	4	743	5713	244

The near-source accelerometers and seismometers were placed in a shallow hole, oriented to true north, and lightly covered with dirt. True north was 16° west of magnetic north at our location for the experiment. For placement of the Endevco accelerometers, very shallow holes were dug into the granite with a rock bar. The sensors were coupled to the granite with dirt and granite flour from the drilling. Data were recorded at 250 sps on 24-bit Reftek 72A-08 DAS for all stations except N6, which was digitized on a Reftek RT130. More recording parameters can be found in Table 2. The DAS and GPS clock were placed in a plastic tub and covered by a garbage bag. The external GPS clock acquired GMT time. A 17 Ah deep-cycle battery powered each station. Figure and Figure 9 show examples of the sensor installation and the plastic tub with

recording equipment. Information on the near-source vertical-component only sensors shown in Figure 7 can be found in the following "Texan Network" section.

Table 2. Near-Source Recording Parameters.

Parameter	Value
Digitizer	Reftek 72A-08 (N1-N5, N7) Reftek RT130 (N6)
Channels	Reftek 72A-08 – 6 Reftek RT130 – 3
Resolution	24-bit
Gain	1
Sample Rate	250
Record Mode	Continuous
Data Format	Reftek 72A-08 – PASSCAL* 32 bit Reftek RT130 – PASSCAL Compressed

Figure 6. Test site station N1 (blue triangles) and shots (red stars). N1 consisted of two Endevco accelerometers. N1A remained stationary for all 5 shots, while N1B moved to be less than 5 m from each shot. Station N2 and the camera are also shown on a hill overlooking the test site. (Google Earth Background)

---

* Program for Array Seismic Studies of the Continental Lithosphere
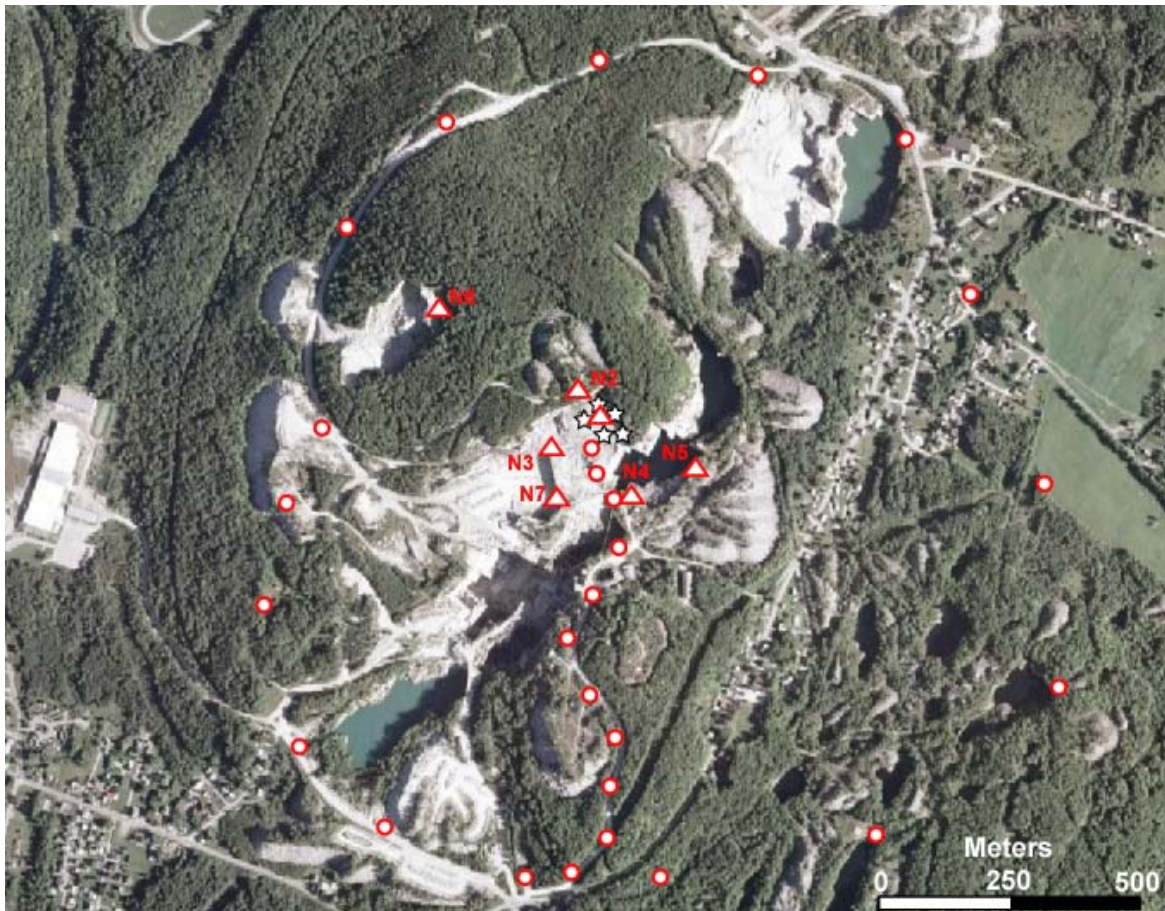
Figure 7. Near-source stations N1-N7 (white triangle with red outline) and Texans[†] NT01-NT27 (white dot with red outline). N1 consisted of two sensors, one of which moved for each shot (Figure 6). The shots (white stars with black outline) can be seen in the middle of the image. (Google Earth Background)

[†] "Texans" refer to single-component geophones recorded on a small digitizer with internal memory and power.

Figure 8. Example of near-source instrument installation. Katherine Murphy levels and orients a TerraTek accelerometer to true north while Sam Huffstetler installs the Reftek 72A-08 digitizer and battery.

Figure 9. A second example of installing a near-source accelerometer and seismometer (Delaine Reiter, Sam Huffstetler, and Mark Leidig).

Station N3 had a timing issue. It is unclear whether this was a problem with the DAS or clock, but at the beginning of a new data file, the time would jump 1 second forward and then back. This would happen a few times for each file. Arrivals at N3 came in late by an increasing number of seconds with respect to the other near-source stations. The offsets seem to be in terms of full seconds as the millisecond accuracy appears to be correct, but we cannot verify this. Corrections to the processed data have been applied by the amounts shown in Table 3. Station N3 should not be used in the development of the velocity model.

Table 3. Station N3 Timing Corrections.

Shot	Correction (sec)
1	3
2	5
3	7
4	11
5	14

Short Period 3C Linear Arrays

Two linear arrays of short-period 3C seismometers were deployed extending away from the test site for 30 km in two directions as shown in Figure and Table 4. Station spacing was designed to be every 3 km "as the crow flies" from the test site. A lack of roads and many inaccessible areas, particularly along the NE line, made maintaining station spacing and a straight line difficult. Station NE06 was not deployed due to a 6 km region void of any roads. The NE line followed the trend of the granite intrusives and the structural trend of the region (Figure), while the SE line cut across the structural trend. The stations were generally located along dirt roads that only saw local resident traffic. Vehicle traffic can be seen in the recordings, and passing cars interfered with a few recordings. Permissions were obtained to install these sensors from the local Vermont towns, but several stations along the NE line required landowner permission as well (Figure 11).

Nine Sercel (formerly Mark Products) 1 Hz L4-3D short period seismometers with Reftek RT130 digitizers were installed along the NE line by Mark Leidig, James Britton, and Katherine Murphy (Weston) and Lisa Foley (PASSCAL). Along the SE line, ten Mark Products 2 Hz L22 short period seismometers were installed by Jessie Bonner, Sam Huffstetler, Delaine Reiter (Weston) and Willie Zamora (PASSCAL). All stations had an external GPS clock for recording GMT time and recorded at 250 sps. More recording information can be found in Table 5.

The sensors were oriented to truth north, placed in a shallow hole, leveled, and loosely covered with soil (Figure). The soil was generally an organic rich dense soil, but sometimes had large amounts of decaying plant matter that left the site somewhat "spongy". No solid bedrock was found at the sites within a foot of the surface. Therefore, it is expected that site responses will have some variation. A huddle test was conducted prior to the experiment and that information can be found in Appendix 2A. PASSCAL collected *in-situ* response information for each of the L22s on the SE line. This information can be found in Appendix 2B. Lisa Foley examined the *in-situ* response data and found sensor 496L (SE02) had a "bad" channel 2 and thinks that a faulty internal connection is the cause. Initial examination of the experiment data did not show any

abnormalities with this sensor. She also noted that the 462L (SE08) sensor had swapped and reversed cables, which made the north/south channel into the east/west channel and vice versa. The polarity on each channel was also flipped. Factory response information for the Sercel L4-3Ds can be found in Appendix 2C.

The RT130 digitizer, GPS clock, and 79 AH deep-cycle battery were placed in a black plastic bag and hidden behind bushes or covered with grass and leaves for camouflage. The GPS clock was held upright by attaching the sensor cable to the DAS through the metal clock loop. At a couple sites, tall grass interfered with satellite reception and the clock was elevated by placing it on top of foam pads that were placed on the battery box.
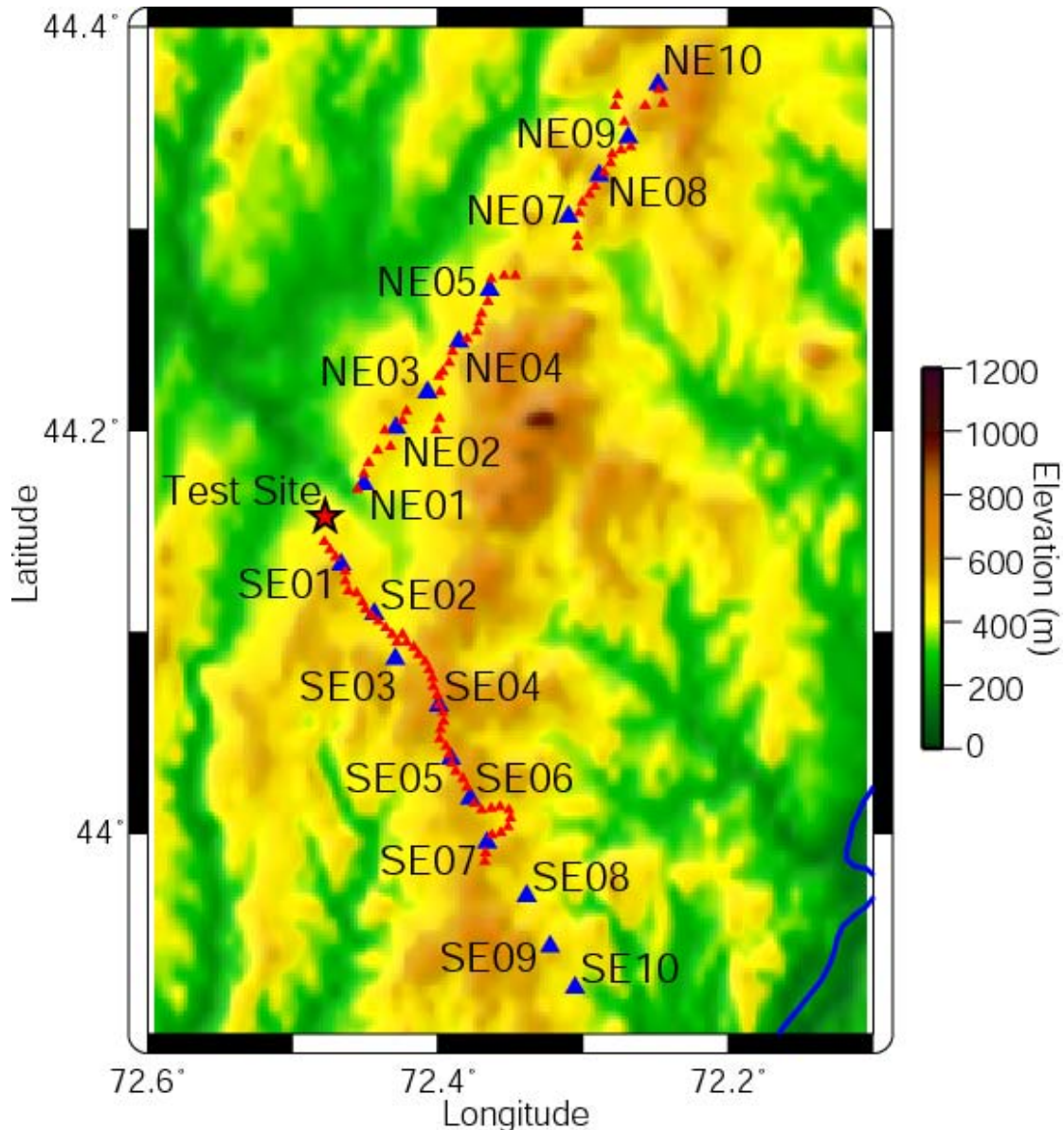
Figure 10. Linear array short period stations (blue triangles) and Texans (red triangles).

Table 4. Short Period Linear Array Stations.

Station	Latitude	Longitude	Elev (m)	Channels 1-3	S/N	DAS	GPS
SE01	44.13362	-72.46659	514	L22	459L	9D63	5155
SE02	44.10946	-72.44367	475	L22	496L	A198	4161
SE03	44.08698	-72.42968	470	L22	479L	9669	4188
SE04	44.06350	-72.39923	595	L22	494L	9E50	4176
SE05	44.03733	-72.39093	588	L22	720L	939E	4175
SE06	44.01771	-72.37772	514	L22	643L	930E	3890
SE07	43.99543	-72.36589	556	L22	449L	9E45	4194
SE08	43.96925	-72.33883	456	L22	462L	9D42	4198
SE09	43.94373	-72.32292	507	L22	642L	9312	4179
SE10	43.92329	-72.30565	369	L22	468L	9E40	4189
NE01	44.17376	-72.45101	420	L4-3D	L41167	9E4B	2449
NE02	44.20178	-72.42899	511	L4-3D	L41166	9D8F	2565
NE03	44.21921	-72.40699	474	L4-3D	L41169	9DEA	2514
NE04	44.24436	-72.38558	462	L4-3D	L41162	9E18	2711
NE05	44.26989	-72.36425	447	L4-3D	L41164	9E1B	2531
NE07	44.30621	-72.30992	436	L4-3D	L41161	9E42	2661
NE08	44.32654	-72.28904	541	L4-3D	L41165	9E4F	2665
NE09	44.34530	-72.26903	461	L4-3D	L41170	9DAA	2516
NE10	44.37157	-72.24832	542	L4-3D	L41163	9E17	2520

Table 5. Short Period Recording Parameters.

Parameter	Value
Digitizer	Reftek RT130
Channels	3
Resolution	24-bit
Gain	32
Sample Rate	250
Record Mode	Continuous
Data Format	PASSCAL Compressed
Sensor	1 Hz Sercel L4-3D (NE01-NE10) 2 Hz Mark L22 (SE01-SE10)
Sensitivity	Appendices B and C

Figure 11. Discussing where to place the station with the landowner of Carrier's Sky Park.

Figure 12. Example of orienting to true north and leveling an L4-3D sensor on the NE line.

Texan Network

Weston Geophysical and IRIS PASSCAL split into three teams and deployed 112 Reftek RT-125 "Texans" (Figure) along the NE and SE short period array lines and around the test site (Figure 7 and Figure). Two of the 112 Texans deployed either had a cable or geophone problem. Data were successfully retrieved from every other instrument in the experiment. The Texan stations are single channel sensors with a 4.5 Hz 3" spike vertical geophone and were installed every 0.5 km along the short period array lines. Willie Zamora and Lisa Foley scouted a possible third line to the west of the test site, but found the road and traffic conditions unfavorable.

The team along the SE line (Sam Huffstetler, Delaine Reiter, and Willie Zamora) installed sensors every 0.5 km of driving mileage, including in close proximity to the short period sensors. Therefore, they installed 45 Texans in about 22 km. Their stations are designated ST01-ST45.

The NE line Texan team (Mark Leidig, Katherine Murphy, and James Britton) installed Texans every 0.5 km ("as the crow flies") with respect to the test site and skipped sites that were near the already installed short period sensors. They were only able to install 40 Texans (NT01-NT40) along their 30 km line with this method because they were confronted with inaccessible regions where no Texans could be placed.

Jessie Bonner, Lisa Foley, and Sam Huffstetler formed the third team and installed 27 Texans around and in the test region (NT01-NT27). These Texans will be helpful in examining any possible radiation patterns generated by the shots.

Table 6 lists the Texan locations and Table 7 details the recording parameters. The Texans were programmed the morning of installation by Willie Zamora to record during specified time intervals for 4 days at 250 sps (Table 7). The recorder was placed in a small plastic bag, to keep it clean, and then placed in a shallow trench. The geophone was placed vertically in the ground using a bubble level and everything was covered with dirt to hide them and provide thermal stability. The recorders were powered by two internal Duracell Procell D size batteries that were installed prior to programming. Since all shots were completed in one day, the sensors were pulled on day two of recording, acquisition was stopped, and the data were downloaded.

Figure 13. (Left) RT-125 "Texan" seismic recorder and attached 4.5 Hz vertical spike geophone (orange). For the experiment, the recorder was placed in a plastic bag, laid on its side in a trench, and everything was buried. (Right) Texans in their carrying crates being programmed prior to deployment.

Table 6. RT-125 "Texan" Sensors.

Station	Latitude	Longitude	Elev (m)	Geophone	S/N
NT01	44.14975	-72.47660	439	4.5 Hz	1847
NT02	44.15050	-72.47139	474	4.5 Hz	1817
NT03	44.15306	-72.46688	469	4.5 Hz	2185
NT04	44.15661	-72.46726	433	4.5 Hz	2988
NT05	44.15994	-72.46902	419	4.5 Hz	2137
NT06	44.16267	-72.47063	399	4.5 Hz	2148
NT07	44.16375	-72.47424	402	4.5 Hz	2087
NT08	44.16403	-72.47813	411	4.5 Hz	3003
NT09	44.16295	-72.48178	446	4.5 Hz	2455
NT10	44.16111	-72.48428	450	4.5 Hz	2218
NT11	44.15758	-72.48488	483	4.5 Hz	2237
NT12	44.15627	-72.48574	471	4.5 Hz	2703
NT13	44.15452	-72.48631	445	4.5 Hz	2464
NT14	44.15202	-72.48542	415	4.5 Hz	1910
NT15	44.15061	-72.48338	424	4.5 Hz	2450
NT16	44.14973	-72.47993	436	4.5 Hz	2161
NT17	44.14983	-72.47882	430	4.5 Hz	2465
NT18	44.15044	-72.47791	441	4.5 Hz	2459
NT19	44.15135	-72.47785	469	4.5 Hz	1919
NT20	44.15220	-72.47769	478	4.5 Hz	2142
NT21	44.15300	-72.47834	481	4.5 Hz	2589
NT22	44.15392	-72.47892	485	4.5 Hz	1555
NT23	44.15469	-72.47827	488	4.5 Hz	2564

Station	Latitude	Longitude	Elev (m)	Geophone	S/N
NT24	44.15552	-72.47762	491	4.5 Hz	2179
NT25	44.15637	-72.47777	489	4.5 Hz	1923
NT26	44.15683	-72.47819	488	4.5 Hz	1683
NT27	44.15724	-72.47828	508	4.5 Hz	1522
ST01	44.14481	-72.47836	415	4.5 Hz	2155
ST02	44.14083	-72.47468	470	4.5 Hz	2089
ST03	44.13749	-72.47077	501	4.5 Hz	1649
ST04	44.12999	-72.46384	527	4.5 Hz	1739
ST05	44.12524	-72.46401	508	4.5 Hz	2253
ST06	44.12048	-72.46160	525	4.5 Hz	1697
ST07	44.11936	-72.45598	517	4.5 Hz	1836
ST08	44.11476	-72.45226	487	4.5 Hz	1941
ST09	44.11152	-72.45009	476	4.5 Hz	1884
ST10	44.10815	-72.44569	453	4.5 Hz	1718
ST11	44.10532	-72.44118	431	4.5 Hz	1694
ST12	44.10210	-72.43603	432	4.5 Hz	2044
ST13	44.09886	-72.43151	456	4.5 Hz	1868
ST14	44.09502	-72.42836	451	4.5 Hz	2362
ST15	44.09881	-72.42456	480	4.5 Hz	1676
ST16	44.09485	-72.42188	502	4.5 Hz	2990
ST17	44.09256	-72.41641	516	4.5 Hz	2234
ST18	44.08877	-72.41341	528	4.5 Hz	1746
ST19	44.08528	-72.40897	555	4.5 Hz	2476
ST20	44.08119	-72.40638	569	4.5 Hz	1706
ST21	44.07713	-72.40380	598	4.5 Hz	2994
ST22	44.07272	-72.40329	641	4.5 Hz	2153
ST23	44.06861	-72.40077	616	4.5 Hz	1815
ST24	44.06423	-72.39933	605	4.5 Hz	2091
ST25	44.06016	-72.39693	587	4.5 Hz	2477
ST26	44.05563	-72.39617	595	4.5 Hz	2480
ST27	44.05147	-72.39829	599	4.5 Hz	2479
ST28	44.04698	-72.39883	623	4.5 Hz	1790
ST29	44.04327	-72.39462	611	4.5 Hz	1808
ST30	44.03915	-72.39230	600	4.5 Hz	2475
ST31	44.03485	-72.39060	606	4.5 Hz	2566
ST32	44.03075	-72.38752	595	4.5 Hz	2474
ST33	44.02710	-72.38279	604	4.5 Hz	2612
ST34	44.02293	-72.38020	618	4.5 Hz	2837
ST35	44.01464	-72.37524	576	4.5 Hz	2461
ST36	44.01176	-72.37000	535	4.5 Hz	2463
ST37	44.01231	-72.36317	520	4.5 Hz	1655
ST38	44.01310	-72.35706	513	4.5 Hz	2451
ST39	44.01176	-72.35107	474	4.5 Hz	1841
ST40	44.00738	-72.34996	483	4.5 Hz	1784
ST41	44.00307	-72.35169	490	4.5 Hz	2458
ST42	44.00023	-72.35682	505	4.5 Hz	2452

Station	Latitude	Longitude	Elev (m)	Geophone	S/N
ST43	43.99909	-72.36286	518	4.5 Hz	2453
ST44	43.99044	-72.36703	549	4.5 Hz	2457
ST45	43.98604	-72.36784	560	4.5 Hz	2230
TN01	44.17101	-72.45563	357	4.5 Hz	1827
TN02	44.17853	-72.45098	461	4.5 Hz	1702
TN03	44.18431	-72.44757	460	4.5 Hz	1762
TN04	44.19030	-72.44159	464	4.5 Hz	1835
TN05	44.19208	-72.43277	490	4.5 Hz	1899
TN06	44.20009	-72.43657	490	4.5 Hz	1934
TN07	44.20498	-72.42451	486	4.5 Hz	2017
TN08	44.20959	-72.42144	475	4.5 Hz	1634
TN09	44.20053	-72.40111	429	4.5 Hz	1652
TN10	44.20614	-72.39907	419	4.5 Hz	1682
TN11	44.21946	-72.39829	417	4.5 Hz	1750
TN12	44.22675	-72.39961	428	4.5 Hz	1569
TN13	44.22939	-72.39684	463	4.5 Hz	2113
TN14	44.23362	-72.39248	452	4.5 Hz	1567
TN15	44.23918	-72.39013	473	4.5 Hz	1570
TN16	44.24562	-72.38012	470	4.5 Hz	1578
TN17	44.24944	-72.37331	476	4.5 Hz	1612
TN18	44.25382	-72.37190	476	4.5 Hz	1520
TN19	44.25821	-72.36987	455	4.5 Hz	1789
TN20	44.26419	-72.36535	437	4.5 Hz	2478
TN21	44.27529	-72.36361	436	4.5 Hz	1972
TN22	44.27692	-72.35464	493	4.5 Hz	2573
TN23	44.27680	-72.34652	524	4.5 Hz	1677
TN24	44.29133	-72.30389	454	4.5 Hz	1736
TN25	44.29651	-72.30374	445	4.5 Hz	2991
TN26	44.30800	-72.30269	454	4.5 Hz	2562
TN27	44.31292	-72.30035	492	4.5 Hz	2561
TN28	44.31717	-72.29567	523	4.5 Hz	2560
TN29	44.32093	-72.29184	537	4.5 Hz	2572
TN30	44.32799	-72.28578	537	4.5 Hz	2563
TN31	44.33274	-72.28131	504	4.5 Hz	2924
TN32	44.33710	-72.27986	469	4.5 Hz	2927
TN33	44.33886	-72.27404	453	4.5 Hz	2926
TN34	44.34054	-72.26735	441	4.5 Hz	2920
TN35	44.35288	-72.27189	431	4.5 Hz	2902
TN36	44.36076	-72.27804	394	4.5 Hz	2901
TN37	44.36620	-72.27633	437	4.5 Hz	2904
TN38	44.36110	-72.25740	518	4.5 Hz	2874
TN39	44.36218	-72.24525	594	4.5 Hz	2921
TN40	44.36885	-72.24784	565	4.5 Hz	2923

Table 7. Texan Recording Parameters.

Parameter	Value
Digitizer	Reftek RT125
Channels	1 - vertical
Resolution	24-bit
Gain	32
LSB (nV/count)	57.37
Sample Rate	250
Record Mode	Time Windows
Window 1 (UTC)	2008:194:14:00 to 2008:194:24:00
Window 2 (UTC)[‡]	2008:195:14:00 to 2008:195:24:00
Window 3 (UTC)	2008:196:19:00 to 2008:196:24:00
Window 4 (UTC)	2008:197:19:00 to 2008:197:24:00
Sensor	4.5 Hz vertical 3" spike

Video Camera

A Sony Hi-8 video camera recorded all of the explosions in order to study the surface manifestations of the explosions. A picture of the camera overlooking the test site is shown in Figure . The camera needed to be moved a few feet for Shot 3 to avoid the vantage angle being blocked by vegetation. The camera was moved back to its initial location for shots 4 and 5. The locations of the camera are listed in Table 8 and plotted in Figure . The Hi-8 analog videos were digitized to small computer movies. Jessie Bonner also recorded many of the explosions using his personal hand held video camera placed on a tripod near the blasts. Those videos provide a view of the blasts from a different angle.

Table 8. Camera Locations.

Station	Latitude	Longitude	Elev (m)	Shots Recorded
Camera1	44.15837	-72.47800	541	1, 2, 4, 5
Camera2	44.15842	-72.47816	538	3

[‡] NOTE: Texan recording stopped on day 195 and data downloaded.

Figure 14. Camera overlooking the test site.

EXPLOSIONS IN BARRE GRANITE

Shot Characteristics

Five explosions were detonated at the test site on 12 July 2008 (Table 9). A delay-fired production shot was conducted on 11 July 2008, and we have the blasters information for this shot (Appendix 2E). A goal of this experiment was to examine how the velocity of detonation (VOD) affects the damage and shear wave generation. Three explosives with dramatically different VOD were used to compare these effects. Our planned single-fired blasts ranged in yield from 134 to 270 lbs of explosives with the first three being ~135 lbs of black powder, ANFO/Emulsion (Heavy ANFO), and Composition B (COMP B), respectively. The blast plan was designed and executed by Mr. Tim Rath of Maxam-North America who was assisted by Peter West and Jason Trippiedi.

Table 9. Origin Characteristics for NEDE Shots.

Shot	Date	Origin Time (GMT)	Latitude	Longitude	Elevation (m)	Borehole/ Centroid Depth (m)	Stemming (m)	Yield (lbs)	Explosive
1	7/12/2008 (194)	14:37:42.160	44.15774	-72.47848	509	9.15/8.33	7.50	134	Black Powder
2	7/12/2008 (194)	16:02:05.020	44.15800	-72.47813	509	11.89/11.31	10.74	135.5	ANFO/Emul 50:50
3	7/12/2008 (194)	17:30:40.730	44.15780	-72.47770	503	11.77/11.30	10.83	136	COMP B
4	7/12/2008 (194)	19:16:15.010	44.15751	-72.47797	508	14.02/12.87	11.73	269.5	ANFO/Emul 50:50
5	7/12/2008 (194)	20:50:12.770	44.15754	-72.47757	503	13.60/12.67	11.73	270	COMP B
P1	7/11/2008 (193)	~19:33:54	-	-	-	-	-	1934	ANFO

Note: Yield is based on explosives + detonators.
        Lat/Long/Elevation error was 4+ meters according to the GPS unit.

Black powder is traditionally used for firearms and fireworks because its slow burn rate produces gases that can propel a bullet but not damage the barrel. It has a low brisance, the rate at which an explosive reaches maximum pressure, which means it generates relatively fewer fractures in the rock around the explosive source. The fractures generated will be longer due to the escape of the explosive gasses. Occasionally, it is used to break monument stone, such as granite, without damaging the stone itself due to properties of gas expansion only along pre-existing cracks.

ANFO/Emulsion (Figure) is the primary blasting agent used in the mining industry due to its stability, low cost, easy production as well as optimum blast effects for rock fracturing. ANFO is considered a high explosive when properly confined and especially when mixed with an emulsion. We use the phrase "Heavy ANFO" to describe the 50:50 ANFO:Emulsion mix used for the NEDE.

Composition B (Figure) is a military grade explosive composed of RDX and TNT. It is primarily used in military applications such as munitions. COMP B is a shapeable charge and was cast specifically to fit our boreholes. One cast charge was used for Shot 3 and two were used for Shot 5. The high VOD of this explosive allowed it to be used in the first nuclear weapons.

During the experiment, increased care was required handling this explosive due to its increased sensitivity and the booster being strapped to the charge as it was being lowered down the hole (Figure). A small amount of ANFO/Emulsion was poured in the hole prior to loading the COMP B charge to increase explosive coupling to the borehole.

Figure 15. Loading of ANFO/Emulsion explosive.

Figure 16. COMP B charge and the tube taped on to hold the detonator.

Figure 17. Lowering the COMP B charge into the hole.

Table 9 lists the total depth of the boreholes, the centroid depths of the explosive column, and the amount of stemming. Stemming consisted of granite flour from drilling, a blast plug (Figure) designed to lock into the borehole walls, and ½" gravel. The boreholes had a 9" diameter as logged by Hager-Richter Geoscience (Figure).

The shot time was determined by placing an Endevco accelerometer (N1B) within 5 m of the borehole and examining the first large positive break on the vertical component. With the explosives at a maximum depth of 13 m, the compressional wave took less than three milliseconds to reach the sensor. The origin time is accurate to better than 0.05 seconds.

Velocity of Detonation
The velocity of detonation (VOD; Table 10) was measured using a MREL HandiTrap II. A resistance wire is taped to the booster and lowered down the hole. As the explosives burn up the borehole, the resistance wire is melted and the recorder measures the decreasing resistance at 1

million samples per second. The resistance was then converted to distance and a velocity calculated.

Black powder burns the slowest with a VOD of 0.49 km/s (1608 ft/s; Figure). The ANFO/Emulsion (Figure) and COMP B (Figure) explosives are considered high explosives due to their 5.26 and 8.31 km/s VOD, respectively. The first ANFO/Emulsion shot detonated with a VOD of 5.06 km/s. It is not clear why there is a VOD difference between these two shots. Explosive confinement can play an important role in explosive performance and may have been a factor. The blaster forgot to attach the VOD resistance wire to Shot 3, the first COMP B charge, as he was focused on safely handling the charge.

NOTE: The VOD data were more thoroughly processed after we left the field and the values were adjusted. Figure and Table 11 show the data and improved values.

Figure 18. Blast plug (white ball) used to help stem the holes.
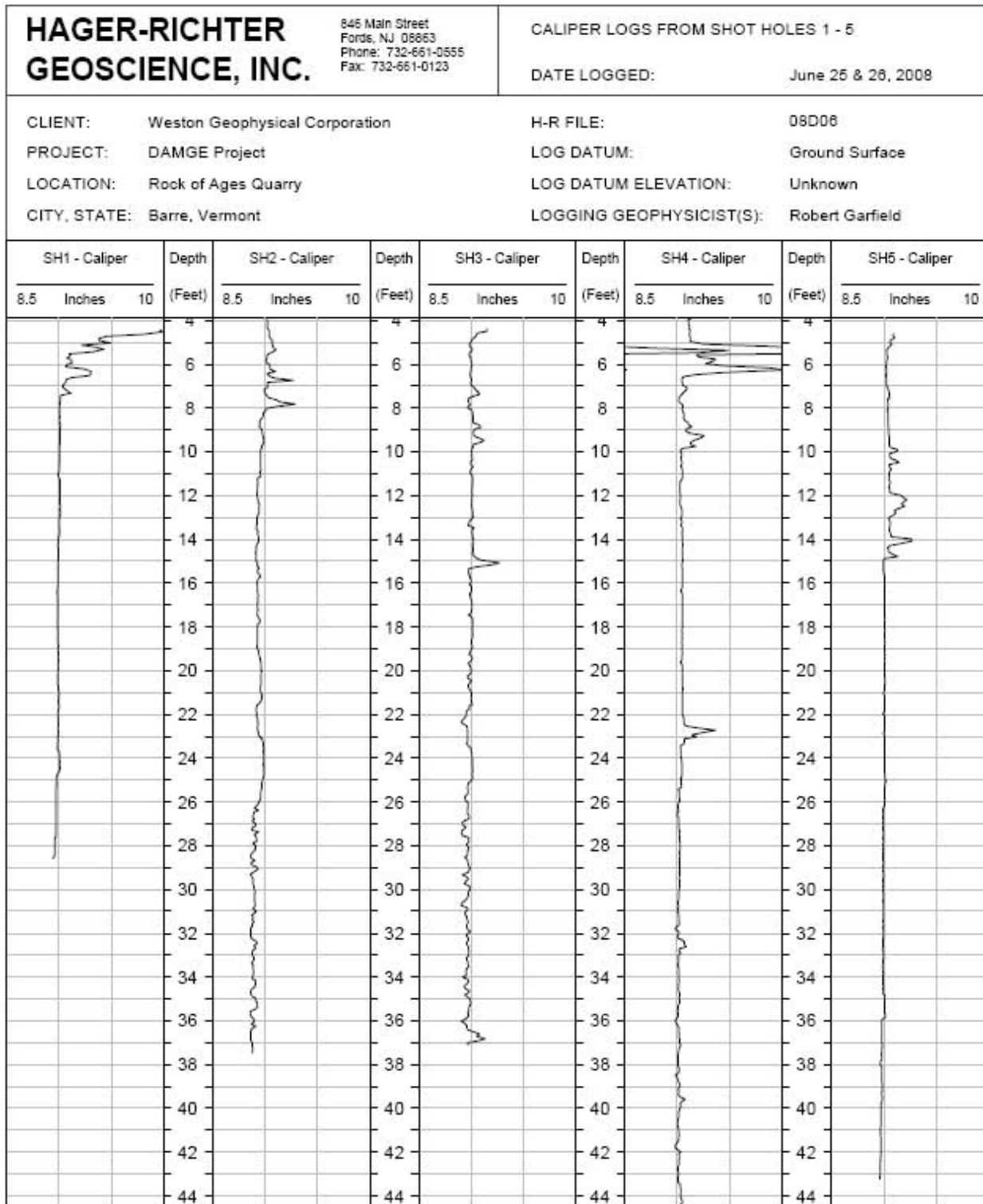
Caliper Logs from Shot Holes 1 - 5

Figure 19. Caliper logs from each blast borehole.

Table 10. Velocity of Detonation.

Shot	Explosive	VOD (km/sec)
1	Black Powder	0.49
2	ANFO/Emul 50:50	5.06
3	COMP B	-
4	ANFO/Emul 50:50	5.26
5	COMP B	8.31
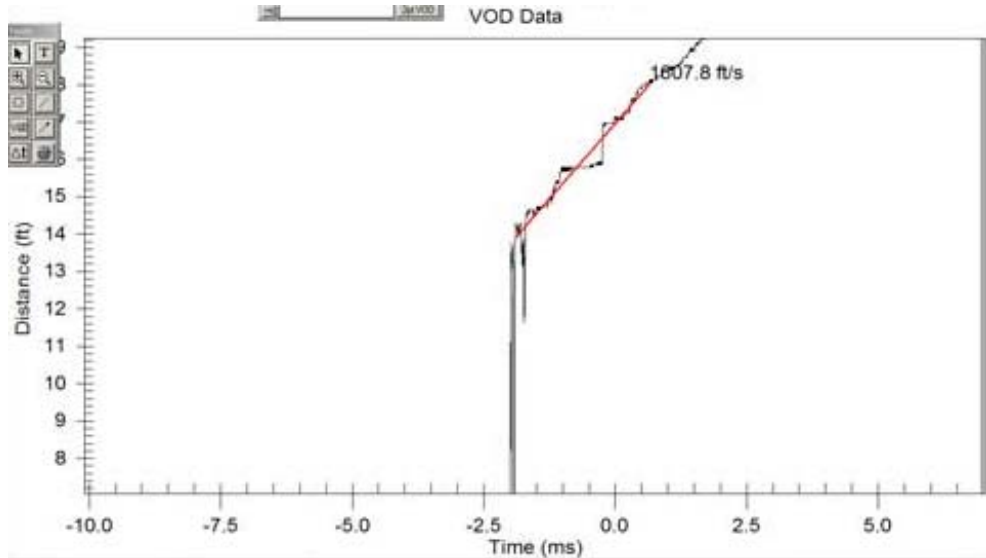
Figure 20. Black powder VOD of 0.49 km/s (1608 ft/s) from Shot 1.
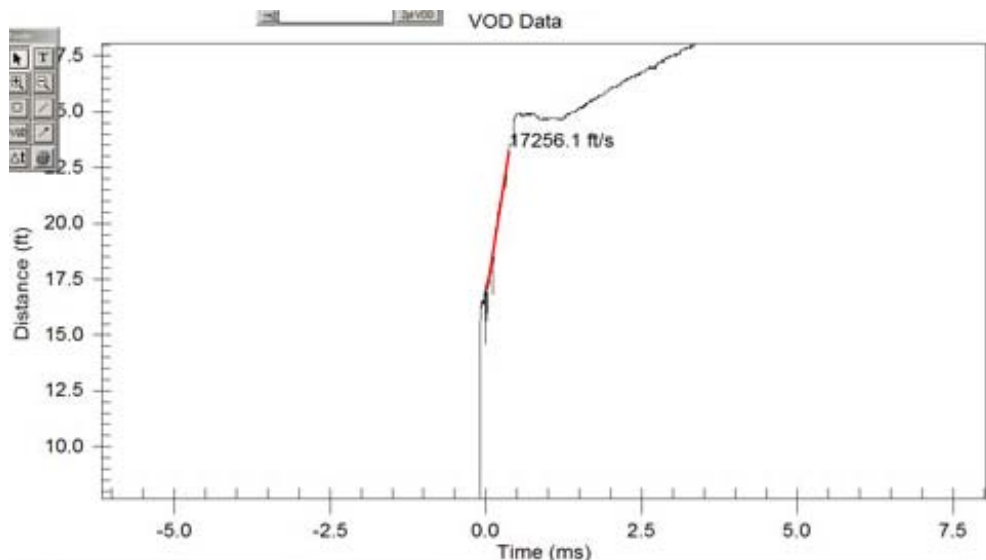
Figure 21. ANFO/Emulsion VOD of 5.26 km/s (17256 ft/s) from Shot 4.

27
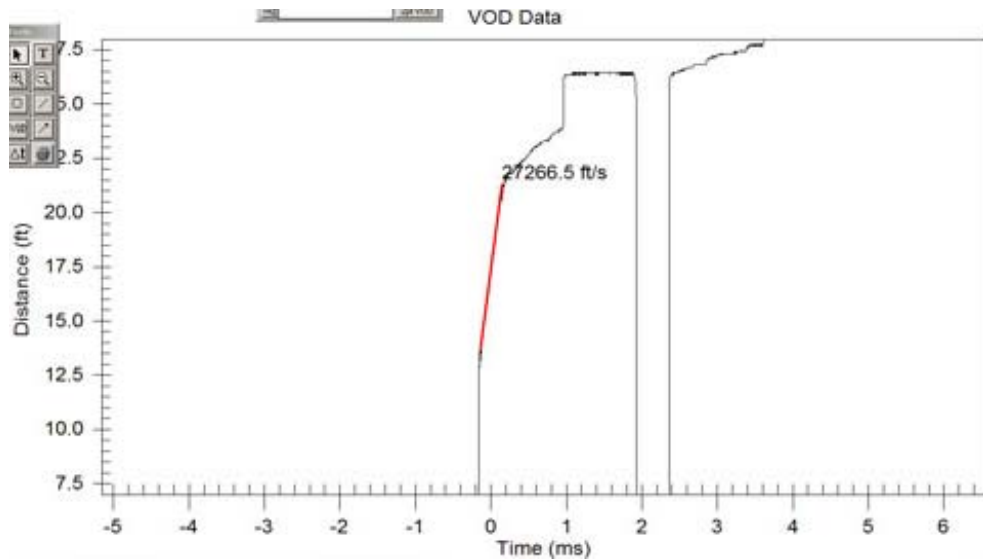
Figure 22. COMP B VOD of 8.31 km/s (27267 ft/s) from Shot 5.

Table 11. Velocity of Detonation Reprocessed.

Shot	Explosive	VOD (km/sec)
1	Black Powder	0.53±0.3
2	ANFO/Emul 50:50	4.76±0.7
3	COMP B	N/A
4	ANFO/Emul 50:50	4.89±0.3
5	COMP B	8.1±0.2
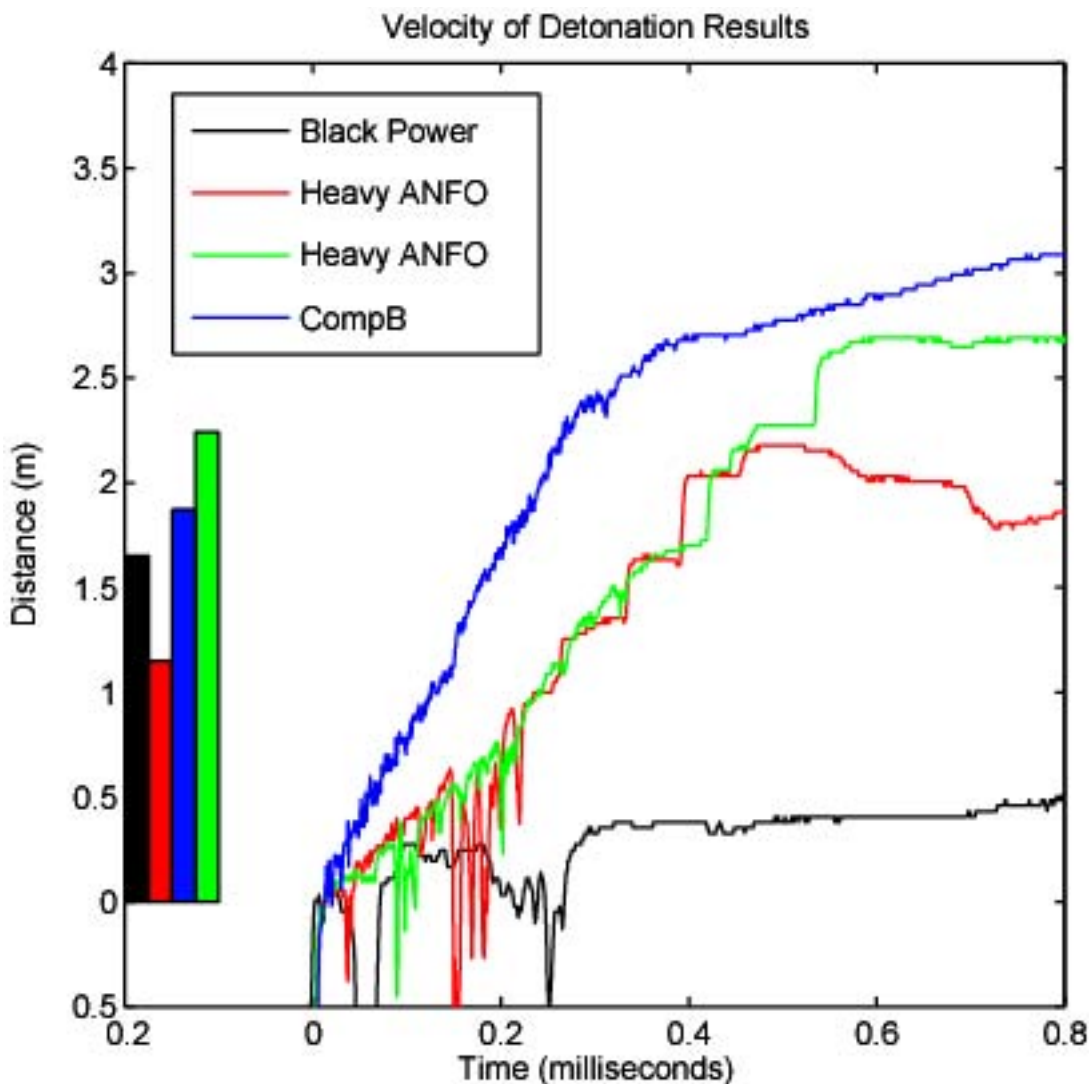
Figure 23. Velocity of detonation recordings for four shots of the five shots. A fifth shot was not recorded using VOD equipment. The raw VOD data were aligned so that the approximate start of the resistance wire burn was at distance=0. Also shown are the lengths of the explosives column (bars at left) which correlate fairly well with the VOD data.

Surface Effects

A Sony Hi-8 video camera (Figure) recorded each explosion. The analog video was digitized into mpeg movies available via e-mail from Weston Geophysical Corporation. The video data show the surface processes that occurred during the explosion so that secondary effects of the source can be modeled. All shots spalled, but no shots cratered or produced fly rock. Shot 1 generated the most observable surface fracturing and still video images are shown in Figure . A photo of the largest crack generated by Shot 1 is shown in Figure . This crack both opened and had vertical displacement of a few centimeters.

Along with the black powder shot, the small ANFO/Emulsion Shot 2 produced some surface fracturing (Figure), although the extent was not the same as from Shot 1. Neither Shot 3 (Figure

29

) or Shot 4 (Figure) produced any surface fracturing visible in the video, although small cracks were observed on the ground after the Shot 4 (Figure). The two larger shots, shots 4 and 5, produced significantly more dust.

Figure 24. Digitized still images of the Shot 1 detonation. Note the two fractures developing after 0.8 s and the further fractures after 1.2 s in the red ellipses.

Figure 25. Largest crack generated by Shot 1.

Figure 26. Digitized still images of the Shot 2 detonation. Three fractures develop in the white granite flour at 0.8 s and a larger opening releases a plume of gases to the right of the flour at 1.4 s.

Figure 27. Digitized still images of the Shot 3 denotation. From the hilltop camera, there were no observable surface effects other than dust.

Figure 28. Digitized still images of the Shot 4 denotation. This shot produced significantly more dust than Shots 1-3. There may be small amounts of gas release in the gravel pile after 0.8 s, but there were no large fractures observable on the video like for Shots 1 and 2.

Figure 29. Crack from Shot 4 observed while walking around the borehole.

Two sections of PVC pipe (~20') were ejected from a nearby borehole, used for cross-hole tomography, by the explosive gasses during Shot 5. This hole as well as its partner hole on the other side of Shot 5 ejected large volumes of the bentonite grout. Individual snapshots of the video from Shot 5 are provided in Figure . The pipe can be seen leaving the borehole and the grout being ejected beginning 0.6 s and 0.8 s, respectively, after the detonation. Calculations to determine the maximum height attained by the PVC pipe returned values ranging from 20.3 to 45.6 m. The pipe hit a guy line, attached to a quarry tower crane, on the way down (Figure) making exact determination of height difficult, although we believe it to be approximately 33 m. Gas can be seen shooting from the borehole under high pressure for 4-5 s after the detonation. This loss of containment will affect the amount of gas available for driving fractures in the granite and will have to be taken into account during analyses.
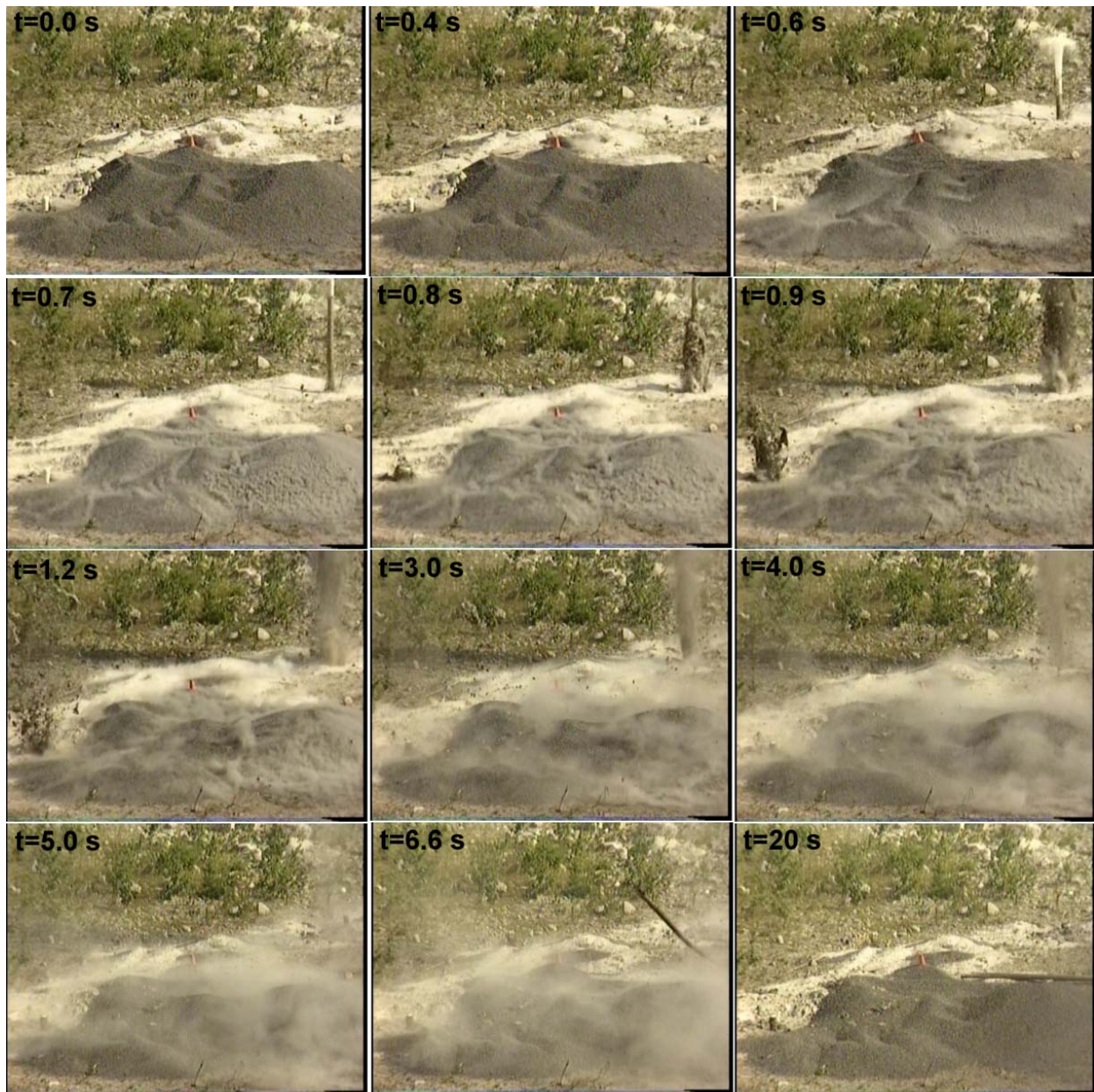
Figure 30. Digitized still images of the Shot 5 denotation. The PVC pipe begins to leave the borehole at 0.6 s and hits the ground at 6.6 s after detonation. No observable fractures were noted in the video.

Figure 31. PVC pipe breaking on guy line during free fall after being ejected from a nearby borehole during Shot 5.

Peak Particle Velocities

The proximity to nearby structures such as a cell/radio tower, the quarry high wall, and quarry cranes constrained the maximum size of the blasts we could conduct. The U.S. Bureau of Mines (USBM) sets peak particle velocity limits (U.S. Bureau of Mines RI 8507, 1980) that we followed. To allow for larger blasts, a second prospective test site was investigated in another region of the mine (Figure). Unfortunately, this site contained large xenoliths and the granite did not have a low fracture density (Figure).

The site in closer proximity to the tower and quarry structures was chosen due to the quality of granite. The predicted peak particle velocities were calculated to determine the maximum shot size using the following equation:

$$PPV = K * SD^A \qquad\qquad (1)$$

where PPV is the peak particle velocity (in/s), K is a site constant (we used 605, the most conservative K value for an overly-confined explosion), SD is scaled distance (ft/lb$^{0.5}$), and A is another site constant (we used -1.6, a value based on low attenuation media).

The results of applying the planned shot sizes (either 200 or 400 lbs) and test site geometry in equation 1 are shown in Figure . Also shown are the USBM limits for above and below 10 Hz and observed peak particle velocities from previous Weston Geophysical experiments. The values used in equation 1 are very conservative and no prior observed data have exceeded the predicted values.
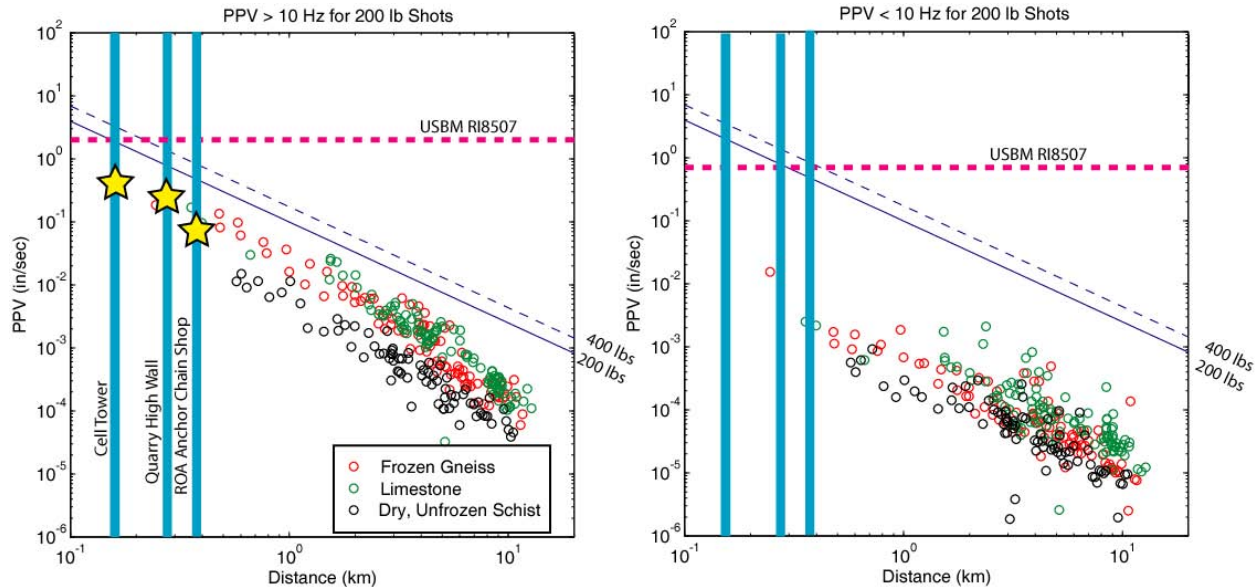
Figure 32. Vibration limits set by the U.S. Bureau of Mines (red dashed lines), the predicted values from our blasts (thin blue solid and dashed lines), distance to the nearby structures (thick vertical blue lines), and actual values from previous experiments (multi-colored circles). The peak particle velocities measured at the three structures from the NEDE blasts are shown as yellow stars.

Rob Haas of PreSeis, Inc. deployed "Instantel" seismic sensors at the cell/radio tower, quarry high wall, and the World War II anchor chain shop to provide rapid (and independent) measurements of PPV. The location of the WWII anchor chain shop was close to the nearest residential structure. Our plan was to shoot the smaller shots, measure the PPVs at each site, then decide whether or not to shoot the larger charges as planned or decrease their sizes. Figure compares the observed maximum PPVs from the Instantels and the predictions. Table 12 shows which NEDE shot provided the maximum seismic vibration and acoustic signal at each structure. The values were all below the estimated PPVs and the USBM limits for safe vibration limits. The data seem to align along the trend of our measured values from previous explosion experiments.

Table 12. PPVs Measured by PreSeis, Inc

Location	Distance (ft)	Max PPV (in/sec)	Shot #	Max Acoustic (db)	Shot #
Cell/Phone Tower	403	0.420	2	114	4
Quarry Wall	875	0.290	5	114	4
Anchor Chain Shop	1192	0.060	3	105	2

35

SEISMIC DATA EXAMPLES AND ANALYSES

In this section, we present examples of the waveforms collected during the experiment.

Near-Source
Below are a few examples of the near-source data recordings. In Figure , the vertical spall from all five shots are recorded on station N1B. Note the classic spall from Shot 5 with an impulsive shock wave arrival, 0.2 seconds of spall, and then a small spike from the slap down. Shot 4 has a double spike from the shock wave and a longer spall before three smaller slap downs. Shot 1 has a long duration shock wave arrival possibly caused by a "burning" of the explosives column instead of an instantaneous detonation. The origin times for the shots were determined from these data as well.
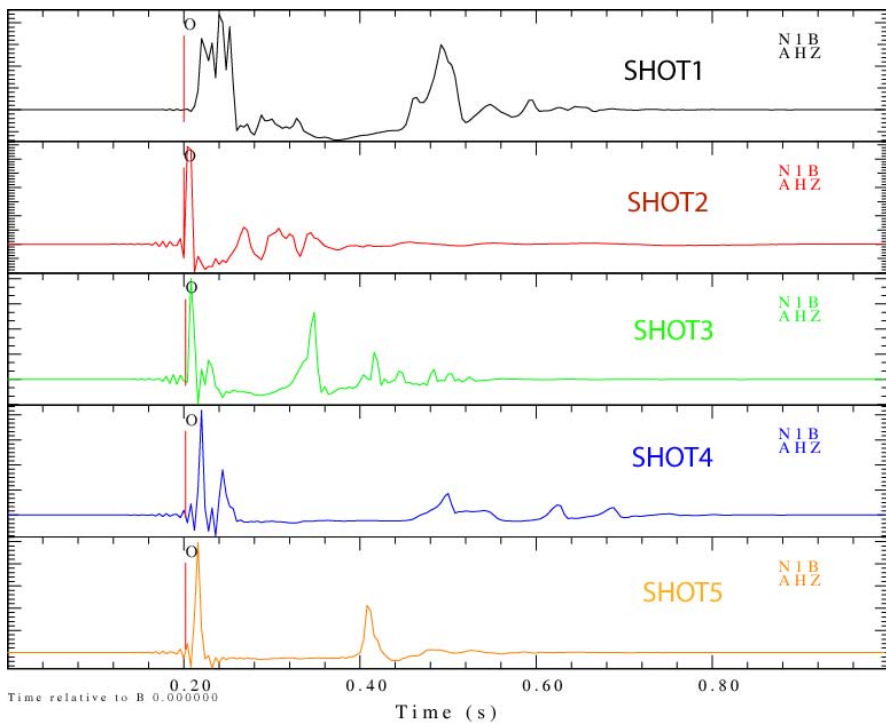
Figure 33. Near-source phenomenology for all five shots recorded on sensor N1B about 5 m from each blasthole collar. These data are not plotted on the same amplitude scales in order to better show the characteristics of the initial shock wave, the -1 g spall, and the spall slapdown(s). Figure provides a better representation of the relative amplitudes between the shots.

Close-in vertical recordings of the shots look remarkably similar, particularly for shots 2, 3, 4, and 5 (Figure). Shot 1 appears to have lower frequency energy content in Figure . Three component data are shown in Figure for the first three shots. It is interesting to note the large amplitude transverse components at these close-in distances, which have also been observed in prior experiments such as the Frozen Rock Experiment in Alaska.

36
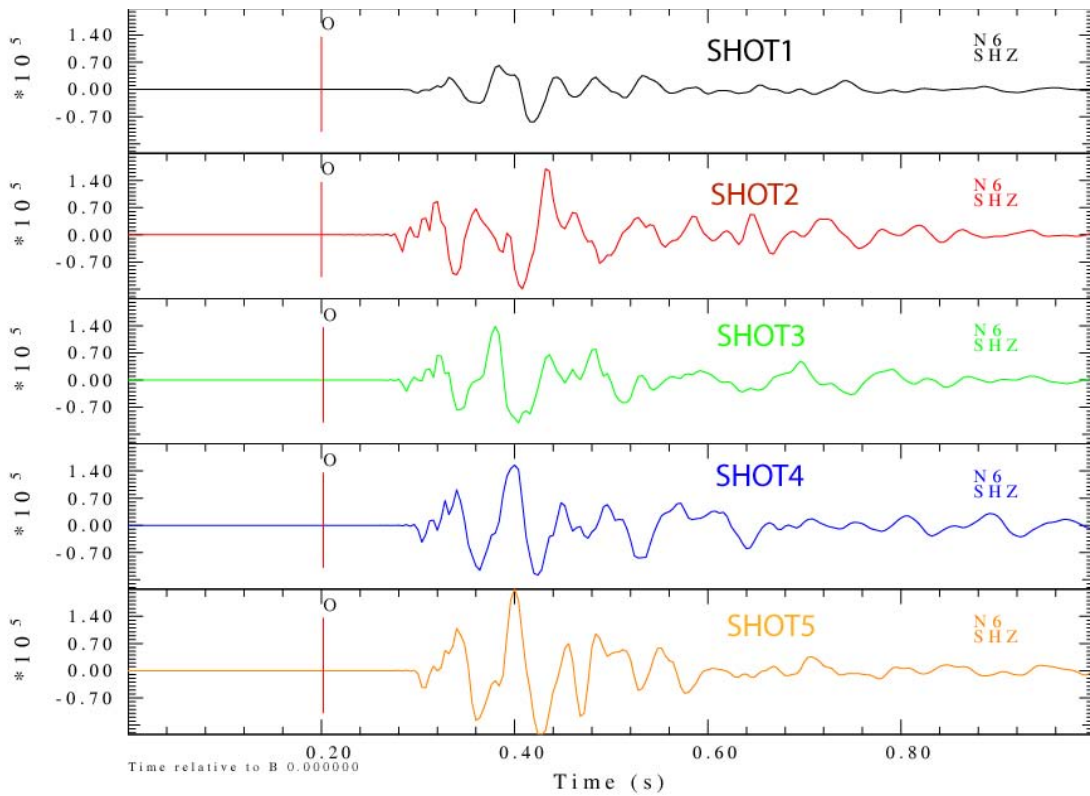
Figure 34. All five shots recorded on the L4-3D vertical channel of station N6. The data were scaled to the maximum amplitude on Shot 5.
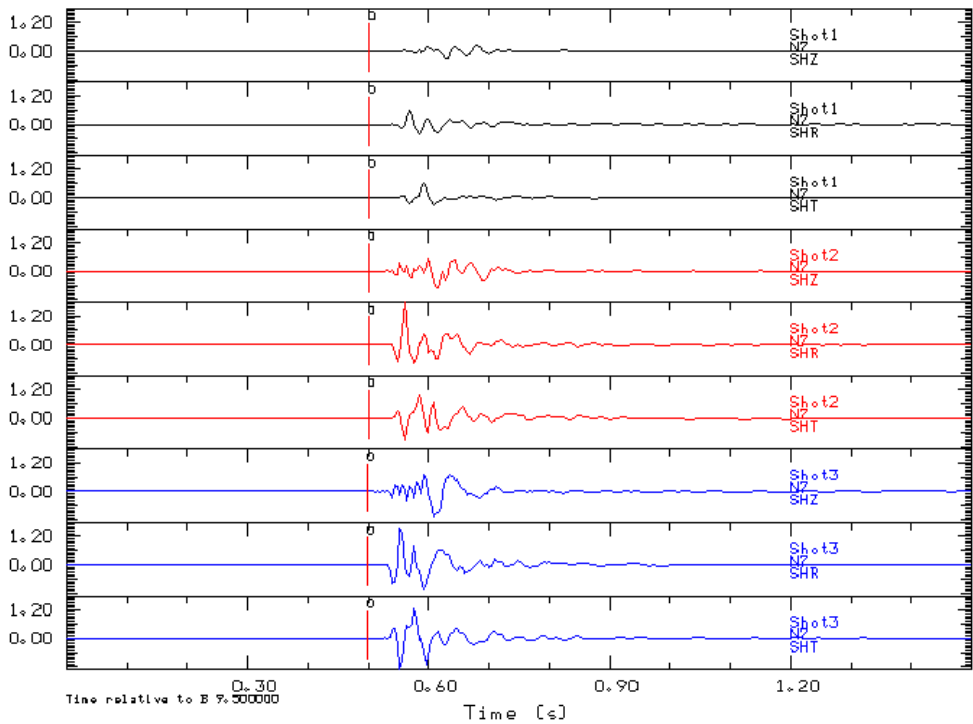
Figure 35. Vertical, radial, and transverse data of shots 1, 2, and 3 recorded on an L4-3D at station N7.

Short Period Linear Arrays

Band-passed, short-period linear array data is presented in Figure through Figure highlighting the *P*, *S*(?), and surface waves. The pre-event noise data from NE08 (third from the top) are contaminated by the seismic response of a passing automobile.
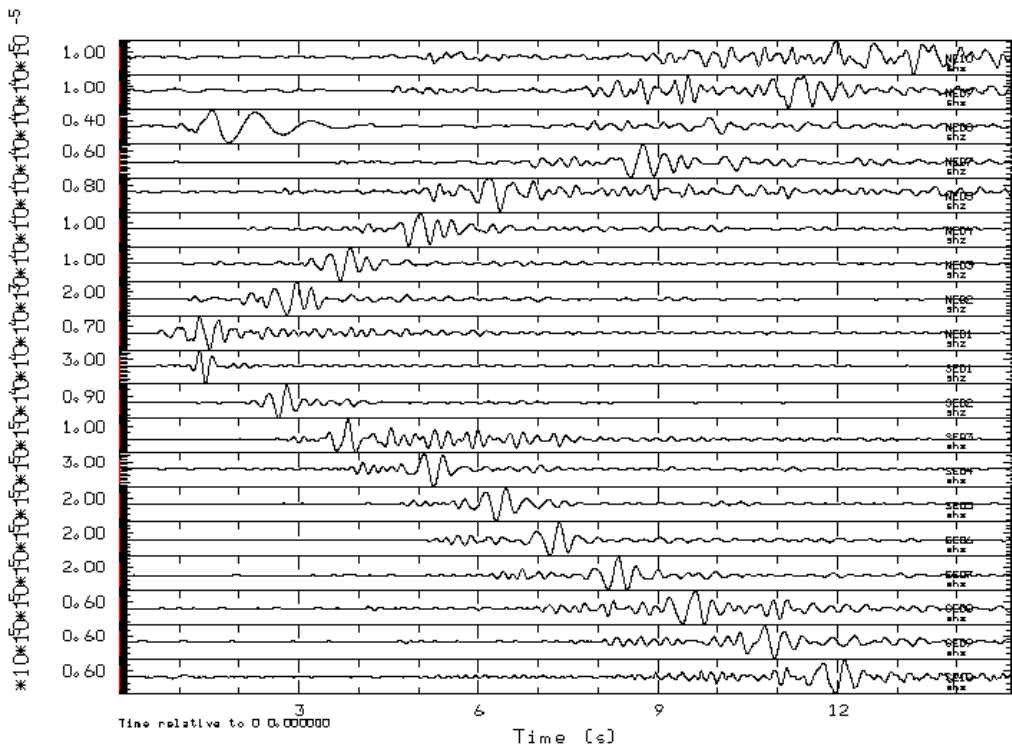
Figure 36. Shot 5 vertical recordings on the short period linear array from north (top) to south (bottom) band passed from 1-4 Hz showing the surface waves.
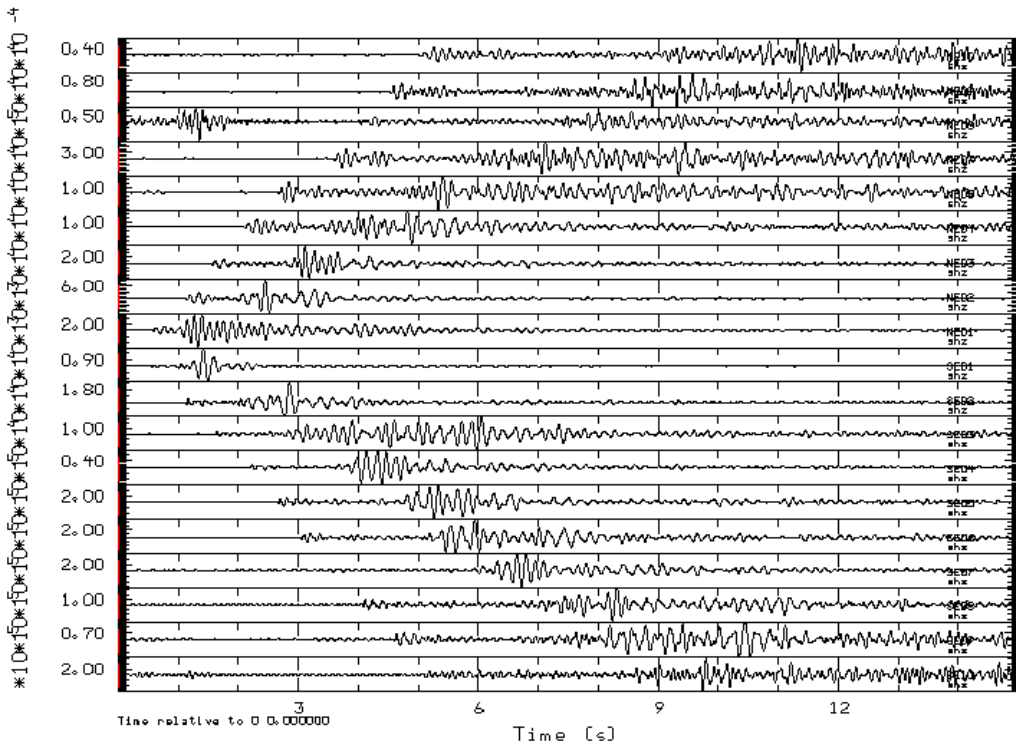
Figure 37. Shot 5 vertical recordings on the short period linear array from north (top) to south (bottom) band passed from 4-10 Hz showing the *P* and *S* (?) waves.
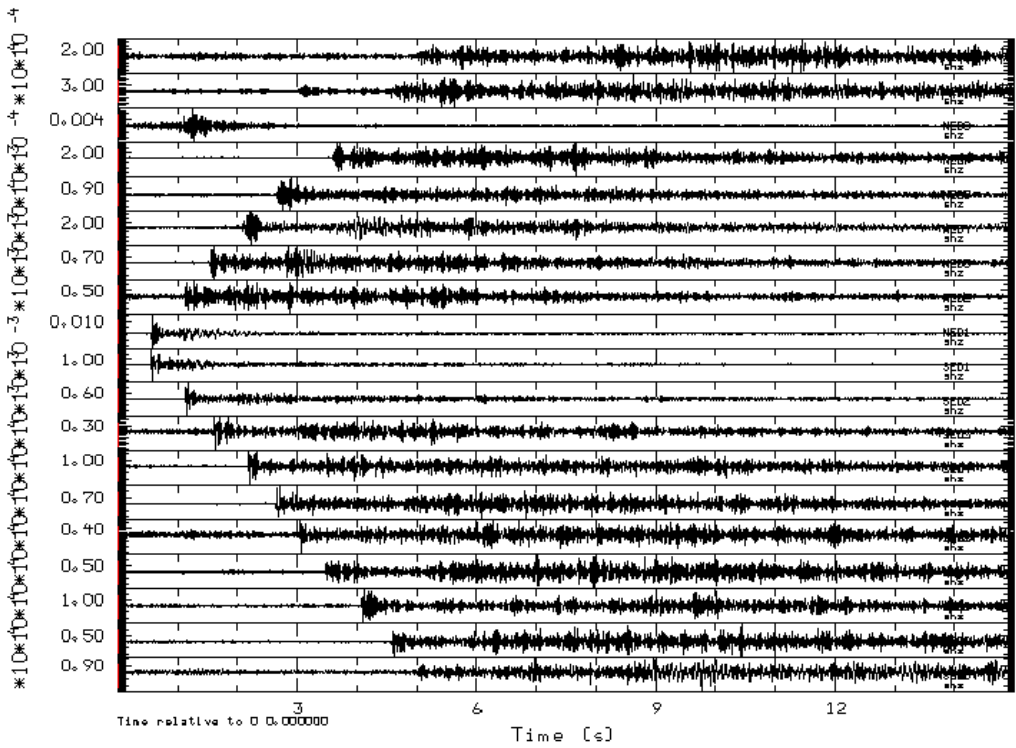
Figure 38. Shot 5 vertical recordings on the short period linear array from north (top) to south (bottom) high passed above 10 Hz showing the *P* waves and *P-* and *S-* coda.

In Figure , the Rayleigh waves from the five shots recorded at NE02 are plotted. At this station, the surface wave amplitudes are inversely related to the VOD of the explosives. If this trend is observed at other stations, and it is found that the slower VOD explosions generated more damage as the video and surface observations indicate, then these results may suggest that damage around the source is at least partly responsible for the generation of surface waves.
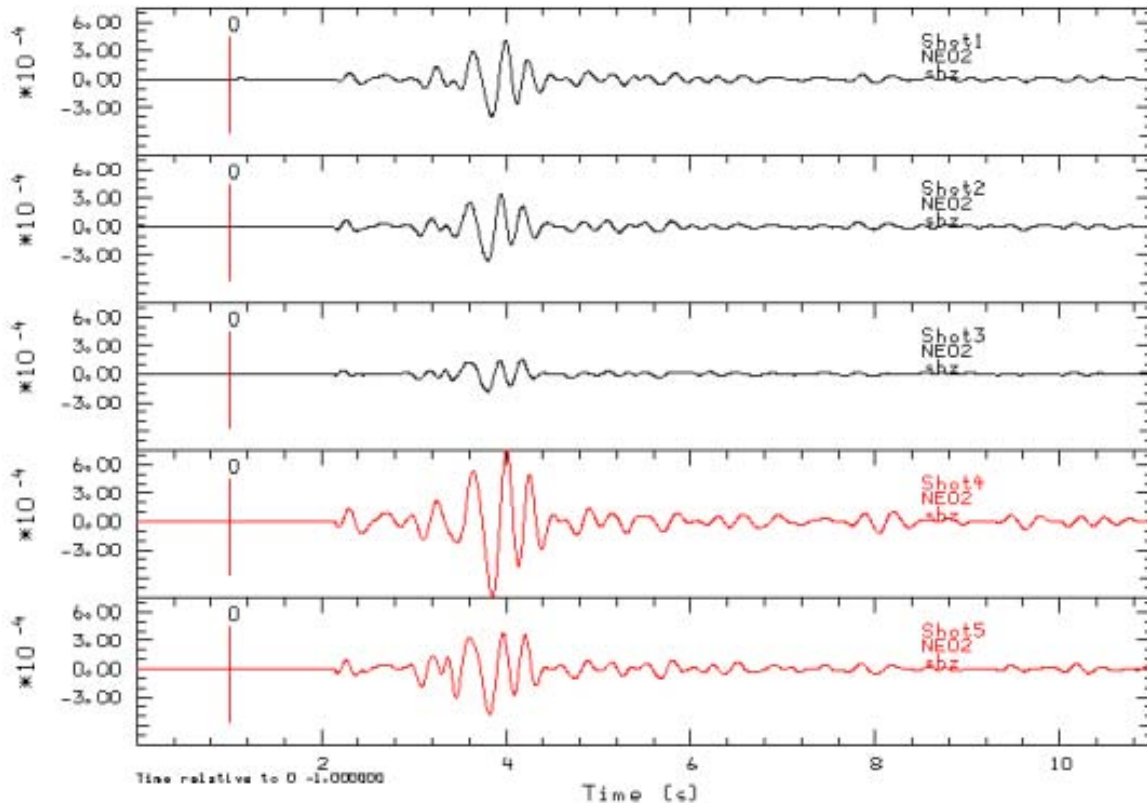
Figure 39. Rayleigh waves at station NE02 for all five shots. Vertical data are band passed between 0.5 and 4 Hz. Note decreasing amplitude of the Rayleigh waves from black powder (Shot 1) to ANFO/Emulsion (shots 2 and 4) to COMP B (shots 3 and 5). The waveforms are color coded by shot size, black=135 lbs, red=270 lbs.

Texans

Data from Shot 5, recorded on the two Texan profiles, are shown in Figure and Figure . The data were band pass filtered between 4 and 10 Hz and plotted as a function of distance. The two Texans with either a bad cable connection or geophone are apparent in the plots. *P* and *S* arrivals are obvious in the data. The SE line of Texans appears to have a change in the shear wave arrival times around 13 km distance.

40
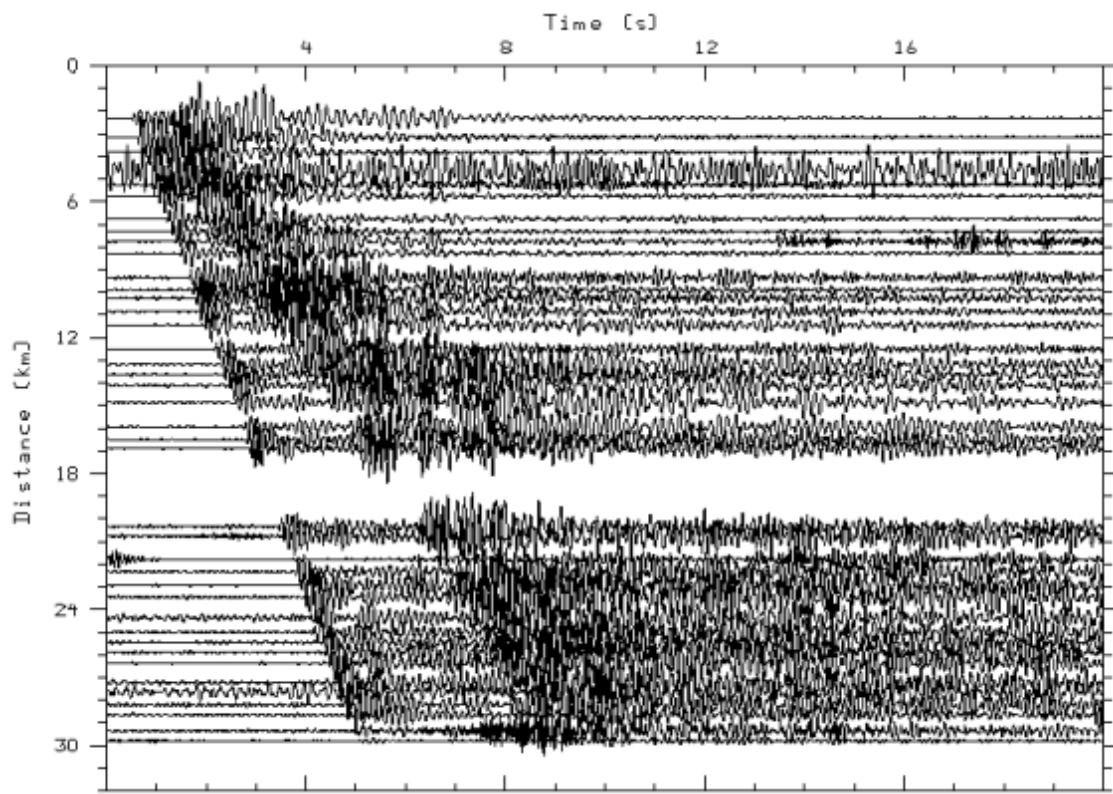
Figure 40. NE Texan line band passed from 4 to 10 Hz.
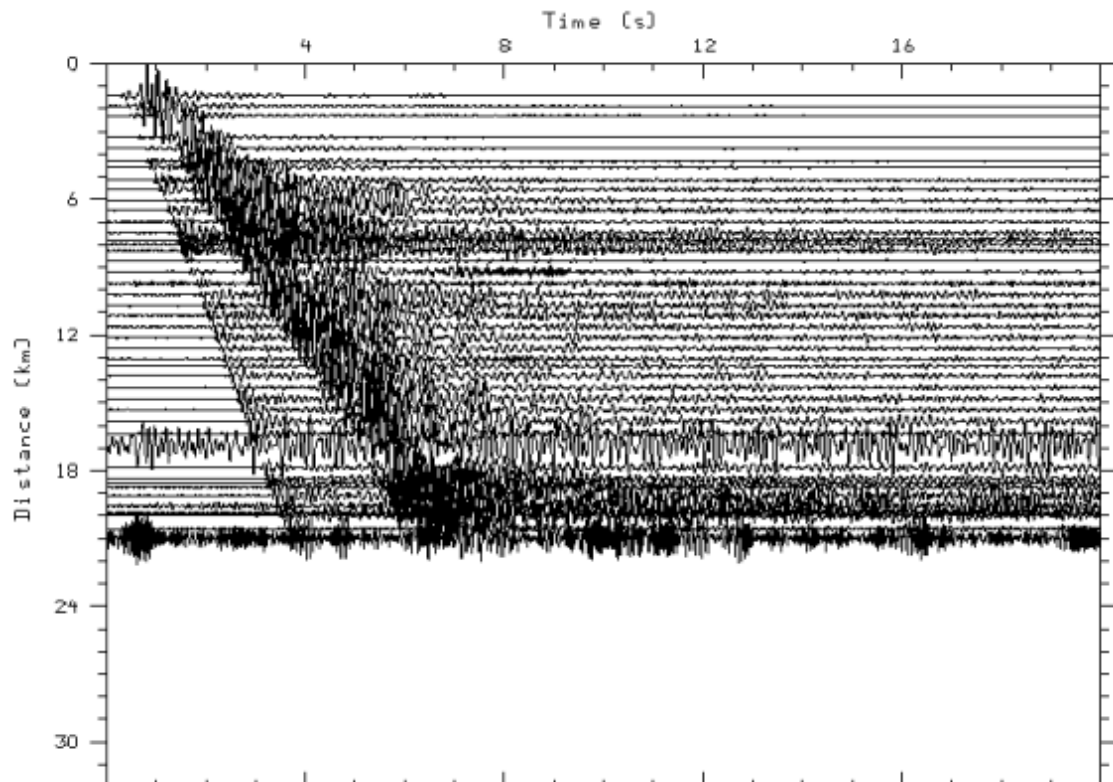
Figure 41. SE Texan line band passed from 4 to 10 Hz.

41

Regional

A number of regional stations in New England (Figure) recorded some or all of the NEDE shots. The signal-to-noise ratio (SNR) varies from excellent at Lisbon, New Hampshire (LBNH) to not very good at most of the stations for Shots 1-3. With these data, our seismic data recording distance range varies from less than 5 meters (e.g., station N1B) to 281 km (174 miles as recorded at the USGS station in Peaks-Kenny State Park, Maine, PKME). The fact that the *Lg* phase from a 134 lb black powder explosion can be recorded over 280 km from the blast highlights both the low attenuation in New England and the quality of the PKME station. Examples of Love (Figure) and Rayleigh (Figure) waves from LBNH are plotted along with shots 4 and 5 recorded at PKME (Figure).

While the larger shots were recorded on the New England Seismic Network (NESN) stations HNH, QUA2, and FFD, the SNR is very low. HNH seems to be a very noisy station. QUA2 has harmonic noise dominating one of the components. The EHZ-only stations MDV and MIV of the Lamont-Doherty network have adequate SNR. The 3C station FRNY is probably the second-best recording (after LBHN) of the events from these permanent stations.
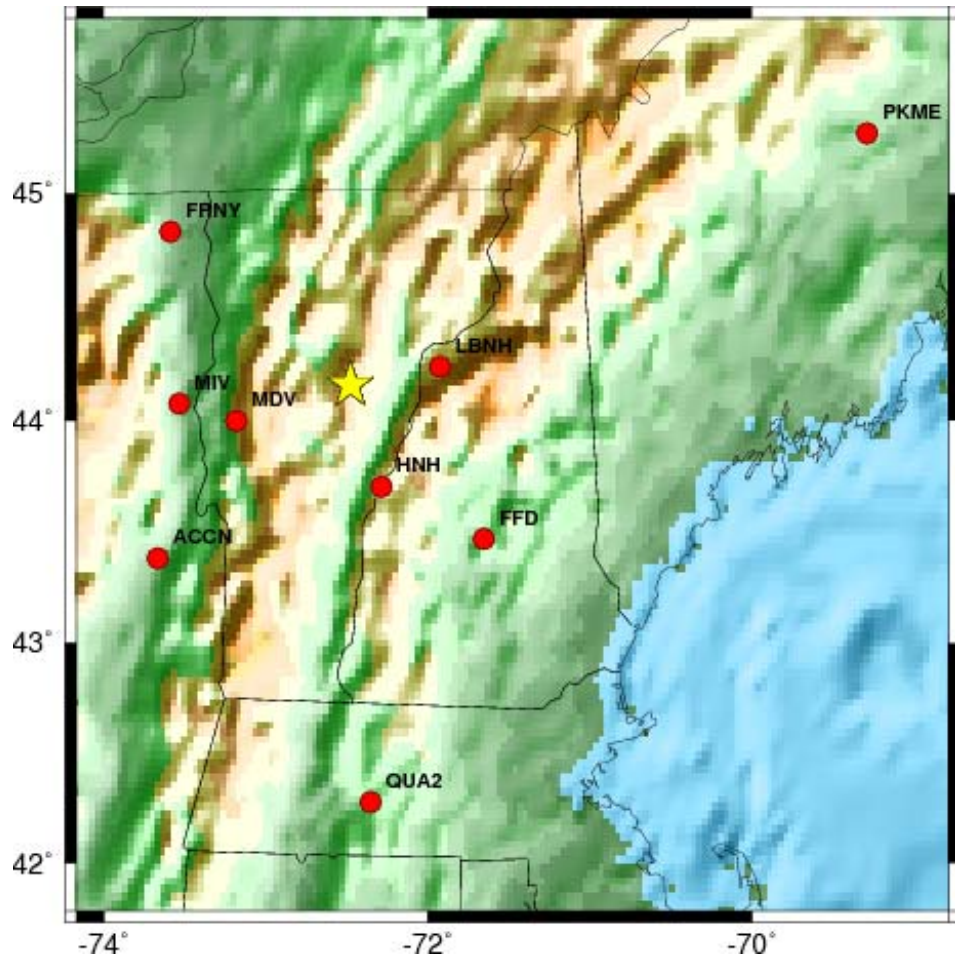
Figure 42. Seismic stations in New England that recorded some of the NEDE blasts (star).
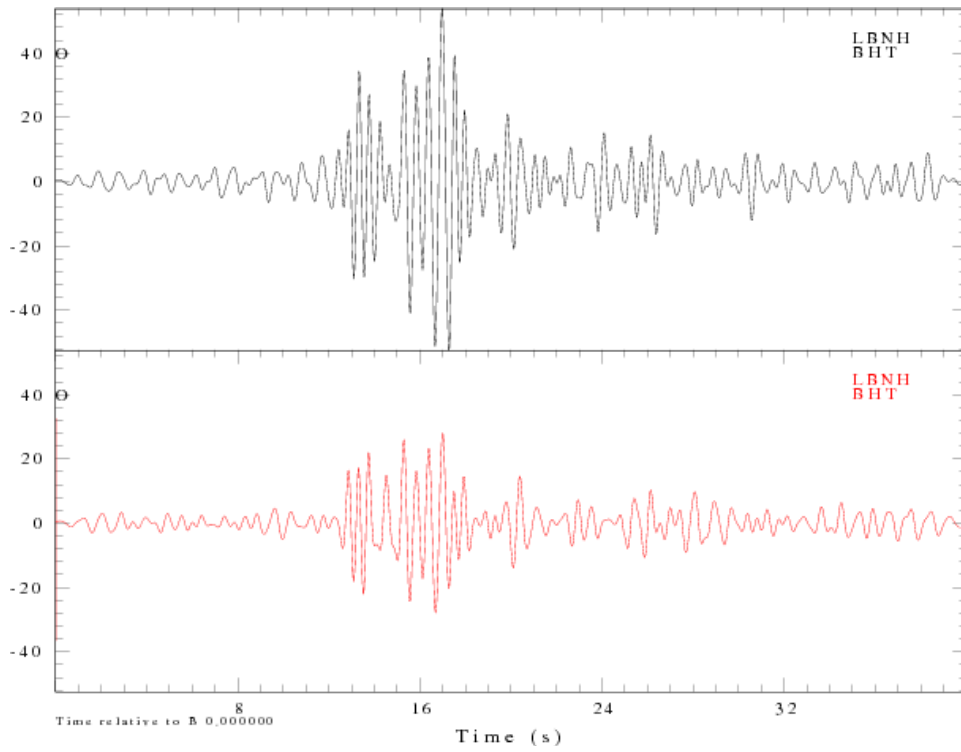
Figure 43. Love waves recorded on the BHT component of LBNH for Shot 4 (black) and Shot 5 (red). The later part of the wave train may be Rayleigh-waves that have scattered onto the transverse components. However, the first part of the wave train is definitely SH motion.
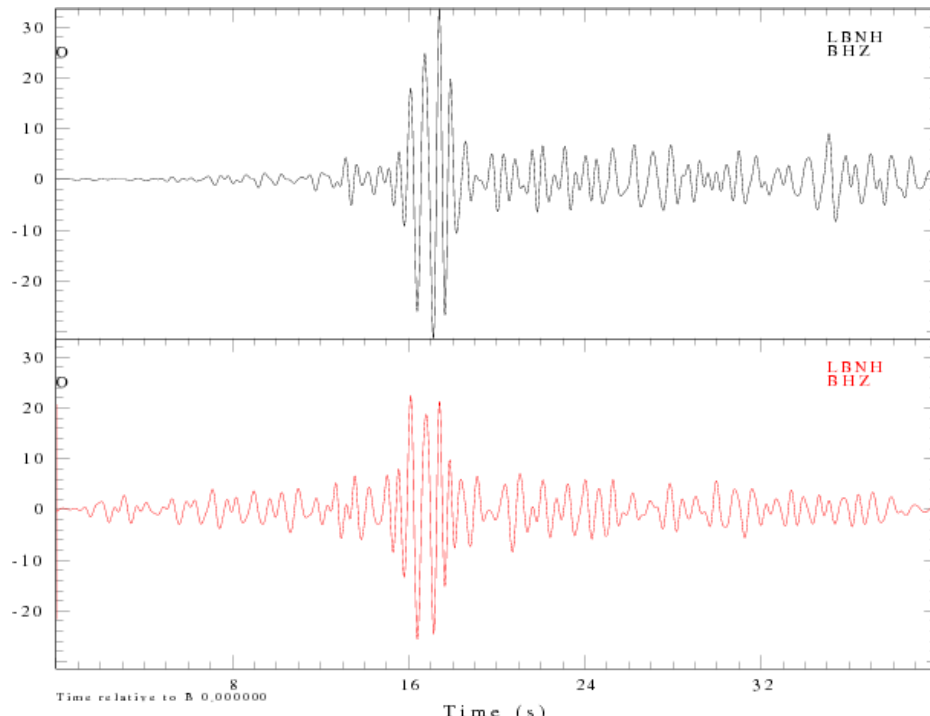
Figure 44. Rayleigh-waves recorded on the BHZ component at LBNH from Shots 4 (black) and 5 (red).

43
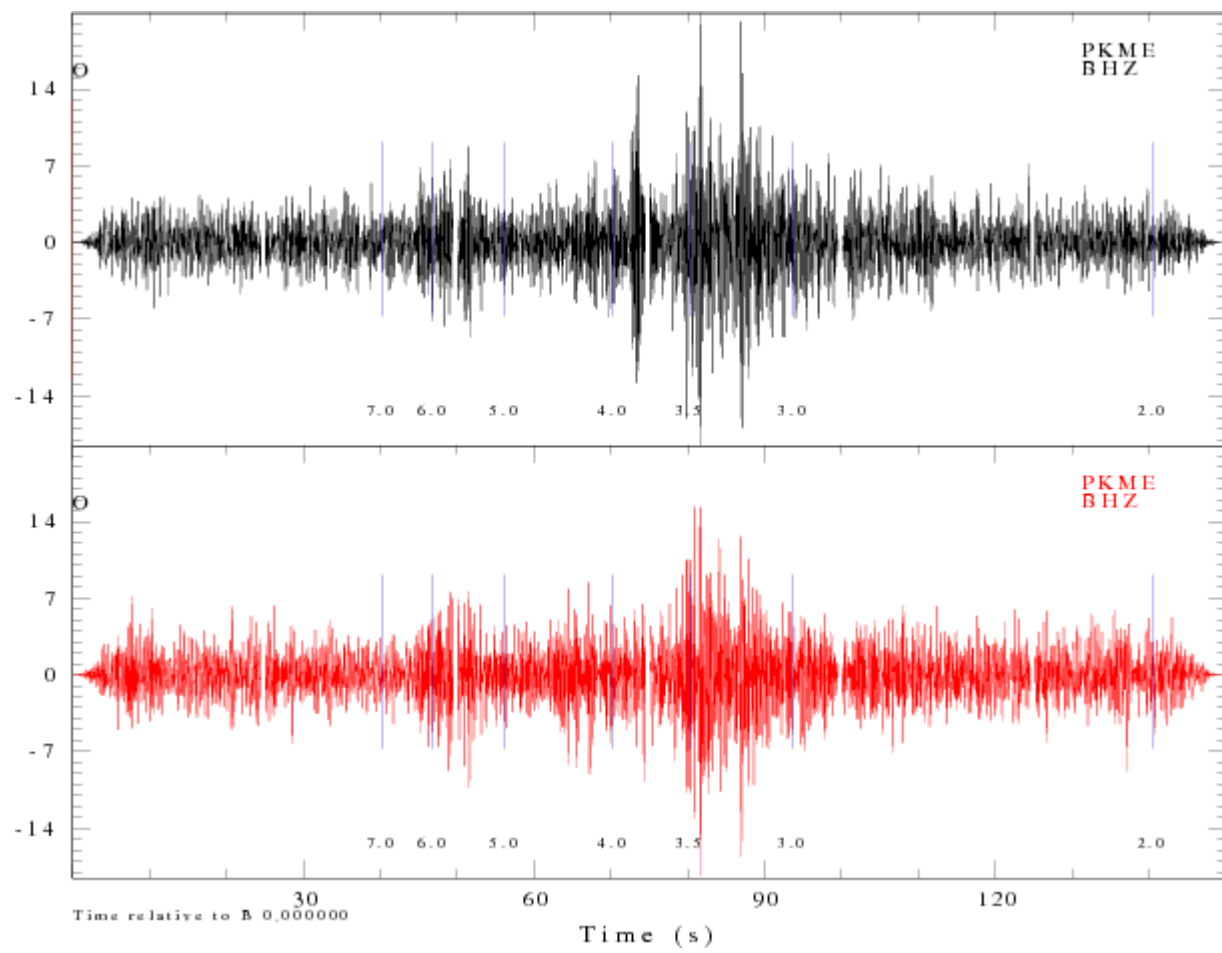
Figure 45. Shots 4 (black) and 5 (red) recorded at PKME (280 km). Note the impulsive arrival at group velocity 4 km/s only on the Shot 4 record.

PRE- AND POST-BLAST SOURCE ROCK CHARACTERIZATION

To quantitatively and qualitatively measure the damage caused by the blasts, geophysical studies were conducted on the source rock before and after the explosions. Figure shows initial planning for determining the damage to the source rock by drilling observational boreholes near the planned explosion. The pre-existing fractures and rock properties could be measured before the blast and then the fractures and damage could be observed in the boreholes after the explosions. This plan was modified for the actual experiment in that 2" diameter core was drilled near the explosion borehole and two boreholes were drilled on either side of the explosion borehole to perform a cross-hole tomography (Figure).
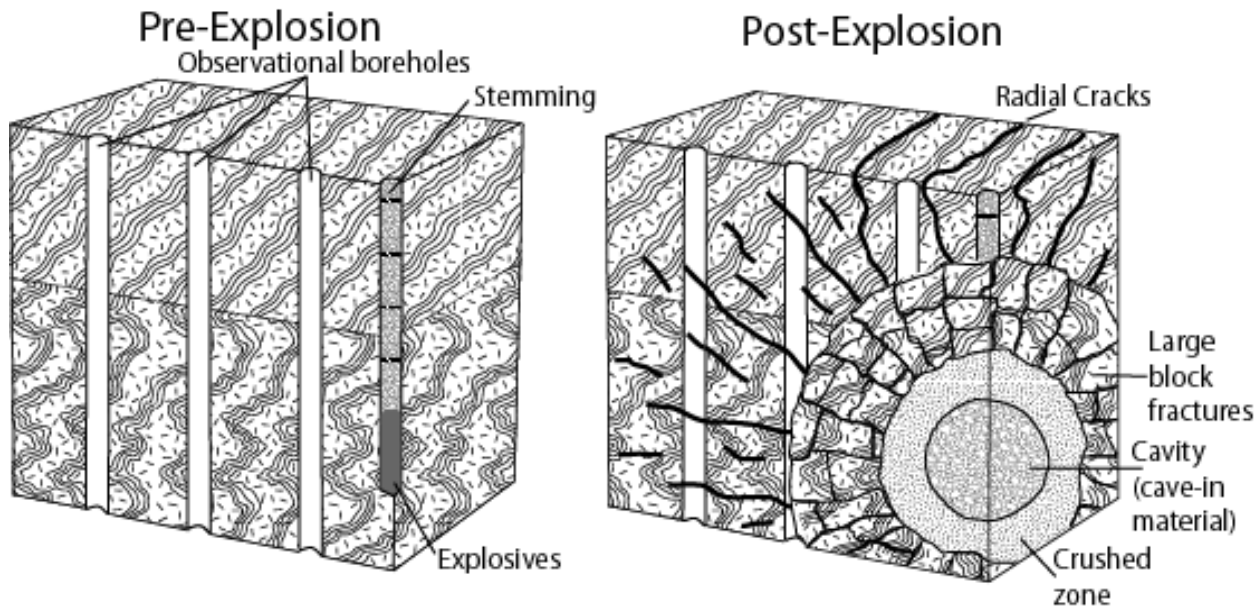
Figure 46. Diagram showing the initial planning for geophysical logging of the source rock before and after the explosions.

Core Samples

A photo of core taken from the test site is shown in Figure . The driller, Mike McGinley, had to break much of the core from the bottom of the hole due to the lack of natural fractures in the granite. Post-blast core samples were extracted to compare to the pre-blast samples.

A velocity analysis of the core extracted from near Shot 2 was completed by Peter Boyd (New England Research, Inc). Figure plots the compressional wave velocity as a function of depth in the core hole. The velocity increases with depth and has a change in slope at approximately 30 feet. The increase in compressional wave velocity with orientation, at a single depth, can approach 25 percent.

Figure shows the diametrally-transmitted compressional wave velocity, as a function of chord orientation, in the core specimen recovered from near Shot 2. The "Fast" chord defines the strike of the rift plane in the Barre granite, which is N30E° at this site (Donald Murray, pers. comm. 2008). The rift plane is considered to be near-vertical and is the orientation that the granite

blocks break cleanly when being quarried. The fastest compressional wave velocity is ~19 percent greater than the slowest velocity in this specimen.
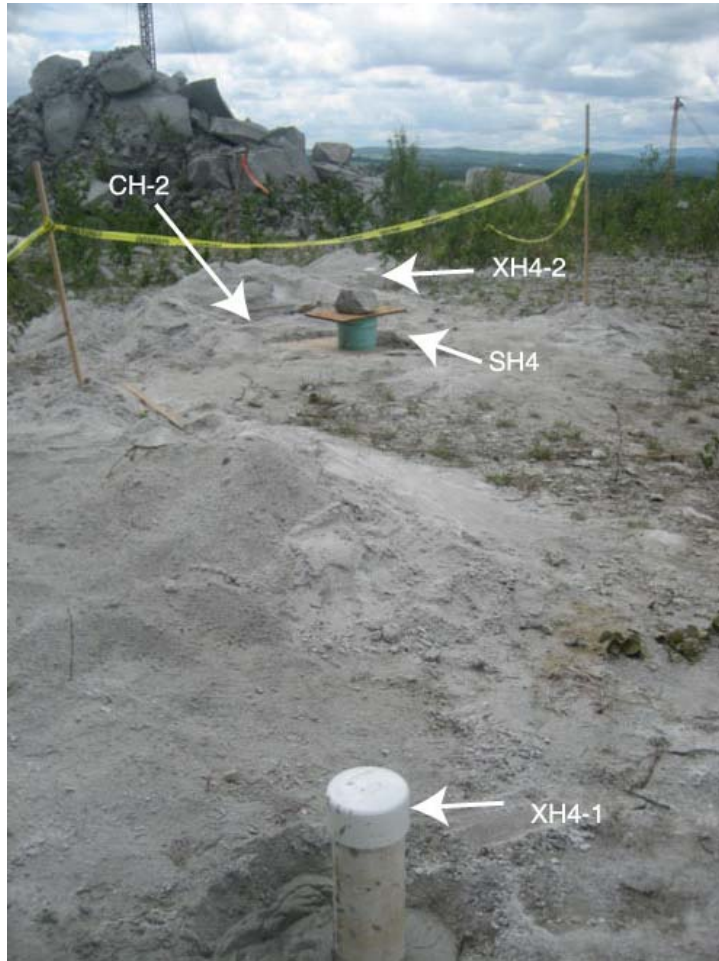
Figure 47. Typical layout of blast hole (SH4), core hole (CH-2), and cross-hole tomography holes (XH4-1 and XH4-2) for all five shots.

<u>**Televiewer**</u>
Dorothy Richter, Rob Garfield, and Alexis Martinez of Hager-Richter Geoscience were responsible for performing optical and acoustic televiewer logging of the test site (Figure) before and after the blasts. The resulting images provide a 360° view of the borehole walls for mapping fractures (Figure). Table 13 lists the fractures found in core hole 1 (CH-1), and the rank defines the size and aperture of the fracture. This examination was carried out for all five core holes.

Figure 48. Example of unfractured core taken from the test site.
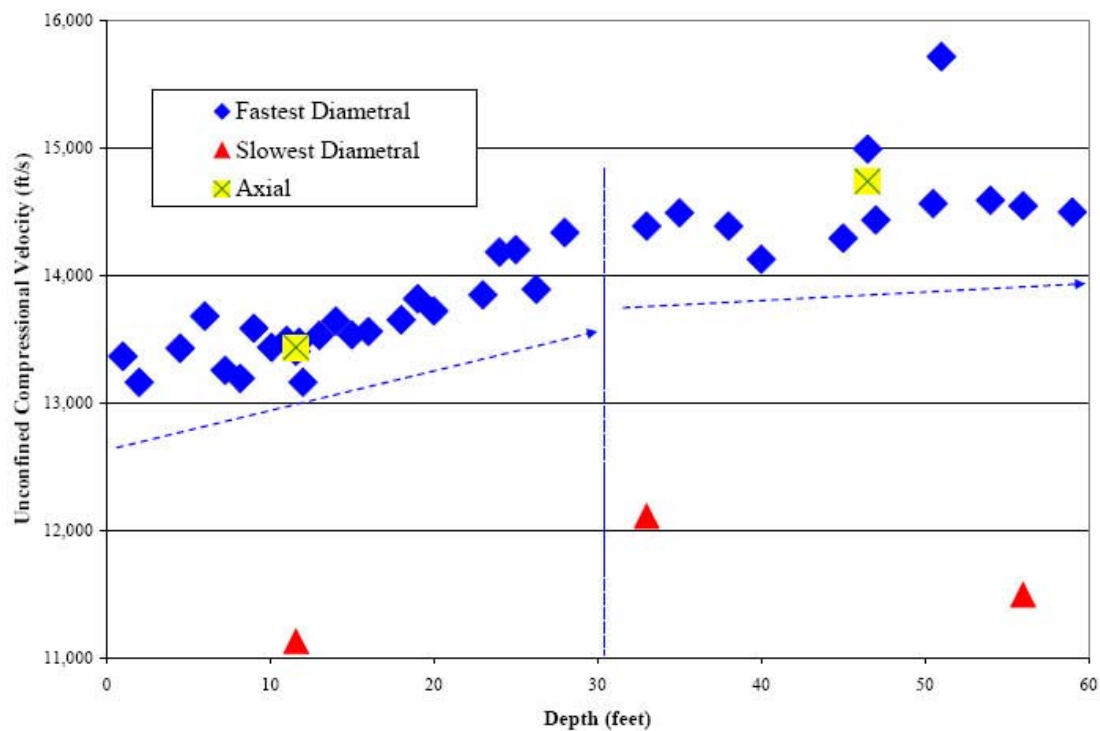
Figure 49. Compressional wave velocity determined in a laboratory study of core taken from near Shot 2. The diametrals indicate orientation in the core hole.
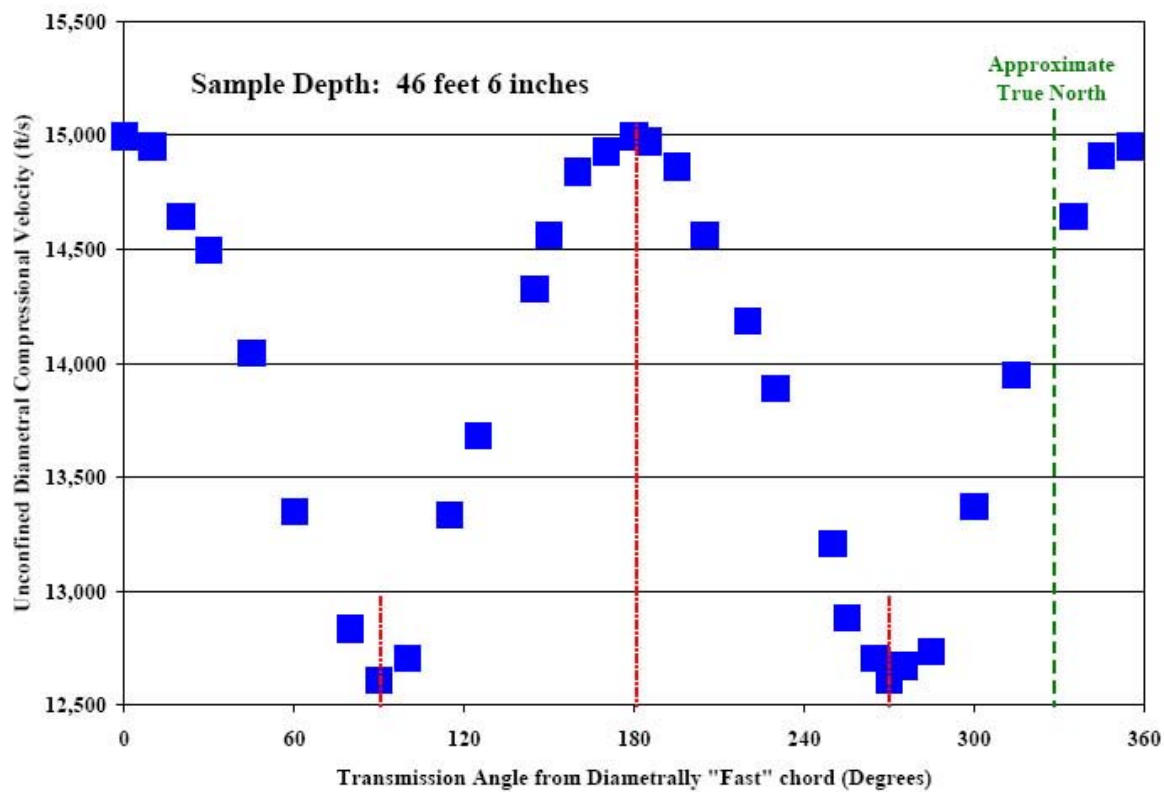
Figure 50. Compressional wave velocity as a function of azimuth in the Barre granite near Shot 2. The fast direction is oriented ~30° east of true north and is believed to follow the "rift" of the granite.

Figure 51. Logging with acoustic and/or optical televiewer.

Table 13. Structures in the Granite of Core Hole 1.

Depth (ft)	Dip Azimuth (°)	Dip Angle (°)	Bedrock Structure
6.5	187	82	Fracture Rank 1
7.7	101	4	Fracture Rank 3
8.3	185	17	Fracture Rank 2
8.4	265	14	Fracture Rank 2
8.5	263	19	Fracture Rank 2
9.9	179	67	Fracture Rank 1
10.1	195	7	Fracture Rank 2
10.2	172	20	Fracture Rank 2
11.9	82	41	Fracture Rank 1
11.9	260	16	Fracture Rank 2
13.2	353	45	Fracture Rank 1
13.6	224	39	Fracture Rank 2
14.6	65	48	Fracture Rank 2
21.1	241	68	Fracture Rank 2
39.6	105	26	Fracture Rank 2
50.8	105	26	Fracture Rank 2
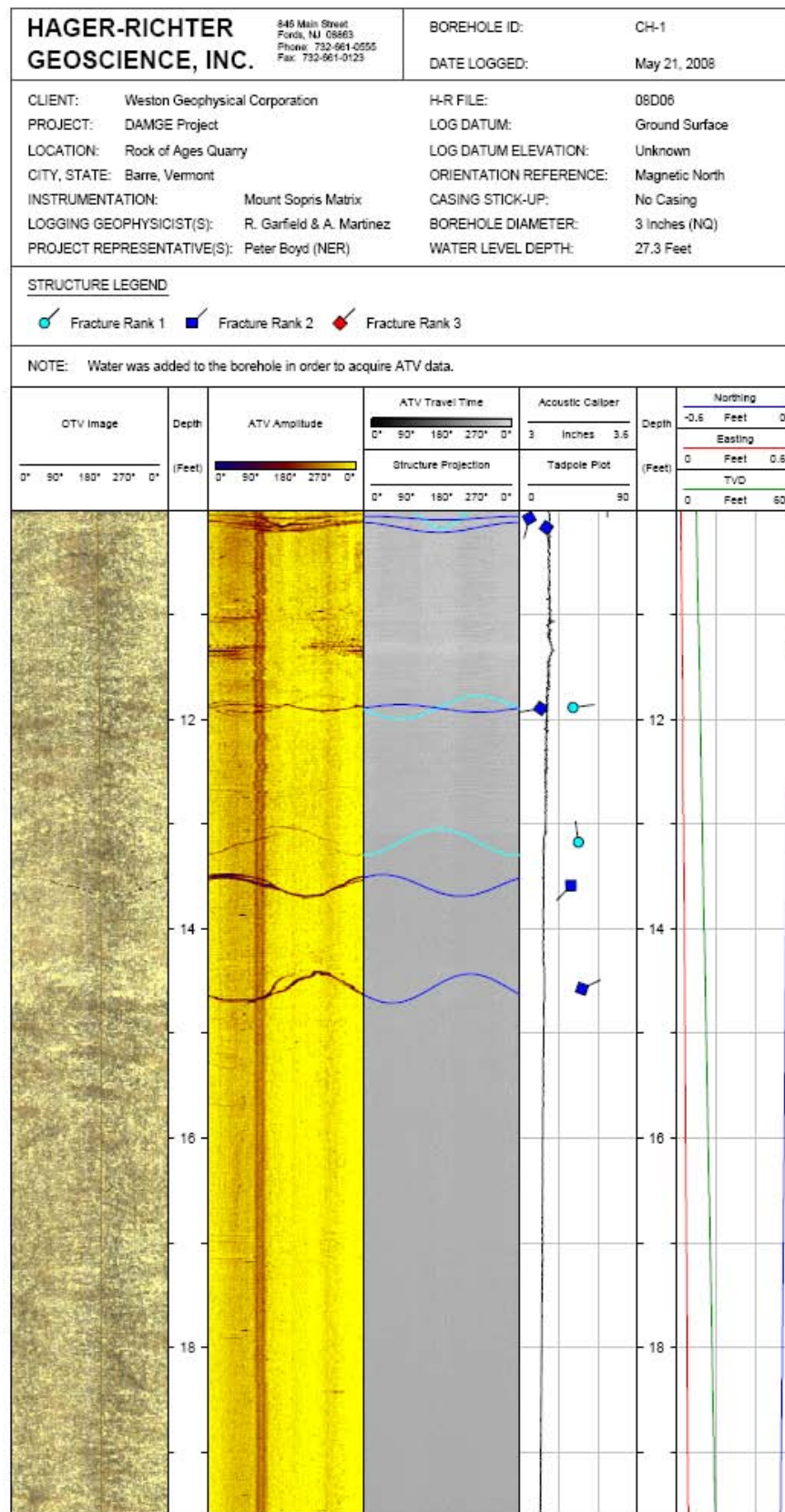
Figure 52. Optical and acoustic televiewer log documenting fractures in the granite.

Cross-hole Tomography

A cross-hole tomography was to be conducted prior to the blasting across each blast hole, but the grout used to hold the PVC pipe in the holes was bentonite-based instead of cement based. The result is shown in Figure . The grout did not solidify properly to secure the PVC pipe and "attach" it to the bore hole wall. It was therefore not possible to conduct the cross-hole tomography. New holes may be drilled after the blasting and grouted properly so the tomography can be conducted. The tomography will highlight the region with seismic velocities that are decreased from the background level and therefore have sustained damage and fracturing during the blasting. Jeff Reid of Hager-Richter Geoscience will be responsible for acquiring the data for this study.

Figure 53. Grout collapsed around PVC pipe in a cross-hole tomography bore hole.

APPENDIX 2A. HUDDLE TEST

We conducted a huddle test with all the near-source and linear short period array sensors in Lexington, MA, on 6 July 2008 prior to packing the equipment up and trucking it to Barre, VT. The two primary goals of this test were to assemble working stations with DAS, GPS clocks, hard drives, and sensors and to record the same signals on all the sensors so we can compare instrument response for correcting the NEDE blast data.

Figure shows the Weston, PASSCAL, and LANL sensors with batteries and digitizers in close proximity to record the same signals at 250 sps. Table 14 lists the equipment used during the huddle test. The PASSCAL and LANL sensors did not have feet so it was a challenge to level them on the sloping parking lot.

Figure 54. Huddle test in the Weston Geophysical parking lot prior to the experiment.

Some of the old LANL sensors had bad channels and were not used for the actual experiment. For the short period equipment, a Weston RT130 power cable was found to have reversed polarity connectors. Reversing the connection to the battery fixed this problem. In addition, the parameter files did not upload properly to two DAS and the data were set to be downloaded to disk and ethernet. This caused the internal memory to fill and dump to disk once and then stop recording. Data were collected for the majority of the huddle test though. A PASSCAL RT130 would not boot so no data were collected. This DAS was repaired in the field and used for the

experiment. We also found that leaving the new RT130 Palm controllers in the sun causes the screen and system to act erratically.

Table 14. Huddle Test Setup.

DAS	Disk	GPS	CH 1-3	CH 4-6	Notes
734	5715	663	Endevco 6	Endevco 2	All chans good
738	87	664	L4-3D 619	TerraTek 9	All chans good (TT hi-freq noise on Z and E)
716	5106	248	L4-3D 84	TerraTek 13	L4 bad E; TT has bad N
745	5236	299	L4-3D 37	TerraTek ??	Re-do test
739	5237	674	L4-3D 623	TerraTek 6	L4 bad E and N valid >30 Hz; TT good, Z may be enhanced
737	5180	670	L4-3D 189	TerraTek 4	Re-do test
744 (1768)	5713	244	L4-3D 257	TerraTek 7	Re-do test
733	5959	669	L4-3D 628		All chans good
9E4B	-	2514	L4-3D L41167		Good
9D8F	-	2661	L4-3D L41166		Good; 1 data dump
9DEA	-	2448	L4-3D L41169		Good
9E18	-	2565	L4-3D L41162		Good
9E1B	-	2711	L4-3D L41164		Good; 1 data dump
9D63	-	2665	L4-3D L41168		Good
9E42	-	2516	L4-3D L41161		Good
9E4F	-	2531	L4-3D L41165		Good
9DAA	-	2520	L4-3D L41170		Good
9E17	-	2809	L4-3D L41163		Good
939E	-	4194	L22 449L		Good
930E	-	3890	L22 643L		Good
9E45	-	4175	L22 642L		Good
9E40	-	4161	L22 468L		DAS would not boot; not tested
A198	-	4176	L22 462L		Good
9E50	-	4188	L22 720L		Good
940F	-	4196	L22 479L		Good
9312	-	4189	L22 496L		Good
9D42	-	4198	L22 494L		Good
9669	-	4179	L22 459L		Good

Data examples from the huddle test are shown in the following figures. The "flip test" (Figure and Figure 56) for accelerometers involves turning the accelerometer upside down for a moment to record 1 g of acceleration. For the seismometers, various signals were examined to determine if all channels are working and how the signals vary from sensor to sensor (Figure through Figure 59). Both the Weston L4-3D (Figure 60) and the PASSCAL L22 (Figure 61) sensors have self-similar responses. It is important to understand the response difference between the L4-3D and L22 sensors. Figure compares the same vertical signal on the two types of sensor after the data have been converted to velocity (cm/s). The signals are almost identical. The polarity on the Weston L4-3D horizontal components needs to be reversed, but almost identical signals were produced for these components after correction as well.
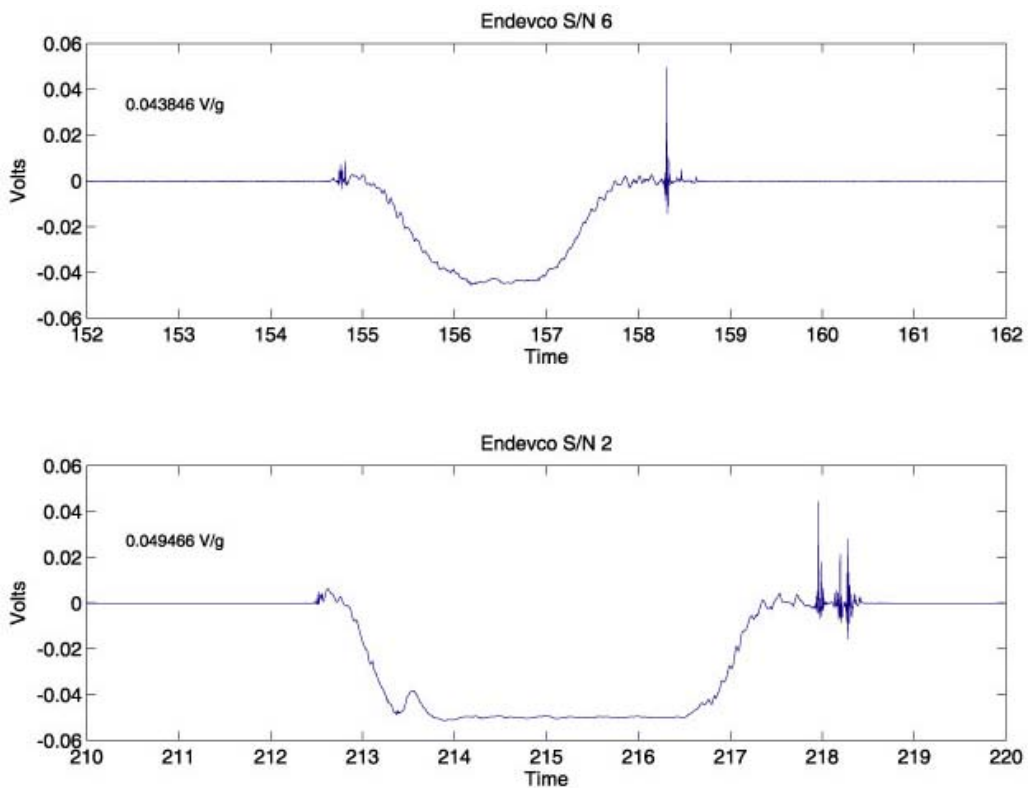
Figure 55. "Flip test" for Endevco sensors.
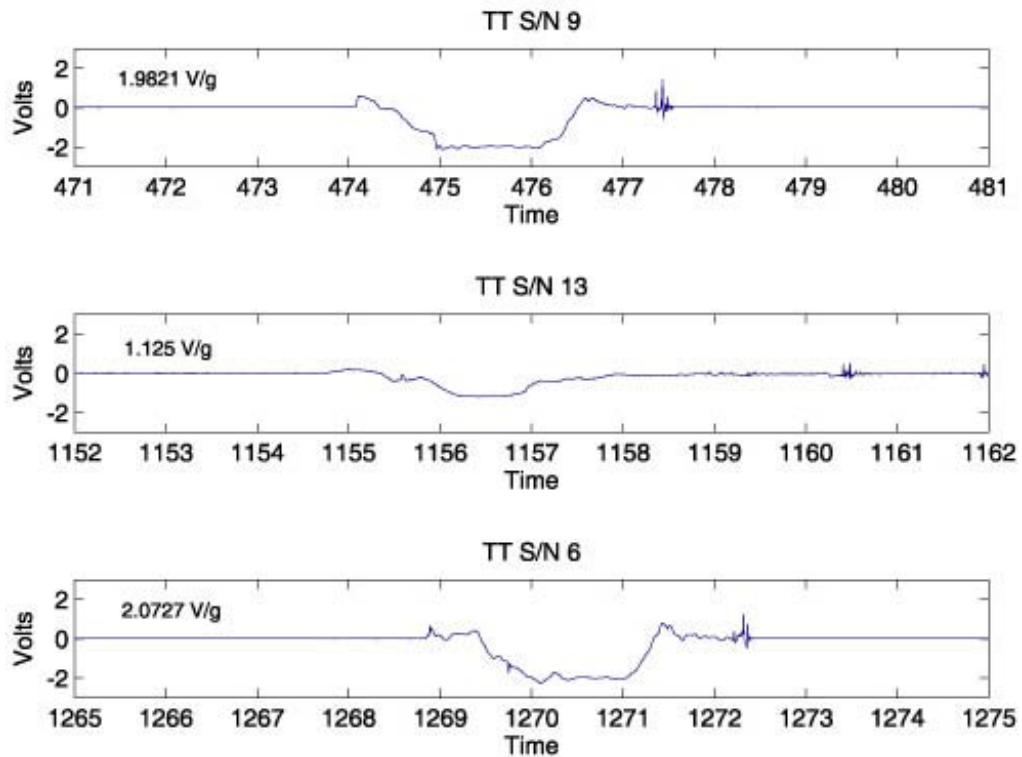
Figure 56. "Flip test" for TerraTek sensors.

54
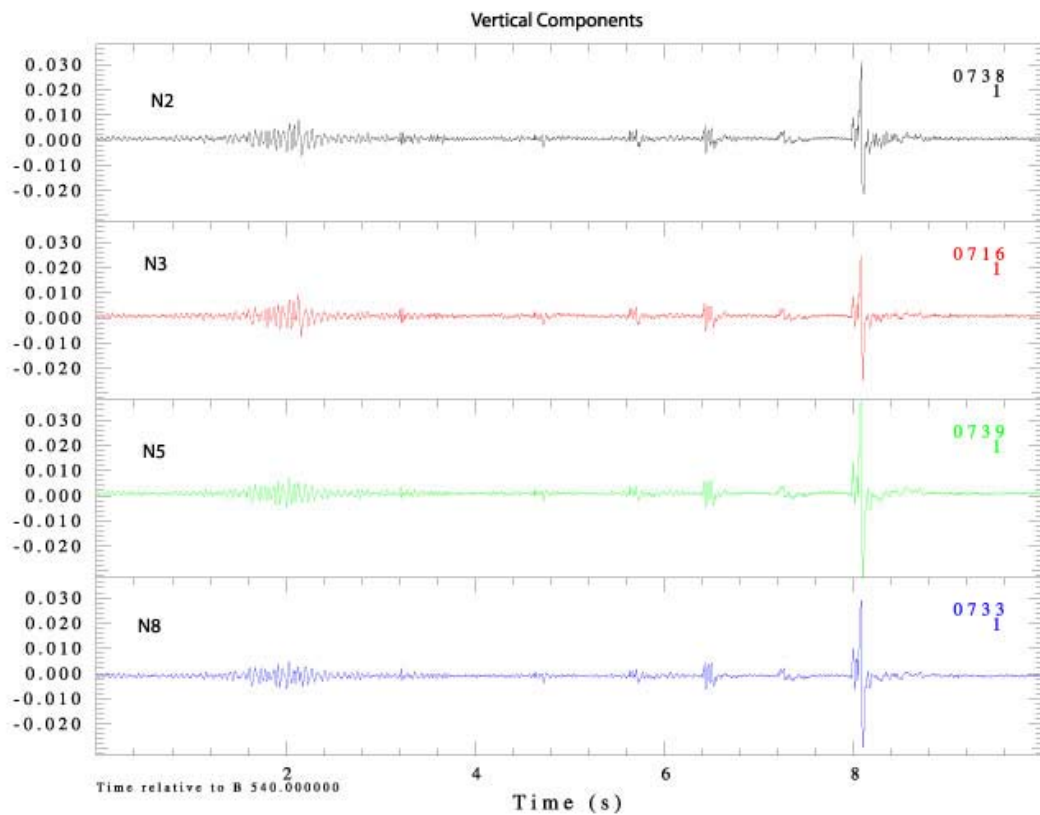
Figure 57. Near-source vertical L4-3D components.
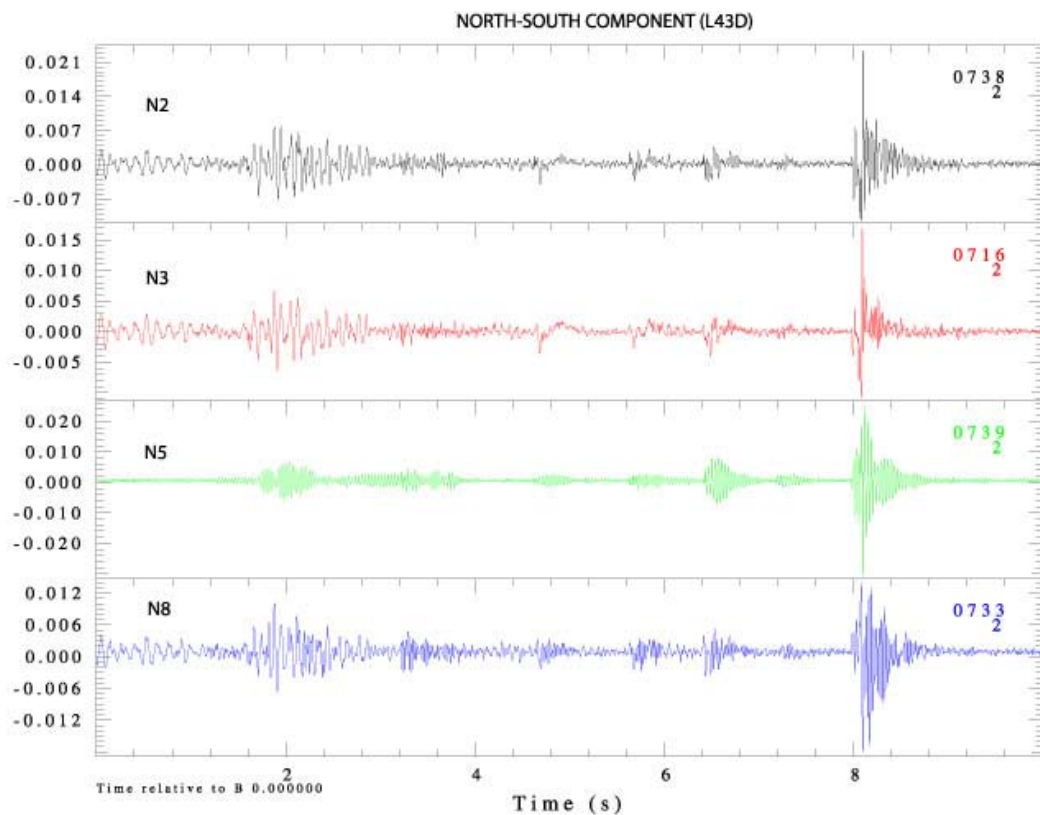
Figure 58. Near-source north/south L4-3D components.

EAST-WEST COMPONENT (L43D)
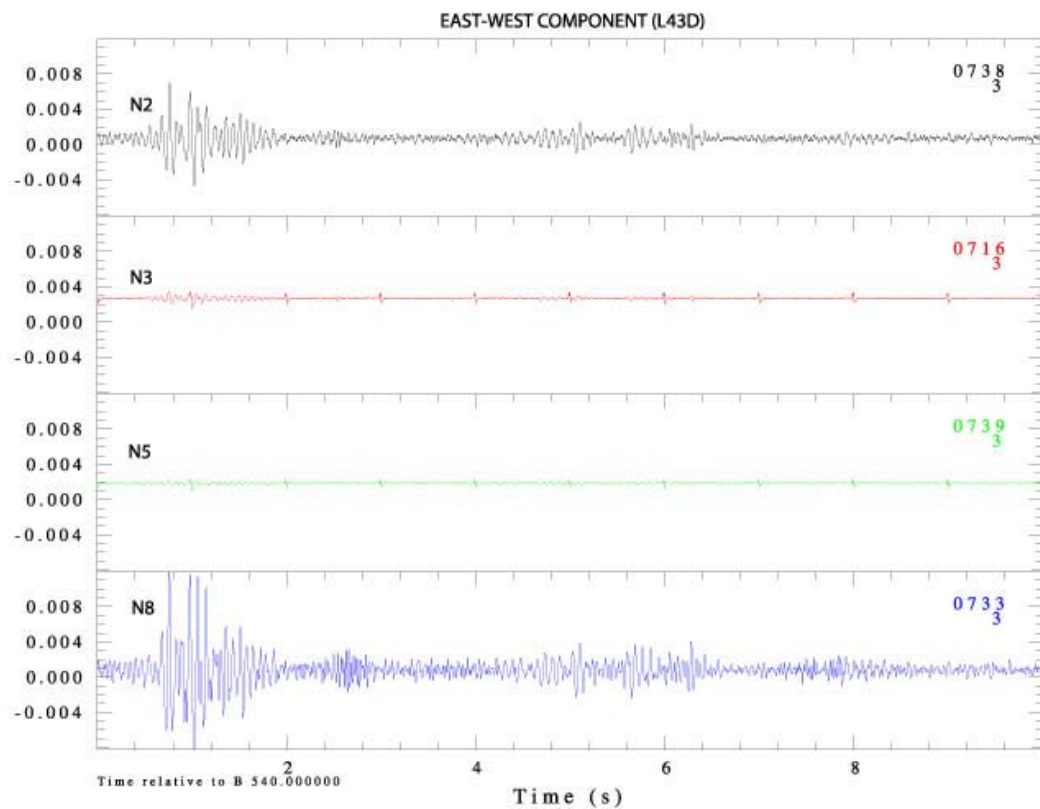
Figure 59. Near-source east/west L4-3D components.
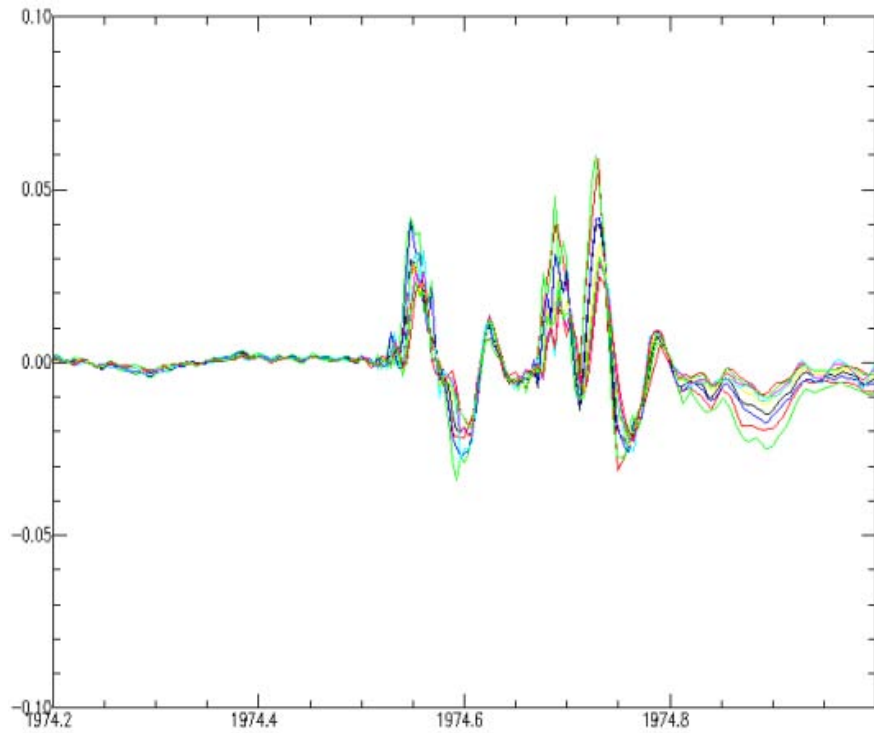
Figure 60. Weston L4-3D vertical component huddle data for all sensors.

56
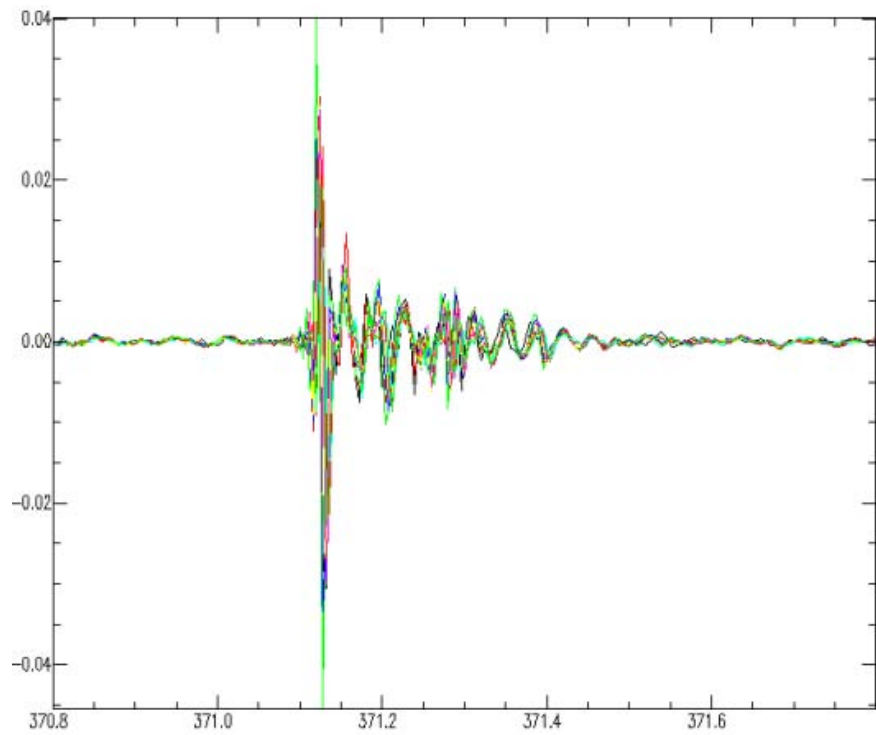
Figure 61. PASSCAL L22 vertical component huddle data for all sensors.
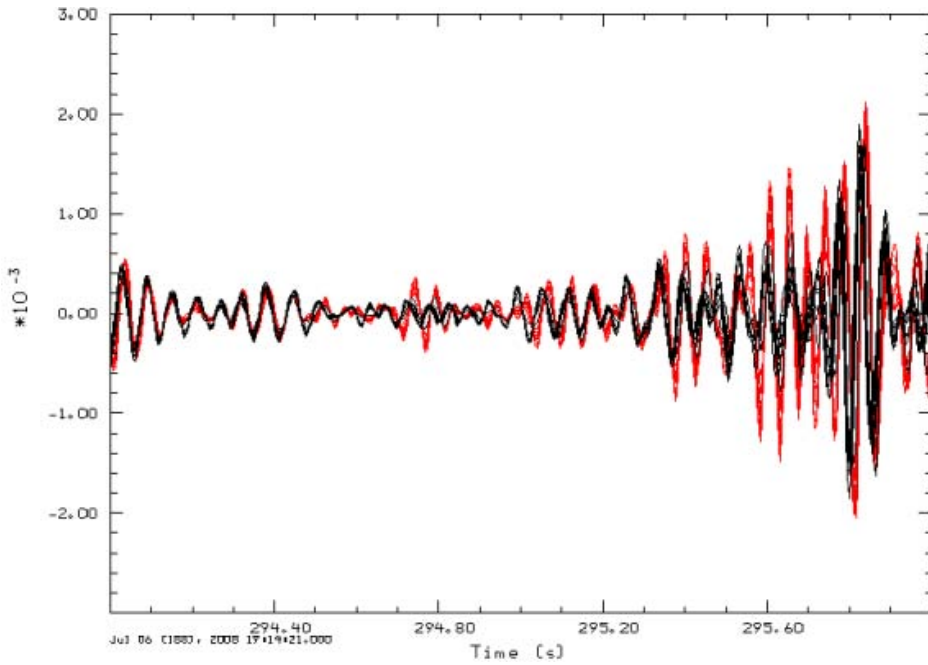
Figure 62. Comparison of Weston L4-3D (red) and PASSCAL L22 (black) vertical huddle data between 2 and 20 Hz after converting all data to velocity (cm/s).

APPENDIX 2B. L22 IN-SITU RESPONSE

Serial #	Channel	String	Frequency	Damping	Resistance	Sensitivity (V/cm/s)	Impedance	LoDrv Impedance	Distortion	Polarity	Leakage	GeoType
449L	1	Single	2.11	0.7	4501	0.893	5012.4	5017	0.05	0	0	L-22D-200804
449L	2	Single	2.07	0.728	4447	0.859	4989.2	4994	0	0	0	L-22D-200804
449L	3	Single	2.01	0.75	4442.6	0.935	4997.8	5002	0.17	0	0	L-22D-200804
459L	1	Single	2.17	0.765	4281	0.934	4927.1	4947	0.01	0	0	L-22D-200804
459L	2	Single	1.88	0.812	4300.9	0.872	4791.2	4795	0.12	0	0	L-22D-200804
459L	3	Single	2.1	0.702	4287.9	0.878	4787.9	4792	0.04	0	0	L-22D-200804
462L	1	Single	2.05	0.762	4344.1	0.919	4970.6	4975	0.08	0	0	L-22D-200804
462L*	2	Single	2.07	0.785	4392	0.9	5045	5049	0.14	0	0	L-22D-200804
462L*	3	Single	2.09	0.818	4403.9	0.989	5145.1	5150	0.14	0	0	L-22D-200804
479L	1	Single	2.23	0.633	4369.8	0.959	4946.2	4957	0.12	0	0	L-22D-200804
479L	2	Single	1.99	0.697	4258.8	0.806	4885.8	4894	0.55	0	0	L-22D-200804
479L	3	Single	1.97	0.804	4269.5	0.917	4884.3	4890	0.03	0	0	L-22D-200804
494L	1	Single	1.99	0.773	4532.2	0.906	5101.2	5105	0	0	0	L-22D-200804
494L	2	Single	2	0.752	4574	0.866	5074.8	5079	0	0	0	L-22D-200804
494L	3	Single	2.04	0.769	4489.7	0.938	5050.9	5056	0.23	0	0	L-22D-200804
496L	1	Single	1.96	0.745	4536	0.917	5026.7	5031	0.72	0	0	L-22D-200804
496L**	2	Single	-5.11	0.431	4470.6	1.194	4993.7	4998	0.03	0	0	L-22D-200804
496L	3	Single	2.01	0.727	4559.5	0.893	5058.5	5063	0.04	0	0	L-22D-200804
642L	1	Single	2.03	0.808	4465.7	0.99	5194.8	5199	0.36	0	0	L-22D-200804
642L	2	Single	2.02	0.818	4487.1	0.953	5161.3	5166	0.03	0	0	L-22D-200804
642L	3	Single	1.85	0.826	4340	0.844	4817.4	4822	0	0	0	L-22D-200804
643L	1	Single	2.13	0.733	4298.9	0.929	4919.5	4924	0	0	0	L-22D-200804
643L	2	Single	2.07	0.742	4169.7	0.915	4728.3	4733	0.18	0	0	L-22D-200804
643L	3	Single	2.5	0.623	4387.7	1.041	5073.2	5078	0.44	0	0	L-22D-200804
720L	1	Single	2.13	0.607	4434.1	0.89	4863.5	4869	0.33	0	0	L-22D-200804
720L	2	Single	2.32	0.683	4534.2	0.916	5188.1	5193	0.2	0	0	L-22D-200804
720L	3	Single	2.03	0.707	4299.3	0.939	4954.6	4960	0.46	0	0	L-22D-200804

*Note: For sensor 462L, channels 2 and 3 were swapped. This table reflects data as collected in the field and has not been modified to fix that problem.
** Response information for this channel appears incorrect.

APPENDIX 2C. L4-3D FACTORY REPSONSE

1. **General**
   a) Serial Number: L41161
   b) Tested at 78 ° F
   c) Leakage to case >100 Megohms at 500 volts.

2. **Calibration Coils, In Series**
   a) Resistance: 21.3 Ohms
   b) Polarity: Negative voltage at socket A with respect to socket B
      when suspended mass moves toward to the case bottom

3. **Signal Coil (Vertical Detector)** Serial Number: L41171
   a) Electrodynamic Constant: 7.09 V/in/sec
   b) Resistance: 5652 Ohms
   c) Calibration Constant: 40.1 KDynes/Ampere
   d) Frequency (fo): 0.98 Hz
   e) Open circuit damping (bo): 0.28 of critical damping
   f) Suspended mass (m): 969.4 grams
   g) Polarity: Negative voltage at socket E with respect to socket F
      when suspended mass moves toward to the case bottom

4. **Signal Coil (Longtitudinal Detector)** Serial Number: Ø508725
   a) Electrodynamic Constant: 7.05 V/in/sec
   b) Resistance: 5644 Ohms
   c) Calibration Constant: 39.6 KDynes/Ampere
   d) Frequency (fo): 0.96 Hz
   e) Open circuit damping (bo): 0.285 of critical damping
   f) Suspended mass (m): 969.9 grams
   g) Polarity: Negative voltage at socket C with respect to socket D
      when suspended mass moves toward to the case bottom

5. **Signal Coil (Transverse Detector)** Serial Number: Ø508726
   a) Electrodynamic Constant: 7.24 V/in/sec
   b) Resistance: 5647 Ohms
   c) Calibration Constant: 40.5 KDynes/Ampere
   d) Frequency (fo): 0.99 Hz
   e) Open circuit damping (bo): 0.274 of critical damping
   f) Suspended mass (m): 968.4 grams
   g) Polarity: Negative voltage at socket G with respect to socket H
      when suspended mass moves toward to the case bottom

Figure 63. L4-3D L41161 factory calibration specifications.

1. **General**
   a) Serial Number: L41162
   b) Tested at   76 ° F
   c) Leakage to case   >100   Megohms at 500 volts.

2. **Calibration Coils, In Series**
   a) Resistance: 20.9   Ohms
   b) Polarity: Negative voltage at socket   A   with respect to socket   B
      when suspended mass moves toward to the case bottom

3. **Signal Coil (Vertical Detector)**   Serial Number: L41172
   a) Electrodynamic Constant: 7.1   V/in/sec
   b) Resistance: 5649   Ohms
   c) Calibration Constant: 40.4   KDynes/Ampere
   d) Frequency (fo):   0.98   Hz
   e) Open circuit damping (bo):   0.287   of critical damping
   f) Suspended mass (m):   966.8   grams
   g) Polarity: Negative voltage at socket   E   with respect to socket   F
      when suspended mass moves toward to the case bottom

4. **Signal Coil (Longtitudinal Detector)**   Serial Number: 508727
   a) Electrodynamic Constant: 6.93   V/in/sec
   b) Resistance: 5647   Ohms
   c) Calibration Constant: 40.3   KDynes/Ampere
   d) Frequency (fo):   0.98   Hz
   e) Open circuit damping (bo):   0.288   of critical damping
   f) Suspended mass (m):   971.3   grams
   g) Polarity: Negative voltage at socket   C   with respect to socket   D
      when suspended mass moves toward to the case bottom

5. **Signal Coil (Transverse Detector)**   Serial Number: 508728
   a) Electrodynamic Constant: 7.27   V/in/sec
   b) Resistance: 5645   Ohms
   c) Calibration Constant: 39.2   KDynes/Ampere
   d) Frequency (fo):   0.96   Hz
   e) Open circuit damping (bo):   0.273   of critical damping
   f) Suspended mass (m):   970.7   grams
   g) Polarity: Negative voltage at socket   G   with respect to socket   H
      when suspended mass moves toward to the case bottom

Figure 64. L4-3D L41162 factory calibration specifications.

1. **General**
    a) Serial Number: L41163
    b) Tested at 78 °F
    c) Leakage to case >100 Megohms at 500 volts.

2. **Calibration Coils, In Series**
    a) Resistance: 20.2 Ohms
    b) Polarity: Negative voltage at socket A with respect to socket B
       when suspended mass moves toward to the case bottom

3. **Signal Coil (Vertical Detector)**   Serial Number: L41173
    a) Electrodynamic Constant: 7.14 V/in/sec
    b) Resistance: 5638 Ohms
    c) Calibration Constant: 41.4 KDynes/Ampere
    d) Frequency (fo): 1 Hz
    e) Open circuit damping (bo): 0.276 of critical damping
    f) Suspended mass (m): 967.2 grams
    g) Polarity: Negative voltage at socket E with respect to socket F
       when suspended mass moves toward to the case bottom

4. **Signal Coil (Longtitudinal Detector)**   Serial Number: 508729
    a) Electrodynamic Constant: 7.29 V/in/sec
    b) Resistance: 5636 Ohms
    c) Calibration Constant: 41.2 KDynes/Ampere
    d) Frequency (fo): 1.01 Hz
    e) Open circuit damping (bo): 0.276 of critical damping
    f) Suspended mass (m): 970.7 grams
    g) Polarity: Negative voltage at socket C with respect to socket D
       when suspended mass moves toward to the case bottom

5. **Signal Coil (Transverse Detector)**   Serial Number: 508730
    a) Electrodynamic Constant: 7.24 V/in/sec
    b) Resistance: 5622 Ohms
    c) Calibration Constant: 40.9 KDynes/Ampere
    d) Frequency (fo): 1 Hz
    e) Open circuit damping (bo): 0.275 of critical damping
    f) Suspended mass (m): 966.7 grams
    g) Polarity: Negative voltage at socket G with respect to socket H
       when suspended mass moves toward to the case bottom

Figure 65. L4-3D L41163 factory calibration specifications.

61

1. **General**
    a) Serial Number: L41164
    b) Tested at 79 °F
    c) Leakage to case >100 Megohms at 500 volts.

2. **Calibration Coils, In Series**
    a) Resistance: 19.9 Ohms
    b) Polarity: Negative voltage at socket A with respect to socket B
       when suspended mass moves toward to the case bottom

3. **Signal Coil (Vertical Detector)**   Serial Number: L41174
    a) Electrodynamic Constant: 7.26 V/in/sec
    b) Resistance: 5630 Ohms
    c) Calibration Constant: 41.5 KDynes/Ampere
    d) Frequency (fo): 0.99 Hz
    e) Open circuit damping (bo): 0.283 of critical damping
    f) Suspended mass (m): 974.5 grams
    g) Polarity: Negative voltage at socket E with respect to socket F
       when suspended mass moves toward to the case bottom

4. **Signal Coil (Longtitudinal Detector)**   Serial Number: 508731
    a) Electrodynamic Constant: 7.28 V/in/sec
    b) Resistance: 5637 Ohms
    c) Calibration Constant: 39.2 KDynes/Ampere
    d) Frequency (fo): 0.96 Hz
    e) Open circuit damping (bo): 0.268 of critical damping
    f) Suspended mass (m): 971.6 grams
    g) Polarity: Negative voltage at socket C with respect to socket D
       when suspended mass moves toward to the case bottom

5. **Signal Coil (Transverse Detector)**   Serial Number: 508732
    a) Electrodynamic Constant: 7.25 V/in/sec
    b) Resistance: 5636 Ohms
    c) Calibration Constant: 39.3 KDynes/Ampere
    d) Frequency (fo): 0.97 Hz
    e) Open circuit damping (bo): 0.283 of critical damping
    f) Suspended mass (m): 969 grams
    g) Polarity: Negative voltage at socket G with respect to socket H
       when suspended mass moves toward to the case bottom

Figure 66. L4-3D L41164 factory calibration specifications.

1. **General**
   a) Serial Number: L41165
   b) Tested at 78 ° F
   c) Leakage to case >100 Megohms at 500 volts.

2. **Calibration Coils, In Series**
   a) Resistance: 20.5 Ohms
   b) Polarity: Negative voltage at socket ___A___ with respect to socket ___B___
   when suspended mass moves toward to the case bottom

3. **Signal Coil (Vertical Detector)** Serial Number: L41175
   a) Electrodynamic Constant: 7.05 V/in/sec
   b) Resistance: 5636 Ohms
   c) Calibration Constant: 41.2 KDynes/Ampere
   d) Frequency (fo): 0.98 Hz
   e) Open circuit damping (bo): 0.277 of critical damping
   f) Suspended mass (m): 970.2 grams
   g) Polarity. Negative voltage at socket ___E___ with respect to socket ___F___
   when suspended mass moves toward to the case bottom

4. **Signal Coil (Longtitudinal Detector)** Serial Number: 508733
   a) Electrodynamic Constant: 7.21 V/in/sec
   b) Resistance: 5633 Ohms
   c) Calibration Constant: 39.6 KDynes/Ampere
   d) Frequency (fo): 0.98 Hz
   e) Open circuit damping (bo): 0.275 of critical damping
   f) Suspended mass (m): 972.5 grams
   g) Polarity: Negative voltage at socket ___C___ with respect to socket ___D___
   when suspended mass moves toward to the case bottom

5. **Signal Coil (Transverse Detector)** Serial Number: 508734
   a) Electrodynamic Constant: 7.1 V/in/sec
   b) Resistance: 5613 Ohms
   c) Calibration Constant: 41.9 KDynes/Ampere
   d) Frequency (fo): 1 Hz
   e) Open circuit damping (bo): 0.274 of critical damping
   f) Suspended mass (m): 972.1 grams
   g) Polarity: Negative voltage at socket ___G___ with respect to socket ___H___
   when suspended mass moves toward to the case bottom

Figure 67. L4-3D L41165 factory calibration specifications.

1. **General**
   a) Serial Number: L41166
   b) Tested at: 79 ° F
   c) Leakage to case: >100 Megohms at 500 volts.

2. **Calibration Coils, In Series**
   a) Resistance: 22 Ohms
   b) Polarity: Negative voltage at socket ___A___ with respect to socket ___B___
      when suspended mass moves toward to the case bottom

3. **Signal Coil (Vertical Detector)**   Serial Number: L41176
   a) Electrodynamic Constant: 7.15 V/in/sec
   b) Resistance: 5637 Ohms
   c) Calibration Constant: 40.2 KDynes/Ampere
   d) Frequency (fo): 0.98 Hz
   e) Open circuit damping (bo): 0.272 of critical damping
   f) Suspended mass (m): 969.3 grams
   g) Polarity: Negative voltage at socket ___E___ with respect to socket ___F___
      when suspended mass moves toward to the case bottom

4. **Signal Coil (Longtitudinal Detector)**   Serial Number: 508735
   a) Electrodynamic Constant: 7.33 V/in/sec
   b) Resistance: 5653 Ohms
   c) Calibration Constant: 39.7 KDynes/Ampere
   d) Frequency (fo): 1 Hz
   e) Open circuit damping (bo): 0.284 of critical damping
   f) Suspended mass (m): 971.9 grams
   g) Polarity: Negative voltage at socket ___C___ with respect to socket ___D___
      when suspended mass moves toward to the case bottom

5. **Signal Coil (Transverse Detector)**   Serial Number: 508736
   a) Electrodynamic Constant: 7.3 V/in/sec
   b) Resistance: 5646 Ohms
   c) Calibration Constant: 40.3 KDynes/Ampere
   d) Frequency (fo): 0.99 Hz
   e) Open circuit damping (bo): 0.273 of critical damping
   f) Suspended mass (m): 971.8 grams
   g) Polarity: Negative voltage at socket ___G___ with respect to socket ___H___
      when suspended mass moves toward to the case bottom

Figure 68. L4-3D L41166 factory calibration specifications.

64

1. **General**
   a) Serial Number: L41167
   b) Tested at 81 ° F
   c) Leakage to case >100 Megohms at 500 volts.

2. **Calibration Coils, in Series**
   a) Resistance: 31.9 Ohms
   b) Polarity: Negative voltage at socket A with respect to socket B
      when suspended mass moves toward to the case bottom

3. **Signal Coil (Vertical Detector)**   Serial Number: L41177
   a) Electrodynamic Constant: 7.12 V/in/sec
   b) Resistance: 5674 Ohms
   c) Calibration Constant: 40.9 KDynes/Ampere
   d) Frequency (fo): 1 Hz
   e) Open circuit damping (bo): 0.28 of critical damping
   f) Suspended mass (m): 971.6 grams
   g) Polarity: Negative voltage at socket E with respect to socket F
      when suspended mass moves toward to the case bottom

4. **Signal Coil (Longtitudinal Detector)**   Serial Number: 508737
   a) Electrodynamic Constant: 7.36 V/in/sec
   b) Resistance: 5694 Ohms
   c) Calibration Constant: 39.6 KDynes/Ampere
   d) Frequency (fo): 0.99 Hz
   e) Open circuit damping (bo): 0.279 of critical damping
   f) Suspended mass (m): 972.8 grams
   g) Polarity: Negative voltage at socket C with respect to socket D
      when suspended mass moves toward to the case bottom

5. **Signal Coil (Transverse Detector)**   Serial Number: 508738
   a) Electrodynamic Constant: 7.13 V/in/sec
   b) Resistance: 5676 Ohms
   c) Calibration Constant: 41.6 KDynes/Ampere
   d) Frequency (fo): 1 Hz
   e) Open circuit damping (bo): 0.271 of critical damping
   f) Suspended mass (m): 969.5 grams
   g) Polarity: Negative voltage at socket G with respect to socket H
      when suspended mass moves toward to the case bottom

Figure 69. L4-3D L41167 factory calibration specifications.

1. **General**
   a) Serial Number: L41168
   b) Tested at: 81 ° F
   c) Leakage to case: >100 Megohms at 500 volts.

2. **Calibration Coils, In Series**
   a) Resistance: 22.4 Ohms
   b) Polarity: Negative voltage at socket __A__ with respect to socket __B__
   when suspended mass moves toward to the case bottom

3. **Signal Coil (Vertical Detector)** Serial Number: __L41178__
   a) Electrodynamic Constant: 7.05 V/in/sec
   b) Resistance: 5646 Ohms
   c) Calibration Constant: 41.1 KDynes/Ampere
   d) Frequency (fo): 0.98 Hz
   e) Open circuit damping (bo): 0.289 of critical damping
   f) Suspended mass (m): 966.8 grams
   g) Polarity: Negative voltage at socket __E__ with respect to socket __F__
   when suspended mass moves toward to the case bottom

4. **Signal Coil (Longtitudinal Detector)** Serial Number: __C508739__
   a) Electrodynamic Constant: 7.23 V/in/sec
   b) Resistance: 5676 Ohms
   c) Calibration Constant: 40.4 KDynes/Ampere
   d) Frequency (fo): 1 Hz
   e) Open circuit damping (bo): 0.266 of critical damping
   f) Suspended mass (m): 974.4 grams
   g) Polarity: Negative voltage at socket __C__ with respect to socket __D__
   when suspended mass moves toward to the case bottom

5. **Signal Coil (Transverse Detector)** Serial Number: __C508740__
   a) Electrodynamic Constant: 7.25 V/in/sec
   b) Resistance: 5669 Ohms
   c) Calibration Constant: 41.8 KDynes/Ampere
   d) Frequency (fo): 1 Hz
   e) Open circuit damping (bo): 0.274 of critical damping
   f) Suspended mass (m): 971.3 grams
   g) Polarity: Negative voltage at socket __G__ with respect to socket __H__
   when suspended mass moves toward to the case bottom

Figure 70. L4-3D L41168 factory calibration specifications.

1. General
   a) Serial Number: L41169
   b) Tested at 75 °F
   c) Leakage to case >100 Megohms at 500 volts.

2. Calibration Coils, In Series
   a) Resistance: 23.8 Ohms
   b) Polarity: Negative voltage at socket A with respect to socket B
      when suspended mass moves toward to the case bottom

3. Signal Coil (Vertical Detector)   Serial Number: L41179
   a) Electrodynamic Constant: 7.03 V/in/sec
   b) Resistance: 5594 Ohms
   c) Calibration Constant: 41 KDynes/Ampere
   d) Frequency (fo): 0.97 Hz
   e) Open circuit damping (bo): 0.28 of critical damping
   f) Suspended mass (m): 970 grams
   g) Polarity: Negative voltage at socket E with respect to socket F
      when suspended mass moves toward to the case bottom

4. Signal Coil (Longtitudinal Detector)   Serial Number: 0508741
   a) Electrodynamic Constant: 6.93 V/in/sec
   b) Resistance: 5672 Ohms
   c) Calibration Constant: 44.5 KDynes/Ampere
   d) Frequency (fo): 1 Hz
   e) Open circuit damping (bo): 0.257 of critical damping
   f) Suspended mass (m): 968.9 grams
   g) Polarity: Negative voltage at socket C with respect to socket D
      when suspended mass moves toward to the case bottom

5. Signal Coil (Transverse Detector)   Serial Number: 0508742
   a) Electrodynamic Constant: 7.23 V/in/sec
   b) Resistance: 5631 Ohms
   c) Calibration Constant: 41.1 KDynes/Ampere
   d) Frequency (fo): 1 Hz
   e) Open circuit damping (bo): 0.271 of critical damping
   f) Suspended mass (m): 972.7 grams
   g) Polarity: Negative voltage at socket G with respect to socket H
      when suspended mass moves toward to the case bottom

Figure 71. L4-3D L41169 factory calibration specifications.

1. **General**
   a) Serial Number: L41170
   b) Tested at: 73 °F
   c) Leakage to case: >100 Megohms at 500 volts.

2. **Calibration Coils, In Series**
   a) Resistance: 23 Ohms
   b) Polarity: Negative voltage at socket ___A___ with respect to socket ___B___
      when suspended mass moves toward to the case bottom

3. **Signal Coil (Vertical Detector)**   Serial Number: ___L41180___
   a) Electrodynamic Constant: L41180 V/in/sec
   b) Resistance: 5600 Ohms
   c) Calibration Constant: 41.1 KDynes/Ampere
   d) Frequency (fo): 0.98 Hz
   e) Open circuit damping (bo): 0.283 of critical damping
   f) Suspended mass (m): 964.8 grams
   g) Polarity: Negative voltage at socket ___E___ with respect to socket ___F___
      when suspended mass moves toward to the case bottom

4. **Signal Coil (Longtitudinal Detector)**   Serial Number: ___0508743___
   a) Electrodynamic Constant: 6.73 V/in/sec
   b) Resistance: 5565 Ohms
   c) Calibration Constant: 45.1 KDynes/Ampere
   d) Frequency (fo): 1 Hz
   e) Open circuit damping (bo): 0.257 of critical damping
   f) Suspended mass (m): 972.8 grams
   g) Polarity: Negative voltage at socket ___C___ with respect to socket ___D___
      when suspended mass moves toward to the case bottom

5. **Signal Coil (Transverse Detector)**   Serial Number: ___0508744___
   a) Electrodynamic Constant: 6.85 V/in/sec
   b) Resistance: 5552 Ohms
   c) Calibration Constant: 42.1 KDynes/Ampere
   d) Frequency (fo): 0.98 Hz
   e) Open circuit damping (bo): 0.283 of critical damping
   f) Suspended mass (m): 972.2 grams
   g) Polarity: Negative voltage at socket ___G___ with respect to socket ___H___
      when suspended mass moves toward to the case bottom

Figure 72. L4-3D L41170 factory calibration specifications.

APPENDIX 2D. DATA RECORDS WITH HIGH NOISE OR CONTAMINATION

Near-source
No near-source data had issues with noise or signal contamination when the data were examined in a band pass of 1 to 20 Hz.

Short Period
The following short period stations had signal quality problems due to the listed issue when the data were examined in a band pass of 1 to 20 Hz. Filtering can help with noise issues.

Table 15. Short Period Data Quality Issues.

Shot 1	Shot 2	Shot 3	Shot 4	Shot 5
NE10-Noise	**NE08**-Car prior to shot arrival	**NE05**-Noise, possibly from lawn mower	**NE05**-Noise, possibly from lawn mower	**NE02**-Car prior to shot arrival
SE03-Noise	**NE09**-Car	**NE10**-Noise	**SE05**-Car?	**NE08**-Car
SE07-Noise	**SE05**-Car			
SE10-Noise	**SE09**-Car			
	SE10-Noise			

Texan
The following Texan stations had signal quality problems due to the listed issue when the data were examined in a band pass of 4 to 20 Hz. Filtering can help with noise issues.

Table 16. Texan Data Quality Issues.

Shot 1	Shot 2	Shot 3	Shot 4	Shot 5
ST11-Cont	**ST09**-Cont	**ST19**-Cont	**ST10**-Cont	**ST34**-Bad
ST20-Noise	**ST10**-Cont	**ST34**-Bad	**ST11**-Cont	**ST40**-Cont
ST22-Cont	**ST34**-Bad	**ST45**-Noise	**ST22**-Cont	**ST45**-Noise
ST23-Cont	**ST44**-Cont	**TN04**-Bad	**ST30**-Cont	**TN04**-Bad
ST34-Bad	**ST45**-Noise	**TN11**-Noise	**ST34**-Bad	**TN26**-Cont
ST40-Noise	**TN04**-Bad	**TN12**-Cont	**ST45**-Noise	**TN36**-Noise
ST41-Noise	**TN06**-Cont	**TN20**-Noise	**TN04**-Bad	**TN39**-Cont
ST42-Noise	**TN09**-Noise	**TN26**-Cont	**TN11**-Cont	**TN40**-Noise
ST43-Noise	**TN11**-Cont	**TN28**-Cont	**TN30**-Cont	
ST44-Noise	**TN30**-Noise	**TN39**-Cont	**TN38**-Cont	
ST45-Noise	**TN33**-Noise	**TN40**-Noise	**TN39**-Noise	
TN04-Bad	**TN34**-Cont		**TN40**-Noise	
TN11-Noise				
TN25-Cont				
TN28-Cont				
TN30-Noise				
TN32-Cont				
TN33-Noise				
TN40-Cont				

Noise=High noise levels; Cont=Contamination by other unspecified signals; Bad=Geophone or cable connection was bad

GREEN MOUNTAIN GME EXPLOSIVES

UNIFORM BLASTER'S LOG

Location of Blast Rock of Ages | **GPS Information**

Street Address:		At shot
City: Barre VT		At protected structure
Date of Blast: 7-11-08	Time of Blast: 3:40 ☐ AM ☑ PM	Description of Blast: ☐ Construction ☐ Quarry ☐ Trench

Weather Conditions

Conditions: ☐ Cloudy ☑ Clear ☐ Rain ☐ Snow	Temperature: /Degrees F 80	Wind Velocity: /MPH and Direction:

Design Information

Face Height: /ft —	Over Burden: /ft 0'-2'	Burden: /ft 5'	Cubic yards 855
Type of Material Blasted: Granite	Hole Diameter: /in 3½"	Spacing: /ft 5'	Tons: 1890
Hole Depth: /ft 7'-15	Deck Stem: /ft —	Number of holes: 84 7 8rec lbs/yd³ 1.5	
Sub Drill: /ft —	Type of Stemming: crushed stone	Collar Stem: /ft 5'-7'	Tons /Lb. 104
Blast Mat / Cover Used: none	Drill Co. Yankee	Face Direction:	Total Drill footage: 1001

Explosives Used

Type	1. 2Boost	2. Presplit 7/6	3. Emsel 250 2x16	4. Emsel 250 2¾x16
Lbs.	84	55	226	990
Type	5.	6.	7.	8.
Lbs.				

Max. holes per 8ms delay:	Max. lbs.per 8ms delay:	Total lbs: 1349	

Initiation System

Type of Initiation System
☐ Electric ☑ Non Electric ☐ Other: ☐ Sequential Machine ☐ CD ☐ Other:

ELECTRIC See attachments

Timer Setting Hole to Hole:	Nominal Cap Delay Hole to Hole:	Timer Setting Row to Row:	Cap Nominal Delay Row to Row:
Cap Delays per Circuit:	Number of Circuits:	OHMS: (Resistance each series or circuit)	

NON ELECTRIC (8 MS RULE) ☐ See attachments

Number of Rows: 7	Delay(s) parallel to free face along spacing: 12
Delay(s) Perpendicular to the face, in echelon or row to row: 7	

Nearest Protected Structure

Street Address:

Type of Structure:	Distance: /ft

Allowable Limits of Vibration	
☐ OPTION 1 ☑ OPTION 2	
Scaled Distance:	
☐ 50 ☐ 55 ☐ 60 ☐ 65 ☐ Other:	

(Conforms to M.G.L. c 14

Post-It® Fax Note	7671	Date 7/29	# of pages ▶ 1
To Jessie Bonner		From Don Murray	
Co./Dept.		Co.	
Phone #		Phone #	
Fax # 936 632 4226		Fax #	

70

3. SOURCE SCALING OF SMALL, SINGLE-FIRED EXPLOSIONS WITH VARIABLE VELOCITY OF DETONATION IN BARRE GRANITE

ABSTRACT

A series of five single-blasthole explosions were conducted in a granite quarry in Barre, Vermont. The explosions spanned yields from 60 to 122 kg and were all detonated in an approximate 100 m by 100 m area. In an attempt to fracture the emplacement rock—granite— differently, the individual explosions were detonated with three different types of explosives, including black powder, an Ammonium Nitrate Fuel Oil (ANFO)/Emulsion mix (termed "Heavy" ANFO), and Composition B, a military-grade weapons explosive. The velocity of detonation (VOD) for these explosives range from 0.53 km/sec (black powder) to 8.1 km/sec (COMP B). The ANFO/Emulsion VOD was ~5 km/sec. The purposes of these experiments were to investigate: (1) generation of fractures from small explosions in homogenous, relatively un-fractured granite, (2) quantify the near-source, local, and regional distance phase generation from the explosions, and (3) compare and contrast the seismic phase generation to the rock damage. The paper addresses the second objective. Instrumentation was deployed at near-source (<1.5 km) and local to near-regional (1.5-30 km) distances and supplemented by permanent network stations at regional distances.

Empirical source scaling relations using the near-source and local data are compared for the three different explosive types in five different explosions. In most cases, spectral ratio data from each distance range document similar scaling. The near-source data at distances less than 1.5 km show the highest variability in the source scaling, probably due to the fact that small differences in the explosion locations (< 100 m) invalidate the equivalent propagation path assumption in the spectral ratio technique. The source scaling studies show that the 61 kg black powder explosion was deficient in high-frequency energy when compared to the 62 kg Heavy ANFO and COMP B charges. At frequencies above 5 Hz, the black powder explosion amplitudes were up to an order of magnitude smaller than the faster VOD explosives. The black powder explosion generated surface waves that were equivalent to the ANFO explosion at frequencies below 5 Hz. The Rayleigh-waves generated from the 61 kg black powder shot were larger than the equivalent COMP B explosion, especially for stations deployed northeast of the shots. The black powder charge generated larger-amplitude short-period Love-waves than the COMP B explosion for all azimuths studied, which may provide important data in addressing the continuing problem of *S*-wave generation from explosives. The Mueller-Murphy (MM71) explosion source model cannot explain the black powder effects using standard empirical relationships between explosion yield and source elastic and cavity radii and static pressures, and will require more detailed study after the damage zones from the explosions have been quantified and the nominal explosion pressures have been estimated.

Comparisons of the Heavy ANFO and COMP B explosions show small differences at body-wave frequencies (> 8 Hz) and larger effects at surface-wave frequencies. The slower VOD Heavy ANFO explosions generated larger-amplitude Rayleigh (up to a factor of 2x larger) and Love-waves (as large as 3x) than the equivalent COMP B charges. These differences are not modeled adequately using the MM71 source. We plan to use the results from this source scaling

study to relate seismic phase generation, particularly for *S*-waves (e.g., *Lg*, Love waves), to damage effects from the explosions.

OBJECTIVES

Two of the proposed mechanisms for *S*-wave generation from explosions involve secondary processes related to the damage and deformations caused by the explosions. First, outside the cavity radius, there is a "shell" of fragmented rock. Sammis (2002) theoretically showed that the integrated effect of the nucleation and growth of the fractures in this shell can generate secondary seismic waves as large as the *P*-waves from the explosion itself.

A second proposed method is the CLVD, which is an elastodynamic equivalent of a conical source. In this case, it is an inverted cone with apex at the detonation point (Patton *et al*., 2005). Media within the cone deforms and fails as a result of tensile stresses caused by the downgoing shock wave reflected off the free surface. Spallation is an obvious example of such failure. Driven block motions at depth, as envisioned by Masse (1981), is another example which may have greater significance for seismic wave generation.

A problem for researchers trying to relate damage to *S*-wave generation is a paucity of detailed, readily-available, damage characterization data from explosions. Weston Geophysical Corporation and New England Research, Inc planned and detonated five small chemical explosions in relatively unfractured, homogeneous Barre granite in Vermont, USA. Barre granite has been a worldwide standard for homogeneous granite in commercial, monument, and industrial settings. The focus of the experiment was to quantify the damage caused by these explosions and to provide a unique dataset that should have important ramifications for models of *P*- and *S*-wave generation from explosions in hard rock in areas of monitoring interest. The purpose of this paper is to quantify the source scaling for these explosions.

SUMMARY OF EXPERIMENT

Experiment Purpose
In the summer of 2003, groups from Weston Geophysical and New England Research, Inc., together with a variety of explosives and geotechnical engineers, conducted five explosions at a granite quarry in Barre, VT. With the help of IRIS (the Incorporated Research Institutions for Seismology) PASSCAL, over one hundred seismic stations were deployed to record the explosions. The purposes of these experiments were to investigate: (1) generation of fractures from small explosions in homogenous, relatively un-fractured granite, (2) quantify the near-source, local, and regional distance phase generation from the explosions, and (3) compare and contrast the seismic phase generation to the rock damage.

Blast Design
The NEDE at the Vermont granite quarry included five single-blasthole explosions with total explosive weights ranging from 60 to 122 kg. (Figure ; Table 17). The explosions were small in order to be contained in a single borehole, to reduce drilling costs, and to limit ground vibrations at nearby structures (e.g., cell tower less than 200 meters from the test site). The objective of this project was to relate rock damage to seismic phase generation; therefore we attempted to design the experiments in order to fracture rock differently. Rock fracturing has been related to velocity

of detonation. A slow explosive will often generate a large amount of gas that will drive crack formation; while a faster explosive will tend to rubbleize the material immediately adjacent to the borehole, and the powdered rock may impede the effects of gas-driven crackage. For more on these effects, the reader is referred to http://www.johnex.com.au/index.php?section=105 (last accessed in June 2009).
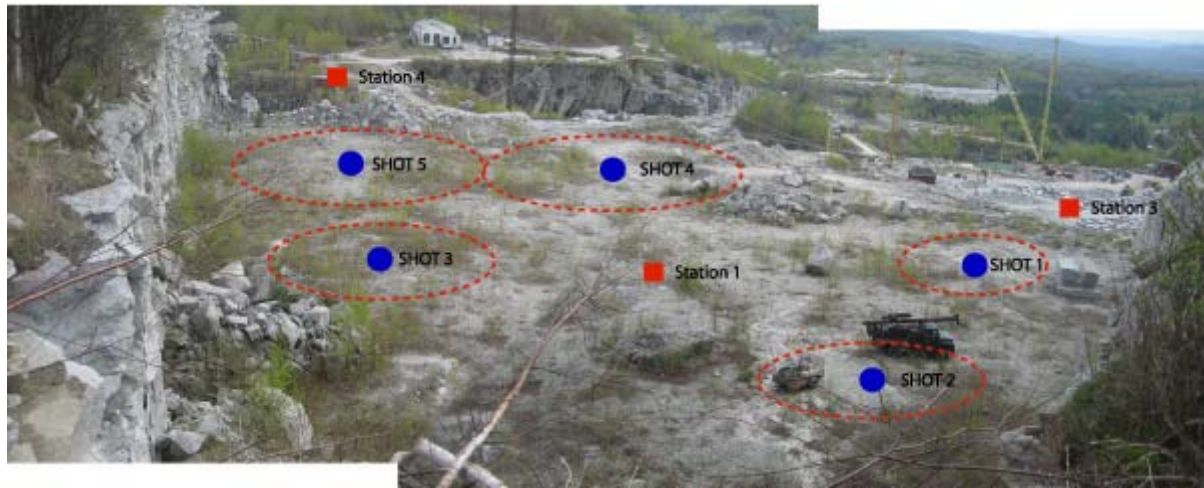

Figure 73. Photos of the test bed where the NEDE explosions (blue circles) were detonated. Also shown are three near-source station locations (red squares) and the estimated elastic radii (red dashed circles).

Table 17. NEDE Origin Parameters

Shot	Date	Origin Time	Latitude	Longitude	Elevation (m)	Depth (m)	Yield (kg)	Explosive	VOD (km/sec)
1	12-Jul-08	14 37 42.16	44.1577	-72.47848	509	8.3	60.8	Black Powder	0.53
2	12-Jul-08	16 02 05.02	44.158	-72.47813	509	10.7	61.5	ANFO/EMUL 50:50	4.76
3	12-Jul-08	17 30 40.73	44.1578	-72.4777	503	10.7	61.7	COMP B	
4	12-Jul-08	19 16 15.01	44.1575	-72.47797	508	12.8	122.2	ANFO/EMUL 50:50	4.89
5	12-Jul-08	20 50 12.77	44.1575	-72.47757	503	12.8	122.5	COMP B	8.10

With the help of Mr. Tim Rath of Maxam-North America, we designed the NEDE to have a wide range of VODs. For Shot 1, we detonated 60.8 g of black powder (Figure) at a centroid depth of 8.3 meters in a 22.86 cm diameter borehole. The explosives column extended approximately 1 meter on each side of the centroid. Schist rock in 1.27 cm-sized particles was used to stem the boreholes. Black powder was used exclusively for hundreds of years in mining and military applications. Today, the use of black powder as a blasting agent has diminished considerably, but it is often used to detach rock along pre-existing fractures such as in the Vermont slate district. The "velocity of detonation" was measured at 0.53 km/sec for Shot 1; however, we note that the black powder typically "deflagrates" rather than "detonates" unless under highly-confining conditions.

Shots 2 and 4 consisted of a 50:50 blend of Ammonium Nitrate Fuel Oil (ANFO) and Emulsion explosives. The mining industry typically refers to this blend as "Heavy" ANFO, because the mixture increases the density allowing more explosives to be loaded into a borehole. It also helps to waterproof the explosive as compared to pure ANFO. Heavy ANFO is often used in

73

today's commercial blasting industry because of low cost (e.g., $2/kg) and abundant gas formation that helps fracture the rocks efficiently. Shot 2 consisted of 61.5 kg of Heavy ANFO detonated at a centroid depth of 10.7 m while Shot 4 had almost double the explosives at a centroid depth of 12.8 m. The thicknesses of the explosive columns were approximately 1 and 2 meters for Shots 2 and 4. Both Heavy ANFO shots were detonated in 22.86 cm diameter boreholes with schist stemming. The measured VOD was 4.76 km/sec and 4.89 km/sec for Shots 2 and 4, respectively.

Shots 3 and 5 consisted of Composition B, a military grade explosive. According to GlobalSecurity.org, "COMP B explosives are made from TNT, RDX, and wax, such as 59.5 percent RDX, 39.5 percent TNT and 1 percent wax. Desensitizing agents are added. Composition B is used by the military in land mines, rockets, and projectiles. Cast Composition B has a specific gravity of 1.65 and a detonation velocity of about 25,000 fps and is used as a primer and booster for blasting agents" ((http://www.globalsecurity.org/military/systems/munitions/explosives-compositions.htm)). Mr. Rath had the COMP B charges cast as 45 kg cylinders of 19.1 cm diameter and 94 cm length (Figure). One cast charge was used for Shot 3 and two for Shot 5. Because of the space between the 19.1 cm charge and 22.86 cm diameter borehole wall, the casts were lowered into bulk emulsion to ensure adequate coupling, thus resulting in final explosive yields of 61.7 kg and 122.5 kg for Shots 3 and 5 respectively and were placed at the same centroid depths as the Heavy ANFO shots 2 and 4. The VOD for Shot 3 was not measured; however, for Shot 5, the VOD was 8.1 km/sec.

Figure 74. Photo of the explosives used in the NEDE. (Left) Packages of "Polvara Negra" or black powder. (Middle) Containers of pre-mixed Heavy ANFO (50:50 ANFO:Emulsion). (Right) A cast charge of Composition B.

<u>Instrumentation Overview</u>
Instrumentation deployed to record the NEDE explosions consisted of several different types and is summarized in this section. The ground motion instruments are divided into two primary groups: (1) near-source (<1.5 km) acceleration and velocity instruments and (2) near-regional distance (1.5-30 km) vertical component geophones and three-component (3C) high-frequency seismometers. Numerous additional regional (> 30 km) seismic stations that comprise seismographic networks in New England also recorded the explosions; however, the signal-to-noise ratio was either too low or the sample rates were not high enough to be included in this spectral ratio study. The design of this instrumentation plan was intended to document the

generation and propagation from near-source to near-regional distances of both the compressional and shear energy from the single blasthole explosions.

Near-Source Instrumentation.   The locations of the initial set of near-source instruments deployed around the test bed are diagrammed in Figure . Stations N1A and N1B (shown under the star of the test site) were equipped with high g accelerometers (Endevco) with sensitivities of ~40 mv/g. The sensor for N1B was moved to within 5 meters of each shot borehole collar in order to document the tensile failure associated with each explosion. Lower g accelerometers (TerraTek) with typical sensitivities of ~2 v/g were deployed at greater ranges (Stations N2, N3, N4, N5, and N7). These stations were digitized at 250 samples/sec using antiquated Refraction Technology 72A digitizers. These sites were co-located with velocity transducers (L4-3D) with sensitivities of 1.71 v/cm/s. Finally, station N6, which consisted of a Refraction Technology RT130 digitizer, was deployed with only an L4-3D velocity seismometer (2.80 v/cm/s). The objective of the near source instruments was to document the wavefield from within the region of tensile failure (< 10 meters) out into the region of linear elastic propagation (>30 m). The near-source instrumentation also includes twenty-seven Refraction Technology 125 "Texans" with 4.5 Hz geophones deployed in and around the quarry (Figure). The deployment of the Texans within the quarry was designed primarily to characterize the ground motion in and around the test site, especially to characterize possible azimuthal variations.

Near-Regional Instrumentation.   19 three-component, high-frequency seismometers were deployed along two profiles as shown in Figure . To the Northeast, 9 L4-3D (2.8 v/cm/s) velocity instruments were deployed at 3 km offsets. The stations were digitized at 250 samples/sec using RT130s. To the Southeast, 10 L22 (0.88 V/cm/sec) velocity instruments were deployed at 3 km offsets and recorded on RT130s.   Both these deployments consisted of seismometers that were buried just below the ground surface, leveled, and oriented toward true North. 88 additional Texans were deployed to the Northeast and Southeast of the quarry in order to document the transition of the wavefield from the near-source to near-regional distances. The locations of these stations are illustrated in Figure . These Texans will also be used to develop high-resolution velocity and attenuation models for the test site region.

DATA EXAMPLES

The vertical and transverse component waveforms from Shots 1-5 as recorded on near-source and near-regional seismic stations are shown in Figure . It is clear on these plots that the 60.8 kg black powder shot produced the smallest *P*-wave seismic amplitudes at all of the seismic stations. Interestingly, at station .NE4, the surface waves on the transverse component from Shot 1 appear to be as large as or larger than the surface waves from the Heavy ANFO and COMP B charges of similar yield. We note that by the time the waves have reached station NE4, there are large amplitude *S*-waves that arrive approximately two seconds after the *P*-waves. It is difficult to determine on these plots which shot produced the largest amplitudes; however it is either Shot 4 or Shot 5, which is expected given the ~122 kg yields. Examples of all the waveforms used in this source scaling study have been included in Appendix 3A.
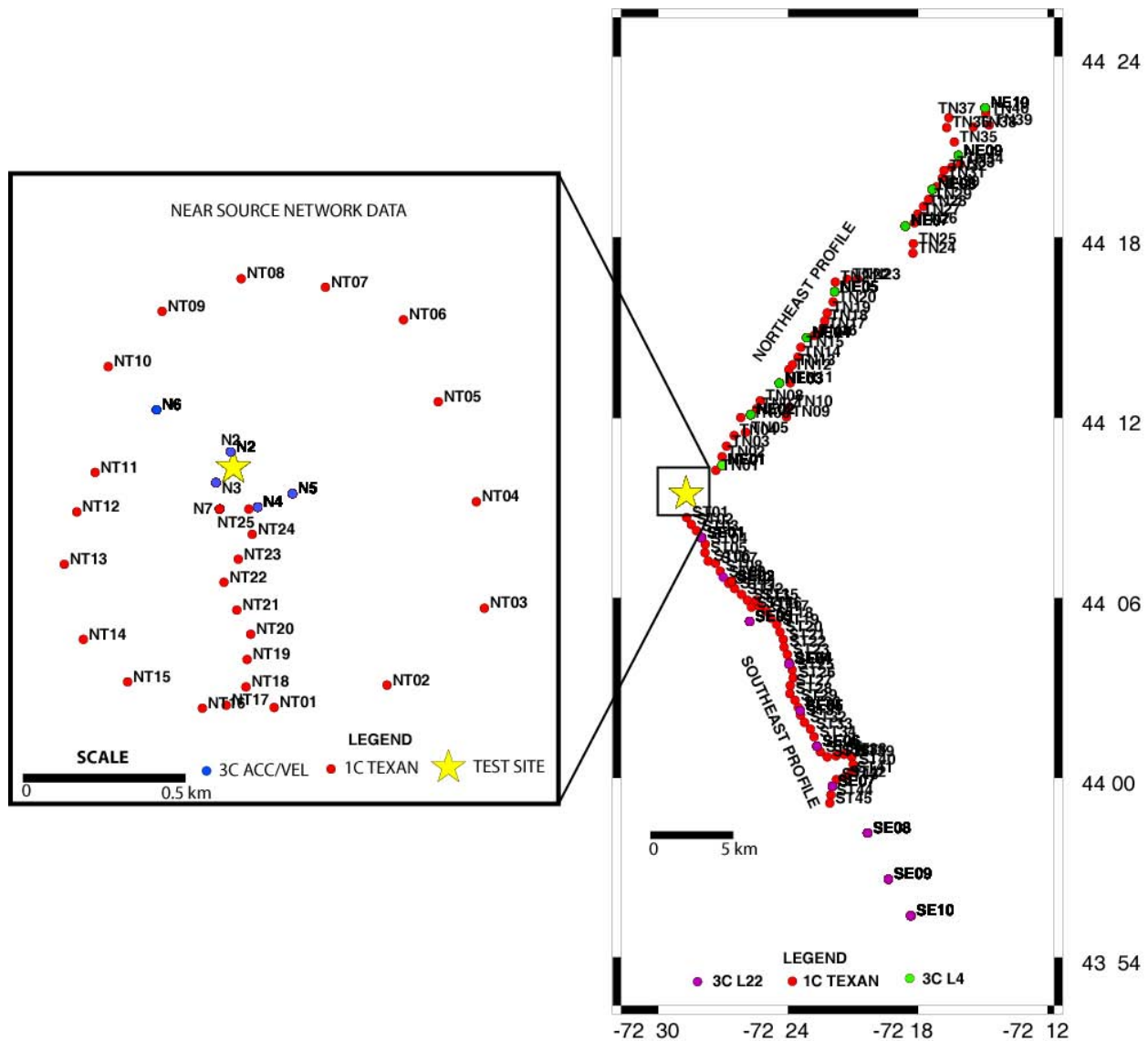
Figure 75. Location of the NEDE explosions and seismometers. (Left) Near-source instrumentation. (Right) Local-to-near-regional distance instrumentation.
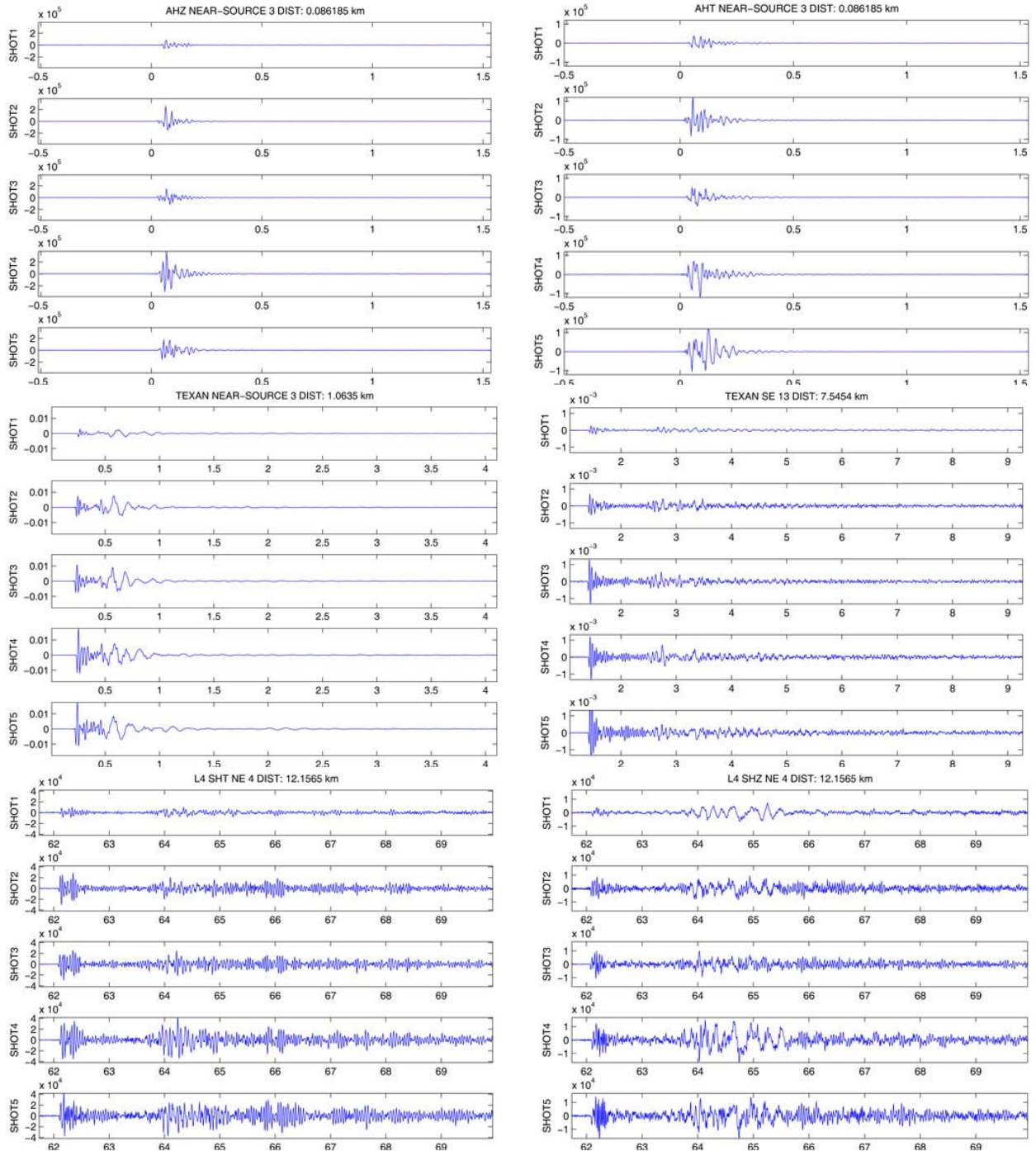
Figure 76. Seismograms for Shots 1-5. The upper two plots show vertical (AHZ) and transverse (AHT) component accelerograms recorded at station N3, which was 86 meters from Shot 1 (distances to the other shots vary slightly). The middle two records show vertical-component velocity seismograms recorded on the "Texans" at near-source (1 km) and local (7 km) distances. The lower two plots show vertical (SHZ) and transverse (SHT) component velocity recordings at station NE04 (12.1 km). The x-axis is in seconds and the data in each subplot were scaled to the maximum amplitude of Shot 4.

77

ANALYSIS METHODOLOGY

To quantify source scaling for the NEDE explosions, we employed the same methodology as Zhou and Stump (2005). Their description of the spectral ratio technique is included in the following paragraphs.

"A number of researchers (Muller, 1985; Chael, 1987; Reamer and Stump, 1992; Stump *et al.*, 2003; and Goldstein *et al.*, 1994) have made relative source comparisons between chemical explosions, nuclear explosions, and earthquakes of different sizes, in some cases including both the phase and modulus of the Fourier representation of the source, and in other, more restrictive cases including only the modulus. Due to the stochastic character of the observations used in this study and in an attempt to quantify the sources in a broadband manner as much as possible, the focus here is on the modulus of the Fourier transform and more specifically the power spectrum. "

"The spectrum from an individual explosion is represented as:

$$U_{kij}(f) = R_{ki}(f) \cdot P_{kij}(f) \cdot S_j(f) \tag{2}$$

where $U_{kij}(f)$ is the spectrum of the kth component (1- vertical, 2- radial, 3- transverse) at the ith receiver from the jth source; $R_{ki}(f)$ is the receiver function for the ith receiver and is assumed to be the same for each source; $P_{kij}(f)$ is the regional propagation path effect; and $S_j(f)$ is the source function for the jth explosion.

$R_{ki}(f)$ and $P_{kij}(f)$ are assumed to be identical for each source, and thus taking the ratio of $U_{kij}(f)$ for two different sources eliminates the local receiver effect and regional propagation path contributions, retaining only the ratio of the two source functions.

$$\frac{U_{ki1}(f)}{U_{ki2}(f)} = \frac{R_{ki}(f) \cdot P_{ki1}(f) \cdot S_1(f)}{R_{ki}(f) \cdot P_{ki2}(f) \cdot S_2(f)} = \frac{S_1(f)}{S_2(f)} \tag{3}$$

The ratio of the spectra removes both the local/regional wave propagation path effect and the strong local receiver effects. What remains is the frequency-dependent source scaling relation for the explosion source function. Averaging over individual components for near-source estimates and over all receivers produces average source estimates. Stump *et al.* (1999) gave a detailed discussion of this approach and we are using similar procedures to process the NEDE data. As Stump *et al.* (1999) pointed out, the equations involve a spectral division that can lead to theoretical difficulties in variance estimation and practical problems in stability when the denominator approaches zero. To minimize these difficulties, careful consideration was given to smoothing windows applied to both the numerator and denominator in these equations. In the process, we first identify the bandwidth with acceptable signal-to-noise ratio by comparing the signal spectra to pre-event noise estimates. Once the bandwidth has been determined, various frequency-domain smoothing windows were tested and an appropriate window was selected to

reduce variances in the individual spectral estimates and ultimately improve source difference. A single window was chosen with a maximum width of 3.66 Hz. The bandwidth time product for any one spectral estimate is smaller than the recommended value of 100 or more (Harris, 1991) although smoothing over multiple ratios stabilizes the estimate. At a given frequency, the smoothing involves frequencies that are within ± half the window width. The lowest frequency included in the smoothing is identified as the frequency where the signal is above the noise *(~1 Hz for the NEDE data)*. The uniform and symmetric window is not allowed to extend below this frequency, and so low frequency values are smoothed with windows that are smaller in width than the maximum windows."

Before we computed spectral ratios, we analyzed the noise at each station, for each component, and for each explosion of the NEDE. Our largest source of noise was automobile traffic given that most of our stations were deployed near Vermont roads and highways. We required that all five shots had to be relatively noise-free at each station before we would estimate spectral ratios. This restriction resulted in numerous stations that recorded the NEDE shots with adequate SNR but were not analyzed nor included in Appendix 3A. In most cases, the noise was only on one blast recording (e.g., a car just happened to drive by the station during Shot 3), so some of these data may be useful for other studies.

DATA PROCESSING

Spectral Ratios for 61 kg Shots
Example spectral ratios for the ~61 kg shots (Shots 1-3) are shown in Figure through Figure . Figure through Figure present the ratios for Shot 1 (black powder) to Shot 2 (ANFO) at the different combinations of stations (e.g., near source accelerometers/velocity sensors, near source Texans, southeast and northeast velocity seismometers and Texans). These spectral ratios are for the entire waveform, from just prior to the *P*-wave arrival to after the surface waves. Each subplot in Figure shows the individual spectral ratios for vertical components at each station color-coded by the distance from the source to the receiver. This allows for possible distance-dependent effects in the spectral ratio analysis to be isolated. The mean spectral ratio is plotted in each subplot as the solid black line and color-coded by region in Figure . The largest scatter in the spectral ratio data is in the near-source data, which is similar to Zhou and Stump's (2005) observation for explosion data in an Arizona copper mine. The variation in the spectral ratios decreases with distance from the source. At short distances (e.g. < 0.5 km), the difference in the Shot 1 and 2 locations (~30 meters) is significant for some azimuths, and possibly invalidates the assumption that path effects are canceled out in Equation 3. The shape and the scale of the mean spectral ratios estimated from the data at different distance ranges are consistent, but much more so for the northeast and southeast datasets than the near-source data. The mean ratios are near 1 for surface wave frequencies (< 5 Hz) and then begin to decay rapidly above 5 Hz, indicative of the corner frequency differences between the two shots. The black powder shot is not a high-frequency source, which is confirmed by recordings made in the non-linear, tensile failure zone which show a broad shockwave instead of the typical impulsive peak. Between 10 and 20 Hz, the black powder shots try to stage a comeback as noticed in the peak in the spectral ratios. The peak is more prominent on the northeast stations. At frequencies above 20 Hz, the mean spectral ratio dips below 0.2 at 60 Hz. We note that the difference in the emplacement depth of ~2.5 m for these two shots should not have a significant effect on the observed spectral ratios at high frequencies.
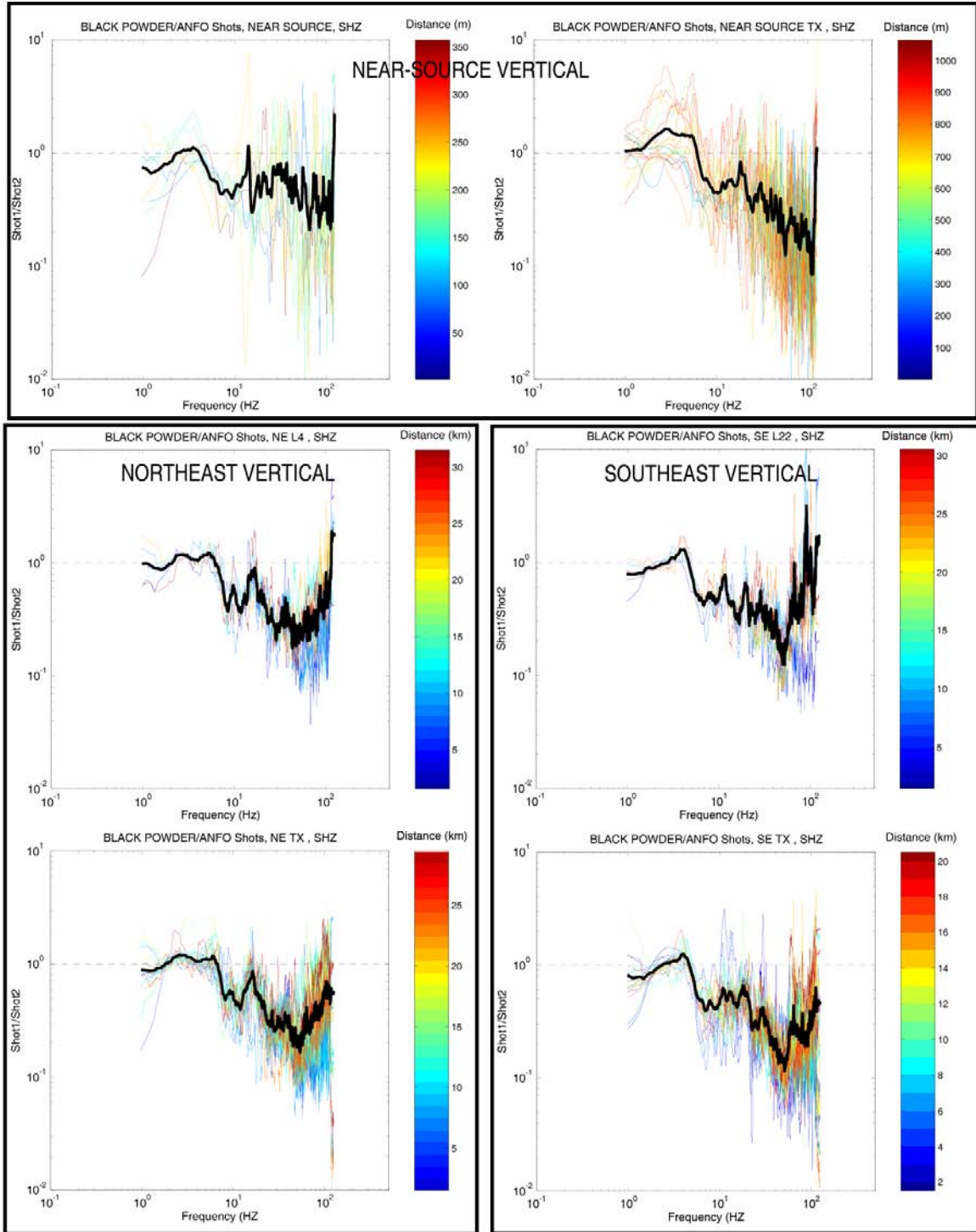
Figure 77. Vertical-component spectral ratio comparison of Shot 1 to Shot 2. Shot 1 was an ~61 kg black powder explosion while Shot 2 was a similar yield ANFO/Emulsion blend. The spectral ratios are shown for near-source accelerometer and velocity data, as well as Texan (TX) and velocity (L4 and L22) sensor data in two linear profiles towards the northeast and southeast. The individual spectra are color-coded by distance from the source. The mean is shown as the thick solid black line. For reference, a spectral ratio of 1 is shown as the black dashed line.

80
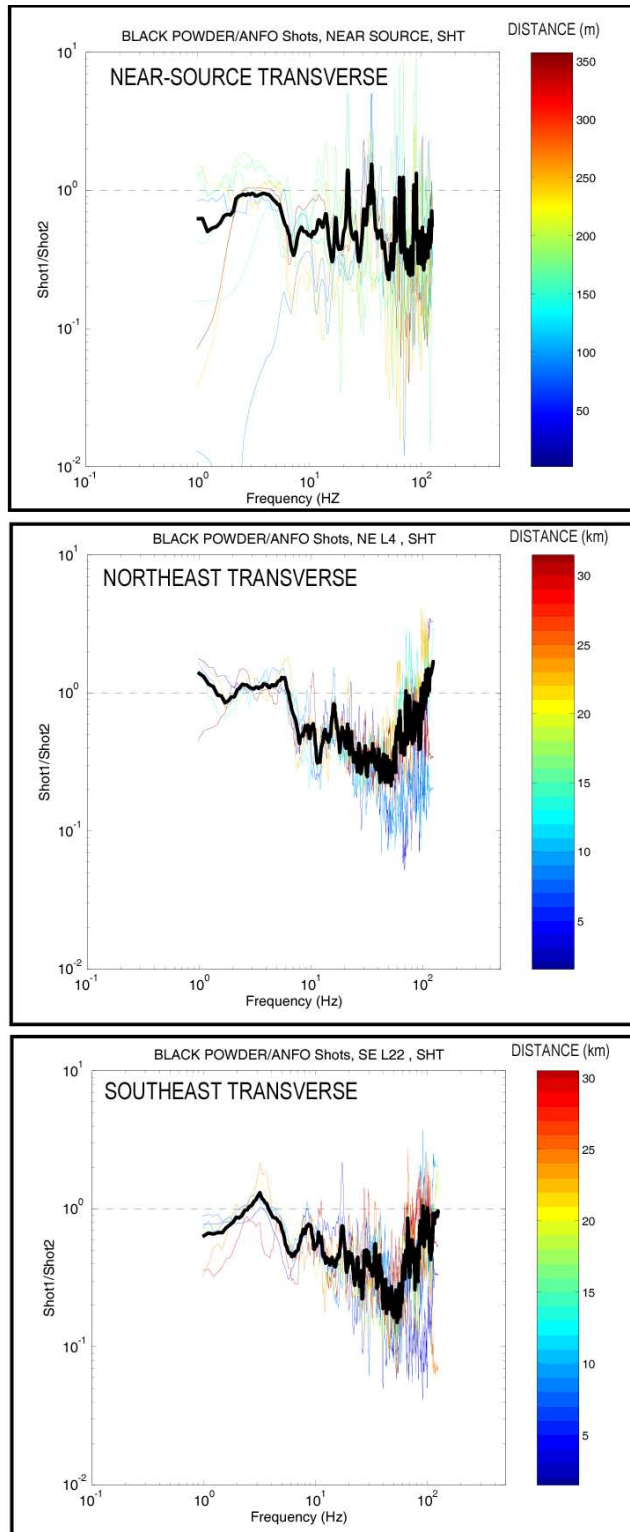
Figure 78. Transverse-component spectral ratio comparison of Shot 1 to Shot 2. (Top) Near-source recordings on accelerometer and velocity instruments. (Middle) Northeast velocity sensor (L4) recordings. (Lower) Southeast velocity sensor (L22) recordings.

81
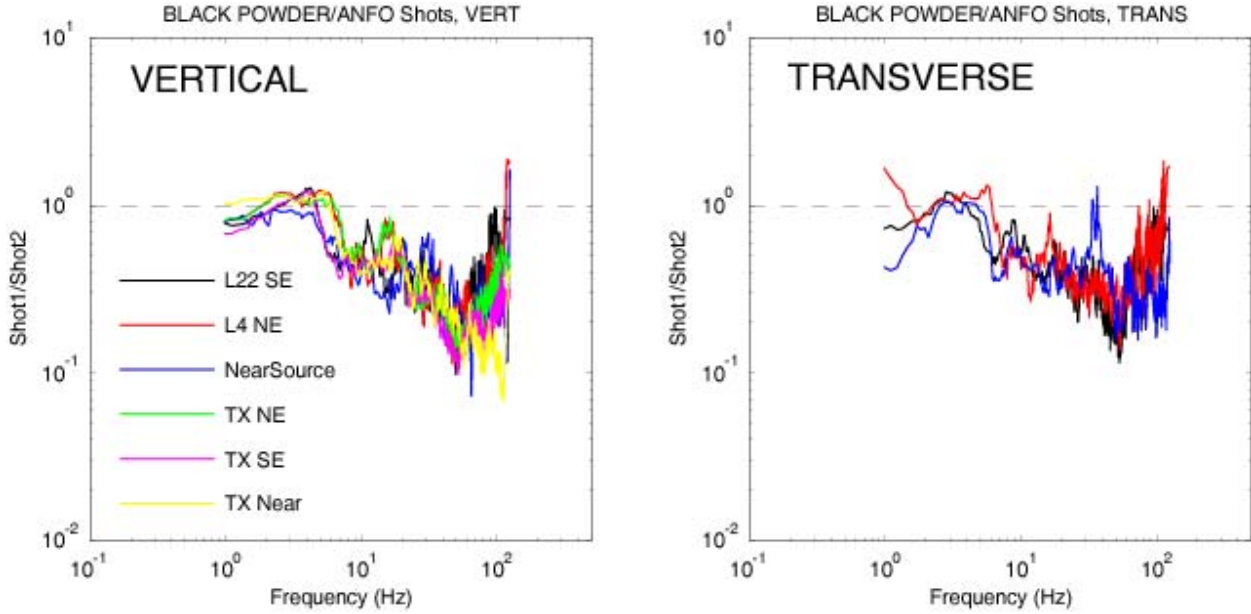
Figure 79. Summary of the mean spectral ratios for vertical (left) and transverse-components for Shot 1 to Shot 2.

In the near-source Texan data and the shorter-distance northeast and southeast data, the spectral ratios continue decreasing up to the Nyquist frequency, even though the scatter is large. In the northeast and southeast data, the spectral ratio begins to increase towards 1 at frequencies above 60 Hz for the stations beyond 5 km, and these stations have considerable influence on the mean. At these distances, the high frequencies are rapidly attenuated and the spectral ratios are returning to ~1, which reflects the background noise levels. This suggests that at frequencies above 60 Hz, the near-source data may provide a better approximation of the differences between these two sources, even though the scatter between the individual spectral ratios is high.

Figure   presents the spectral ratios for the transverse-component recordings for Shot1/Shot2. Since the Texans are only vertical-component geophones, the number of spectral ratio estimates is smaller than for the vertical components shown in Figure . The mean spectral ratios (Figure) for the transverse components are very similar to the vertical component results. At the Love wave frequencies (e.g. < 5 Hz), the black powder and ANFO shot amplitudes are almost the same; however, for frequencies above 5 Hz, the black powder amplitudes are considerably smaller.

Figure   suggest possible anisotropic effects for the explosion recordings. Note the small differences between where the northeast spectral ratios (red and green) and southeast ratios (magenta and black) fall below a value of 1. For the northeast data, it's closer to 5 Hz for both the vertical and transverse data, while it is near 4 Hz for the southeast data. The scatter in these data are small enough at these frequencies (see Figure and Figure) to suggest this difference is significant. A possible source for these differences could be in a radiation pattern for the surface waves, which would suggest the explosions were not completely isotropic.
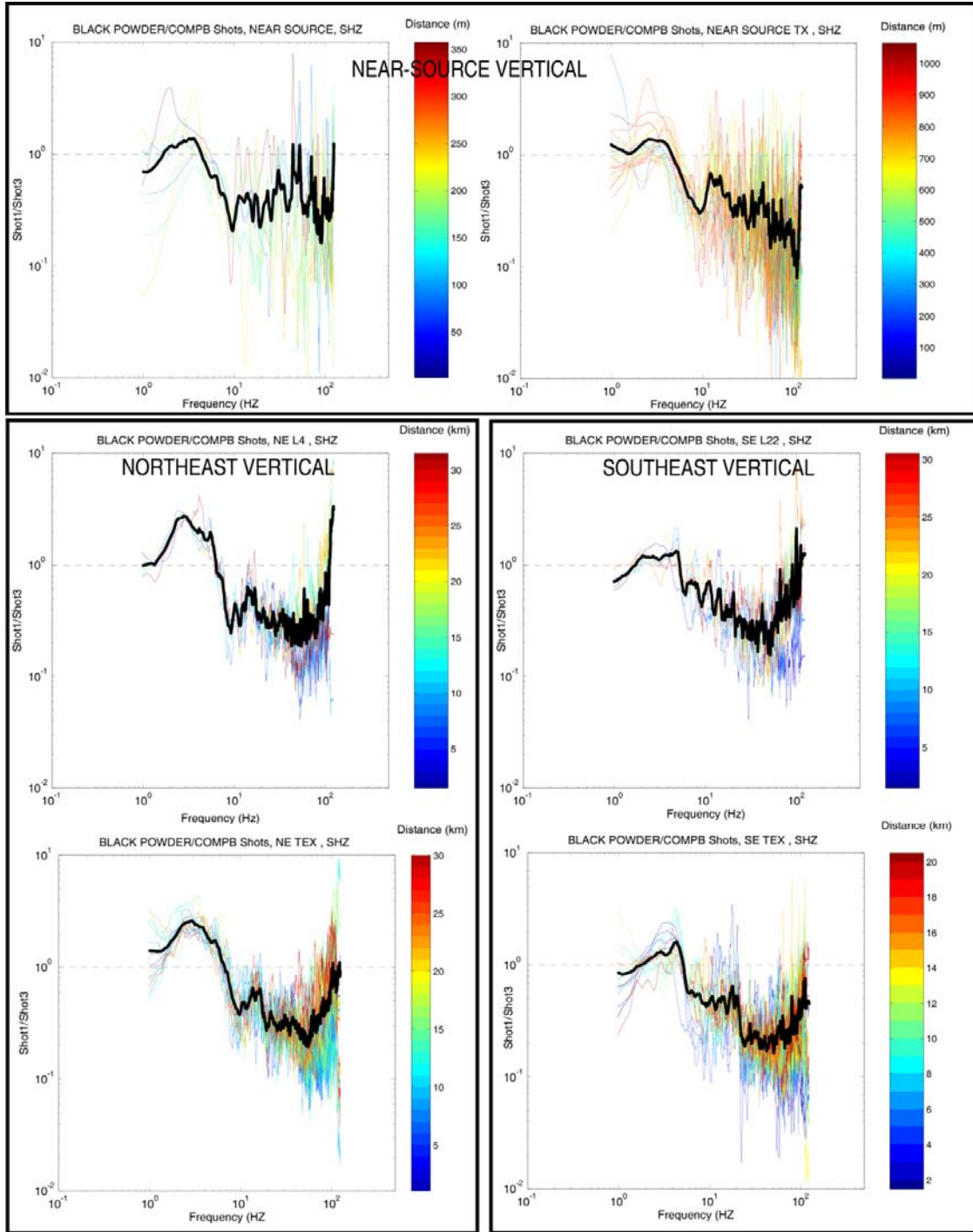
Figure 80. Vertical-component spectral ratio comparison of Shot 1 to Shot 3. Shot 1 was a ~61 kg black powder explosion while Shot 3 was a similar yield COMP B explosion. The spectral ratios are shown for near-source accelerometer and velocity data, as well as Texan (TX) and velocity (L4 and L22) sensor data in two linear profiles towards the northeast and southeast. The individual spectra are color-coded by distance from the source. The mean is shown as the thick solid black line. For reference, a spectral ratio of 1 is shown as the dashed black line.
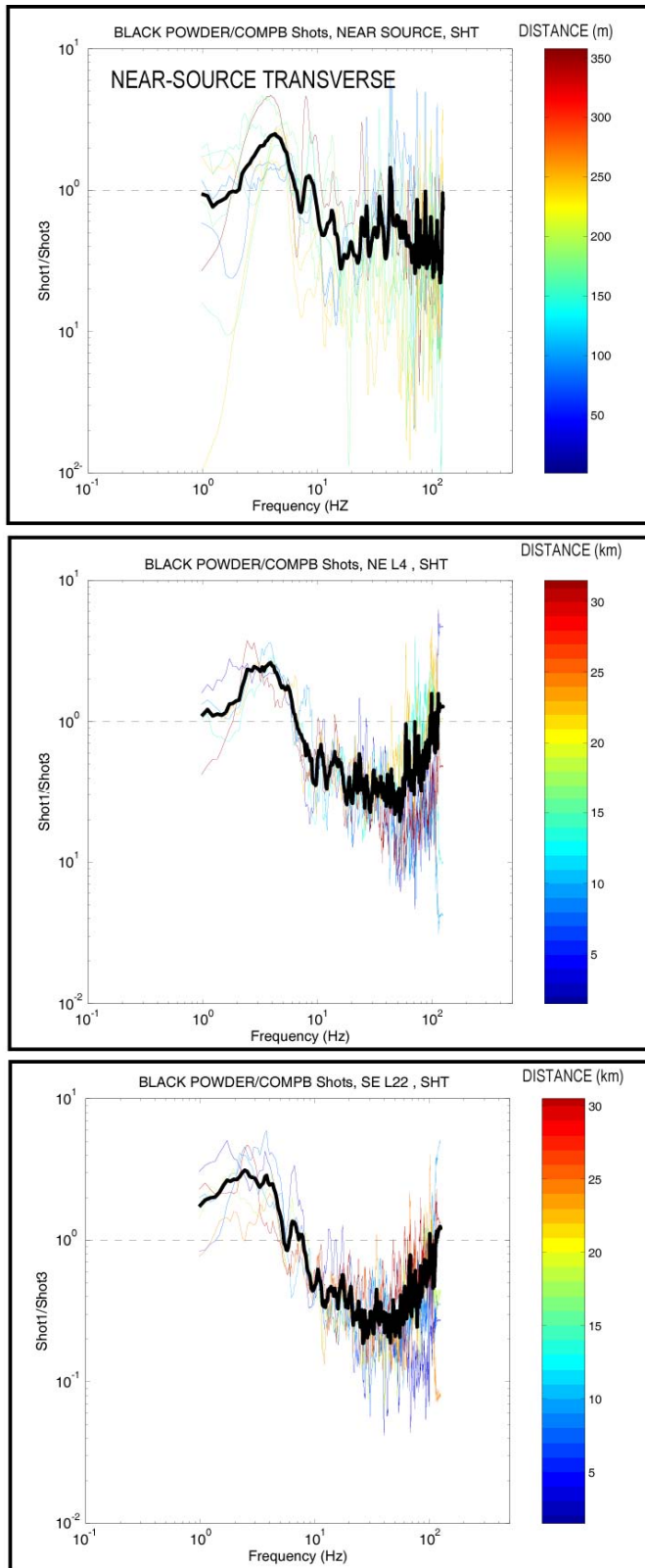
Figure 2. Transverse-component spectral ratio comparison of Shot 1 to Shot 3. (Top) Near-source recordings on accelerometer and velocity instruments. (Middle) Northeast velocity sensor (L4) recordings. (Lower) Southeast velocity sensor (L22) recordings.
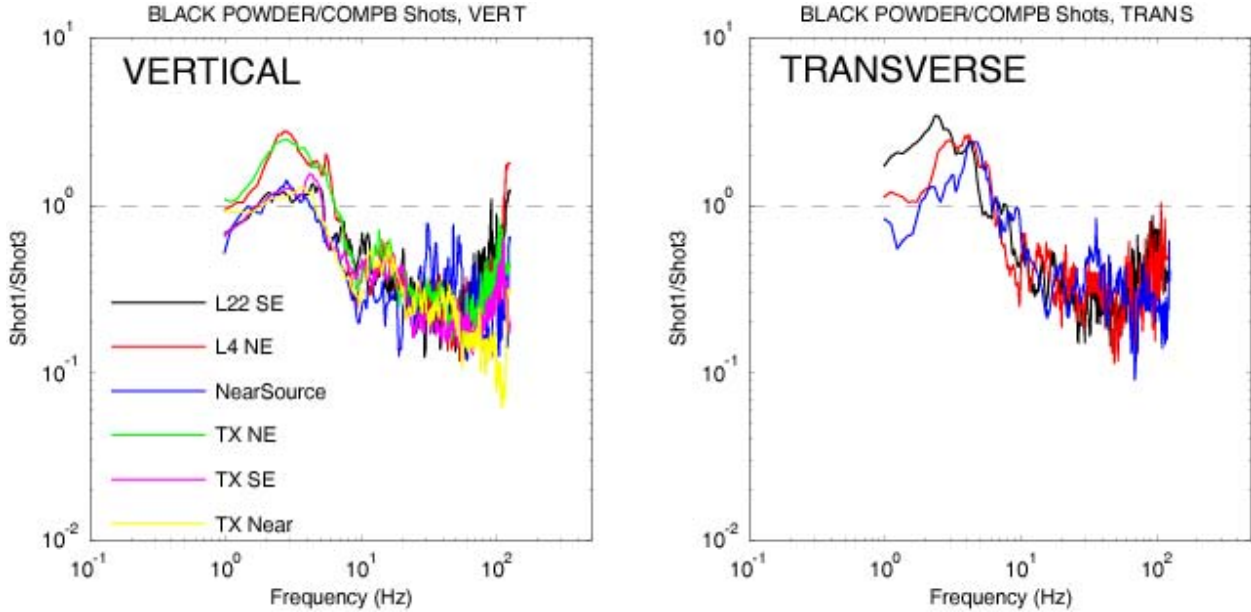
Figure 82.   Summary of the mean spectral ratios for vertical (left) and transverse-components for Shot 1 (black powder) to Shot 3 (COMP B).

Figure through Figure present the ratios for Shot 1 (black powder) to Shot 3 (COMP B) at the different combinations of stations (e.g., near source accelerometers/velocity sensors, near source Texans, southeast and northeast velocity seismometers and Texans). We note similar behavior between these two explosions as we did with the ANFO:Emulsion Shot 2. The COMP B charge, which has the fastest VOD of the three explosives, is a source of much higher frequency seismic energy than the black powder.

The most intriguing aspect of these data is again in the surface waves frequencies (< 5 Hz), especially for the transverse data (Figure -right). The black powder shots generated Love waves with up to 3x the amplitude that the COMP B generated. Determining the reason behind these differences may provide us with an important piece of the *S*-wave generation from explosions puzzle. Visual inspection of the surface after these two blasts found surficial damage associated with the black powder Shot 1 (Figure) and ANFO Shot 2, while little or no surficial damage was observed for the COMP B Shot 3. Cores were extracted from these shots to learn more about the fracturing caused by all five of the NEDE shots.

The possible anisotropic effects of the source first noted in Figure are even more pronounced with these data. At frequencies below 5 Hz, we see different amplitude ratios for the northeast and southeast data.   It is very interesting that the near-source data, which have adequate azimuthal coverage (see Figure) trend very closely with the southeast data.   Could these anisotropic effects be path related, even though we have an assumption in Equation 3 is that path-dependent effects are removed?

Figure 83. Surficial cracks after the Shot 1 (black powder; left) and Shot 2 (ANFO; right) explosions. The cracks shown at left showed permanent displacement of a few centimeters or more.

Spectral Ratios for the ANFO Shots

We compared the spectral ratios between the 122 kg ANFO Shot 4 and the 61 kg ANFO Shot 2 in Figure . This should provide a test to ensure there were no strikingly anomalous features of the blasts that could have been associated with poor coupling or other design or detonation flaws. For a factor of 2 increase in yield, we should observe that the short-period surface wave amplitudes increase by a factor of between 1.8 and 2.2 based on previous studies (Bonner *et al.*, in review). For frequencies less than 5 Hz, we observe ratios slightly above 2 for the vertical-component Rayleigh-waves and approximately 2 for the transverse-component Love waves.

For the *P*-waves, Mueller and Murphy (1971; MM71) source theory predicts a factor of ~1.75 increase in amplitude for a factor of 2 increase in yield at frequencies well below the corner frequency. At or near the corner frequency, there can be complexities if one or both of the shots exhibit overshoot, while above the corner frequencies, the ratios between the larger and smaller yield shots should become smaller (e.g., ~1.1) due to the high frequency falloff of the source spectra. Most of our spectral ratio data for the two ANFO shots seem to fall within these predicted ranges; however, there are some intricate details in the *P*-wave spectral ratios (e.g., above 5 Hz) that cannot be fully explained by simple MM71 source theory (e.g., trough in the ratios near 4-8 Hz for all different combinations of the data).

Spectral Ratios for the COMP B Shots

We also compared the spectral ratios between the 122 kg COMP B Shot 5 and the 61 kg COMP B Shot 3 in Figure . Again, most of the spectral ratios fall within the expected ranges for a factor of 2 increase in yield. We note another trough in the spectral ratios; however, it is located at slightly higher frequencies (8-10 Hz) than was observed for the ANFO shots. Between 10 and 30 Hz, we again note differences in the spectral ratios depending on station location, as the northeast data peak above a ratio of 2 in this bandwidth while the other data have ratios less than predicted from Mueller and Murphy (1971). With the exception of these troughs and possible anisotropic behavior, the spectral ratios for the COMP B and ANFO shots suggest no major problems were associated with the detonation of these explosion (e.g., poor coupling, explosive

malfunction, etc.). It is our hope that these troughs and anisotropic features of the spectral ratios can be explained by differences in the damage from the explosions.
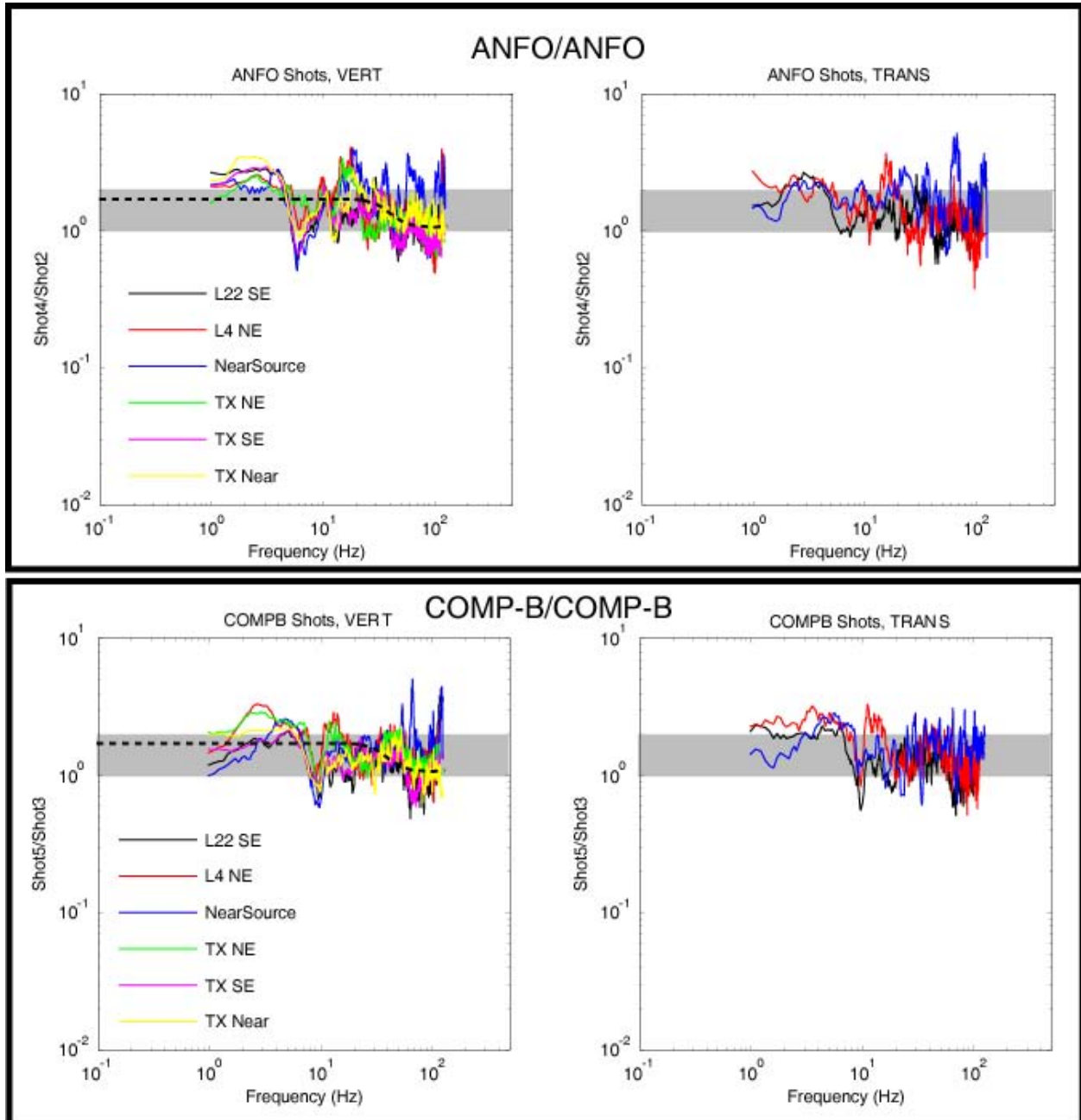
Figure 84. Summary of the mean spectral ratios for the two ANFO shots (Top; Shots 4 and 2) and the two COMP B shots (Bottom; Shots 5 and 3). The left subplot shows the vertical-component spectral ratios while the right subplot presents the transverse-component ratios. The shaded region highlights ratios between 1 and 2, while the dashed black line shows the theoretical source spectra based on Mueller-Murphy (1971).

Spectral Ratios for the ANFO and COMP B Shots

Interesting differences exist between the spectral ratios for the Heavy ANFO and COMP B shots (Figure and Figure). In general, there are four sections to each of these spectral ratios. At frequencies below ~8 Hz, which is dominated by short-period Love (transverse) and Rayleigh-waves (vertical), the Heavy ANFO shots produced larger amplitudes than the equivalent COMP B explosions. At frequencies between ~8-40 Hz, the COMP B shots have slightly larger amplitudes than the Heavy ANFO shots, producing ratios in Figure and Figure just below 1. Between 40-50 Hz, the ANFO shots become larger again, and above 50 Hz, the ratios are scattered near 1. We note that above 40 Hz, the scatter in the data are large enough that it is difficult to form any conclusions about whether one type of explosive dominates the other in terms of body-wave amplitudes. Figure shows isolated peaking at 6 and 10 Hz in the spectral ratios for the ~122 kg shots that was not easily observed in the ratios for the smaller ANFO and COMP B shots.
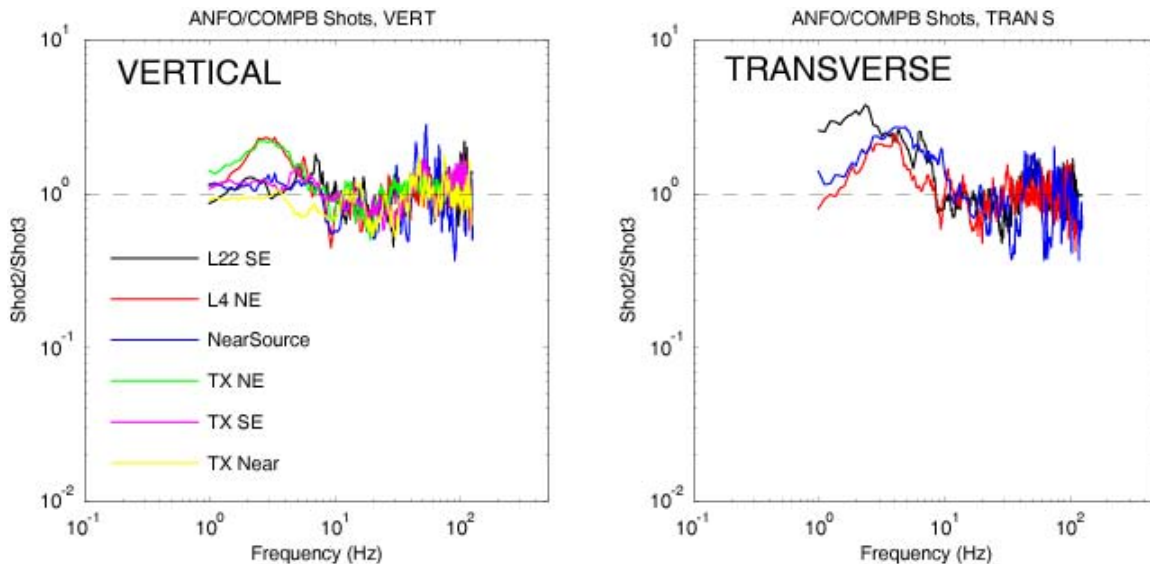
Figure 85. Summary of the mean spectral ratios for the ~62 kg ANFO and COMP B shots for vertical (left) and transverse (right) components.

Anisotropic radiation effects are noted in the left panel of Figure at frequencies below 10 Hz. The paths to the northeast show amplitudes for the ~61 kg ANFO shot were over 2 times larger than the amplitudes observed on stations near the source and to the southeast. We noted a similar effect in the comparisons of Shot 5 to Shot 3 (Figure) and Shot 1 to Shot 3 (Figure). The common shot for this apparent anomaly is Shot 3. These results suggest a possible radiation pattern in the Rayleigh waves generated for Shot 3, which resulted in larger amplitudes generated toward the southeast. Note that the Love waves do not exhibit similar anomalous behavior. In the post-blast examination of Shot 3, we noted no radial cracks on the surface. We did however observe that the crosshole tomography test borehole for shot 5 had spewed small amounts of bentonite grout, suggesting fractures and gas expansion had extended to that site. The test borehole was located over 15 meters southeast of Shot 3, which is further than we had projected for crack development for this ~61 kg shot.
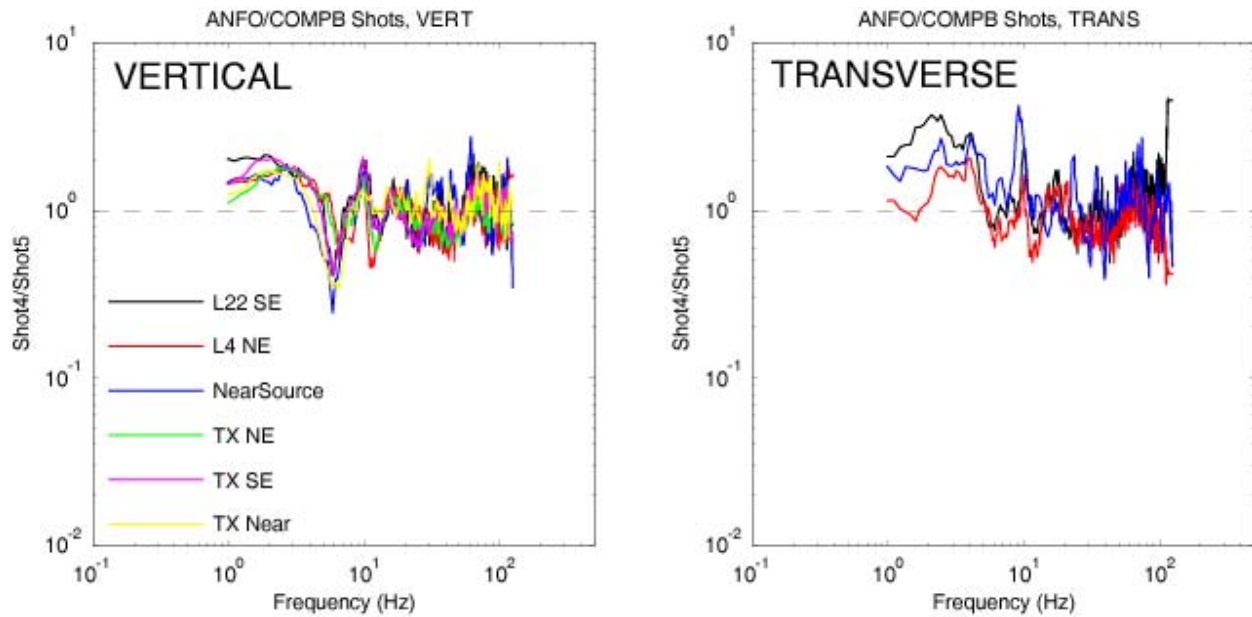
Figure 86. Summary of the mean spectral ratios for the ~122 kg ANFO and COMP B shots for vertical (left) and transverse (right) components.

Mueller-Murphy Spectral Ratios

The MM71 source model was empirically developed based on nuclear explosions at the Nevada Test Site (NTS). It has been successfully applied to nuclear explosions at other test sites, mining explosions (Yang, 1997) and confined chemical explosions (Stump *et al.,* 1999; Stump *et al*., 2003; Hooper *et al.,* 2006; Bonner *et al*., in review).

We attempted to model the observed spectral ratios for the NEDE shots using the MM71 explosion source model. We incorporated *P*- and *S*-wave velocities for the test site (e.g., V_p~5 km/sec and V_s~2.7 km/sec) from laboratory studies (Peter Boyd, pers. comm., 2008) into the MM71 source model as well as the depth and yields of the explosions, then compared shot-to-shot spectral ratios in Figure and Figure . MM71 spectral ratios for Shot4/Shot2 (~122 kg ANFO/~61 kg ANFO) and Shot5/Shot3 (~122 kg COMP B/~61 kg COMP B) were presented in Figure .

For the black powder to Heavy ANFO and COMP B comparisons (Figure), the theoretical spectral ratios fail to predict the observed spectral ratios at frequencies above 8 Hz. Successful modeling below 8 Hz is probably coincidence as the MM71 source has never had much success modeling the short-period surface waves (J. R. Murphy, pers. comm., 2005) in this bandwidth. The corner frequency for an explosion is dependent upon many factors, in particular the cavity and elastic radii. MM71 attempts to estimate these radii based on empirical relationships between yield and pressures for nuclear explosions in different types of emplacement media. Nuclear explosions have much faster detonation velocities than black powder, resulting in different pressures and source effects. The results of Figure suggest these empirical relationships are not valid for a slowly deflagrating black powder explosion, which is not surprising. The way to proceed if we hope to use MM71 to model the black powder explosions

89

is to consider estimated borehole pressures based on the explosives (Tim Rath, pers. comm., 2008) as well as measured estimates for the cavity and elastic radii, which need to be determined through geotechnical means.
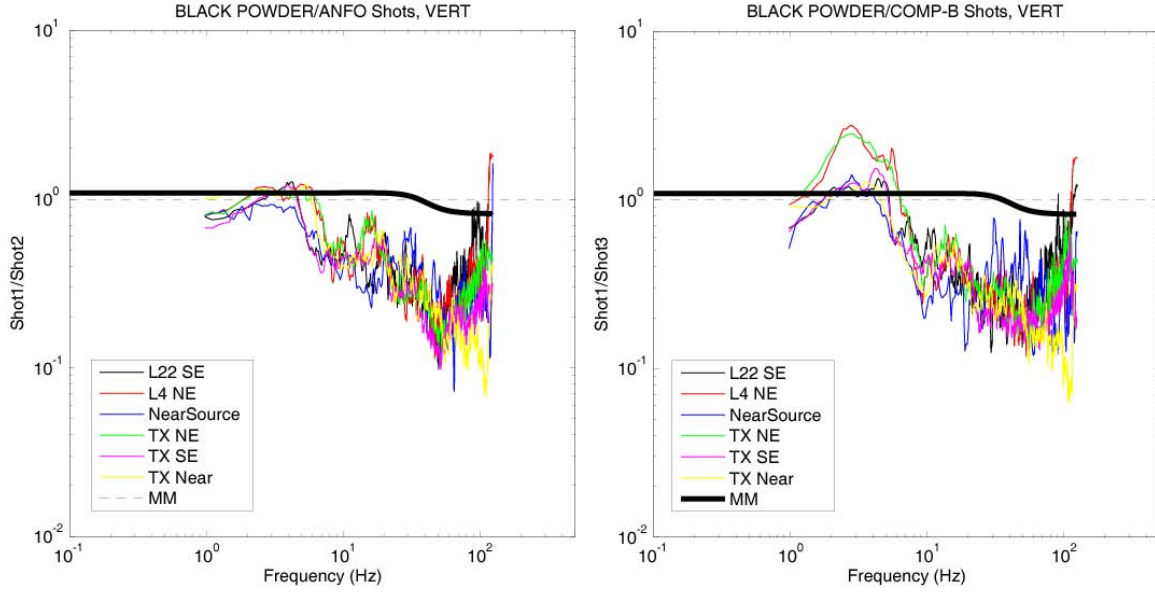
Figure 87. Summary of the mean vertical-component spectral ratios for the ~61 kg black powder to Heavy ANFO (left) and COMP B (right). Also shown is the predicted MM71 spectral ratio.
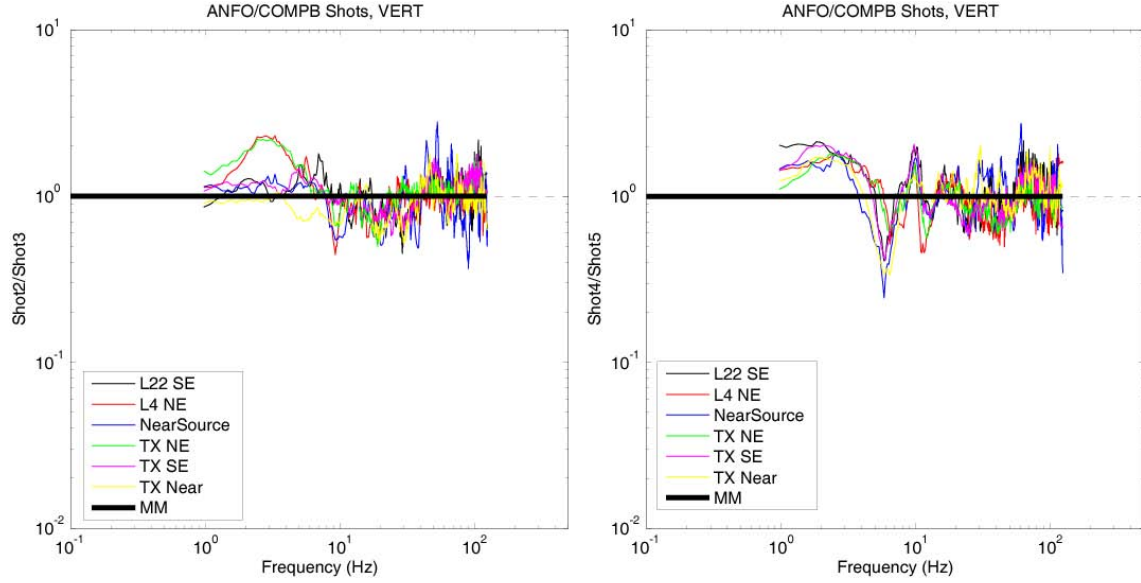
Figure 88. Summary of the mean vertical-component spectral ratios for the Heavy ANFO to COMP B shots. The left subplot shows the results for the ~61 kg shots while the right subplot presents the ~122 kg results. Also shown is the predicted MM71 spectral ratio, which is 1 for these equivalent yield and depth shots.

Figure shows that for two equivalent yield and depth explosions, the MM71 spectral ratio should be ~1. The MM71 was based on our best estimates for the centroid depth and yields of the explosions. We acknowledge that both estimates could be off slightly based on how the explosives were emplaced in the borehole and other possible sources of error. However, the main differences between the equivalent yield Heavy ANFO and COMP B shots must be related to differences in primary source processes (e.g., explosion pressures, non-linear, near-source processes, possible decoupling etc.) or secondary source effects (fracturing, spall, block motions, etc).

CONCLUSIONS

A study of the source scaling for the five explosions conducted during the NEDE project has revealed:

1. In most cases, spectral ratio data from each deployment range (e.g., near-source to near-regional) and instrument (accelerometers and velocity sensors) document similar scaling. The near-source data at distances less than 1.5 km show the highest variability in the spectral ratios used to document the source scaling.
2. The source scaling studies show that the ~61 kg black powder explosion was deficient in high-frequency energy when compared to the ~62 kg Heavy ANFO and COMP B explosions.
3. The black powder explosion generated surface waves that were equivalent to the ANFO explosion at frequencies below 5 Hz. The Rayleigh-waves generated from the ~61 kg black powder shot were larger than the equivalent COMP B explosion, especially for stations deployed northeast of the shots. The black powder charge generated larger-amplitude short-period Love-waves than the COMP B explosion for all azimuths studied, which may provide important data in addressing the continuing problem of *S*-wave generation from explosions.
4. Shot 3 has azimuthally-dependent Rayleigh-wave generation and/or propagation and requires additional study to determine the source effects and radiation mechanism.
5. The Mueller-Murphy (MM1971) explosion source model cannot explain the black powder effects using standard empirical relationships between explosion yield and source elastic and cavity radii and static pressures.
6. The slower velocity of detonation Heavy ANFO explosions generated larger-amplitude Rayleigh (up to a factor of 2x larger) and Love-waves (as large as 3x) than the equivalent COMP B charges.

APPENDIX 3A: SEISMOGRAMS USED TO COMPUTE SPECTRAL RATIOS
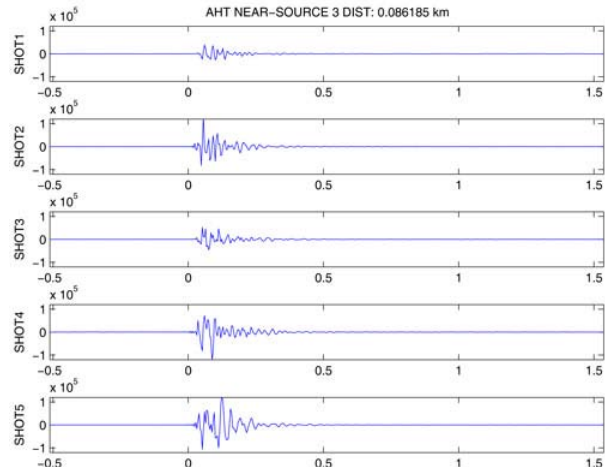
Figure 3A-1. Transverse-component accelerograms for station NS3 for Shots 1 – 5 of the NEDE.
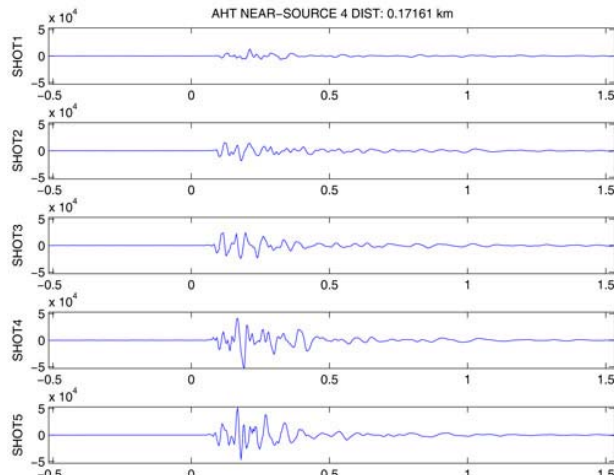
Figure 3A-2. Transverse-component accelerograms for station NS4 for Shots 1 – 5 of the NEDE.
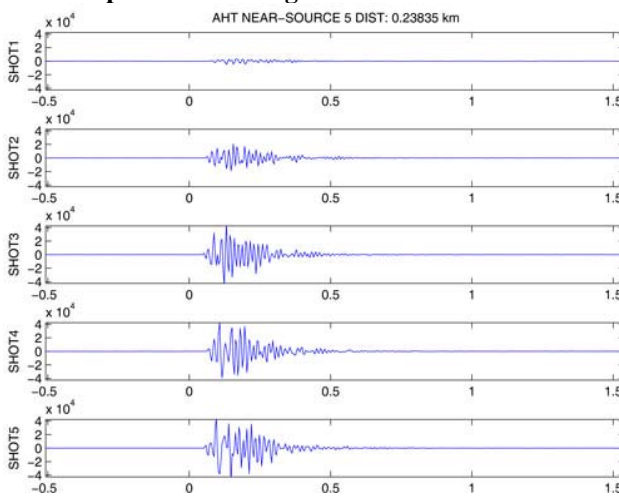

Figure 3A-3. Transverse-component accelerograms for station NS5 for Shots 1 – 5 of the NEDE.
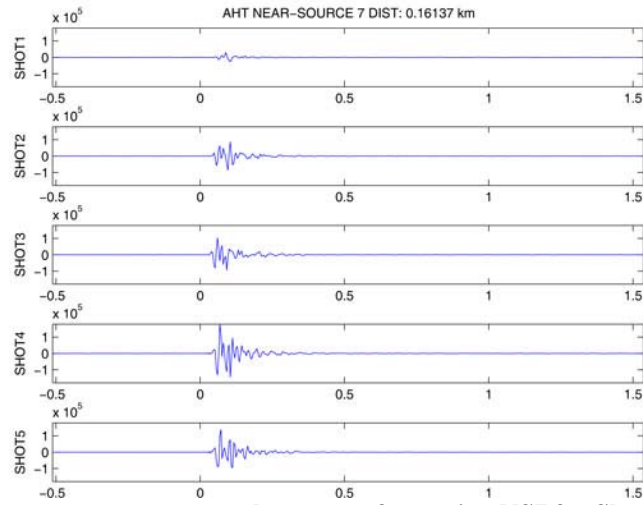
Figure 3A-4. Transverse-component accelerograms for station NS7 for Shots 1 – 5 of the NEDE.
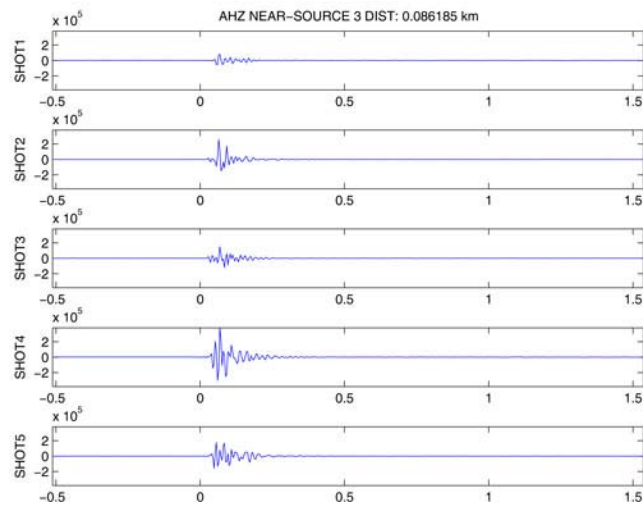

**Figure 3A-5. Vertical-component accelerograms for station NS3 for Shots 1 – 5 of the NEDE.**
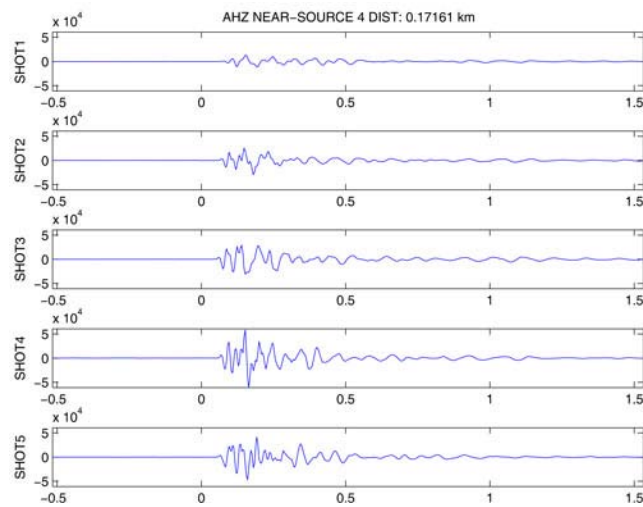
Figure 3A-6. Vertical-component accelerograms for station NS4 for Shots 1 – 5 of the NEDE.
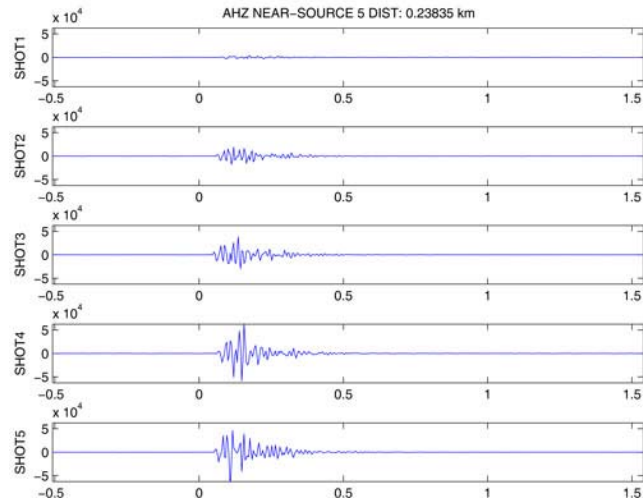
Figure 3A-7. Vertical-component accelerograms for station NS5 for Shots 1 – 5 of the NEDE.
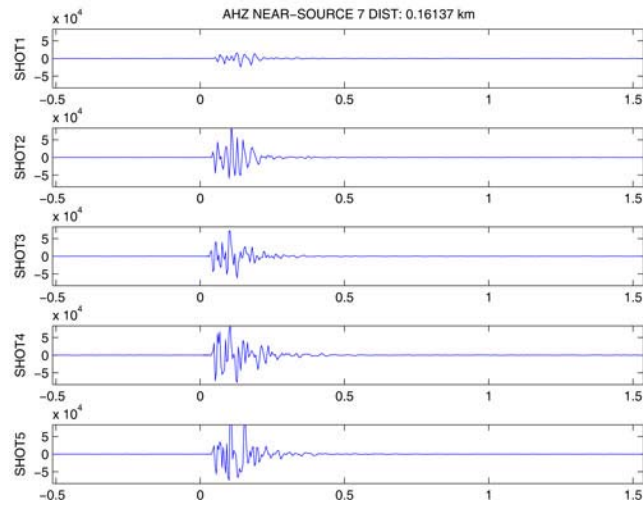

Figure 3A-8. Vertical-component accelerograms for station NS7 for Shots 1 – 5 of the NEDE.
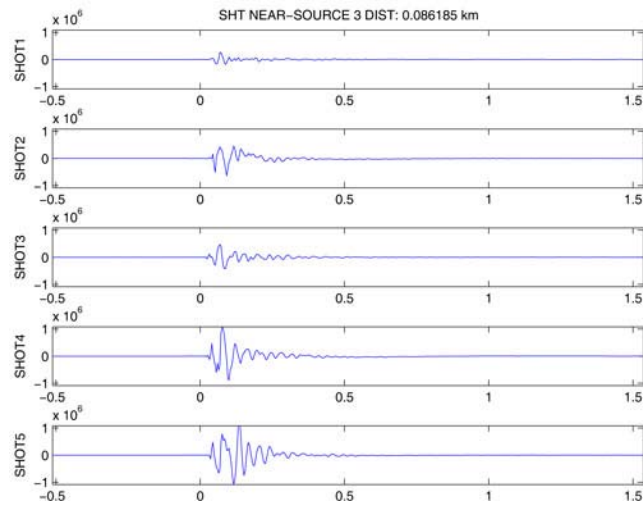

Figure 3A-9. Transverse-component seismograms for station NS3 for Shots 1 – 5 of the NEDE.

94
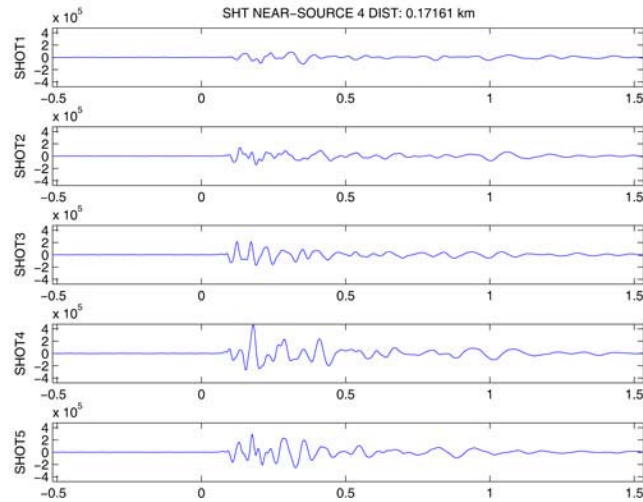
Figure 3A-10. Transverse-component seismograms for station NS4 for Shots 1 – 5 of the NEDE.
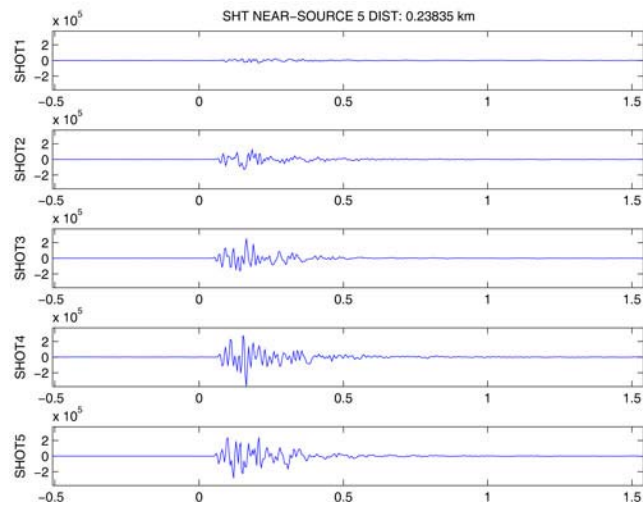
**Figure 3A-11. Transverse-component seismograms for station NS5 for Shots 1 – 5 of the NEDE.**
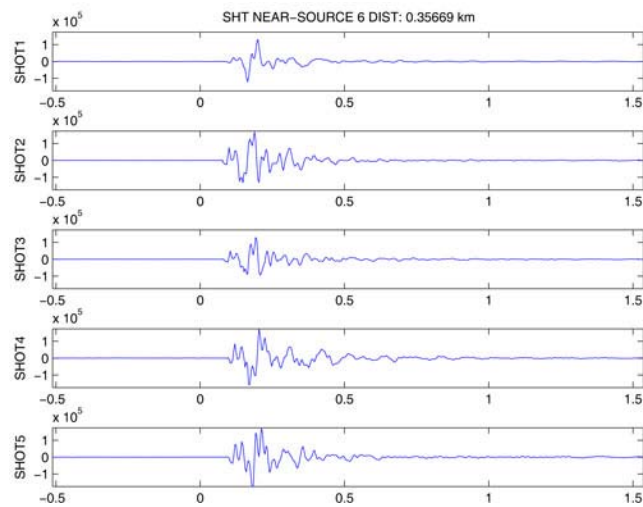
Figure 3A-12. Transverse-component seismograms for station NS6 for Shots 1 – 5 of the NEDE.

95
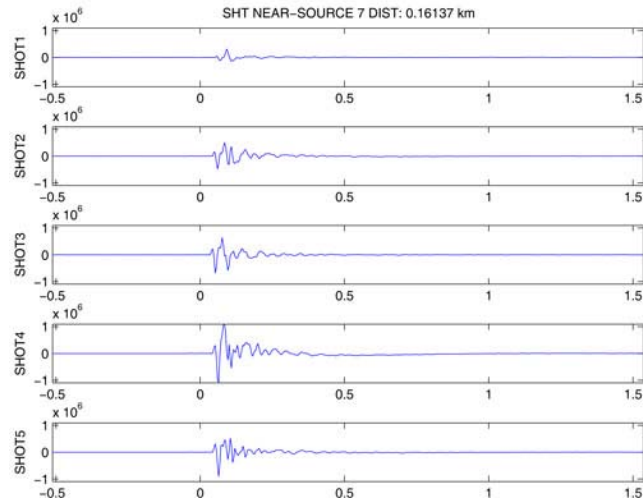
Figure 3A-13. Transverse-component seismograms for station NS7 for Shots 1 – 5 of the NEDE.
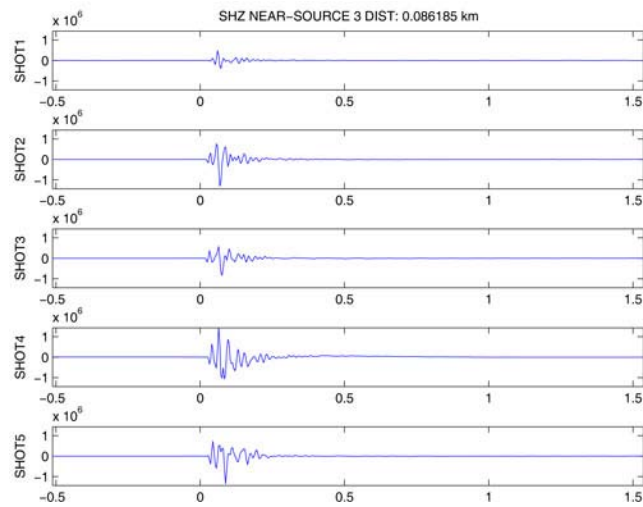
**Figure 3A-14. Vertical-component seismograms for station NS3 for Shots 1 – 5 of the NEDE.**
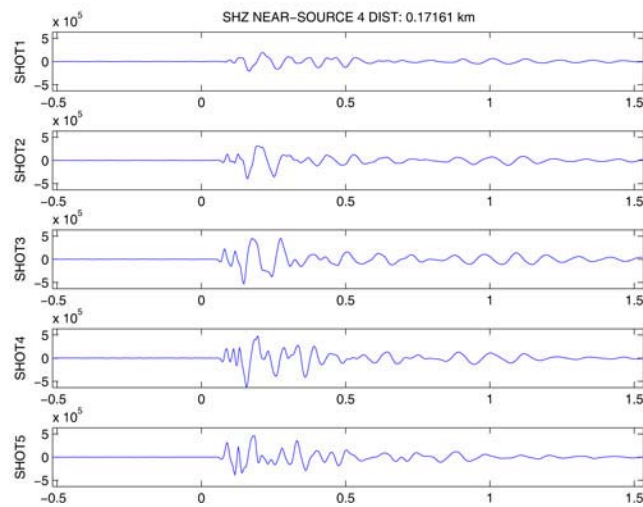
Figure 3A-15. Vertical-component seismograms for station NS4 for Shots 1 – 5 of the NEDE.

96
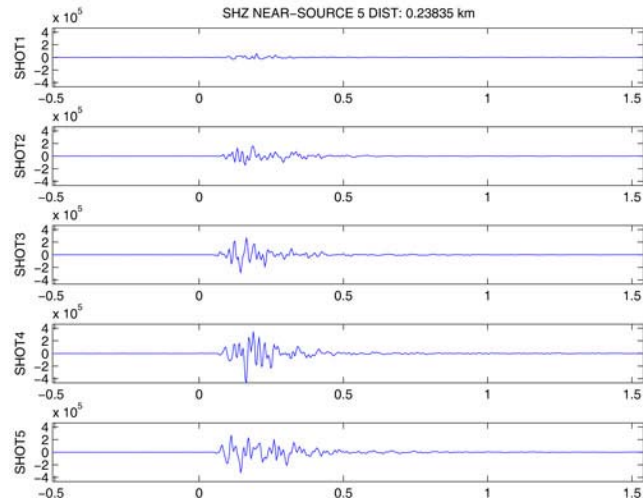
Figure 3A-16. Vertical-component seismograms for station NS5 for Shots 1 – 5 of the NEDE.
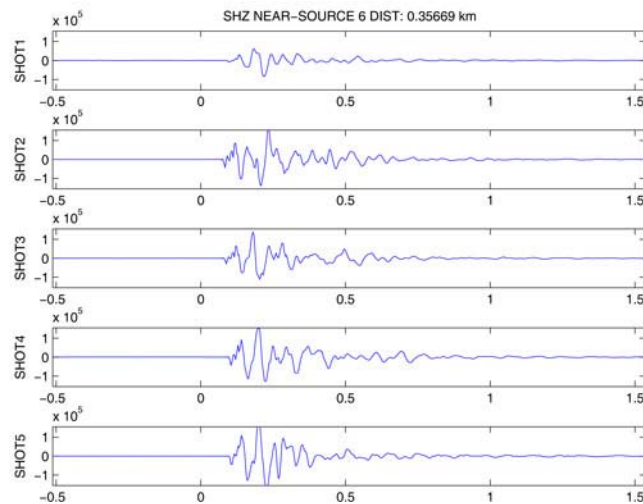
Figure 3A-17. Vertical-component seismograms for station NS6 for Shots 1 – 5 of the NEDE.
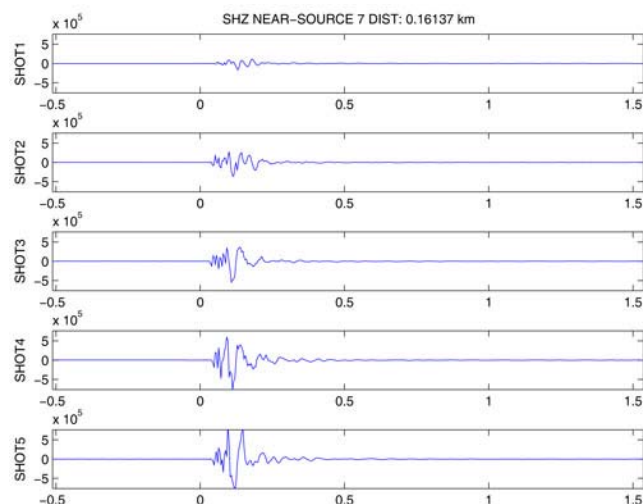
**Figure 3A-18. Vertical-component seismograms for station NS7 for Shots 1 – 5 of the NEDE.**

97
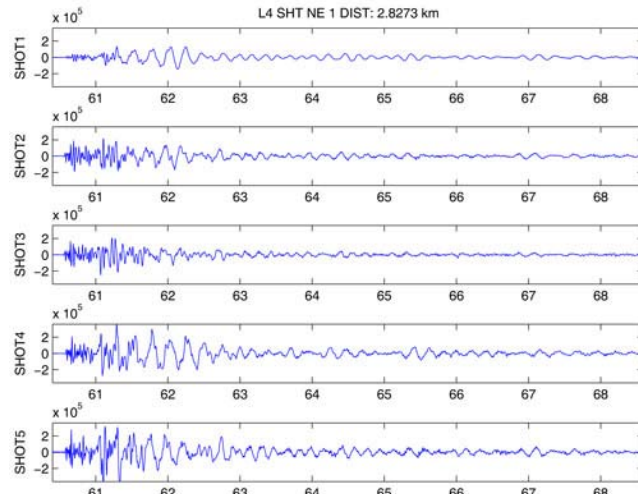
Figure 3A-19. Transverse-component seismograms for station NE1 for Shots 1 – 5 of the NEDE.
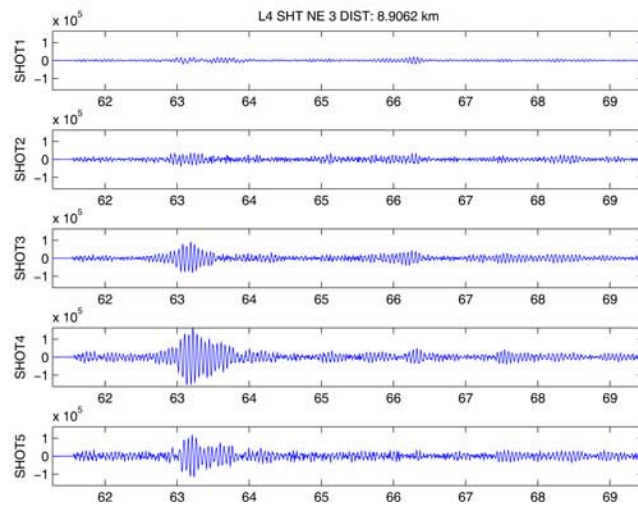

**Figure 3A-20. Transverse-component seismograms for station NE3 for Shots 1 – 5 of the NEDE.**
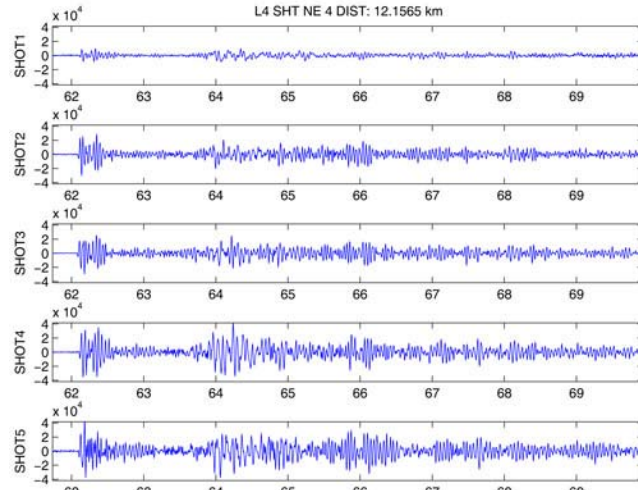
Figure 3A-21. Transverse-component seismograms for station NE4 for Shots 1 – 5 of the NEDE.

98
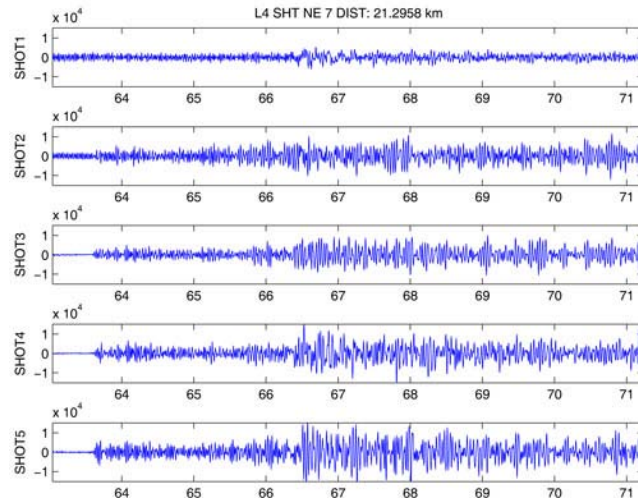
Figure 3A-22. Transverse-component seismograms for station NE7 for Shots 1 – 5 of the NEDE.
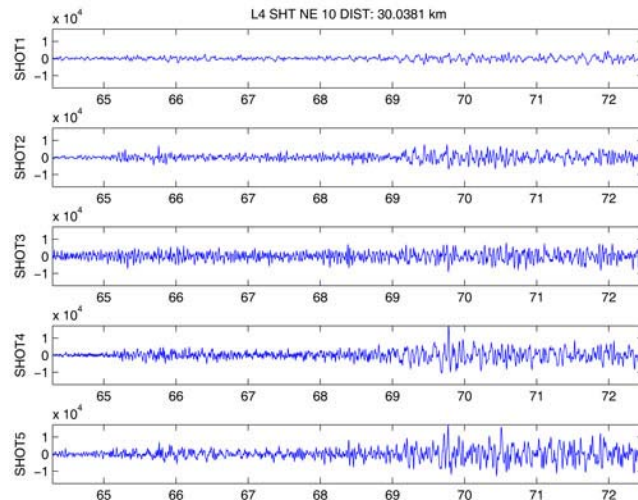
Figure 3A-23. Transverse-component seismograms for station NE10 for Shots 1 – 5 of the NEDE.
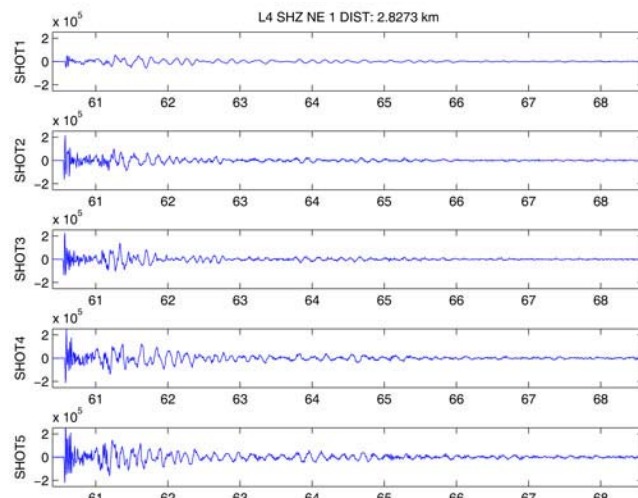
Figure 3A-24. Vertical-component seismograms for station NE1 for Shots 1 – 5 of the NEDE.

99
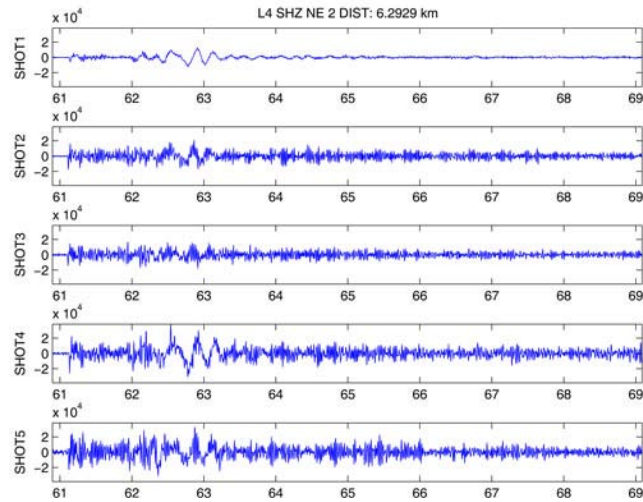
Figure 3A-25. Vertical-component seismograms for station NE2 for Shots 1 – 5 of the NEDE.
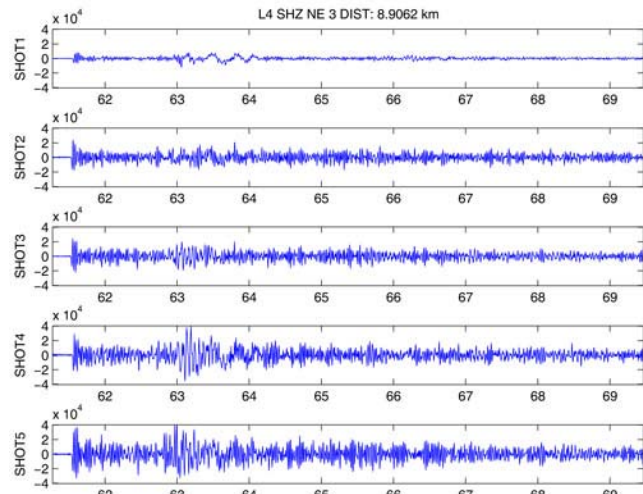

Figure 3A-26. Vertical-component seismograms for station NE3 for Shots 1 – 5 of the NEDE.
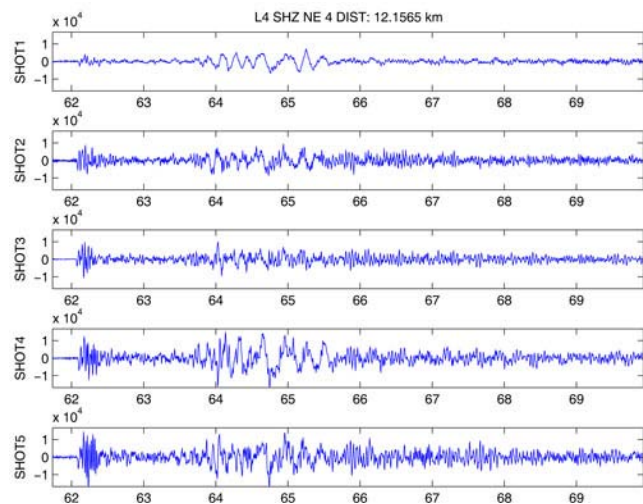
Figure 3A-27. Vertical-component seismograms for station NE4 for Shots 1 – 5 of the NEDE.

100
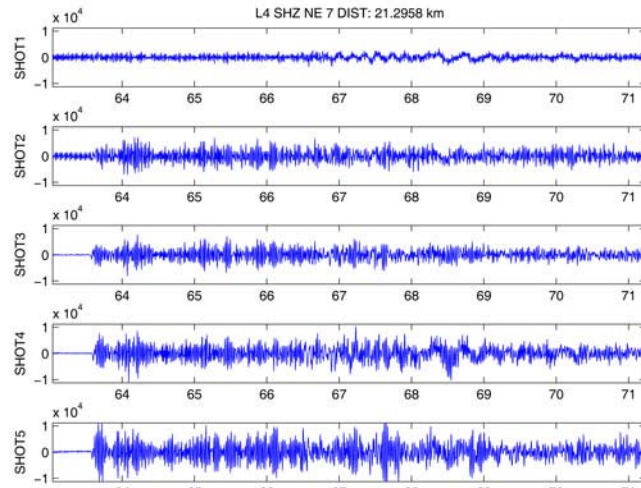
Figure 3A-28. Vertical-component seismograms for station NE7 for Shots 1 – 5 of the NEDE.
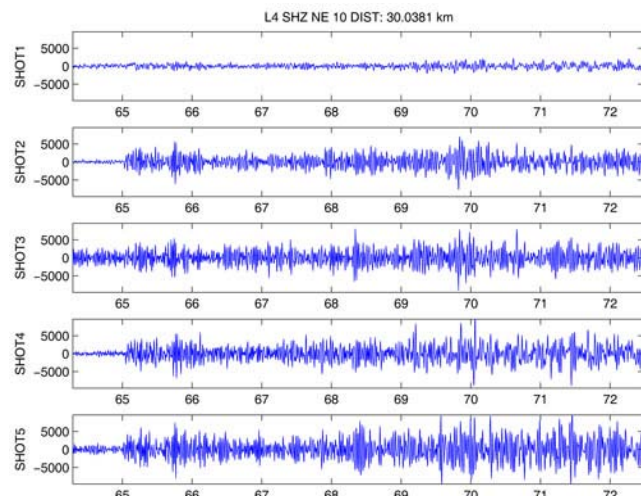
Figure 3A-29. Vertical-component seismograms for station NE10 for Shots 1 – 5 of the NEDE.
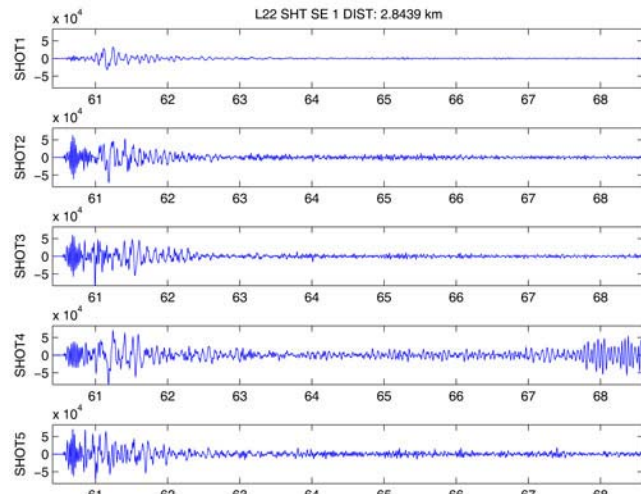
Figure 3A-30. Transverse-component seismograms for station SE1 for Shots 1 – 5 of the NEDE.

101
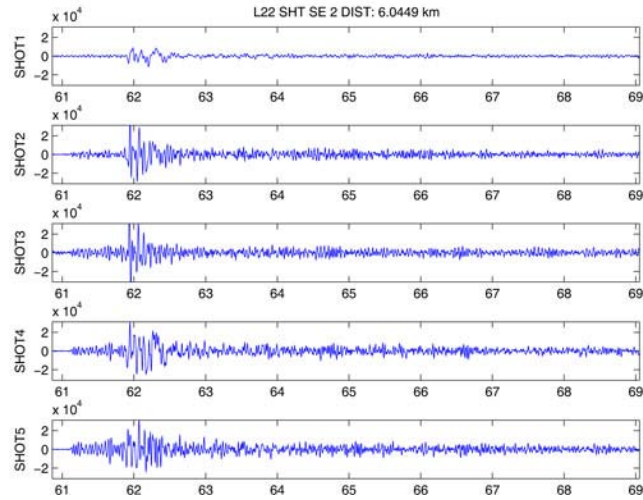
Figure 3A-31. Transverse-component seismograms for station SE2 for Shots 1 – 5 of the NEDE.
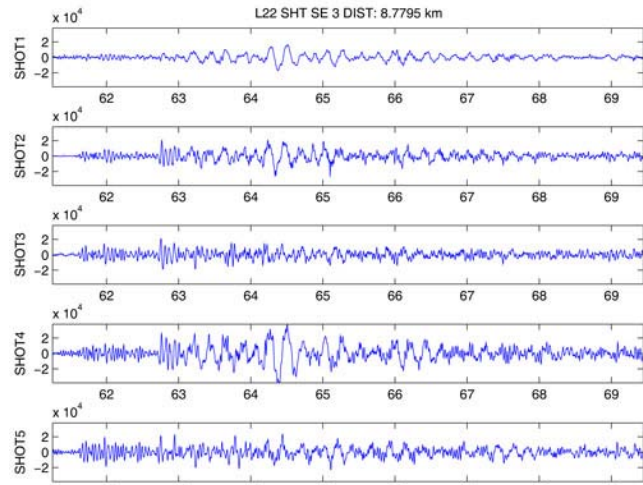
Figure 3A-32. Transverse-component seismograms for station SE3 for Shots 1 – 5 of the NEDE.
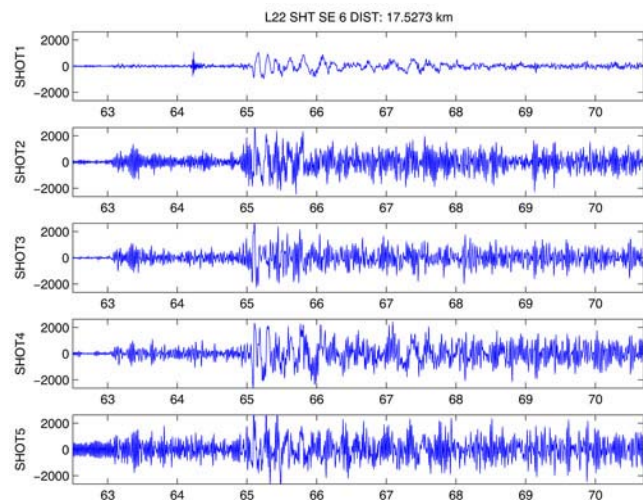
Figure 3A-33. Transverse-component seismograms for station SE6 for Shots 1 – 5 of the NEDE.
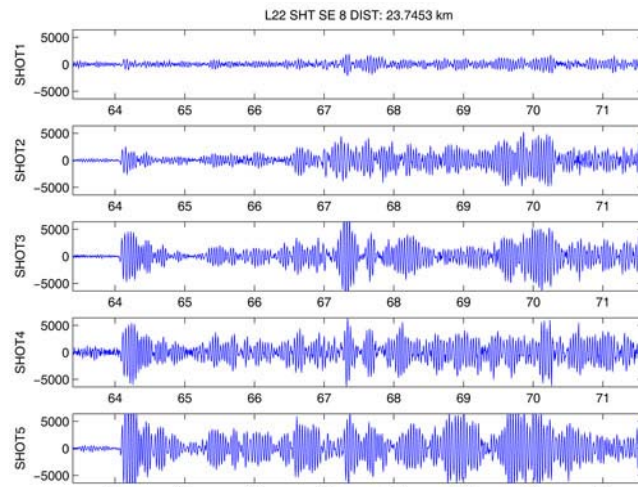
Figure 3A-34. Transverse-component seismograms for station SE8 for Shots 1 – 5 of the NEDE.
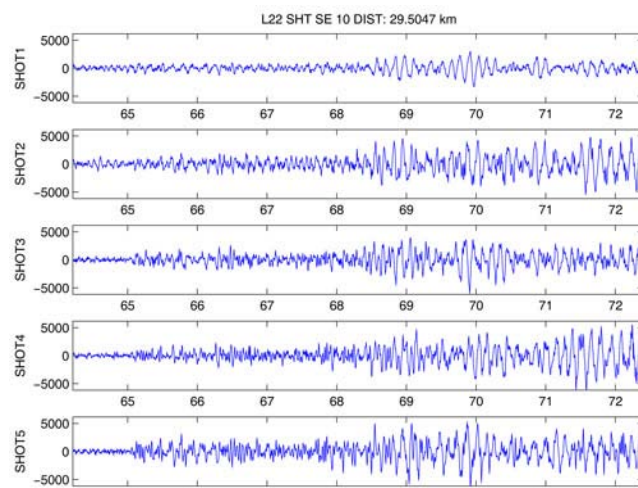
**Figure 3A-35. Transverse-component seismograms for station SE10 for Shots 1 – 5 of the NEDE.**
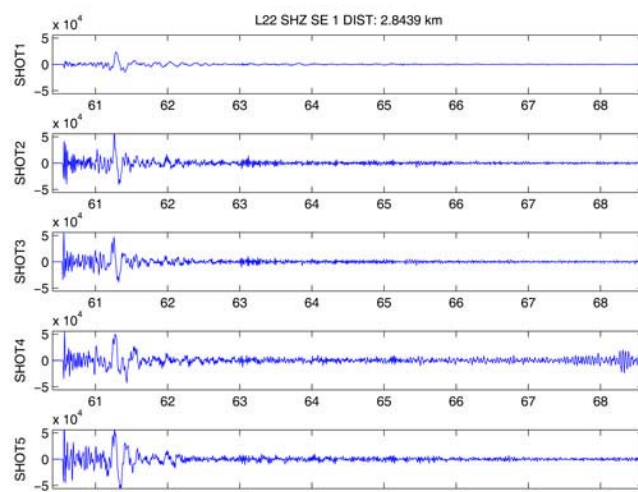
Figure 3A-36. Vertical-component seismograms for station SE1 for Shots 1 – 5 of the NEDE.

103
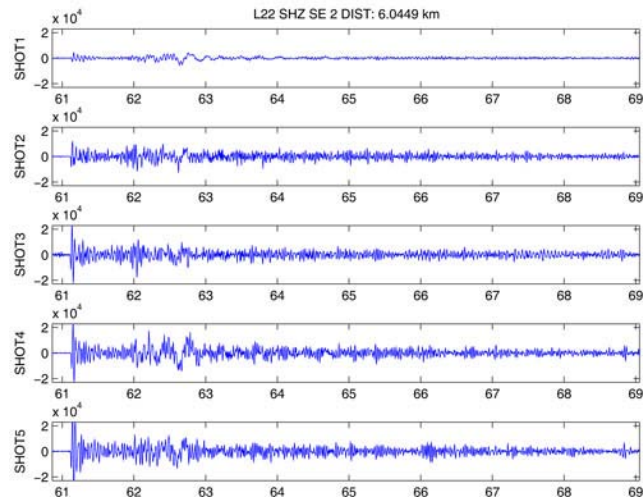
Figure 3A-37. Vertical-component seismograms for station SE2 for Shots 1 – 5 of the NEDE.
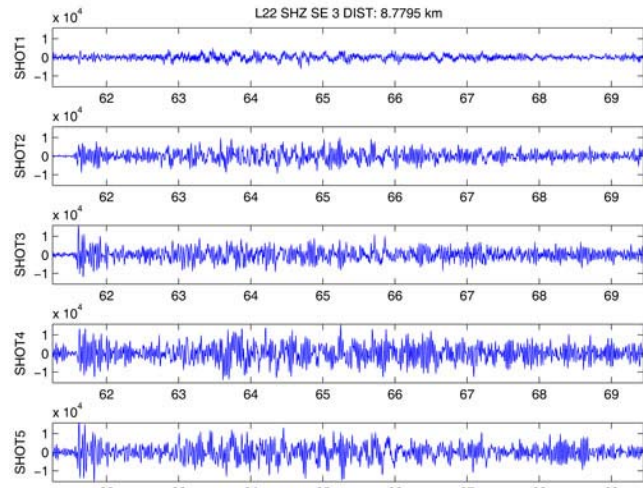
Figure 3A-38. Vertical-component seismograms for station SE3 for Shots 1 – 5 of the NEDE.
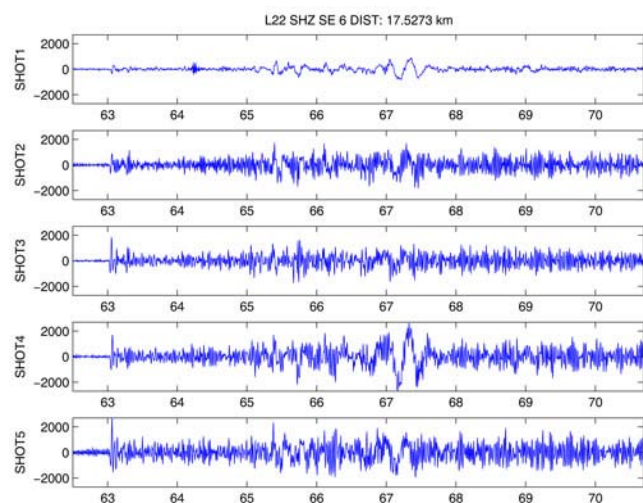
**Figure 3A-39. Vertical-component seismograms for station SE6 for Shots 1 – 5 of the NEDE.**
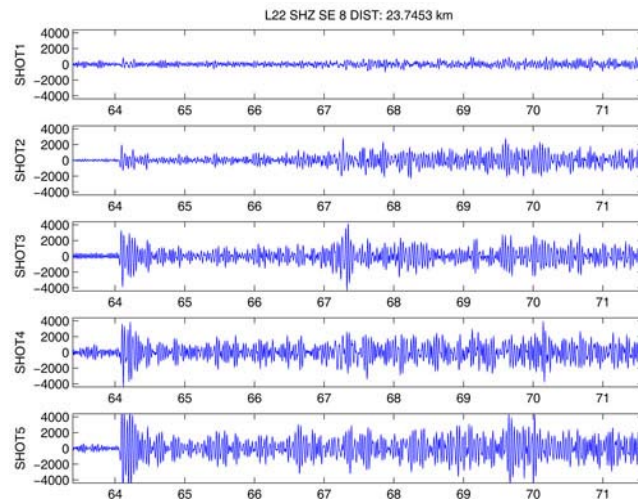
**Figure 3A-40. Vertical-component seismograms for station SE8 for Shots 1 – 5 of the NEDE.**
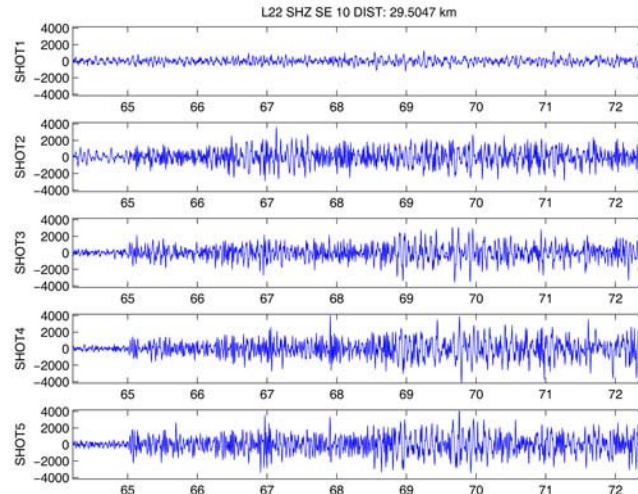
Figure 3A-41. Vertical-component seismograms for station SE10 for Shots 1 – 5 of the NEDE.
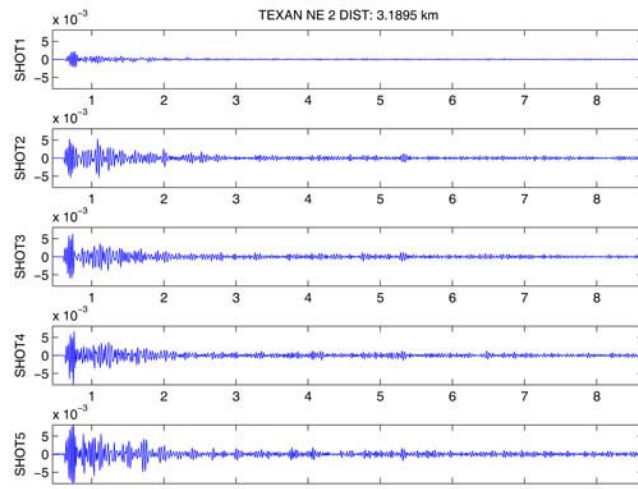

Figure 3A-42. Vertical-component seismograms for Texan station NE2.
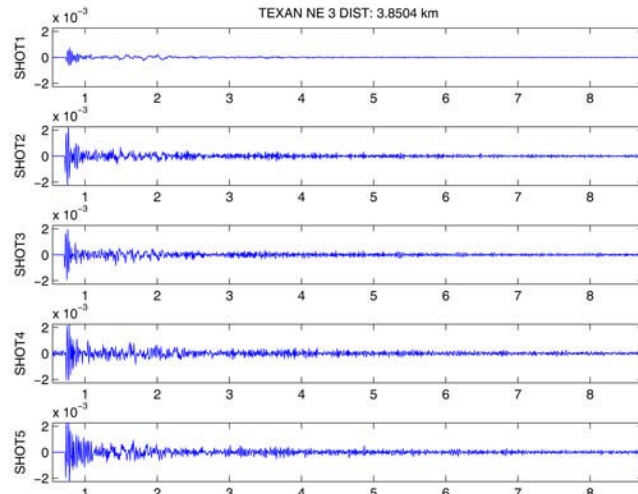
**Figure 3A-43. Vertical-component seismograms for Texan station NE3.**
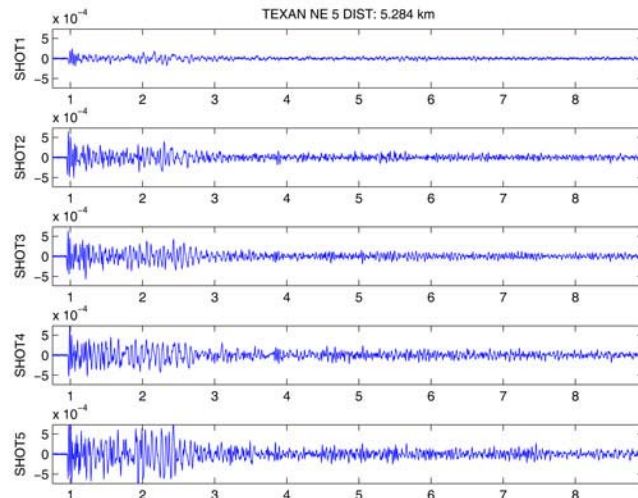
Figure 3A-44. Vertical-component seismograms for Texan station NE5.
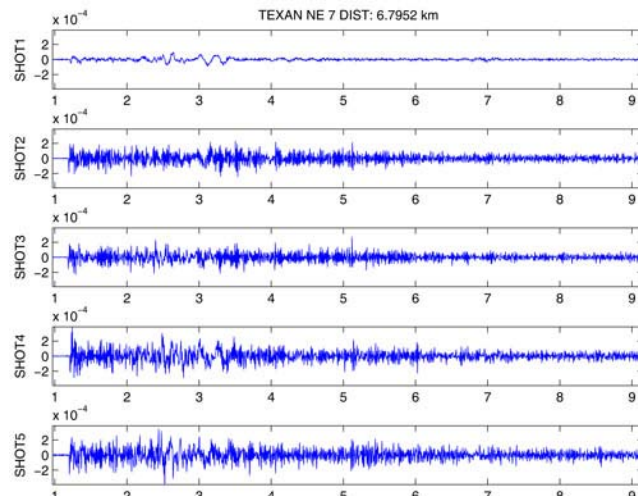

**Figure 3A-45. Vertical-component seismograms for Texan station NE7.**
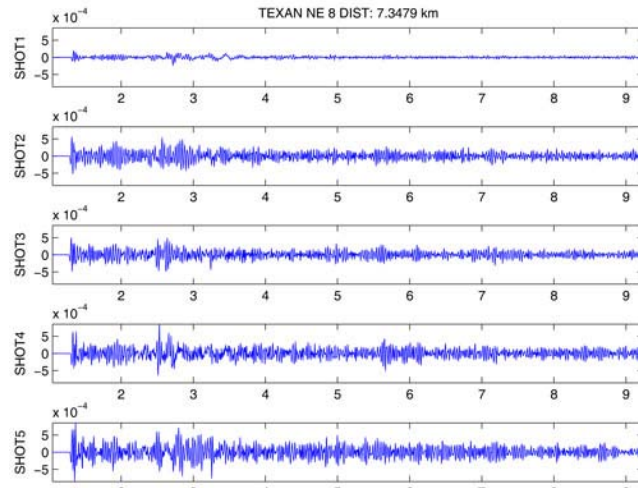
**Figure 3A-46. Vertical-component seismograms for Texan station NE8.**
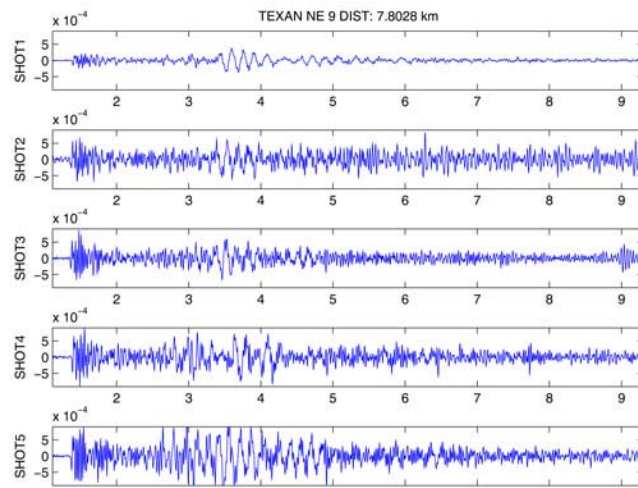
Figure 3A-47. Vertical-component seismograms for Texan station NE9.
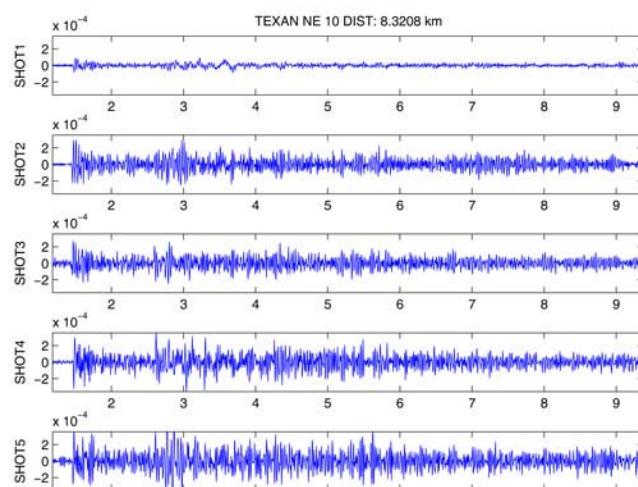
Figure 3A-48. Vertical-component seismograms for Texan station NE10.

107
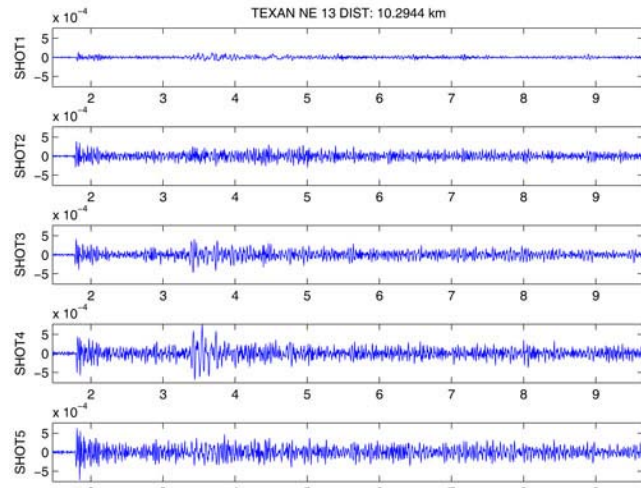
Figure 3A-49. Vertical-component seismograms for Texan station NE13.
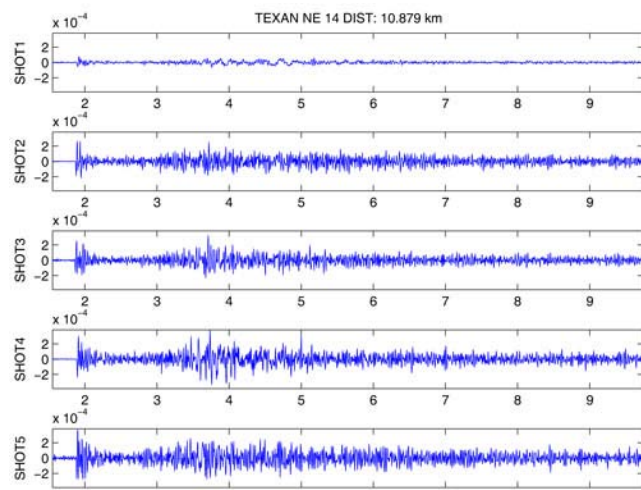
Figure 3A-50. Vertical-component seismograms for Texan station NE14.
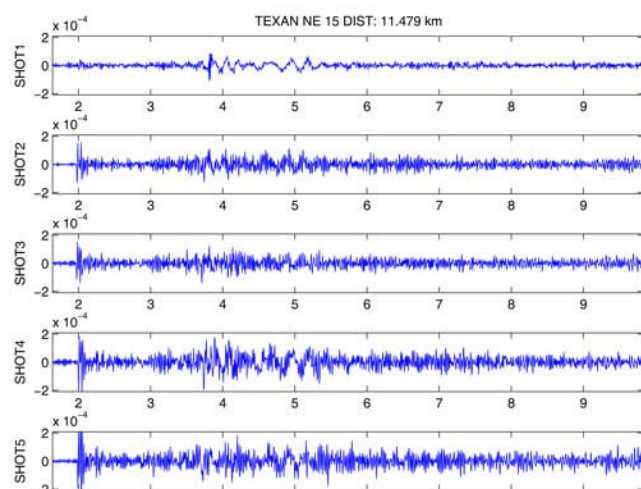
Figure 3A-51. Vertical-component seismograms for Texan station NE15.

108
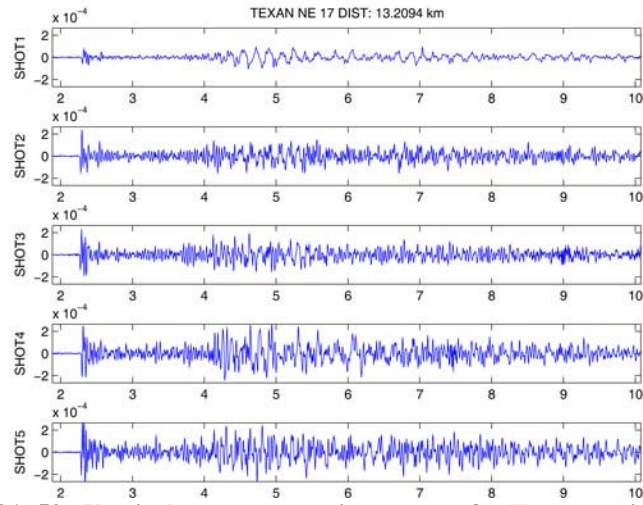
Figure 3A-52. Vertical-component seismograms for Texan station NE17.
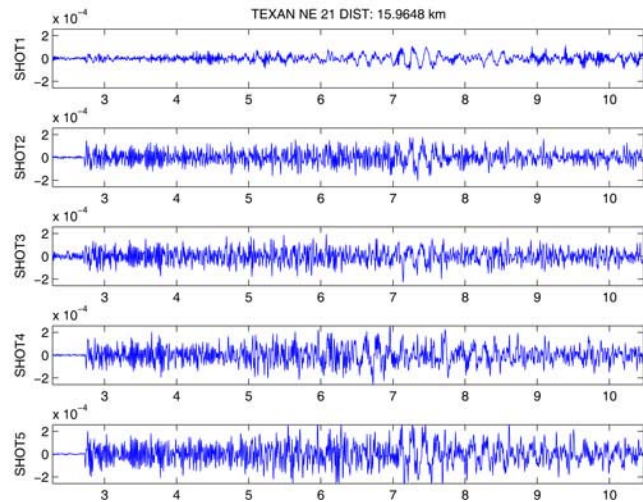
Figure 3A-53. Vertical-component seismograms for Texan station NE21.
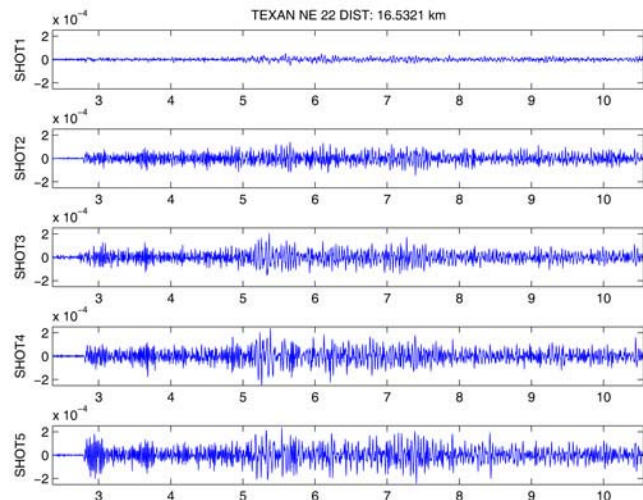
**Figure 3A-54. Vertical-component seismograms for Texan station NE22.**
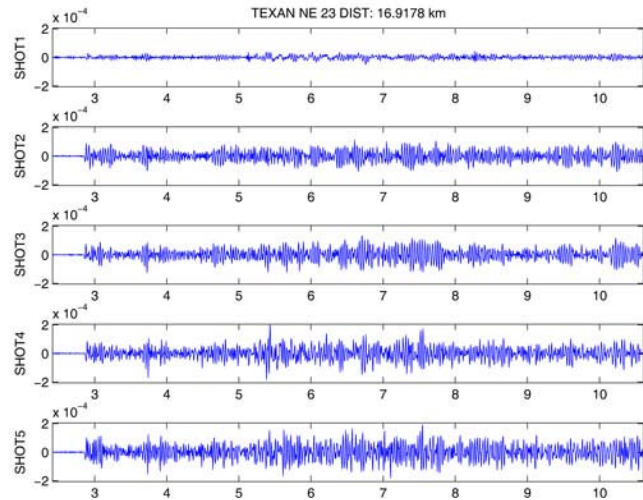
Figure 3A-55. Vertical-component seismograms for Texan station NE23.
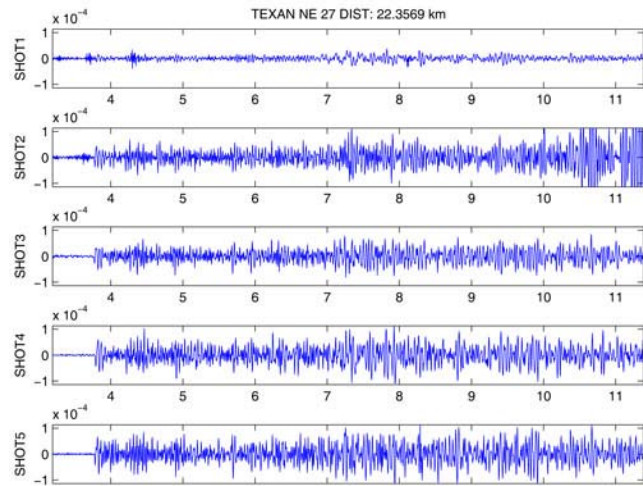
Figure 3A-56. Vertical-component seismograms for Texan station NE27.
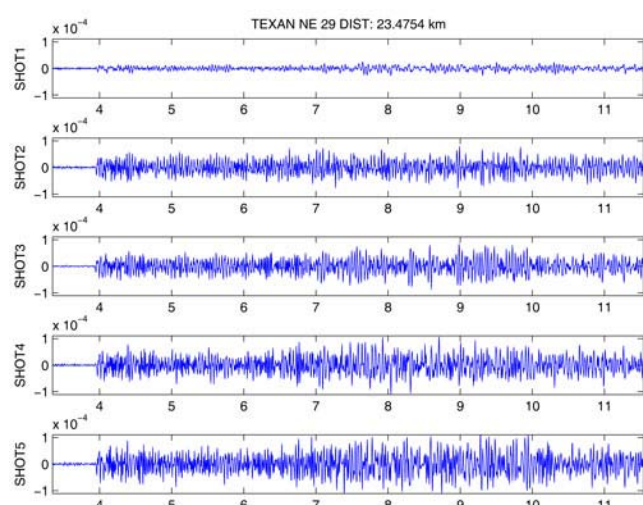
Figure 3A-57. Vertical-component seismograms for Texan station NE29.

110
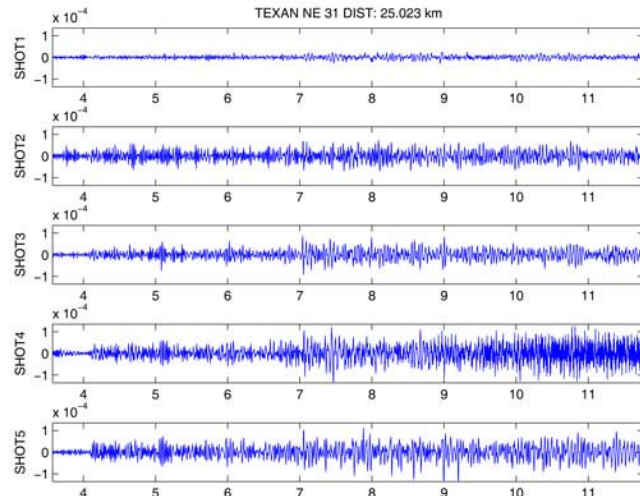
Figure 3A-58. Vertical-component seismograms for Texan station NE31.
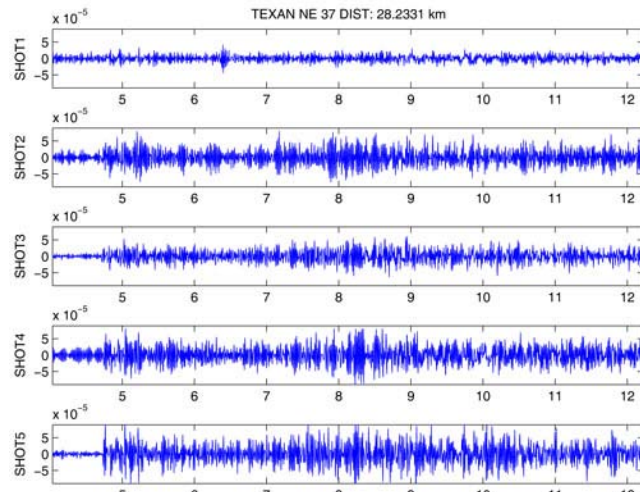
**Figure 3A-59. Vertical-component seismograms for Texan station NE37.**
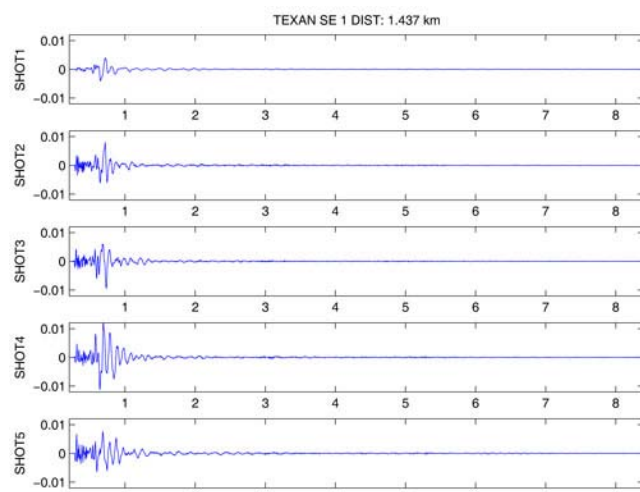
Figure 3A-60. Vertical-component seismograms for Texan station SE1.

111
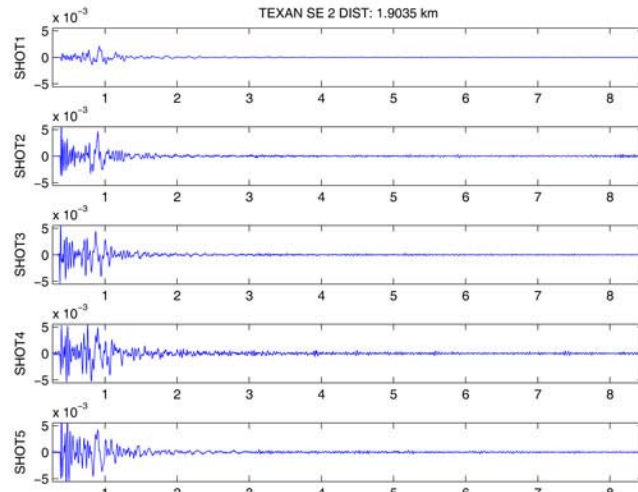
Figure 3A-61. Vertical-component seismograms for Texan station SE1.
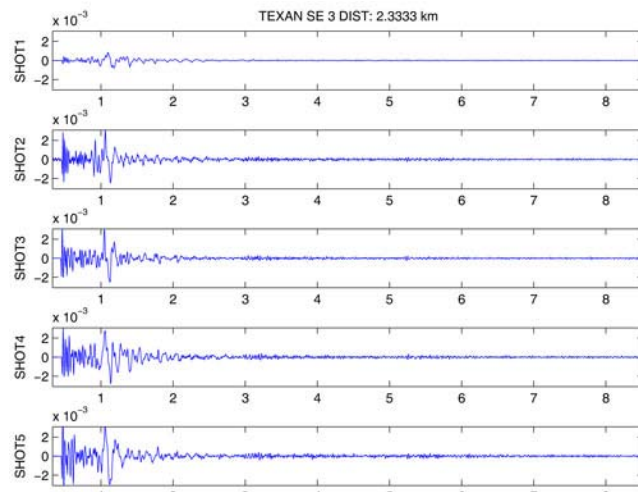

Figure 3A-62. Vertical-component seismograms for Texan station SE3.
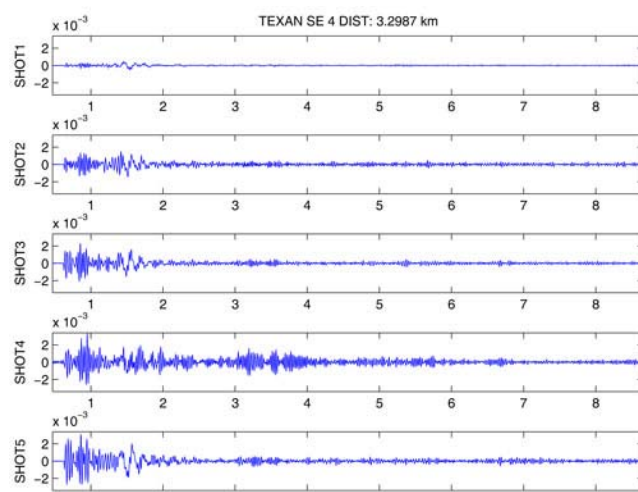
Figure 3A-63. Vertical-component seismograms for Texan station SE4.
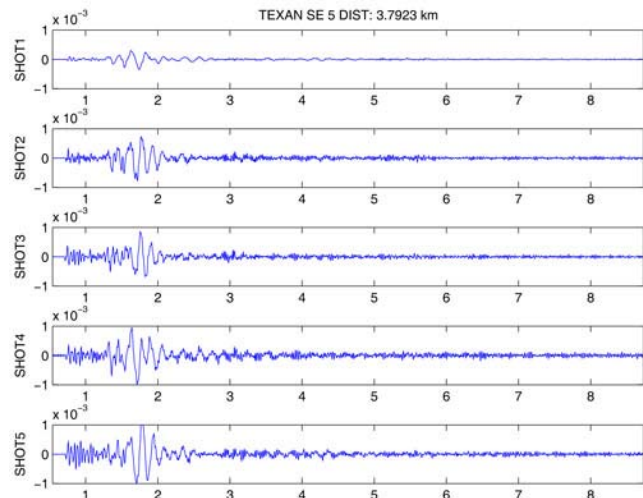
Figure 3A-64. Vertical-component seismograms for Texan station SE5.
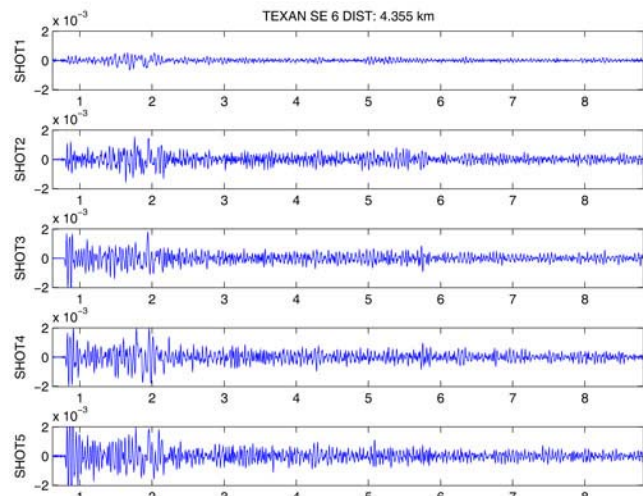
Figure 3A-65. Vertical-component seismograms for Texan station SE6.
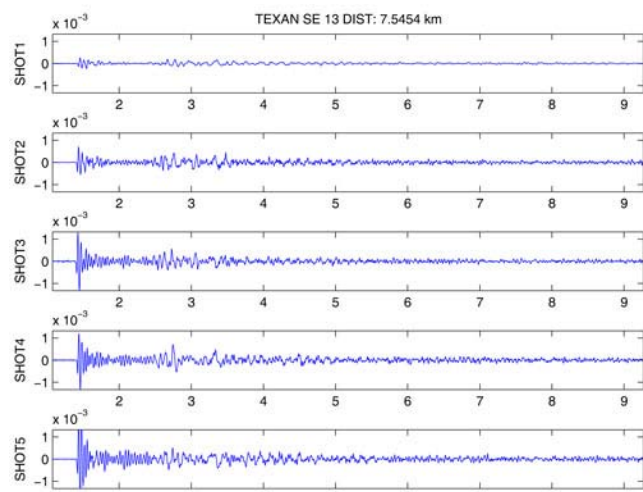
Figure 3A-66. Vertical-component seismograms for Texan station SE13.

113
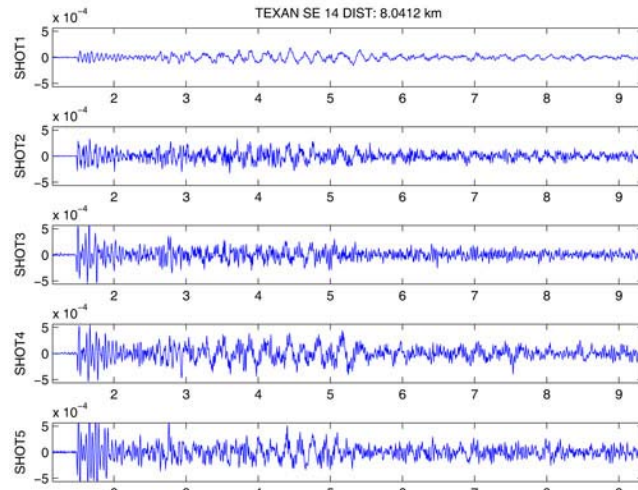
Figure 3A-67. Vertical-component seismograms for Texan station SE14.
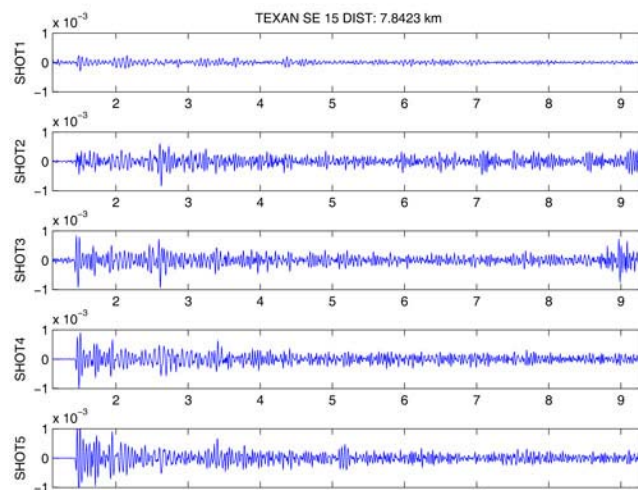
Figure 3A-68. Vertical-component seismograms for Texan station SE15.
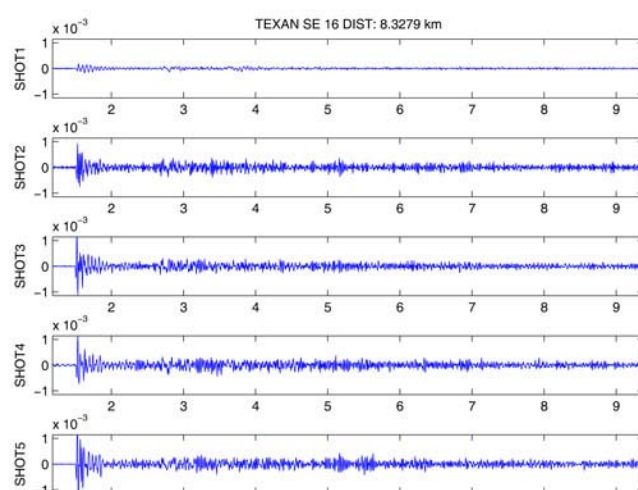
**Figure 3A-69. Vertical-component seismograms for Texan station SE16.**

114
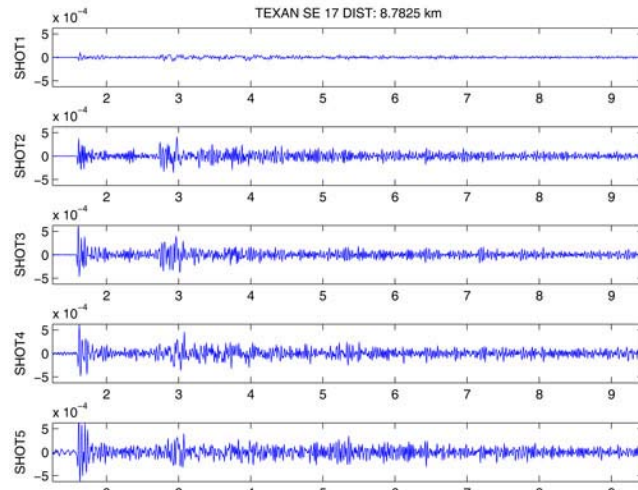
Figure 3A-70. Vertical-component seismograms for Texan station SE17.
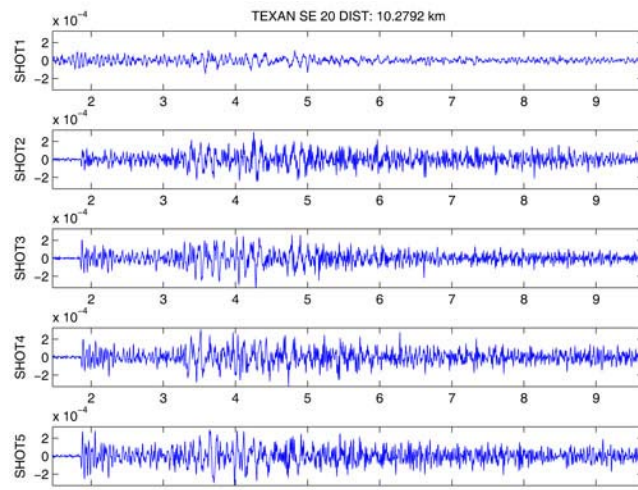
Figure 3A-71. Vertical-component seismograms for Texan station SE20.
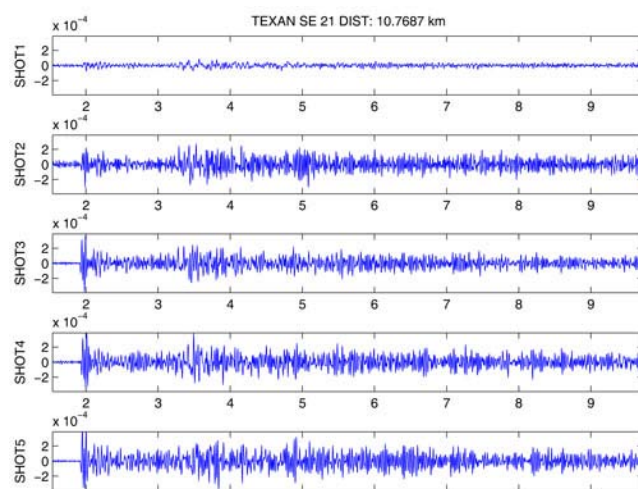
Figure 3A-72. Vertical-component seismograms for Texan station SE21.
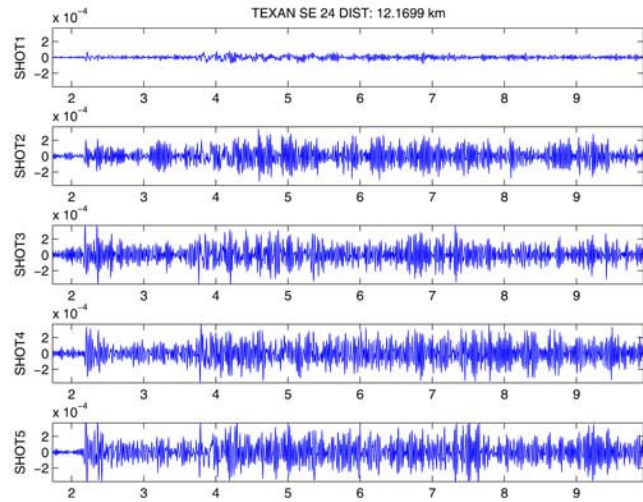
**Figure 3A-73. Vertical-component seismograms for Texan station SE24.**
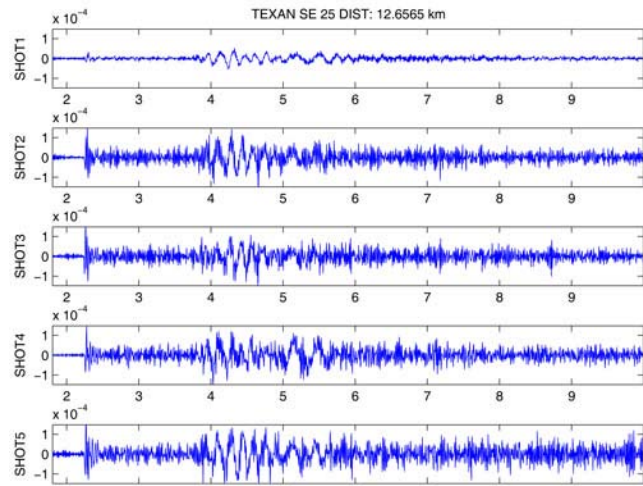
**Figure 3A-74. Vertical-component seismograms for Texan station SE25.**
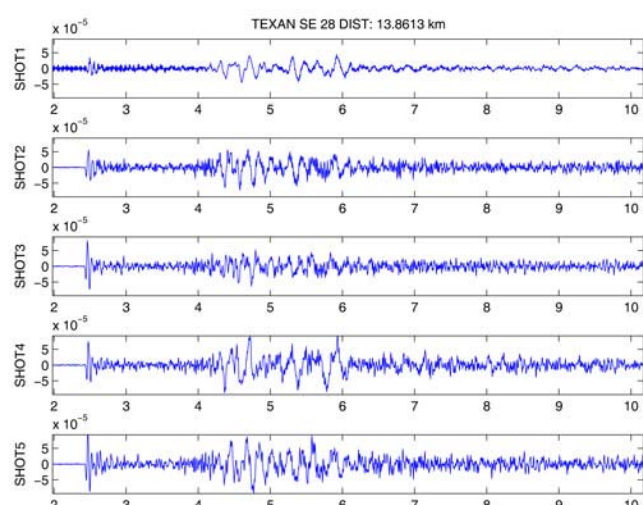
**Figure 3A-75. Vertical-component seismograms for Texan station SE28.**
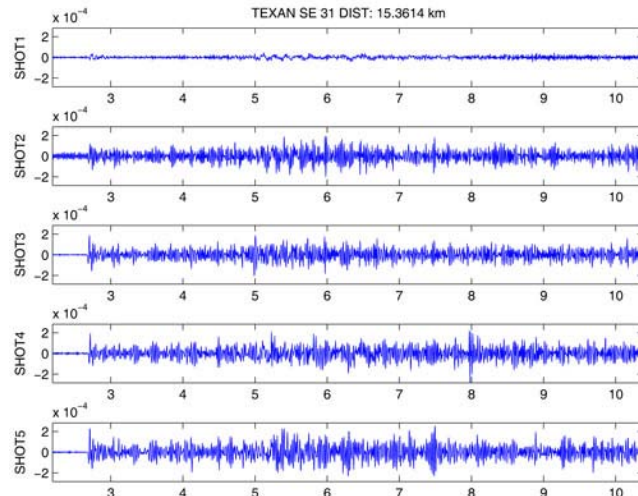
Figure 3A-76. Vertical-component seismograms for Texan station SE31.
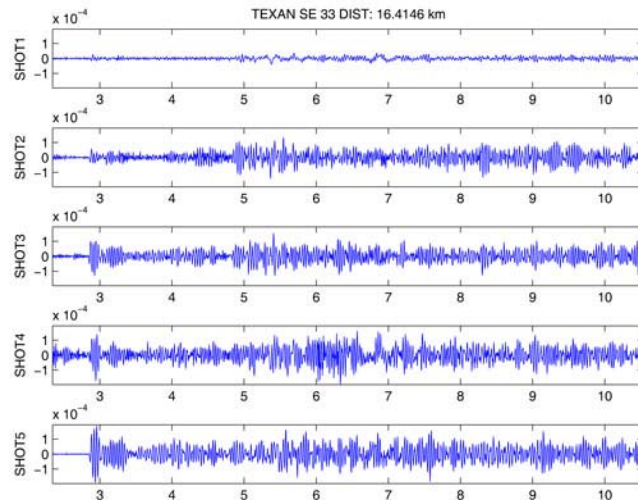
**Figure 3A-77. Vertical-component seismograms for Texan station SE33.**
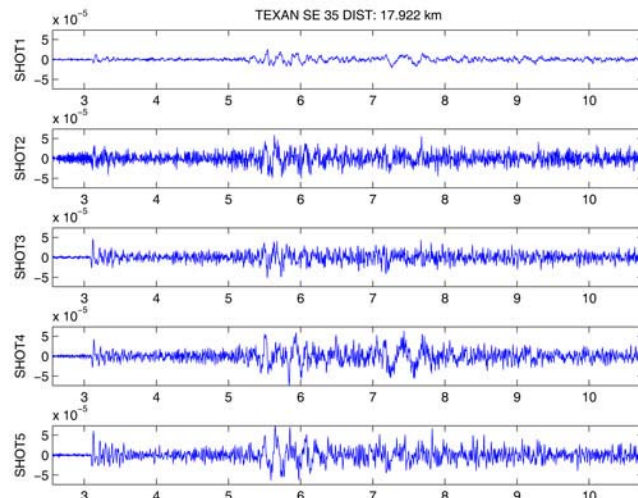
Figure 3A-78. Vertical-component seismograms for Texan station SE35.

117
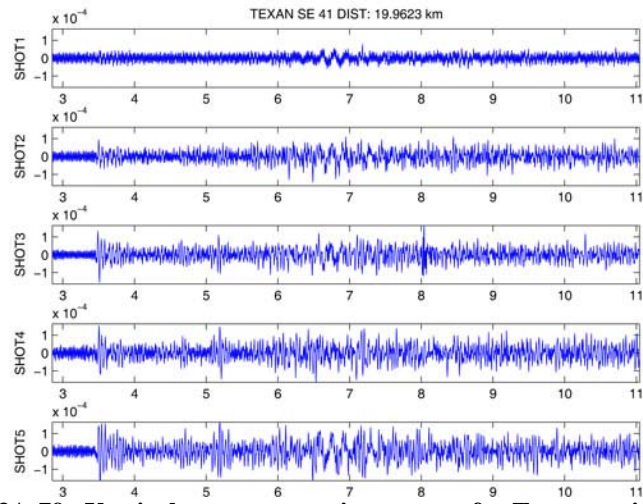
Figure 3A-79. Vertical-component seismograms for Texan station SE41.
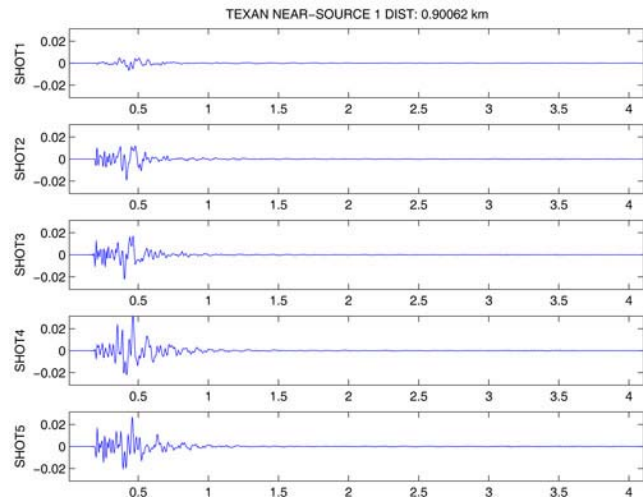
Figure 3A-80. Vertical-component seismograms for Texan near-source station NT1.
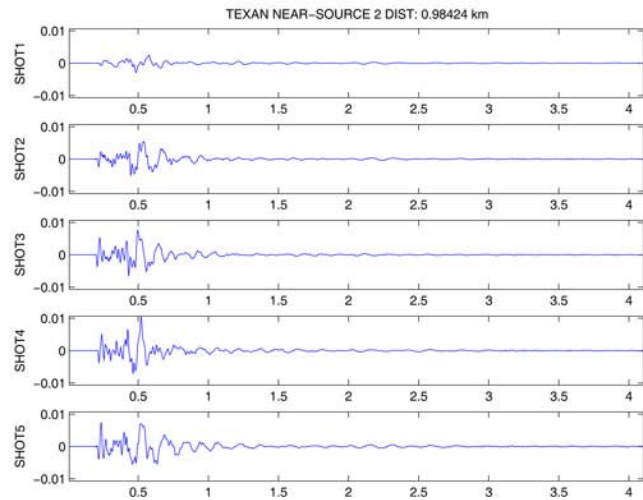
Figure 3A-81. Vertical-component seismograms for Texan near-source station NT2.

118
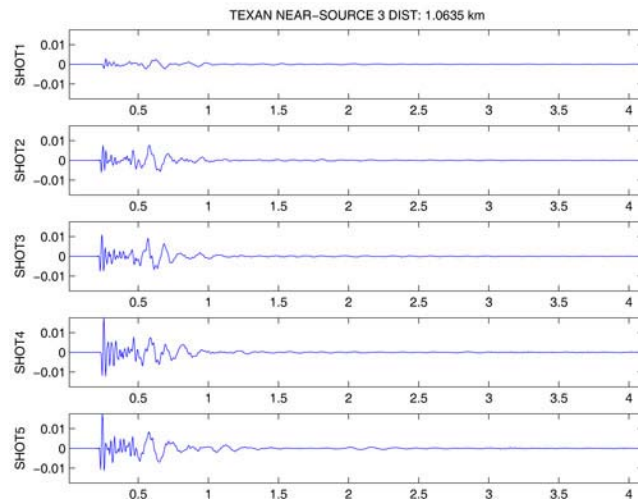
Figure 3A-82. Vertical-component seismograms for Texan near-source station NT3.
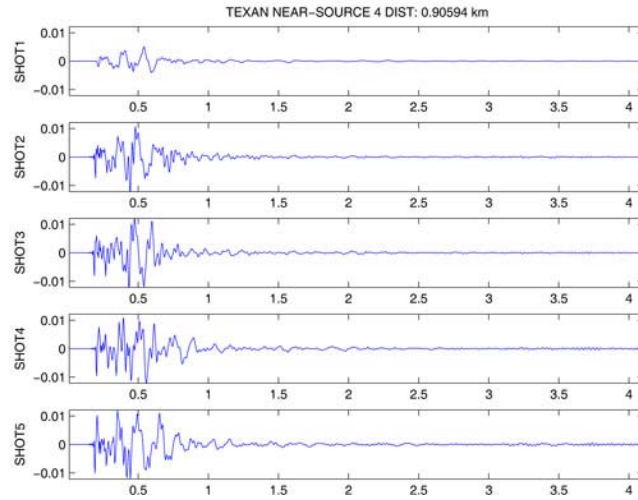
Figure 3A-83. Vertical-component seismograms for Texan near-source station NT4.
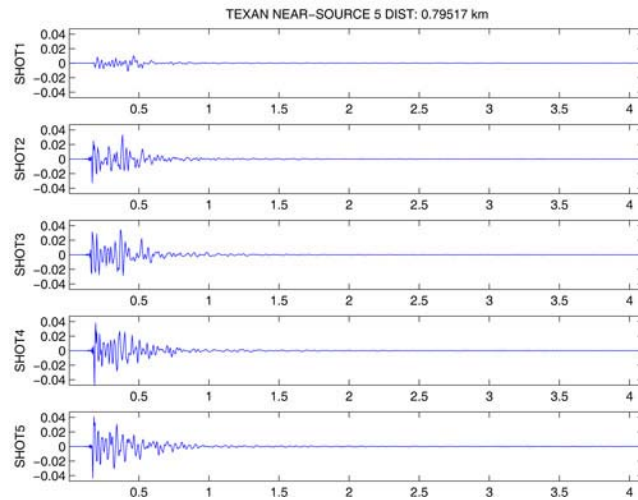
Figure 3A-84. Vertical-component seismograms for Texan near-source station NT5.
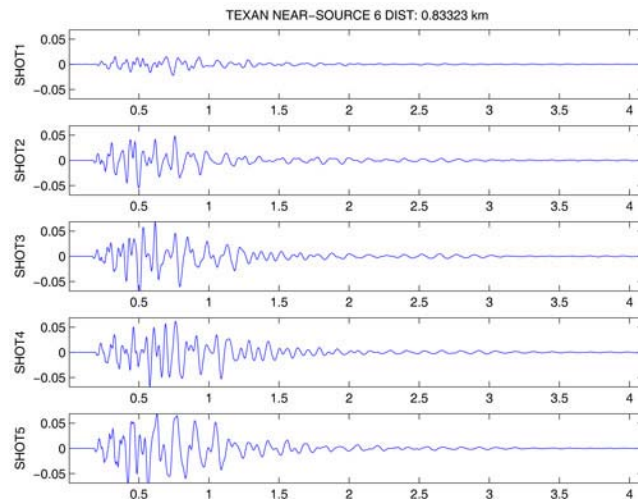
Figure 3A-85. Vertical-component seismograms for Texan near-source station NT6.
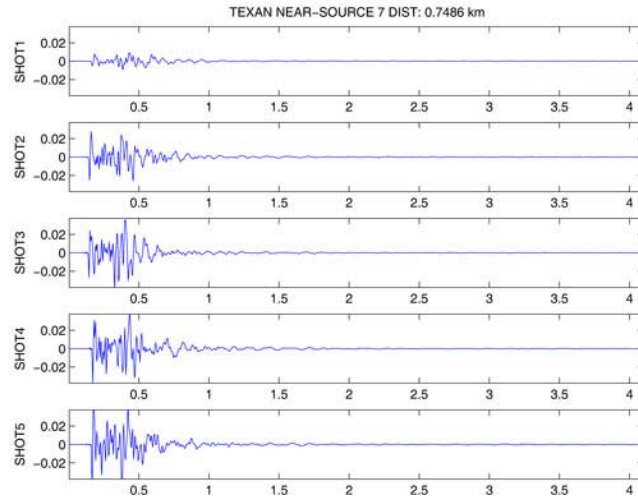
Figure 3A-86. Vertical-component seismograms for Texan near-source station NT7.
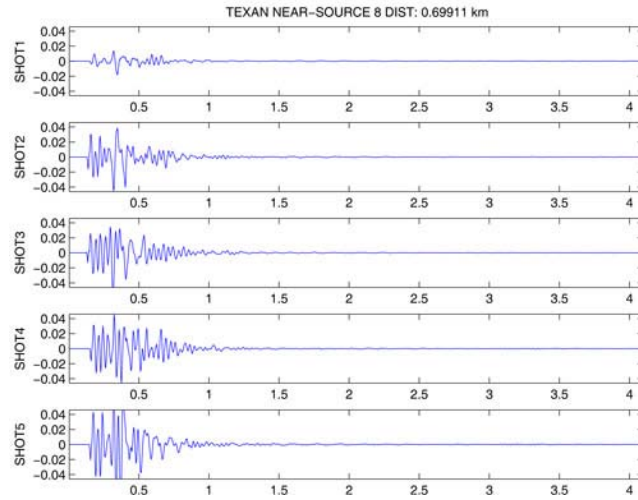
Figure 3A-87. Vertical-component seismograms for Texan near-source station NT8.
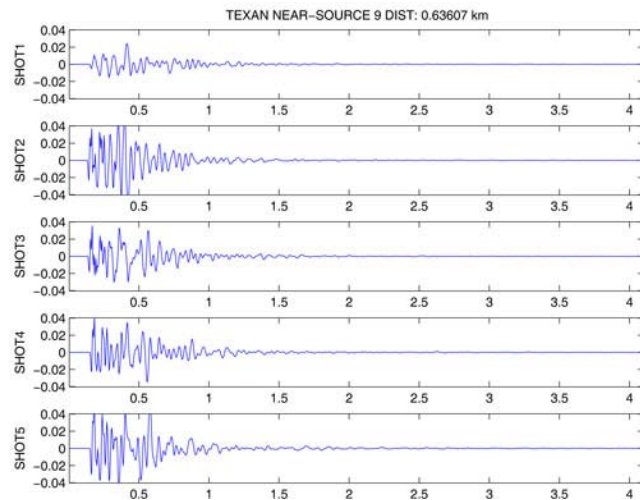
Figure 3A-88. Vertical-component seismograms for Texan near-source station NT9.
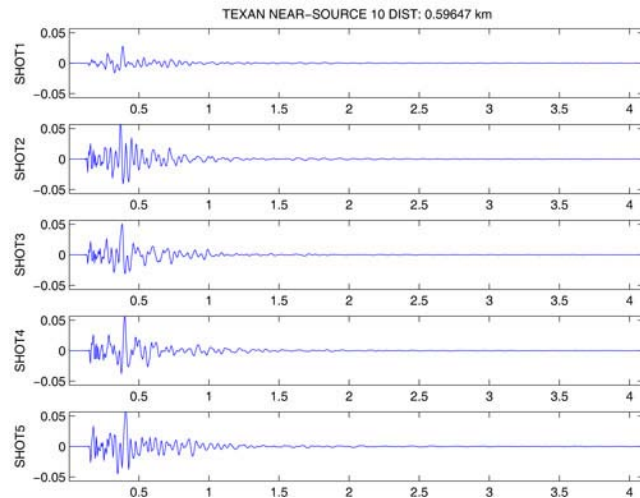
Figure 3A-89. Vertical-component seismograms for Texan near-source station NT10.
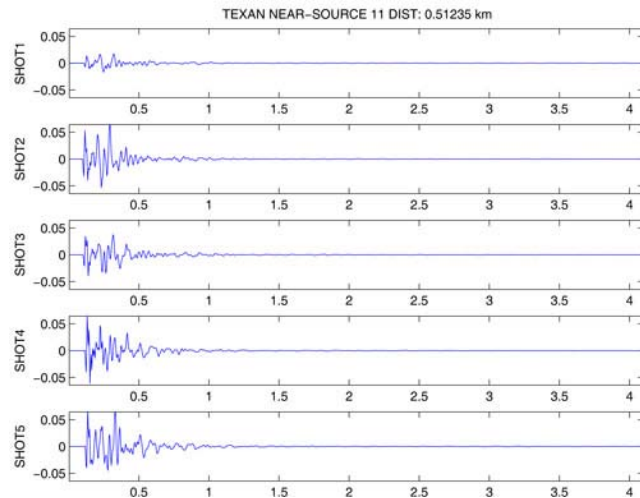
Figure 3A-90. Vertical-component seismograms for Texan near-source station NT11.
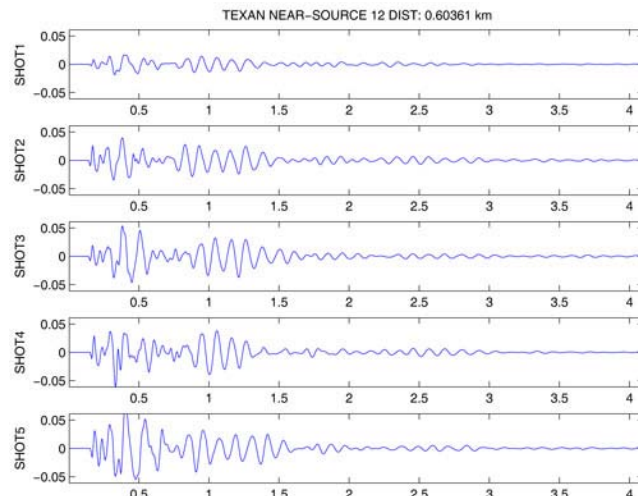
Figure 3A-91. Vertical-component seismograms for Texan near-source station NT12.
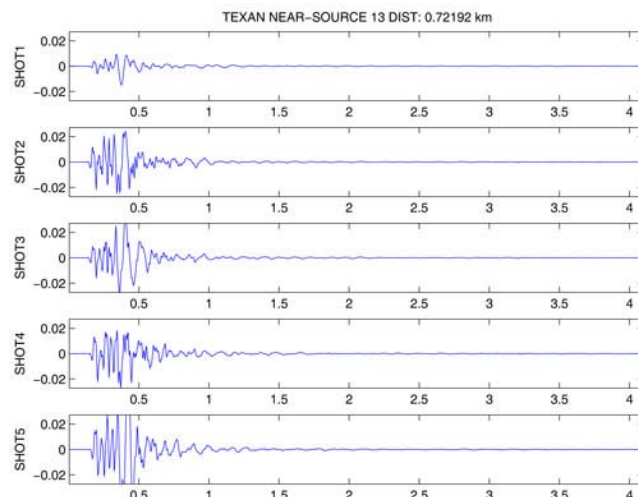
Figure 3A-92. Vertical-component seismograms for Texan near-source station NT13.
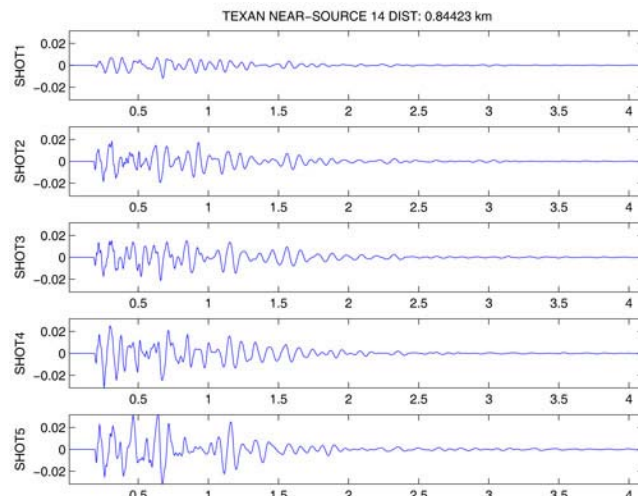
Figure 3A-93. Vertical-component seismograms for Texan near-source station NT14.
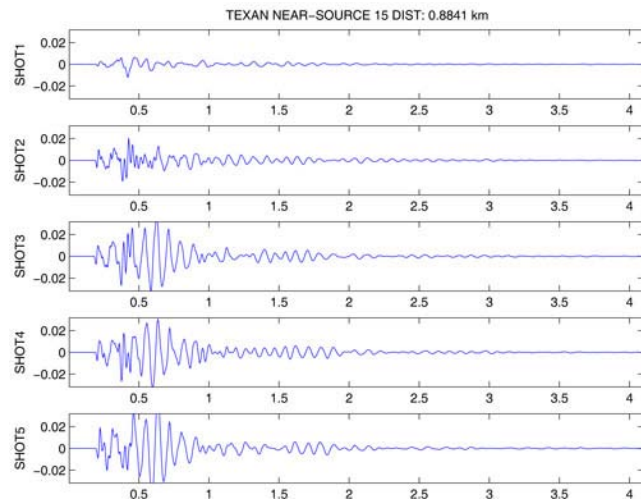
Figure 3A-94. Vertical-component seismograms for Texan near-source station NT15.
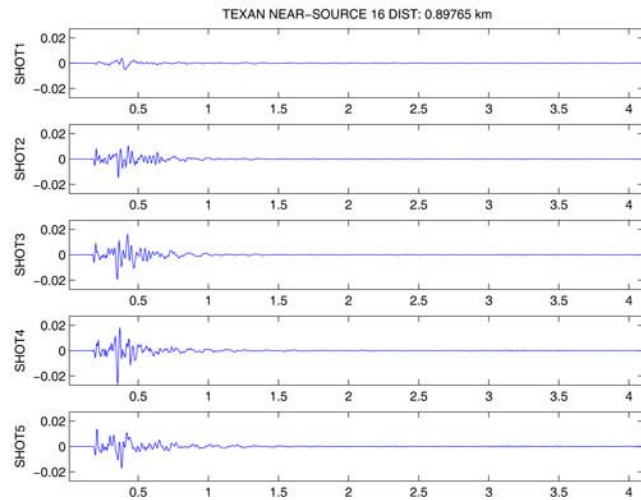
Figure 3A-95. Vertical-component seismograms for Texan near-source station NT16.
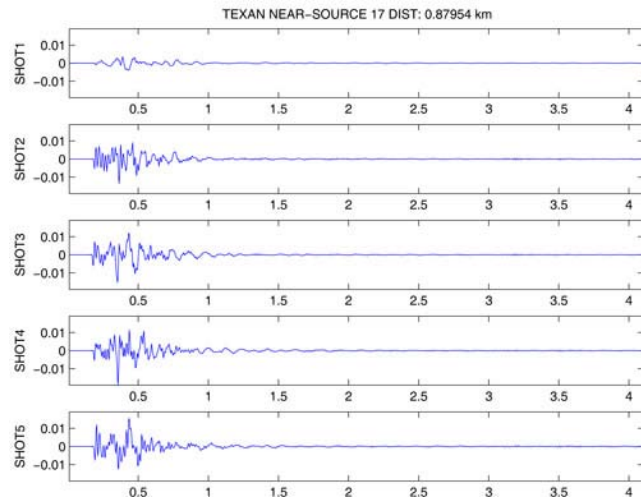
Figure 3A-96. Vertical-component seismograms for Texan near-source station NT17.

123
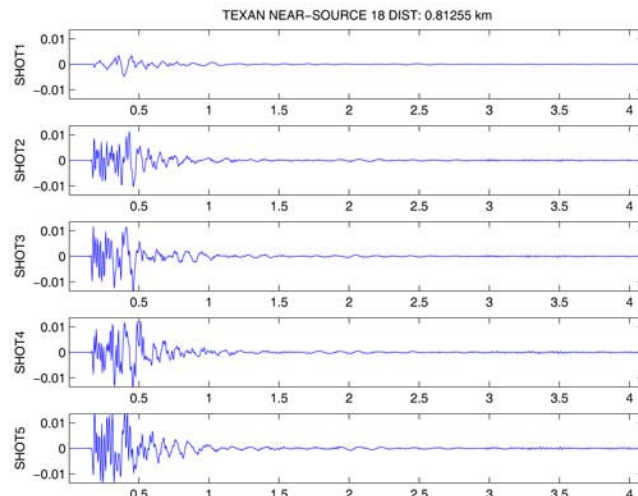
Figure 3A-97. Vertical-component seismograms for Texan near-source station NT18.
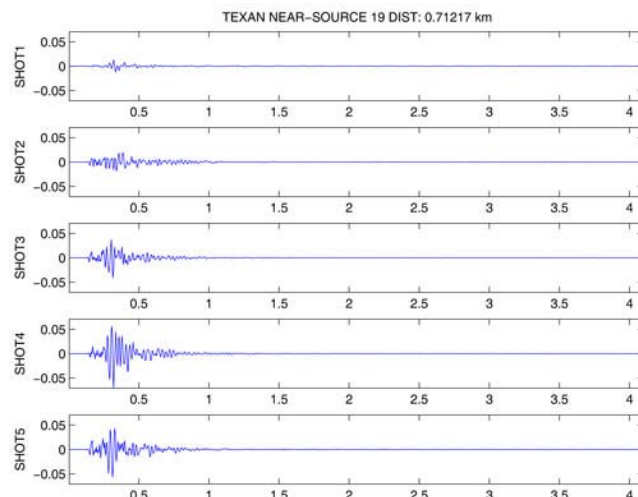
Figure 3A-98. Vertical-component seismograms for Texan near-source station NT19.
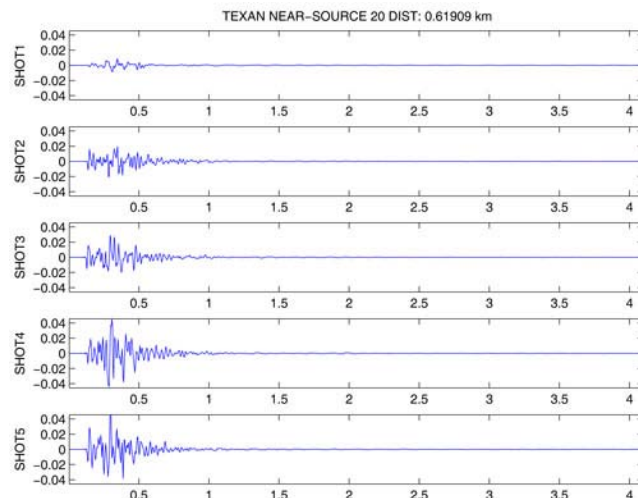
Figure 3A-99. Vertical-component seismograms for Texan near-source station NT20.

124
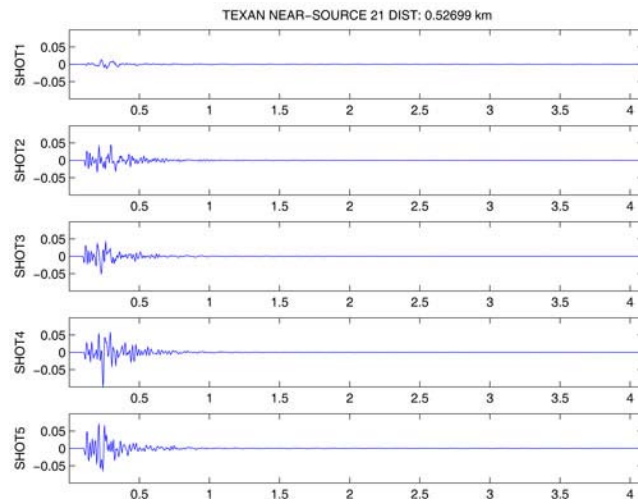
Figure 3A-100. Vertical-component seismograms for Texan near-source station NT21.
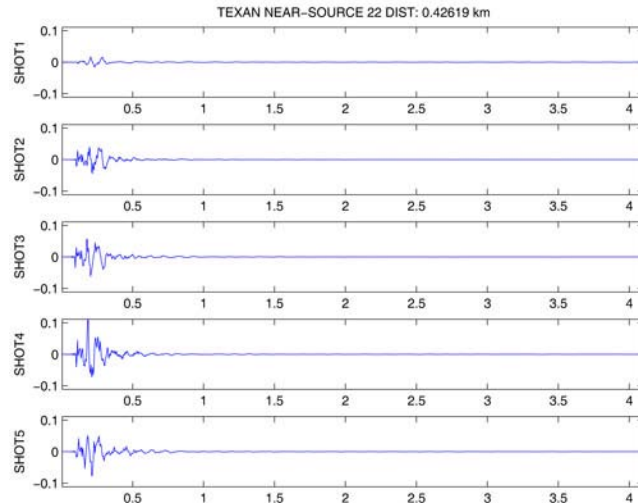
Figure 3A-101. Vertical-component seismograms for Texan near-source station NT22.
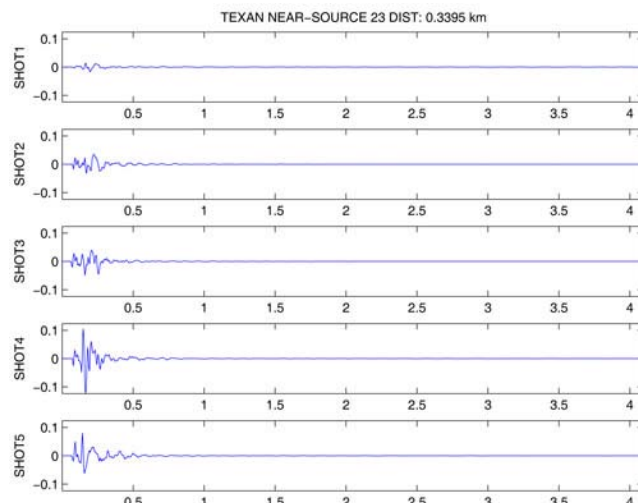
Figure 3A-102. Vertical-component seismograms for Texan near-source station NT23.
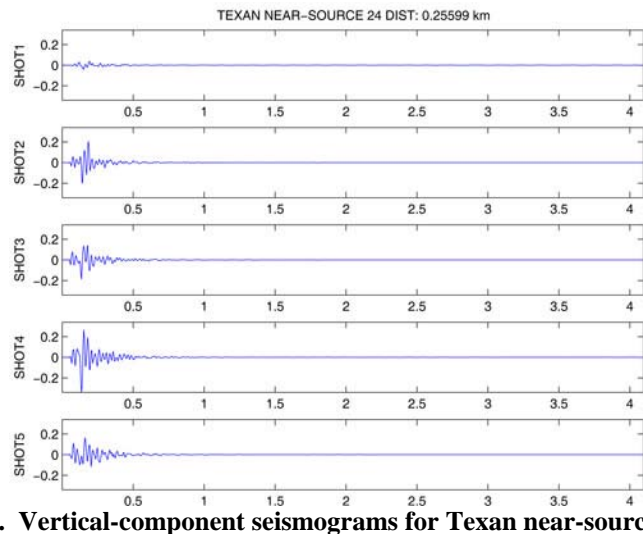
**Figure 3A-103. Vertical-component seismograms for Texan near-source station NT24.**

4. QUANTIFICATION OF GROUND VIBRATION DIFFERENCES FROM WELL-CONFINED SINGLE-HOLE EXPLOSIONS WITH VARIABLE VELOCITY OF DETONATION

ABSTRACT

An explosion experiment was conducted in the Barre granite of central Vermont during July 2008 using five explosions and three different types of explosives with a wide range of velocities of detonation. Black powder, heavy ANFO, and Composition B were used to generate increasing amounts of borehole pressure and different types of rock damage. The velocity of detonation was found to affect the peak particle velocities (PPV). ANFO produced the largest PPV, while the COMP B PPV were slightly lower. Black powder produced much lower PPV, likely due to it deflagrating rather than truly detonating. An equation was fit to the data for predicting the PPV from a confined blast in the Barre granite using two methods, including true vector summation. Vector summation provides a more accurate measure of particle velocity. We found the frequency of the PPV decreases with increasing distance from the blast, and therefore extra care must be taken for large blasts where lower frequency energy may exceed vibration limits at greater distances.

INTRODUCTION

An experiment was conducted in the Barre granite of central Vermont, during July 2008, detonating explosives with a wide range of velocities of detonation (VOD) to examine rock damage and ground vibrations from explosive sources. The Barre granite was chosen for the experiment due to its homogeneity and low fracture density and has been extensively studied and characterized (Goldsmith et al., 1977, Sano et al., 1992, Sawyers, 1968, Xia et al., 2008). We recorded the explosions on a large array of seismic instruments and quantified the resulting ground motions. We examined the peak particle velocities (PPV) as a function of scaled distance (SD) from the blasts. In this chapter, we present the analyses of the PPV and seismic energy generation as related to explosive VOD.

Explosion velocity of detonation and damage

During an explosion, different types of deformation are created around the borehole. As described by Hagan and Gibson (1988), the first zone of damage extending out from the blast is a ring of intensely pulverized and plastically deformed rock caused by the strain wave excessively exceeding the rock's compressive breaking strength. The radius of this crushing is a function of the borehole pressure, which is increased for faster VOD explosives. The heave energy is reduced by the high specific surface area of the powdered rock absorbing heat from the gases. This will also reduce the energy available for damage away from the borehole.

Beyond the crushed zone, the strain wave creates radial compression and tangential tensile fractures. This zone of deformation contains a high fracture density close to the pulverized zone and more widely spaced fractures at greater distances. Finally, the gases generated by the explosion can then penetrate and extend the fractures. A more detailed description of the damage regions and processes can be found in Hagan and Gibson (1988).

A faster VOD increases the borehole pressure and crushes the surrounding rock more intensely and for a longer distance (Essen et al., 2003, Hagan and Gibson, 1988). In addition to the pulverized and powdered material absorbing some of the explosive energy, it may inhibit the explosive gases from escaping and driving fractures, thereby constraining the damage to a smaller area. A slower VOD decreases the volume of pulverized and powdered material and allows the explosive gases to penetrate fractures generated by the strain wave and open long fractures (Hagan and Gibson, 1988).

To vary the amount and type of rock damage, we detonated three types of explosives with a wide range of VOD. All explosives were loaded in 22.9 cm (9 in) diameter boreholes. The explosives were initiated with a booster and blasting cap lowered to the bottom of the hole prior to the explosives being loaded. A small amount of 1¼ cm angular gravel stemming was poured on top of the explosive column, followed by the installation of a blast plug, and finally the remainder of the borehole was filled with the angular gravel. Table 18 lists the characteristics and explosive for each of the five blasts conducted. The VOD was measured in the field for each blast using an MREL Handitrap II recorder system. A resistance wire was taped to the booster and placed at the base of the explosive column. As the detonation moved up the borehole, the wire melted and decreased the resistance recorded by a digitizer at one million samples per second. This analysis allowed confirmation that the entire explosive column detonated and that the explosives performed as planned.

Table 18. Explosion characteristics.

Shot	Yield (kg)*	Charge Bottom/Top Depth (m)	Explosive Density (g/cm^3)	Explosive	Scaled Depth of Burial (m/kt$^{(1/3)}$)	VOD (km/sec)	Charge Ratio
1	60.8	9.15/7.50	0.9	Black Powder	205.0	0.53±0.3	7.2
2	61.5	11.89/10.74	1.3	Heavy ANFO	277.5	4.76±0.7	5.0
3	61.7	11.77/10.83	1.6	COMP B	276.8	-	4.1
4	122.2	14.02/11.73	1.3	Heavy ANFO	251.2	4.89±0.3	10.0
5	122.5	13.60/11.73	1.6	COMP B	246.9	8.10±0.2	8.2

* Yield is based on explosives + detonators.

Figure shows that the slowest VOD of the three explosives used was black powder. It has a low brisance, the rate at which the explosive reaches maximum pressure, and therefore crushes the rock around the borehole less, but the explosive gases can open pre-existing fractures for long distances. The black powder detonated (deflagrated to be more precise) at a rate of 0.5±0.3 km/sec (Table 18). The precise rate is difficult to determine due to electronic noise. Two shots with a mixture of 50% ANFO and 50% emulsion (heavy ANFO) were detonated with VOD of 4.8 and 4.9 km/sec. The fastest VOD explosive used was Composition B, which had a linear-regressed velocity of 8.1±0.2 km/sec. COMP B is a military grade cast charge explosive made from RDX and TNT and is primarily used in demolition, while ANFO is the most commonly used explosive in the mining industry for rock fragmentation. The VOD and explosive density

data from this experiment compare well with published values (Cooper, 1996, Persson, 1994, Meyer, 1987). Both heavy ANFO and Composition B are classified as high explosives, particularly when the heavy ANFO is fully confined.
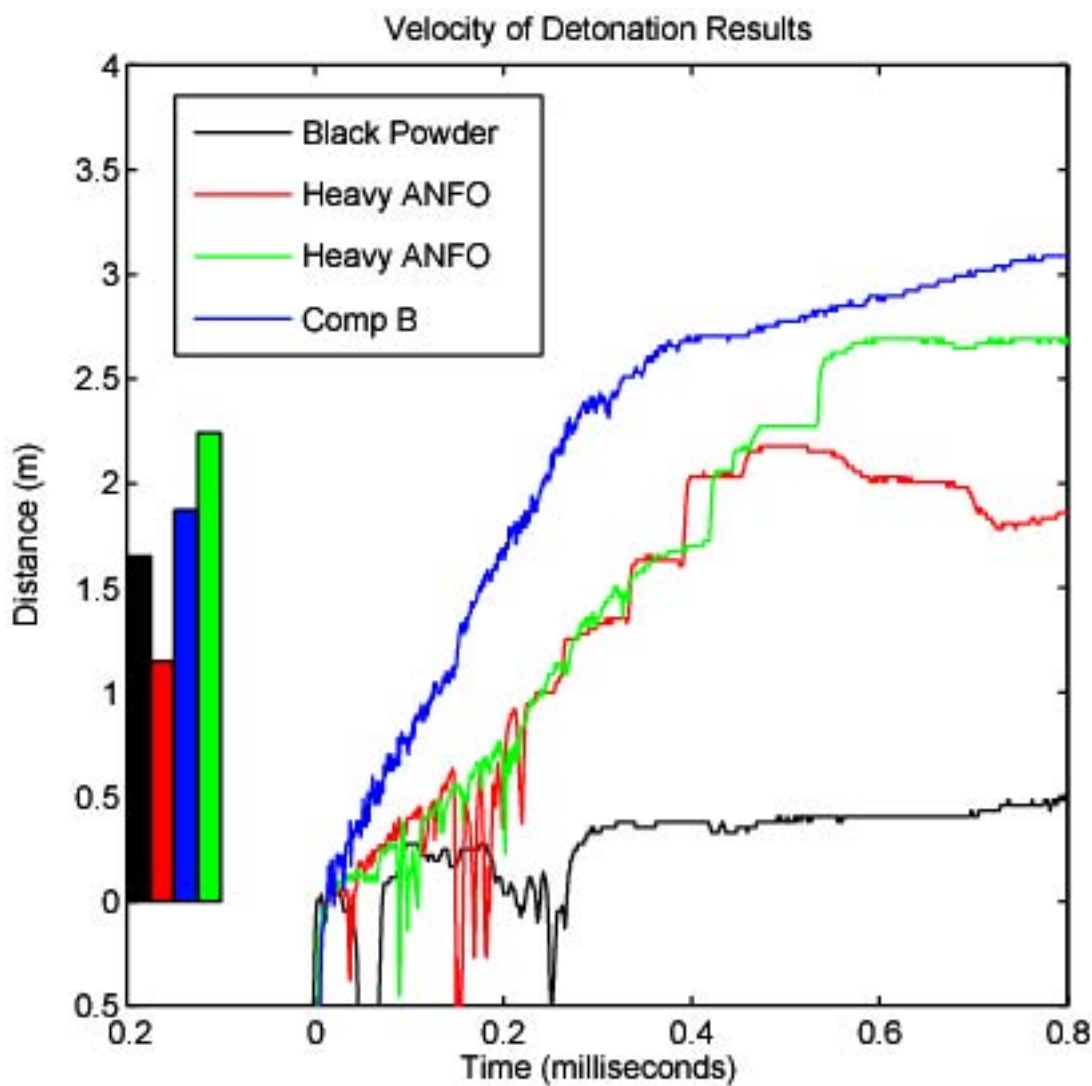
Figure 89. Velocity of detonation recordings for four of the five shots. A fifth shot was not recorded using VOD equipment. The raw VOD data were aligned so that the approximate start of the resistance wire burn was at distance=0. Also shown are the lengths of the explosives column (bars at left) which correlate well with the VOD data.

Surface damage
The explosions at similar depths of burial generated different amounts of surface fracturing that inversely correlated with the VOD. The slowest VOD shot, black powder, created the most and largest surface fractures, one of which had displacement of a couple centimeters. The heavy ANFO blasts produced numerous radial tensile fractures, including some large radial fractures with some vertical displacement. The fast VOD COMP B produced no observable surface fractures. These visual observations indicate the explosives performed as expected with the

slower VOD explosives generating longer fractures, while the damage from the fast VOD explosives was contained in a smaller region.

Seismic array

Over 140 seismic instruments, including single and three-component seismometers and three-component accelerometers, were installed to monitor the ground vibrations from the blasts. We placed sensors from within 5 m to 30 km distance from each blast. The sensors were placed in holes, directly on solid bedrock when possible, and buried to achieve coupling. In this paper, we present data from the three-component (3C) 1 Hz L4-3D and 2 Hz L22 seismometers, along with 3C 10 g TerraTek accelerometers. The accelerometers and six of the seismometers were placed within 1 km of the explosions to obtain good azimuthal recordings, while the remaining 19 seismometers were installed in two linear arrays extending to 30 km from the test site in two directions (Figure).

PEAK PARTICLE VELOCITY

The U.S. Bureau of Mines (USBM) sets limitations on vibrations from blasting to prevent damage to structures and annoyance of nearby land owners. PPV was determined to be the most appropriate measure of vibration instead of acceleration or displacement for limiting structural damage (Siskind et al., 1980). Siskind et al. (1980) examined damage to structures from various vibration levels and found that lower frequency energy produced more damage. Therefore, they proposed a PPV limit that is frequency dependent. Above 40 Hz, the limit is 2.0 in/sec (50.8 mm/sec) and between 4 and 15 Hz, the limit is 0.75 in/sec (19 mm/sec) for modern construction. Between these PPV limits, they recommend not exceeding a PPV corresponding to a displacement of 0.008 in (0.2 mm). Below 4 Hz, the limits are even stricter and vibrations corresponding to 0.03 in (0.76 mm) displacement should not be exceeded.

The PPV with distance from a blast can be approximated using a power law equation (Bollinger, 1971, Dowding, 1985):

$$PPV = K \times SD^A \tag{4}$$

where K and A are site constants. K is a function of the amount of energy transmitted to the source rock from the explosion. A is an attenuation term for the source rock. SD is scaled distance of the form:

$$SD = \frac{D}{\sqrt[E]{W}} \tag{5}$$

where D is distance (meters or feet), W is explosive charge weight (kg or lbs), and E is either the square root or cube root depending on the charge dimensions and distance to the explosion. The square root of charge weight is the most common method of estimating PPV and is appropriate for close-in stations when cylindrical shaped charges for surface mining are used, particularly when the ratio of the charge length to diameter is greater than 6 (Brinkman, 1987, Dowding, 1985, Elseman, 2000, Kuzu, 2008). When that ratio is less than 6 or if the explosion can be approximated by a point source, then the cube root of weight may be more appropriate as it incorporates energy considerations (Dowding, 1985). Cube root scaling may also provide more accurate predicted velocities for underground blasting (Kuzu, 2008).
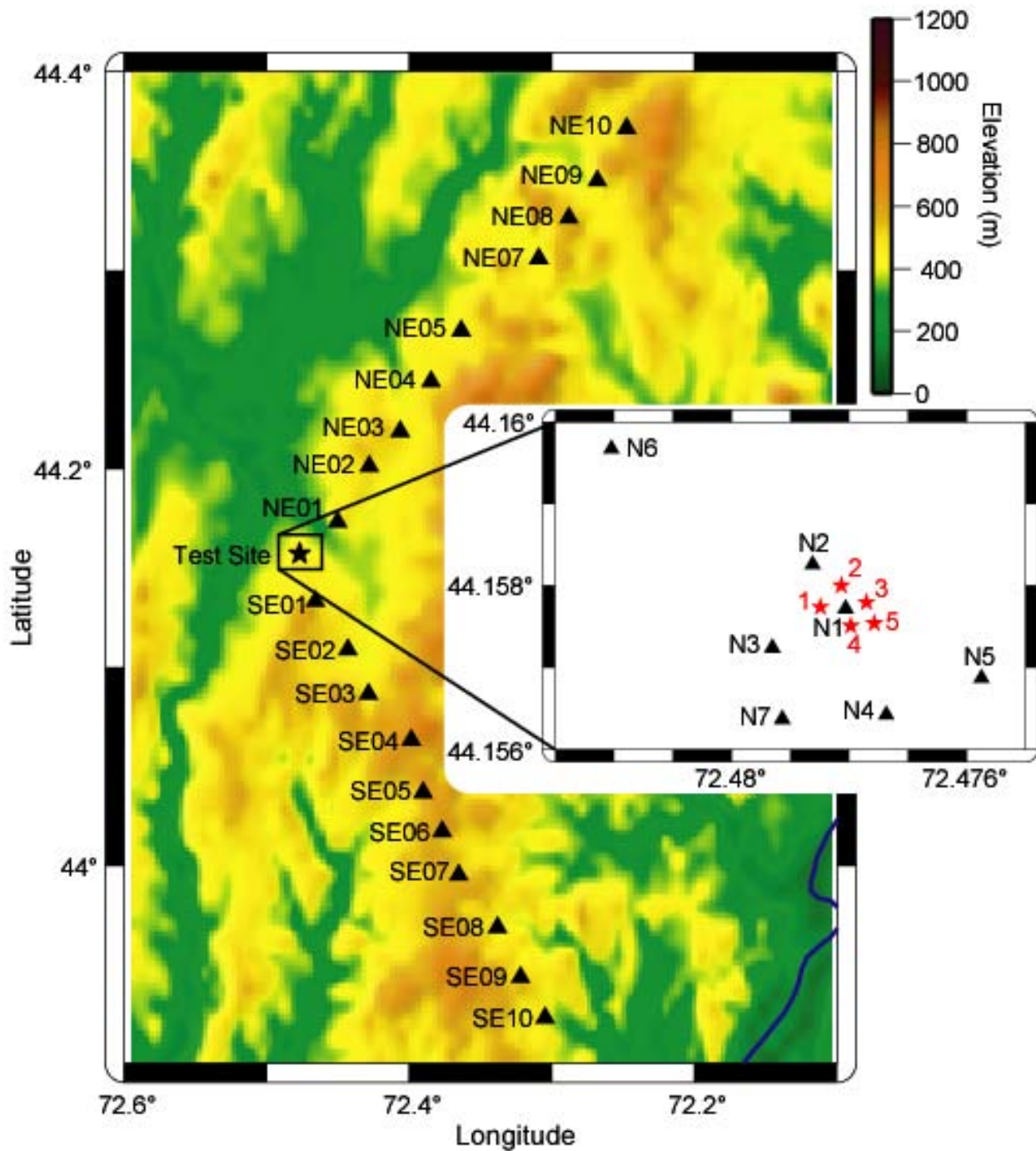
Figure 90. Location maps showing the shot locations (stars) and seismic stations (triangles) Except for station N6, stations N1-N7 comprised a seismometer and an accelerometer. Background shows topography.

The charge length to diameter ratio for each blast in our study is listed in Table 18. The smaller shots have a ratio of 4-7, while the larger shots have a ratio of 8-10. We use square root SD throughout this study, but also display the cube root SD on the figures where appropriate and

determine the *K* and *A* site constants for the 95% confidence level PPV in this region of Vermont using both calculations.

In determining the PPV from a blast, the Office of Surface Mining (OSM) only requires that the particle velocity be measured on the vertical, radial, and transverse components and the largest value used (Rosenthal and Morlock, 1987). Often, the PPV does not occur along one of the three orthogonal components of a seismic sensor, though. A true vector summation (Equation 6) provides a more accurate measurement of particle velocity at each instant in time by summing the three components of motion into an amplitude vector. It should be noted that this is not the same as a maximum vector summation, where the maximum value from each of the three components, regardless of position in time, are summed. In vector summation, the summation is calculated for each time sample, and the PPV is determined by the largest amplitude in the entire summed waveform.

$$\text{Composite Velocity} = \sqrt{Z^2 + R^2 + T^2} \qquad\qquad \textbf{(6)}$$

In this study, the empirical PPV were calculated by using both the OSM requirement method and by performing a vector summation. The vector summation provides a more conservative estimate of PPV than either the OSM method or using a single, vertical component, as has been done in some empirical studies.

Particle velocities from different explosives
In this analysis, we fit the power law equation (Equation 4) to the observed PPV data recorded at distances of 5 m to 30 km. Over such a large distance, the blast energy propagates through rock with varying physical properties, such as attenuation. Therefore, we do not propose that the *K* and *A* constants determined in this section are representative of Barre granite, particularly since not all sensors were placed in the Barre granite. Instead, we present this data to quantify the differences in PPV from the different explosives. In section 2.2, we use only the stations located in the Barre granite to calculate *K* and *A* site constants for blasting in the Barre granite.

It is valid to use PPV data from the full seismic array in this analysis since we are only comparing the relative values of the constants for the different shots. The reason is that the shots were nearly co-located and were recorded by the same seismic sensors. Therefore, each seismic signal was affected by the same travel path, i.e., same rock units, and has the exact same receiver response at each station. If a blast generates a larger PPV near the source than other blasts, the energy will undergo the same modifications, geometric spreading, attenuation, phase conversions, reflections, refractions, etc. before it is recorded at the receiver and will still have a larger PPV than the other blasts. The only difference in the recorded waveforms will be a function of the difference in the source.

The PPV were determined at each station for each shot using the vector summation and OSM methods and are plotted in Figure . The data for each shot were fit by a least squares power law regression (Equation 4) and the optimum equations are shown in the legend of Figure . The borehole diameter was the same for each shot, and the depths to the top of the explosive column were the same for shots 2 and 3 and for shots 4 and 5. Therefore, the only variable when comparing shots of similar size, excluding the different depth of shot 1, is the explosive used.
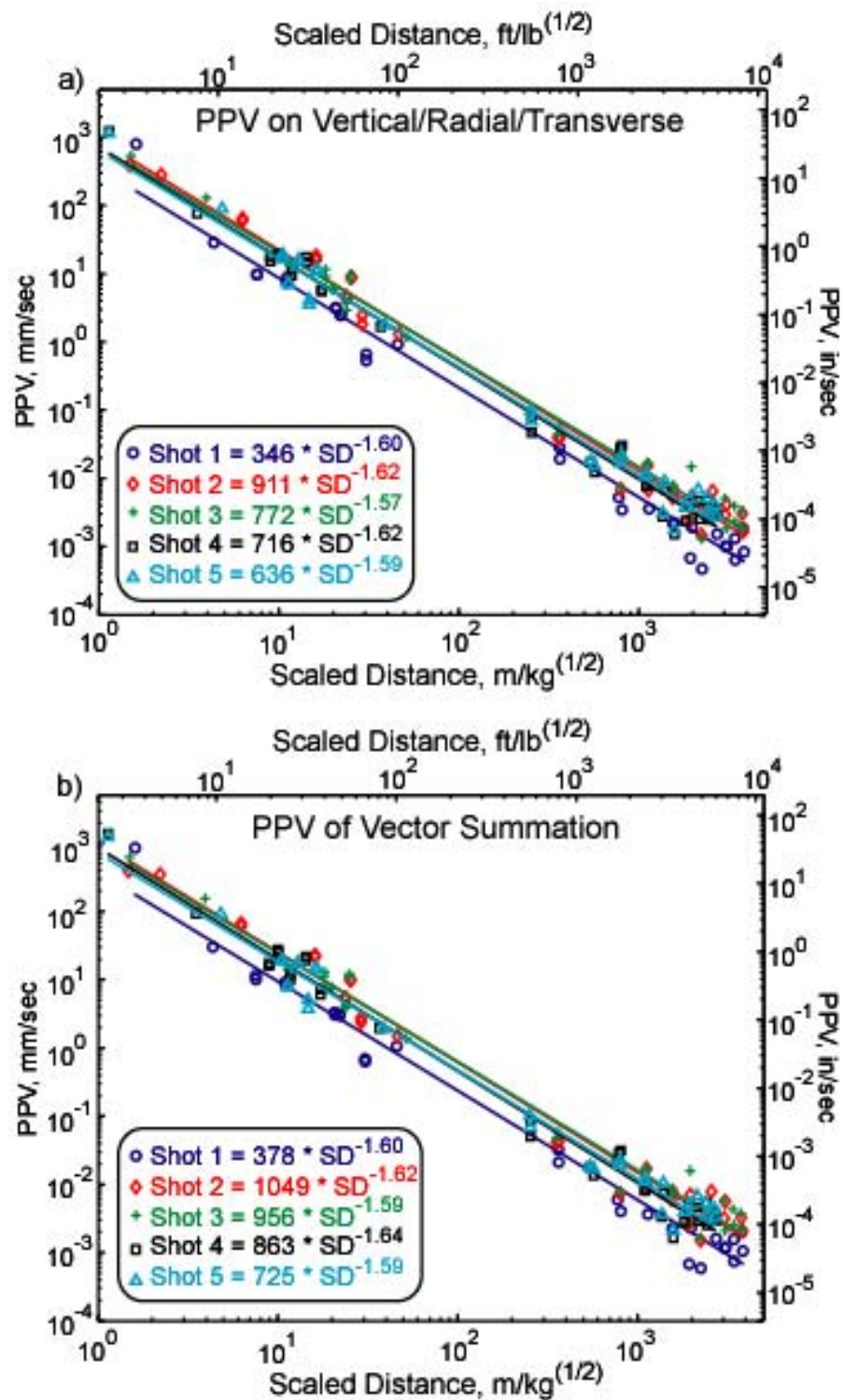
Figure 91. Plots of PPV by shot from a) the maximum of the vertical/radial/transverse components (OSM method) and b) the maximum of vector summation technique. The best fitting power law curves for each shot are shown in the legend.

The slow VOD black powder shot (Shot 1) produced smaller PPV as a function of SD compared to the similar sized heavy ANFO and COMP B high explosives. The black powder *K* is approximately one-third of that for the similarly-sized heavy ANFO and COMP B values. It is unlikely that the difference in explosive depth could be responsible for such a large variation in *K*, but regardless, the difference in depth makes the black powder results uncertain. The best fitting regression lines indicate that the mean PPV values for the heavy ANFO explosives were slightly larger than for the similarly-sized COMP B explosives. The attenuation coefficients (*A*) for all shots are very similar to the standard of -1.6 for low attenuation rock.

The difference in the *K* values for the heavy ANFO and COMP B explosives seems to support the findings that a faster VOD explosive expends more energy to pulverize the rock around the blast and thereby relatively less energy is transmitted away from the source. The *K* values for shots 2 (Heavy ANFO) and 3 (COMP B) are larger than the respective *K* values from the larger blasts, shots 4 (Heavy ANFO) and 5 (COMP B). The top of the explosive columns were 1 m shallower for shots 2 and 3, but they have a deeper scaled depth of burial (SDOB), the ratio of depth to shot size. More research is needed to understand which factor is responsible for the larger *K* values.

Predicting PPV for safe blasting in the Barre granite
In order to ensure a blast will not exceed vibration limits, *K* and *A* in Equation 4 need to be determined such that 95% of the observed PPV measurements fall below the predicted vibration level as required by regulations (Dowding, 1985). The PPV from the four high explosive (heavy ANFO and COMP B) shots recorded on the 3C seismometers and accelerometers installed less than 1 km from the shots were combined to empirically determine the *K* and *A* constants for the Barre granite that define a 95% confidence level. We chose not to include the seismometers along the linear arrays out to 30 km, as in this case, the travel path and receiver site response will affect the empirical site constants. For this portion of the study, all sensors were located within the Barre granite. The black powder data was not used in the calculation because the observed PPV were much lower than those from the high explosives, and black powder is not an often used modern day commercial explosive.

The *K* and *A* constants for both square root and cube root SD and for both the OSM (Figure) and vector summation (Figure) methods were determined. The square root and cube root SD *K* values are reasonable compared to other empirically-determined values and indicate the explosives were over buried (Kuzu, 2008, Brinkman, 1987). It is apparent that the method of using the largest PPV from the three orthogonal components (Figure) underestimates the true PPV, as the *K* value is approximately 10% lower than the *K* value from the vector summation (Figure). The empirical values determined are only valid for the depth range of explosive emplacement shown in Table 18, as we note that varying the depth of explosive emplacement can have a significant effect on PPV. In addition, the observed PPV can increase for structures situated on low seismic velocity material, such as loosely consolidated sediment.
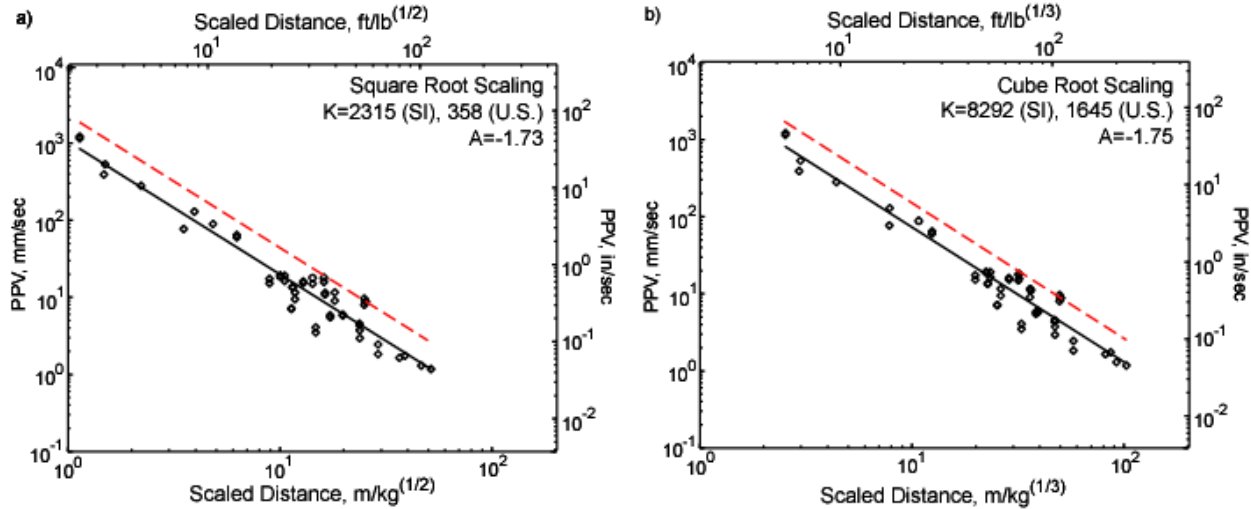
Figure 92. PPV versus scaled distance for a) square root and b) cube root scaling using the OSM method. The least squares regression mean (solid line) and 95% confidence curve (dashed line) are shown with the _K_ and _A_ values for the 95% confidence power law equation curve.
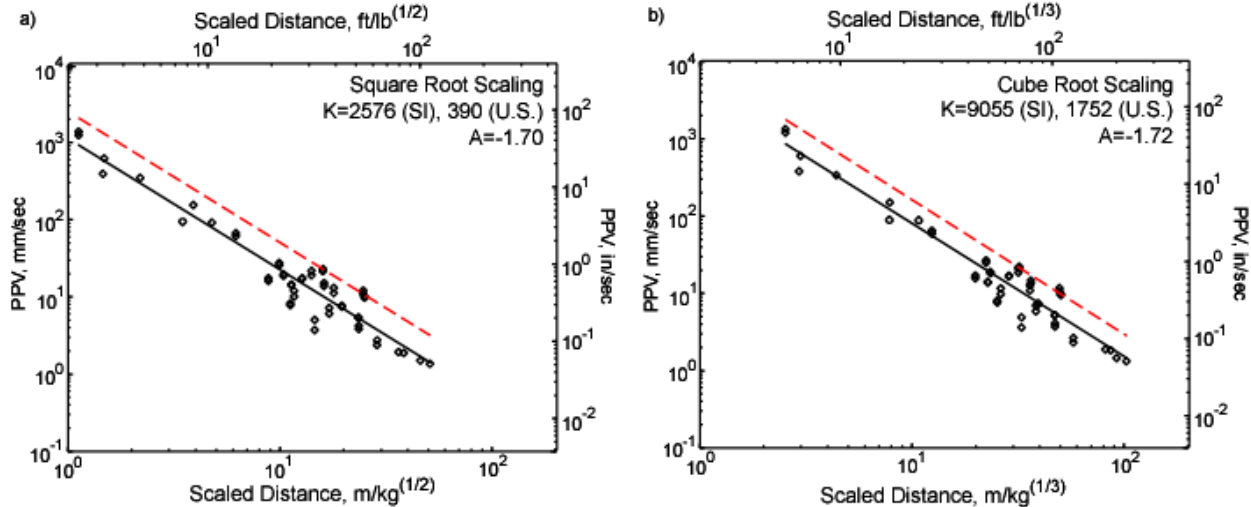
Figure 93. PPV versus scaled distance for a) square root and b) cube root scaling using the vector summation technique. The least squares regression mean (solid line) and 95% confidence curve (dashed line) are shown with the _K_ and _A_ values for the 95% confidence power law equation curve.

Spectral analyses

Explosions generate both body and surface waves. The body waves dive into the earth and typically have the largest amplitudes in the frequency range greater than ~6 Hz. The surface waves travel along the surface of the earth and are composed primarily of energy in the frequency range below ~6 Hz. The USBM vibration limits are reduced between 4 and 10 Hz and lowered even further below 4 Hz, as it is low frequency waves that can do the most damage to structures. According to Siskind (1980), frequencies <10 Hz generate large displacements and couple well into structures, which typically have resonant frequencies between 4 and 12 Hz.

135

Therefore, it is critical to not only understand the expected PPV, but also the frequency band in which the PPV occurs.

An examination of the shot spectra allows determination of the PPV frequency for each type of explosive and scaled distance. Figure shows the spectral content and waveforms of the vertical component of station N3 (Figure) at scaled distances of 10-18 m/kg$^{0.5}$. The five shots reach their peak amplitude between 25 and 50 Hz and the amplitudes generally remain high throughout this frequency range. For station N6 with a SD of 37-52 m/kg$^{0.5}$, the seismic energy peaks near 20 Hz, but is elevated in a range of 10 to 20 Hz (Figure). At a distance of 3 km from the blasts, station SE01, the body waves have attenuated and the surface waves have begun to dominate the seismic signature and the spectral amplitude peak has decreased to 4-8 Hz. By 6 km, the peak frequency occurs at 4 Hz (Figure). A second peak lies in the 20-40 Hz range and is related to the arrival of the body waves. The body waves arrive at 1 second in the waveforms of Figure , while the low frequency surface waves arrive at about 2.3 seconds. Although the SD for this shot is very large, a large mining blast will have a greatly reduced SD, but the PPV frequency will remain near 4 Hz. The decrease in the frequency of the peak amplitude illustrates how the frequency range of interest for PPV calculation shifts from higher frequencies to lower frequencies, where the USBM PPV limits are substantially reduced, with increasing distance.
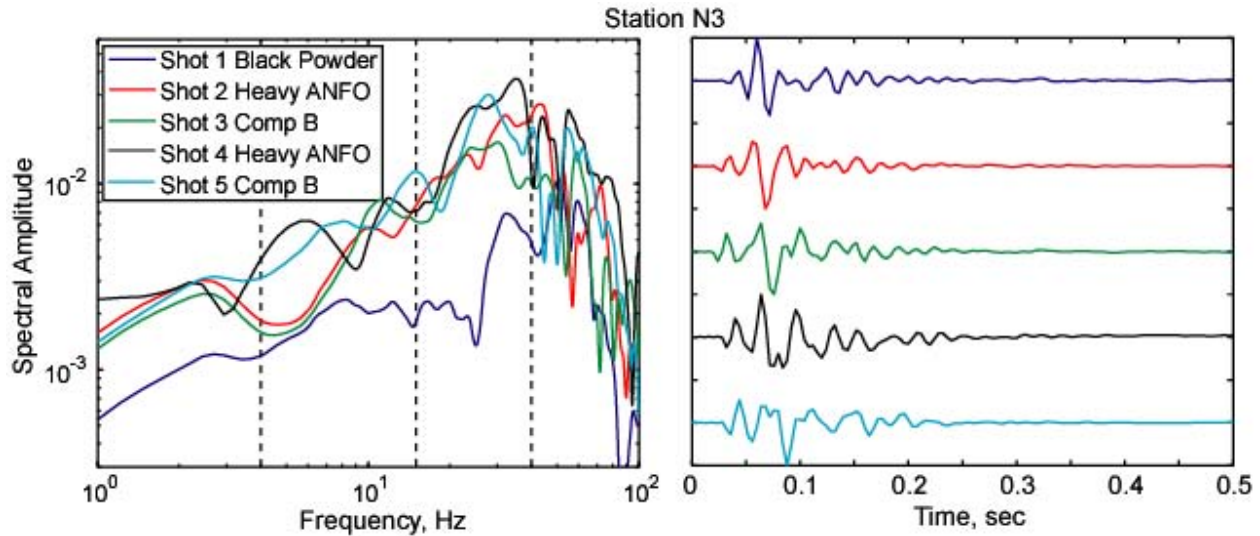
Figure 94. Spectral amplitudes of the five explosions (left) recorded on the vertical component of station N3 (shots 1-3 SD≈15 m/kg$^{0.5}$, shots 4-5 SD≈11 m/kg$^{0.5}$). The vertical dashed lines delineate the different USBM vibration limit frequency ranges. On the right are the seismic waveforms recorded for each shot at station N3.
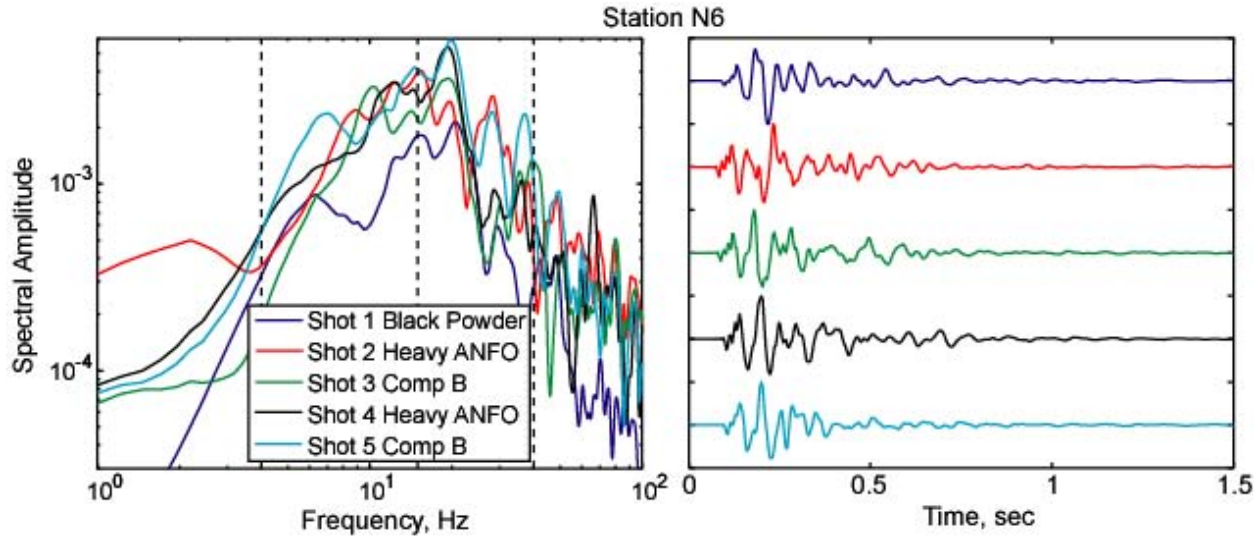
Figure 95. Spectral amplitudes of the five explosions (left) recorded on the vertical component of station N6 (shots 1-3 SD≈48 m/kg$^{0.5}$, shots 4-5 SD≈37 m/kg$^{0.5}$). The vertical dashed lines delineate the different USBM vibration limit frequency ranges. On the right are the seismic waveforms recorded for each shot at station N6.
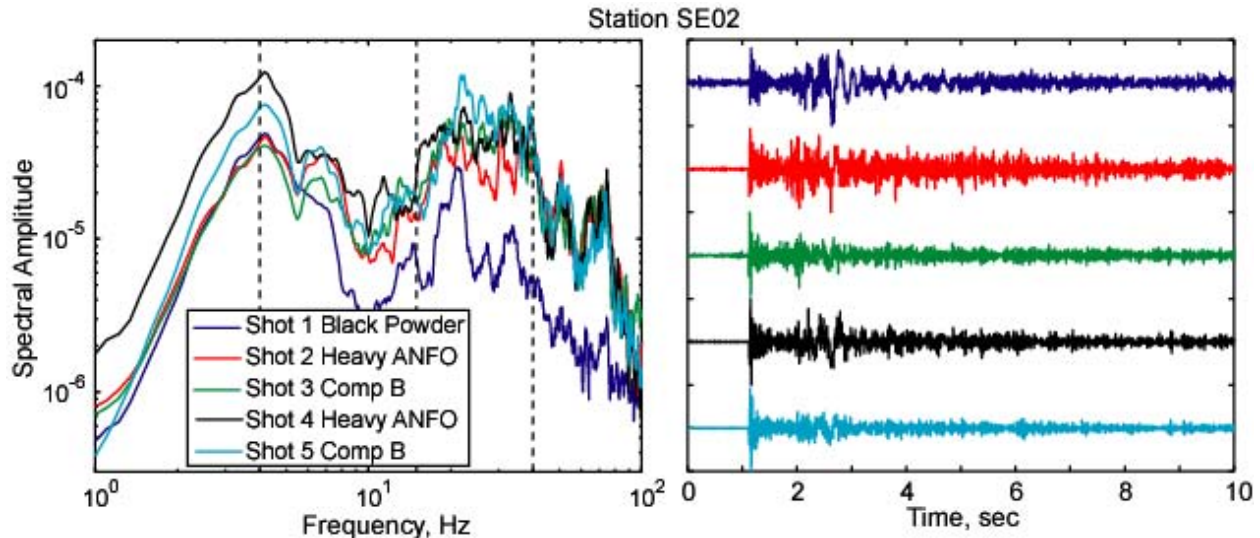
Figure 96. Spectral amplitudes of the five explosions (left) recorded on the vertical component of station SE02 (shots 1-3 SD≈770 m/kg$^{0.5}$, shots 4-5 SD≈540 m/kg$^{0.5}$). The vertical dashed lines delineate the different USBM vibration limit frequency ranges. On the right are the seismic waveforms recorded for each shot at station SE02.

To highlight the spectral differences in the explosives, we examined the source spectral ratios. The spectrum from an individual explosion is represented as:

$$U_{kij}(f) = R_{ki}(f) \times P_{kij}(f) \times S_j(f) \tag{7}$$

where $U_{kij}(f)$ is the spectrum of the kth component (1- vertical, 2- radial, 3- transverse) at the ith receiver from the jth source; $R_{ki}(f)$ is the receiver function for the ith receiver and is the same for

137

each source; $P_{kij}(f)$ is the regional propagation path effect; and $S_j(f)$ is the source function for the jth explosion.

For each receiver, $R_{ki}(f)$ remains constant and $P_{kij}(f)$ is assumed to be identical for each source since all sources are nearly co-located, and thus taking the ratio of $U_{kij}(f)$ for two different sources recorded at the same station eliminates the local receiver effect and regional propagation path contributions, retaining only the ratio of the two source functions.

$$\frac{U_{ki1}(f)}{U_{ki2}(f)} = \frac{R_{ki}(f) \times P_{ki1}(f) \times S_1(f)}{R_{ki}(f) \times P_{ki2}(f) \times S_2(f)} = \frac{S_1(f)}{S_2(f)} \tag{8}$$

What remains is the frequency-dependent source scaling relation for the explosion source function. Averaging over individual components for all receivers produces average source estimates. Stump *et al*. (1999) provides a detailed discussion of this approach.

The vertical and transverse component spectral ratios for our blasts are presented in Figure . It is interesting that the black powder and heavy ANFO shots produced the same amount of energy below 6 Hz on both components, while the fast VOD COMP B shot produced ~60% less. Above 6 Hz, the heavy ANFO and COMP B shots produced similar amounts of energy, while the black powder shot amplitudes were greatly reduced. This indicates that the slow VOD black powder shot generated increased surface wave energy while the faster VOD explosives produced significantly more body wave energy. The medium VOD heavy ANFO was rich in both surface and body wave generation. These results can also be observed in the waveforms of Figure .
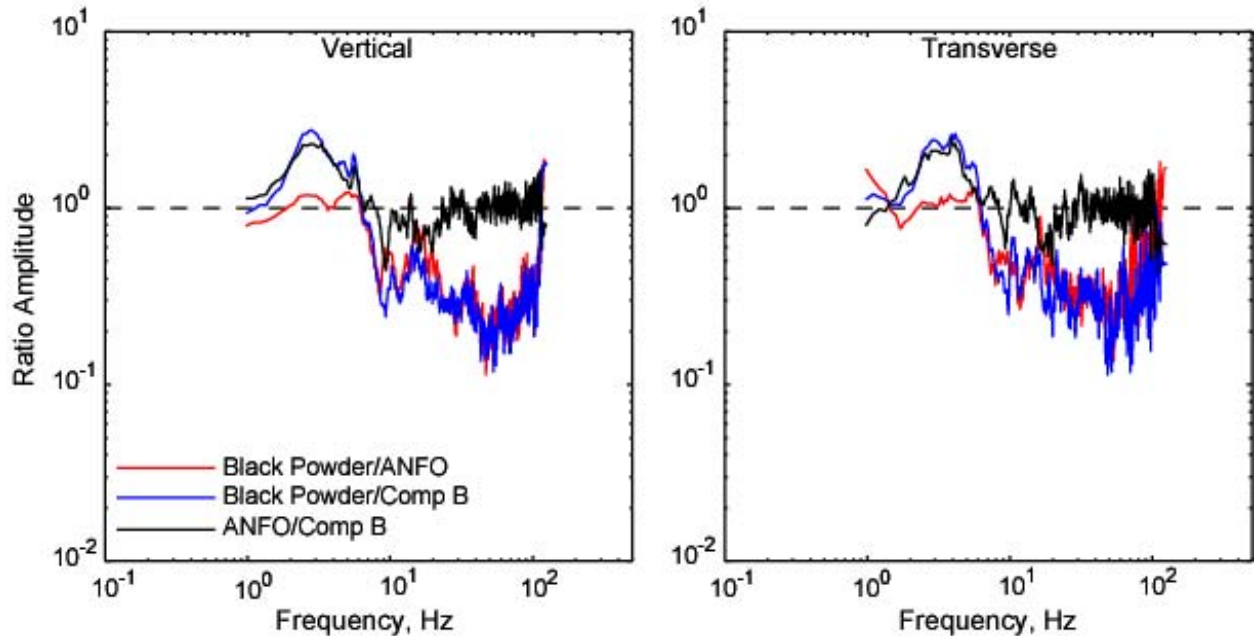
Figure 97. Source spectral ratios for the three 61 kg explosions. They show the increased <6 Hz energy for the heavy ANFO and black powder shots compared to the fast VOD COMP B and the reduced >6 Hz energy for the black powder shot compared to the high explosive shots.

138

CONCLUSIONS

We detonated five explosions in the Barre granite of central Vermont and recorded the seismic signals on a large array of seismometers from 5 m to 30 km distance. The explosive borehole pressure is a function of explosive VOD, and we detonated three types of explosives to vary the types of damage generated to understand the effects on PPV and surface wave generation.

The PPV data indicate that heavy ANFO produces larger ground vibrations than Composition B. The higher borehole pressures caused by the fast VOD of the COMP B pulverized the rock more extensively around the blast. Up to 50% of the energy from fast VOD explosives can be wasted generating fragmentation of the rock in the crushed zone (Melnikov, 1962). The black powder PPV vibrations are considerably lower than the vibrations for either of the high explosives because the energy is generated over a longer time span. The relatively long duration blast for the black powder caused a deficiency in high frequency energy, while opening the long fractures accentuated the low frequency energy. The COMP B shots were deficient in low frequency energy compared to the other shots likely because the explosive gases were unable to drive the long fractures.

The frequency of the PPV decreases with distance as the body waves attenuate. The USBM vibration limits decrease at lower frequencies making the understanding of the surface waves generated by blasting more important, particularly for very large blasts, which will approach the vibration limits at greater distances. Vector summation provides a more accurate measure of PPV and a level of conservatism in comparison to many prior empirical studies of ground vibration. An empirical formula was developed to predict the PPV for blasting high explosives in the Barre granite. The values indicate the granites of central Vermont have low attenuation and that the *K* value with square root SD will estimate the PPV of a well confined blast with 95% confidence.

5. ROCK DAMAGE ANALYSES

The Rock of Ages granite quarry was selected for the explosion study because the Barre Granite is homogeneous with a low fracture density. Although the granite at the site selected is massive with a very low fracture density, it is anisotropic. The anisotropy is a direct result of the rift plane common in most granites. The rift plane is due to the consistent orientation of microcracks. Mineral alignment may also play a small role in the existence of this anisotropy in rock properties. The orientation of the rift at the quarry is well documented and varies between 30° to 60° (Engelder *et al*., 1977). At the test site, the range of variability in the rift was much smaller, consistently at or near 30°. An examination of the quarry faces in the nearby open pits southeast of the test site show well developed working faces at 30°.

Although widely spaced, visible fractures were observed on all quarry faces. At the site selected for this study, the outcrop fracture spacing was 4 to 5 m. The fractures are typically clean and planar with very little brecciation. In a few cases, the fractures appear healed with indications of small scale slip.

The Barre Granite is gray fine to medium grained granodiorite. A photomicrograph of the Barre granite is shown in Figure . The composition of the granite is microcline (21%), orthoclase (35%), quartz (27%), biotite (9%), muscovite (6%) with various accessory minerals (VT Geological Society, web 2008). The composition of the granite is uniform throughout the test site (Richter, 1987).
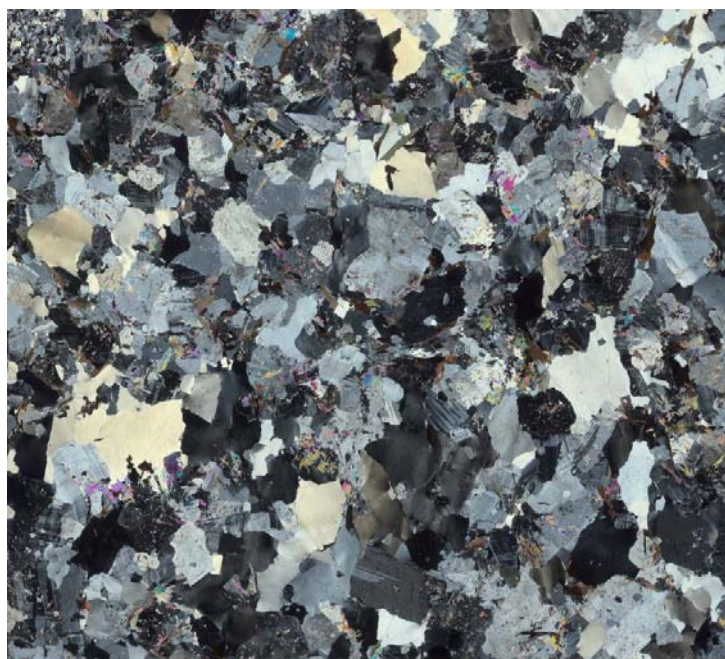
Figure 98. Photomicrograph of a Barre Granite thin section taken at a depth of 46.5 ft (14.2 m) in the CH-1 core. Photo taken with polarized light. The plane of the section is perpendicular to the rift plane.

To determine the effects of the explosions, coreholes were drilled near selected shot holes before and after the detonation of the explosives to thoroughly study the macroscopic and microscopic changes in the core. Two control holes were cored adjacent to the emplacement holes for Shots 2 and 5, (see Table 9 and Chapter 2 for information). Subsequent to the detonations, three additional holes were cored. One post-shot corehole was adjacent to the 61.5 kg Heavy ANFO shot and two were cored adjacent to the two 122 kg shots.

During this phase of the project, core was collected, documented, and analyzed in the New England Research (NER) labs. There was complete core recovery from the two pre-shot coreholes, and very few native fractures were apparent in them. Post-blast core recovery provided a nearly continuous core record, but the core was fragmented and recovery was not complete near the blast intervals. The cored intervals above the blast emplacements had varying degrees of fragmentation compared to the intact pre-shot core. Importantly, there were no large scale induced fractures observed below any of the shot points. Some of these elements are observed in Figure , which compares the pre-shot core from CH-1 with the post-shot core from the adjacent CH-3 corehole.

Figure 99. Comparison between cores recovered from the pre-shot and post-shot coreholes adjacent to Shot 2. The explosives emplacement interval was from 33.14 ft to 37.08 ft (10.1 m to 11.3 m).

Figure   shows an interesting feature observed in the post-shot cores, blast induced disking fragmentation. It developed over a 1.8 m interval in this corehole. In addition, visual observation of the post-shot cores showed gross changes in appearance near the working point. The native rock is bluish gray, while the rock recovered near the blasts is lighter in color than the rock away the working point. The change in appearance is likely due to shattering or crushing of the grains. Further characterization of this observation requires thin section, SEM, and pore structure modeling analysis.

Figure 100. Core disking at 41 ft (12.5 m) depth in CH-4. This corehole is adjacent to Shot 5, which had an explosives emplacement interval between 39.04 ft and 44.95 ft (11.9 m to 13.7 m).

As part of the pre-shot site characterization, a borehole geophysical logging program was undertaken by Hager-Richter Geoscience, Inc. to provide additional details of the nature of the undisturbed granite. Oriented acoustic televiewer logs, optical televiewer logs, and caliper logs were run. The logs verify that there are few fractures in the undisturbed granite. An example of a fracture identifiable in the logs recorded in CH-1 is shown in Figure . As the logs were oriented with respect to magnetic North, they were also valuable in that they allowed for an accurate orientation of the rift plane (as identified by ultrasonic velocity laboratory methods) with respect to fractures. That orientation coincides with the surface observations and reference publications.
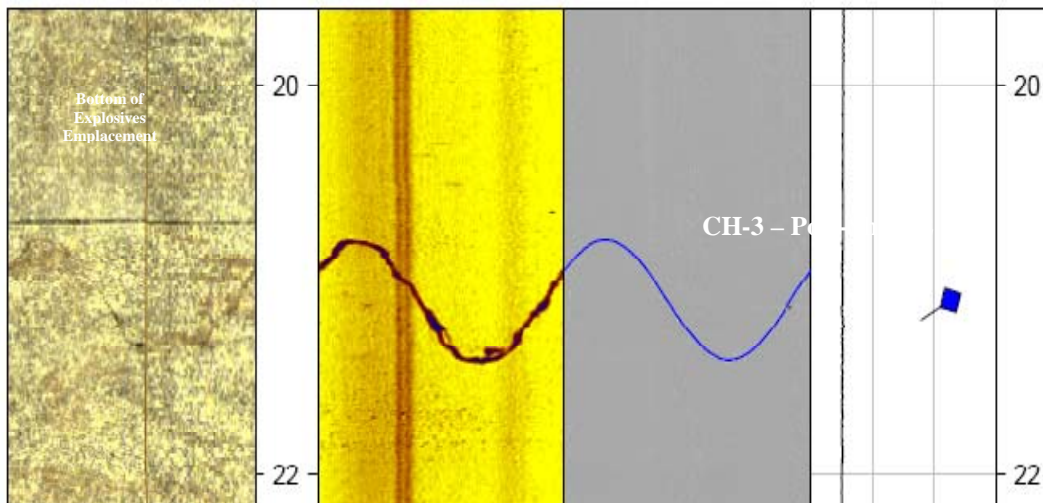
Figure 101. Example of fracture identified by Hager-Richter borehole log run in CH-1. Left to right: Optical Televiewer, Acoustic Televiewer, Fracture outline on borehole wall and tadpole plot showing orientation and dip of fracture. Depths are shown in feet.

Laboratory testing has included extensive velocity measurements to identify the orientation of the rift plane along the length of the core. Continuous linear velocity scans of some of the core, permeability and electrical resistivity measurements at elevated hydrostatic pressures, grain and bulk density determinations, porosity calculations, and thin section preparation complete the suite of tests. All measurements were performed as a function of orientation relative to the rift

plane. The most detailed characterization was undertaken for the pre-shot CH-1 and post-shot CH-3 coreholes to provide initial comparisons between the two conditions.

The Barre granite is mineralogically homogeneous over a wide area. Little variability in bulk density, and especially grain density was observed, so limited measurements were carried out on the pre-shot specimens. Representative data are presented in Table 19. The data show the small variability in the undisturbed cores. There is however, a clear reduction in density (with respective increase in porosity) within the blast impacted interval in CH-3. This change is attributable to an increase in the size and density of microcracks within these otherwise intact core samples.

Table 19. Bulk Properties of the Borehole Core.

Bulk Properties

CH-1: Pre-Shot					CH-3: Post-Shot		
Sample Depth (m)	Dry Bulk Density (g/cm^3)	Grain Density (g/cm^3)	Porosity via Grain Density (%)		Sample Depth (m)	Dry Bulk Density (g/cm^3)	Porosity via Grain Density (%)
0.076	x	2.658	x		3.911	2.64	1.0
0.737	2.63	x	1.2		4.927	2.64	1.0
0.787	2.64	x	1.0		4.978	2.64	0.8
0.838	2.64	x	1.1		5.029	2.65	0.7
1.45	x	2.660	x		7.848	2.64	1.0
2.95	x	2.674	x		8.001	2.64	1.0
3.58	x	2.670	x		8.153	2.64	0.9
5.26	x	2.673	x	Explosive	10.566	2.63	1.4
7.14	x	2.674	x	Interval	10.617	2.61	2.0
7.848	2.64	x	1.0		10.667	2.60	2.5
7.886	2.64	x	1.0		11.023	2.63	1.2
7.937	2.63	x	1.3		12.395	2.64	0.9
8.05	x	2.663	x		12.445	2.64	0.9
9.24	x	2.655	x		12.496	2.64	0.9
11.05	x	2.660	x		14.731	2.63	1.2
13.03	x	2.675	x		14.782	2.64	0.8
14.15	x	2.667	x		14.833	2.64	1.0
15.696	2.64	x	1.0		16.052	2.64	0.9
15.747	2.65	x	0.8		16.128	2.64	0.9
15.785	2.65	x	0.5		16.179	2.64	0.9
15.81	x	2.664	x		16.230	2.64	0.8
16.81	x	2.662	x				
18.36	x	2.663	x				

Ambient condition velocity measurements were performed by transmitting ultrasonic compressional and shear waves through diametral chords in the recovered core. The cores were rotated between the velocity transducers, and data were collected, until the acoustically fastest chord was identified. The "Fast" chord was determined to lie within the rift plane, and the chord oriented at 90° to it is always the "Slow" direction. Identifying the orientation of the rift in all of

the cores allows for proper handling while performing other rock properties testing. Those data were also valuable in characterizing the vertical variability in velocity.

The velocities measured on the core recovered from the pre-shot coreholes produced consistent data as shown in Figure . The "Fast" (parallel to rift plane) compressional velocities increased with depth. This is a subtle trend that persists over the entire site. There is no evidence of density contrast that would explain this observation, although bulk property measurements are incomplete. The compressional velocities of the intact core ranged from 3,400 to 4,800 m/sec. The compressional velocities from the CH-2 are somewhat greater at equivalent depths than the velocities of CH-1.

Pre-Shot
Fast P-Wave Velocities
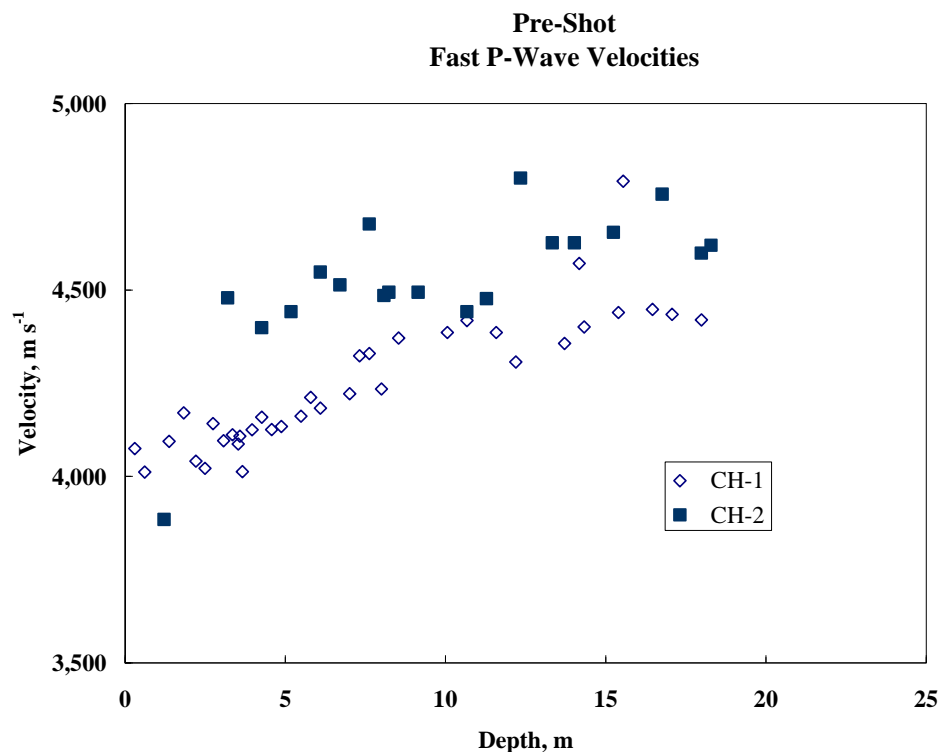
Figure 102. Summary plots of velocity data from the two pre-shot coreholes.

Velocity measurements were also carried out on intact sections of core recovered from post-shot coreholes CH-3, 4, and 5. The coreholes were adjacent the 61.5 kg heavy ANFO, the 122 kg comp B, and the 122 kg heavy ANFO shots, respectively. Figure through Figure show comparisons of pre- and post-shot compressional wave velocities as a function of depth from the corehole in proximity to the 61.5 kg heavy ANFO shot. Open red diamonds show the pre-shot data, while solid green diamonds show the post-shot velocities. For reference, the centroid depth of the charge was at 10.7 m. The post-blast velocities are significantly lower near the working point. For example, "Fast" velocities of 3,300 m/sec were observed near the working point compared with the control velocities of 4,300 m/sec, a decrease of 23%. There is anomalous behavior below the working point; the post-shot velocities actually exceed the pre-shot velocities. There is no explanation for this observation at this time. Analysis of additional information, including compositional variations and densities needs to be carried out to resolve these issues.
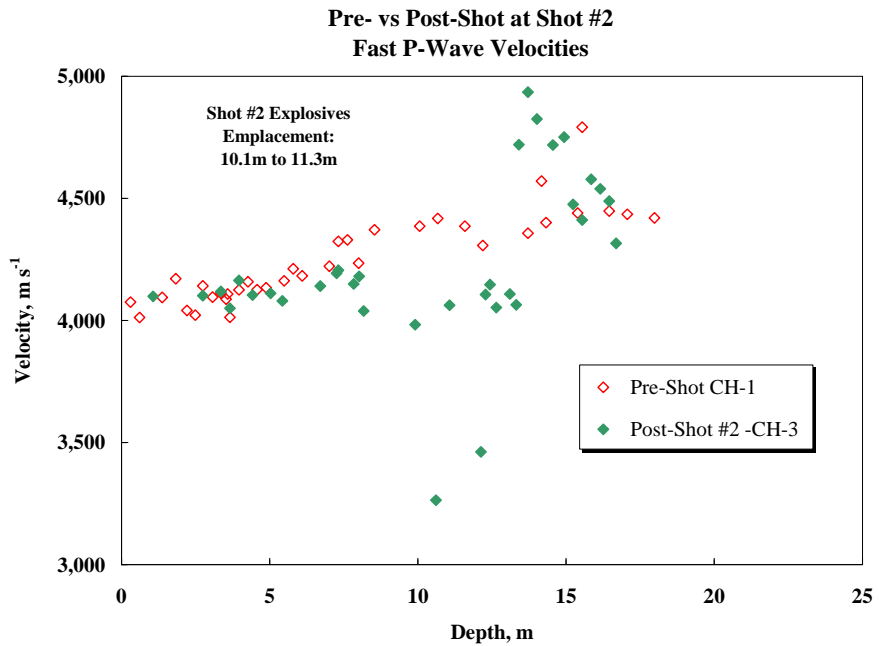
Figure 103. "Fast" compressional wave velocity vs. depth at Shot 2 location. Data from pre- and post-shot coreholes are plotted.
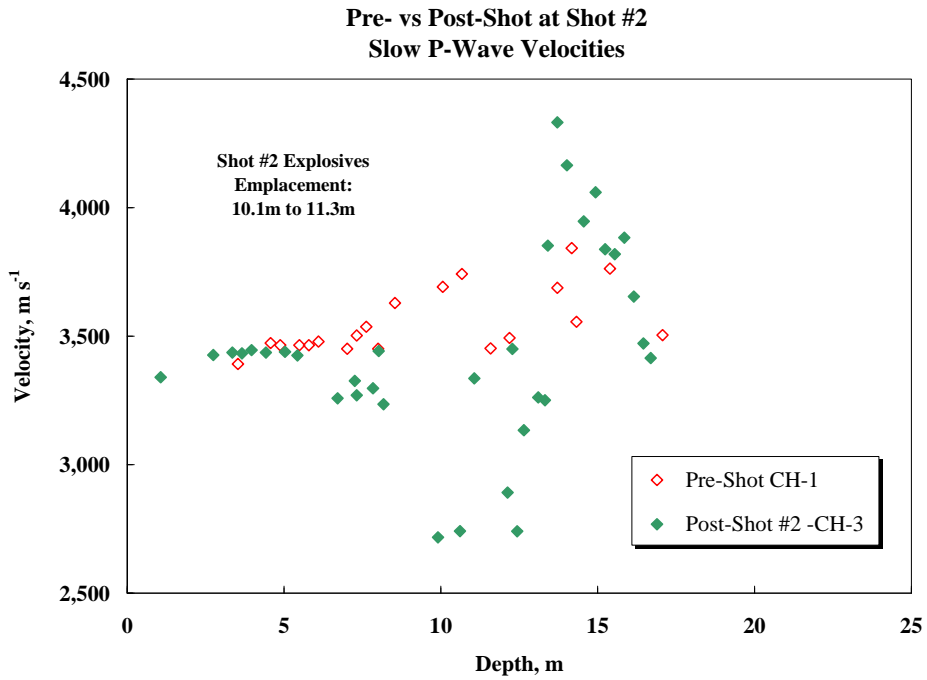

Figure 104. "Slow" compressional wave velocity vs. depth at Shot 2 location.
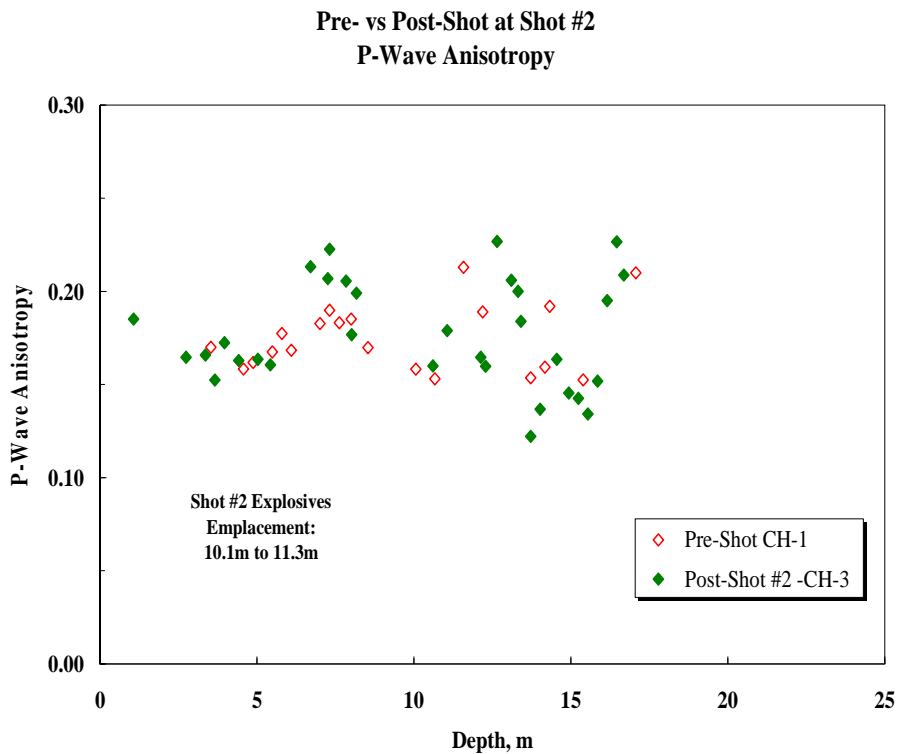
Figure 105. Compressional wave velocity anisotropy vs. depth at Shot 2 location.

In Figure , the slow P-wave velocity is shown as a function of depth for the pre- and post-blast data. The data show similar behavior to that observed for the fast direction. Although there is a pronounced decrease in velocity near the working point (up to approximately 26%), the velocity again increases abruptly near 12.25 m. This effect needs further investigation.

The *P*-wave anisotropy, the difference between the "Fast" and "Slow" *P*-wave velocities, divided by the "Fast" *P*-wave velocities, is presented as a function of depth in Figure . The anisotropy remains relatively constant, near 17%, at all depths. There is little indication that the explosion affected the anisotropy.

The velocity data from the coreholes near the 122 kg shots are shown in Figure through Figure . In each plot, the pre- and post-shot data are shown as a function of depth. The data exhibit a similar trend to that observed for the 61.5 kg shot, namely a pronounced decrease in velocity near the working point. The control data exhibit a "Fast" compressional velocity of ~4,600 m/sec. However, near the working points, the "Fast" velocity decreases to a low of 3,200 m/sec, a change of 30%. The vertical extent of the velocity decrease at these locations is significantly greater than at the 61.5 kg shot, and appears to be greatest for Shot 4. An effect similar to that for the "Fast" *P*-wave velocities is observed on the "Slow" *P*-wave velocities. The scatter at depths less than 5 m for both pre- and post-shot velocities is likely due to weathering and/or mining induced damage near the surface.

146
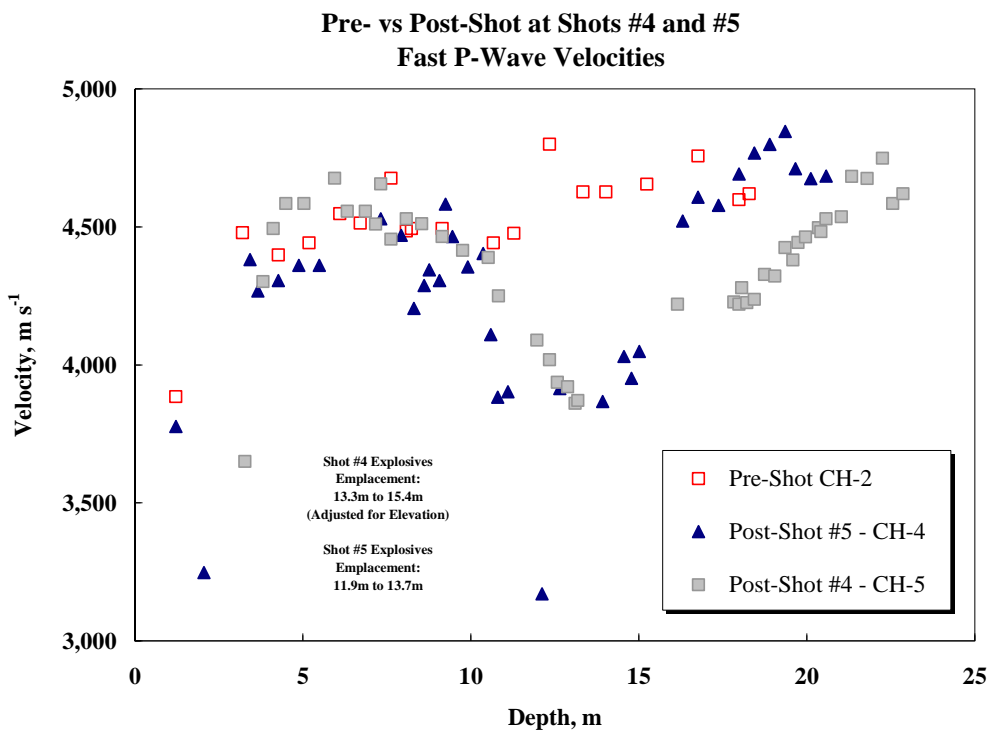
Figure 106. "Fast" compressional wave velocity vs. depth at Shots 4 and 5 locations.
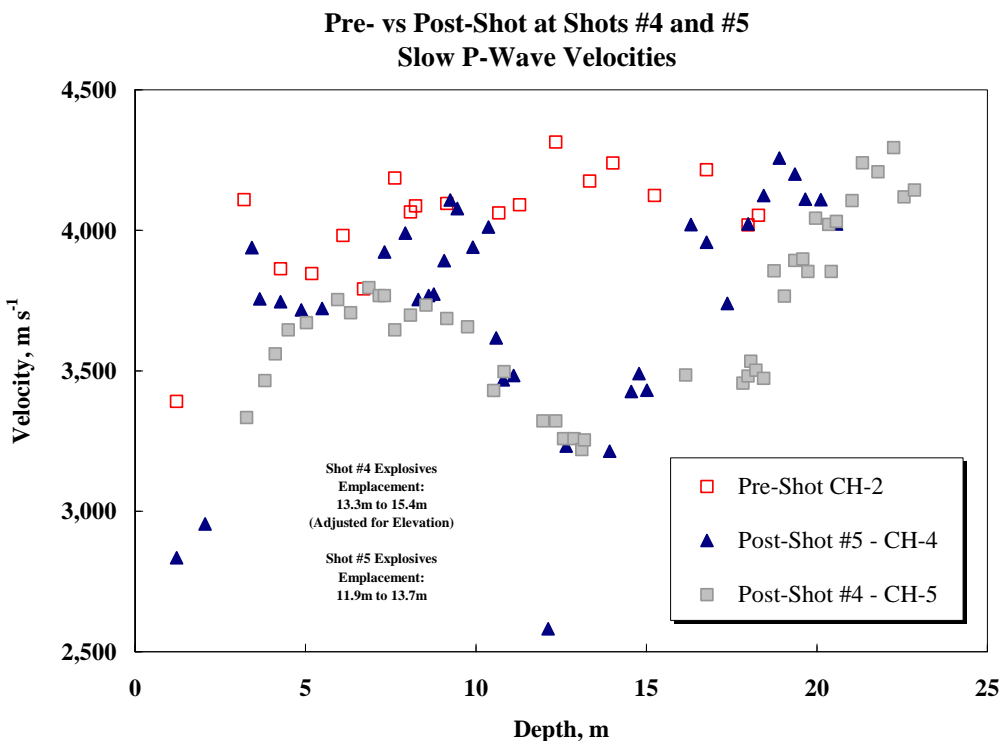

Figure 107. "Slow" compressional wave velocity vs. depth at Shots 4 and 5 locations.
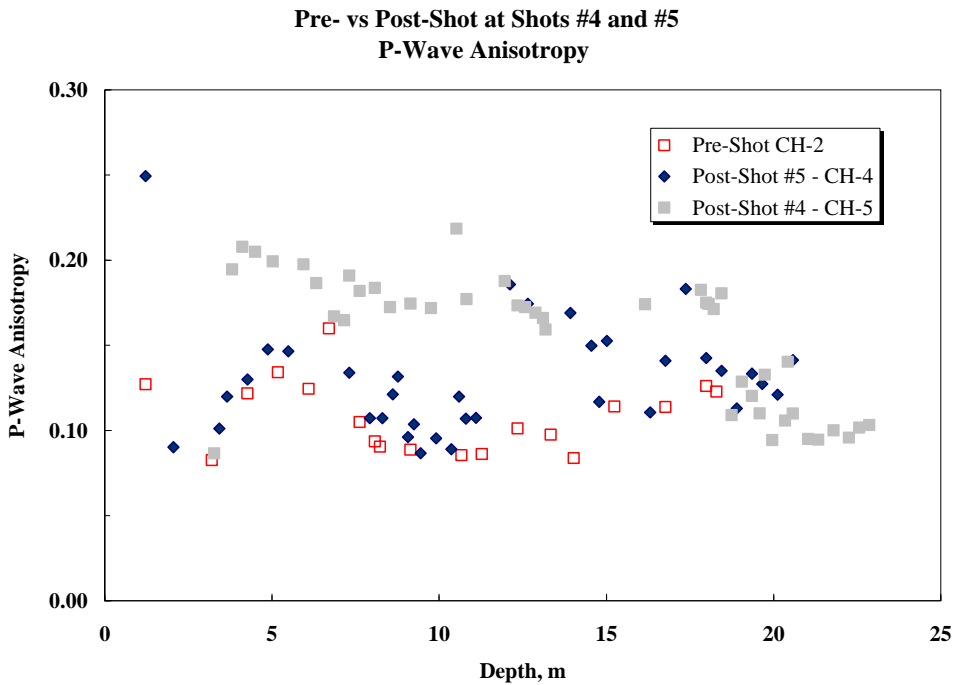
Figure 108. Compressional wave anisotropy vs. depth at Shots 4 and 5 locations.

Figure shows velocity anisotropy as a function of depth for each core. There is no definite trend in the anisotropy for either the pre- or post-shot data. The anisotropy varies between 9% and 21%. However, it is interesting to note that the anisotropy in CH-5 is generally greater than for the other cores, and it is similar to the magnitude of the anisotropy near Shot 2. CH-2 and CH-4 are adjacent to one another, and may be more directly comparable. The anisotropy does not change significantly around the explosions in any case.

After the orientation of the rift had been identified in the raw core, linear velocity scans were performed on both pre-shot cores, and on the intact portions of the core recovered from CH-3. NER's AutoScan test apparatus was utilized to continuously measure compressional and shear wave velocities along the entire axis of the cored intervals. The scans were taken with the transducers impinging on the diameter paralleling the rift plane. The velocity profiles presented by this data correspond very closely to those developed by the diametral velocity measurements.

Once the rift plane orientation was identified, permeability and resistivity measurements were performed on consistently oriented cores. Both of these properties were measured on cylindrical cores with their axes either parallel to the recovered core (vertical), parallel to the rift plane, or perpendicular to the rift plane. Although limited, these data clearly verify the anisotropy observed in the bulk core and further quantify the impact of blasting on the granite. Core samples aligned with their axis parallel to the rift plane exhibit higher permeabilities and lower resistivities than for other orientations. Post-shot cores consistently have lower resistivities and higher permeabilities within the blast impacted intervals. These results are consistent with the velocity data, and suggest blast induced enhancement of microcracks.

Thin sections have been obtained for limited intervals of the core. Although a thorough examination and characterization of them was not completed, a photomicrograph of one of them is shown in Figure . Detailed analysis of thin sections would provide additional information regarding the nature of the fabric (microcracks) that cause the rift plane, and would provide insight as to how the fabric may change due to explosive stresses. Important and very germane research in this area has previously been performed by Nasseri and Mohanty (2007), where they carefully characterized the microcracks in Barre granite, and investigated the impact the rift plane had on fracture toughness of the granite.

6. FUTURE WORK

The funding to complete this project was provided by the Air Force Research Laboratory and was only for a one-year pilot study. Most of the funds for the project were used for geotechnical characterization and data collection and only initial analyses were completed. Seismic recordings show increased low frequency energy (shear and surface waves) and decreased high frequency energy (body waves) for the slower VOD explosives in comparison to the fast VOD explosives. Physical characterization of the pre- and post-blast borehole cores found dramatic differences in the seismic velocities, permeabilities, and porosities of the rock. Damage to the rock from the blasting caused these property changes.

Unanswered questions that we hope to answer in the future include:

- What are the effects of micro- and macro-damage from explosions in granite? Can the effects be correlated to the differences in seismic characteristics of the explosions?
- What are the possible reasons for larger *S* waves observed from ANFO and Black Powder shots? Is it due to damage effects, differences in free-surface conversion of *P*-to-*S* energy, scattering effects unrelated to the explosions, or other explanations?
- What were the effective cavity and elastic radii for the different explosions? How do the observed data compare with model-based predictions for moment, cavity, and elastic radii?

Although we were not able to solve the shear wave source enigma, the data we collected contains information that may eventually provide insight to help resolve this issue. In the future, we hope to continue the analysis of these dataset, including more studies of the pre- and post-shot cores to determine:

- Bulk Properties, Density, and Porosity
- Geophysical Properties at Stress
- Fragmentation
- Identification of Damage Zones
- Pore Structure Modeling

The shape of the damage zone (e.g., elastic and cavity radii) and the determination of whether the zones of increasing damage are concentric or variable as a function of depth need to be quantified in order to model the energy distribution throughout the source region. Furthermore, the variations may also occur radially. Remember that the rift zone introduces fairly strong anisotropy into the site. The anisotropy may affect the shape of the damage zones in the horizontal plane. Once the data are complete, then the active data modeling, either using the Sammis (2002) model or the compensated linear vector dipole (CLVD) model will be tested.

ACKNOWLEDGMENTS

REFERENCES

Ashby, M.F. and C. G. Sammis, (1990). The Damage Mechanics of Brittle Solids in Compressions. *Pure appl. Geophys*. **133**. 489-521.

Bollinger, G. A., (1971). Blast vibration analysis. Southern Illinois University Press.

Bonner, J. L., M. Leidig, C. Sammis, and R. Martin (in review). Explosion coupling in frozen and unfrozen rock: Experimental data collection and analysis. Submitted to *Bull. Seism. Soc. Am.*

Brinkmann, J . R., (1987). The control of ground vibration from colliery blasting during the undermining of residential areas. *Jour. S. African Inst. Min. Metall*., 87, 53-61.

Chael, E.P. (1987). Spectral scaling of earthquakes in the Miramichi region of New Brunswick, Bull. Seism. Soc. Am., 77, 347-365.

Cooper, P. W., (1996). Explosives Engineering. VCH Publishers, 460 p.

Doolan, B., (1996). The Geology of Vermont, *Rocks and Minerals Magazine*, Vol. 71, No. 4, pp. 218-225.

Dowding C. H., (1985). Blast vibration monitoring and control. Prentice Hall.

Elseman, I. A., (2000). Measurement and analysis of the effect of ground vibrations induced by blasting at the limestone quarries of the Egyptian Cement Company. *ICEHM2000*, 54-71.

Engelder, T., M. Sbar, R. Kranz, (1977). A mechanism for strain relaxation of Barre Granite: opening of microfractures, *Pure Appl. Geoph*., **115**, 27-40.

Essen, S., I. Onederraa, H. A. Bilgin, (2003). Modelling the size of the crushed zone around a blasthole, *Inter. Jour. of Rock Mechanics and Mining Sci*., 40, 485-495.

Goldsmith W, J. L. Sackman, and R. L. Taylor, (1977). Property determination and wave propagation in a block of Barre granite. *Bull. Seism. Soc. Am.*, 67 (1), 87-102.

Goldstein, P. M., D. Denny, T. Hauk, and S. P. Jarpe (1994). On-site seismic yield (OSSY) estimates for BRISTOL based on nuclear to chemical spectral ratios and yield scaling. *Bull. Seism. Soc. Am*., 84, 343-349.

Gupta, I.N., T.R. Zhang, and R.A. Wagner (1997). Low frequency Lg from NTS and Kazakh nuclear explosions-observations and interpretation. *Bull. Seism. Soc. Am*. **87**, 1115-1125.

Hagan, T. N. and I. M. Gibson (1988). Lower blasthole pressures: a means of reducing costs when blasting rocks of low to moderate strength. *Inter. Jour. of Mining and Geological Engineering*, 6, 1-13.

Harris, D. B. (1991). A waveform correlation method for identifying quarry explosions, Bull. Seism. Soc. Am., 81, 2395-2418.

Hooper, H., J. Bonner, and M. Leidig, (2006). Effects of confinement on short-period surface waves: observations from a new dataset. Bull. Seism. Soc. Am. 96, 697-712.

Kuzu, C. (2008). The importance of site-specific characters in prediction models for blast-induced ground vibrations. *Soil Dynamics and Earthquake Engin*., 28, 405-414.

Masse, R. P. (1981). Review of seismic source models for underground nuclear explosions, *Bull. Seism. Soc. Am*. **71**, 1249 - 1268.

Melnikov, NV. (1962). Influence of explosive charge design on results of blasting. International Symposium on Mining Research, edited by G.B. Clark. V. 1. London: Pergamon Press.

Melosh, H. J., (1979). Acoustic Fluidization: A New Geologic Process. *J. Geophys. Res*., **84**, 7513-7520.

Meyer, R. (1987). Explosives. VCH Publishers, 452 p.

Mueller, R. A., and J. R. Murphy (1971). Seismic characteristics of underground nuclear detonations: Part I, Seismic scaling law of underground detonations, Bull Seism. Soc. Am., 61: 1675.

Muller, C. S. (1985). Source pulse enhancement by deconvolution of an empirical Green's function, Geophys. Res. Letts, 12, 33-36.

Myers, S. C., W. R. Walter, K. Mayeda, and L. Glenn (1999). Observations in support of *Rg* scattering as a source for explosion *S* waves: regional and local recordings of the 1997 Kazakhstan depth of burial experiment, *Bull. Seism. Soc. Am.* **89**, 544 - 549.

Myers, S.C. (2007). Numerical experiments invesigating the source of explosion S-waves. *Seism. Res. Letts.* **78**, p 240.

Patton, H. J. and S. R. Taylor (1995). Analysis of *Lg* spectral ratios from NTS explosions: implications for the source mechanism of spall and the generation of *Lg* waves, *Bull. Seism. Soc. Am.* **85**, 220 - 236.

Patton, H. J. and S. R. Taylor, (1995). Analysis of *Lg* Spectral Ratios from NTS Explosions: Implications for the Source Mechanism of Spall and the Generation of *Lg* Waves, *Bull. Seism. Soc. Am.* **85**, 220 - 236.

Patton, H., J. Bonner, and I. Gupta, (2005). *Rg* Excitation by Underground Explosions: Insights from Source Modeling the 1997 Kazakhstan Depth of Burial Experiments. *Geophys. J. Int*. doi:10.1111/j.1365-246X.2005.02752.x.

Persson, P-A, R. Holmberg, and J. Lee. (1994) Rock Blasting and Explosives Engineering. CRC Press, 540 p.

Reamer, S.K. and B.W. Stump (1991). Source parameter estimation for large, bermed surface chemical explosions, Bull. Seism. Soc. Am., 82, 406-621.

Richter, D. A., (1987). Barre granite quarries, Barre, Vermont, in *Geological Society of America Field Guide – Northeastern Section*, p 239-242.

Rodean, H.C., (1971). Nuclear-Explosion Seismology, U. S. Atomic Energy Commission, TID-25572, 156 pp.

Rosenthal, M. F. and G. L. Morlock, (1987). Blasting guidance manual. Office of Surface Mining Reclamation and Enforcement Directive 315.

Sammis, C. (2003). Scaling laws for secondary seismic radiation generated by fracture damage. Proceedings from the 2003 Research Review. Tucson, AZ.

Sammis, C. G. (2002), Generation of High-Frequency *P* and *S* Wave Energy by Rock Fracture During a Buried Explosion: Its Effect on *P/S* Discriminants at Low Magnitude, Proceedings of the 24th Seismic Research Review – Nuclear Explosion Monitoring: Innovation and Integration, Sept. 17-19, 2002, Ponte Verde Beach, Florida, 542-551.

Sano, O, Y. Kudo, and Y. Mizuta. (1992). Experimental determination of elastic constants of Oshima granite, Barre granite, and Chelmsford granite. *J. Geophys. Res*., 97, 3367–3379.

Sawyers, K. N, (1968). Theoretical changes in seismic travel time with changes in stress with depth. *Bull. Seism. Soc. Am*., 58 (5), 1667-1680.

Siskind, D. E., M. S. Stagg, J. W. Kopp, and C. H. Dowding, (1980). Structure response and damage produced by ground vibration from surface mine blasting. US Bureau of Mines Report of Investigation 8507.

Stevens, J.L., G. E. Baker, H. Xu, T.J. Bennett, N. Rimer, and S.M. Day (2003a). The physical basis of *Lg* generation by explosion sources. *Proceedings of the 25th Annual Seismic Research Review on Nuclear Monitoring Technologies*, Tucson AZ.

Stevens, J.L., N. Rimer, H. Xu, G.E. Baker, S.M. Day, (2003b). Near-field and Regional Modeling of Explosions at the Degelen Test Site. SAIC Final Report SAIC-02/2050.

Stump, B. W. (1985). Constraints on explosive sources with spall from near-source waveforms, Bull. Seism. Soc. Am. 75, 361-377.

Stump, B. W., D. C. Pearson, and R. E. Reinke, (1999). Source comparisons between nuclear and chemical explosions detonated at Rainier Mesa, Nevada Test Site. Bull. Seism. Soc. Am., 89, 409-422.

Stump, B. W., D.C. Pearson, and V. Hsu, (2003). Source scaling of contained chemical explosions as constrained by regional seismograms. Bull. Seism. Soc. Am., 93, 1212-1225.

Xia, K, M. H. B. Nasseria, B. Mohantya, F. Lub, R. Chenb, and S. N. Luo, (2008). Effects of microstructures on dynamic compression of Barre granite. *Inter. Jour. of Rock Mechanics and Mining Sci.*, 45 (6), 879-887.

Xie, X. and T. Lay, (1994). The excitation of *Lg* waves by explosions: a finite-difference investigation, *Bull. Seism. Soc. Am.*, **84**, 324-342.

Yang, X., (1997). Mining explosion and collapse source characterization and modeling with near-source seismic data. Ph.D. Thesis, Southern Methodist University, Dallas, Texas.

Zhou, R.M. and B. Stump (2005). Source scaling of single-fired mining explosions with different confinement and explosive size at a copper mine, Arizona. In Leidig *et al*. eds. Source Phenomenology Experiments in Arizona, Final Report, 269-289.

LIST OF SYMBOLS, ABBREVIATIONS, AND ACRONYMS

ANFO   Ammonium Nitrate Fuel Oil
COMP B Composition B Explosive
CLVD   Compensated linear-vector dipole
NEDE   New England Damage Experiment
NER   New England Research, Inc.
SNR   Signal to noise ratio
VOD   Velocity of detonation
WGC   Weston Geophysical Corp.